The Dissertation Committee for Woosuk Bang Certifies that this is the approved version of the following dissertation:

Cluster Fusion Experiments on the Texas Petawatt Laser

Committee:

Todd Ditmire, Supervisor

Roger Bengtson

Michael C. Downer

Wendell Horton

Sheldon Landsberger

Cluster Fusion Experiments on the Texas Petawatt Laser

by

Woosuk Bang, B.S.

Dissertation

Presented to the Faculty of the Graduate School of

The University of Texas at Austin

in Partial Fulfillment

of the Requirements

for the Degree of

Doctor of Philosophy

The University of Texas at Austin

August, 2012

Acknowledgements

It feels always good to have someone who trusts me and supports me. Probably, I should have expressed my gratitude more often than just writing down their efforts here. Most of the work presented in this dissertation would not have been possible without the help and support from many people. First and foremost, I want to thank my advisor, Todd Ditmire. His passion and enthusiasm for physics always inspired me, and his wonderful insight guided me throughout my graduate career. A short discussion with him was always worth more than a few hours of reading the literature. He was also very supportive of my work, and I think every graduate student knows how much that means for his/her research work. I am also very thankful for the great deal of knowledge that I learned from his terrific lectures about the high energy density physics and laser physics.

Next, I want to thank my committee members. When I was a first year graduate student, I met Dr. Horton in his classical mechanics class. His assignments were especially helpful to me in that I was able to develop the basic programming skills to solve physics problems. I remember sending him a thank you note for that after the semester was over. I also thank him for his kind offer to join his research group. Dr. Bengtson always showed much interest in my progress, and that was very encouraging to me. Whenever I updated him with either my simulation results or the experimental results, he generously showed his interest during my update. He also gave me opportunities to present my results in the plasma seminar, and I am very grateful for that. I would like to thank Dr. Jane and Mike Downer for their Glenn Focht Memorial Fellowship. I will never forget the dinner we had together with the remaining family of Dr. Focht. I also want to thank Dr. Downer for his useful advice and suggestions about

the analysis of my experimental results. Dr. Landsberger is a professor at the Nuclear Engineering Teaching Laboratory (NETL), and I took his nuclear analysis techniques class. The class was very well organized, and it was of practical use to me. Though I did not have many chances to interact with him, I always wanted to express my gratitude for his becoming one of my committee members.

When I used Cf-252 neutron source at the NETL for the calibration of the CR-39 detectors and indium activation detectors, I got much help from Dr. Sean O'Kelly. On the Texas Petawatt Laser, I received a lot of help from Dr. Erhard Gaul, Mikael Martinez, Franki Aymond, and Ted Borger. During my experiments, I got much help from Dr. Hernan Quevedo, Dr. Gilliss Dyer, Dr. Aaron Bernstein, Johannes Rougk, Intai Kim, Matt McCormick, and a few undergraduate students in our group. I am truly thankful for their support and help during the experimental campaign.

During the deuterium cluster and helium-3 mixture fusion experiment, I worked with many researchers from Texas A&M University and from Italy. I really enjoyed working with them, and wanted to show my gratitude for their work and efforts. Whenever I visited TAMU, Dr. Aldo Bonasera, Dr. Marina Barbui, Dr. Kris Hagel, Dr. Joe Natowitz, and Dr. Kasia Schmidt all showed their warm welcome. The discussions we had were exciting and really valuable in the analysis of the results, too.

I was lucky to have many excellent teachers in my early days in South Korea. I want to thank Suyeon Lee and Youngmun Shin, both of whom were science teachers in my middle school. They were genuinely interested in my progress, and always supported me. I also want to thank Dr. Chang Hee Nam, whose optics I, II classes were among the best lectures I have taken so far.

I deeply thank my Korean friends at UT, too. We had lunch together almost every weekday, and spent some time talking about our lives. I want to thank Yong-Sup

Ihn, Dr. Seongheon Kim, Hyungdo Nam, Insun Jo, Kidam Mun, Jusang Yang. I also want to thank former UT students, Dr. BI Cho, Dr. Bonggu Shim, Dr. Changbae Hyun, Dr. Jungdae Kim, Dr. Jaekwang Lee, Dr. Juhyung Kim, Dr. Junho Bae, from whom I learned a lot of things.

Finally, I want to thank my family, especially my parents, Hyomu Bang and Bohwa Lee. My parents and my younger sister always supported me in numerous ways. Without their support and love, I would not have been able to complete the work. I thank my wonderful wife, Jungwon Lee, who has been the biggest supporter of my life.

Woosuk Bang

The University of Texas at Austin

August 2012

Cluster Fusion Experiments on the Texas Petawatt Laser

Woosuk Bang, Ph.D.

The University of Texas at Austin, 2012

Supervisor: Todd Ditmire

Interactions between an intense laser pulse and cluster targets are investigated using the recent experimental results of the cluster fusion experiments on the Texas Petawatt Laser (TPW). We achieved about $2x10^7$ DD fusion neutrons per shot on the TPW by optimizing the laser and gas jet parameters. A few different types of cluster targets were used on the TPW including deuterium clusters, deuterated methane clusters, deuterium cluster + helium-3 mixture, and deuterated methane cluster + helium-3 mixture. We designed our own neutron detectors and proton detectors for the measurements of the fusion yields. The calibration method of neutron detectors is described in detail. Through the yield measurements of the 2.45 MeV neutrons from the DD fusion reactions and 14.7 MeV protons from the D-^{3}He fusion reactions in the deuterium-helium-3 mixture target, we successfully measured the ion temperature of the fusion plasma at the time of the fusion reactions.

Table of Contents

List of Tables

List of Figures

Chapter 1. Introduction

1.1. Overview

The interactions between intense laser pulses and atoms or molecules have produced many interesting phenomena, and have drawn much attention for the past few decades.[1-10] Typically in these experiments, solid targets or gas targets have been used. The irradiation of solid targets with intense laser pulses leads to the generation of energetic electron beams,[7,11] x-rays,[12] and energetic ion beams.[13-15] Sometimes, the kinetic energies of these ions are high enough to produce nuclear fusion reactions when the ions collide with themselves.[16-21] The gas targets are also important opening new research areas such as high harmonic generation,[22] attosecond pulse generation, and wakefield acceleration.[9,10,23]

About 20 years ago, researchers started using a new state of matter called clusters [24] in the laser experiments. The atomic clusters are in an intermediate state between solid and gas in the sense that the overall density of cluster targets is similar to a gas density while the local density of each atomic cluster is near solid density. Simply speaking, an atomic cluster is an aggregate of many atoms combined together via their van der Waals potentials. The size of a cluster typically ranges from one nanometer to a few tens of nanometers. Due to its high local density, a cluster can efficiently absorb the laser pulse energy.[4] In our experiments, we used these cluster targets to generate nuclear fusion reactions.

1.2. Motivation

The laser-cluster generated fusion plasma is attractive as a bright, short, and localized neutron source which is potentially useful for neutron radiography or material damage studies. The numerous petawatt lasers currently operating and being built with

pulse durations below 200 fs have the potential to drive such sources. Once a neutron flux higher than 10^9 n/cm^2 is achieved, then the sub-ns neutron pulse can be used as a pump beam to do a time-resolved pump-probe experiment for the neutron damage studies.[25]

1.3. PLAN FOR THE THESIS

In the next chapter, an overview of the physics related to the laser-cluster interaction is discussed with an emphasis on the cluster fusion experiment. Cluster heating mechanisms, expansion of the fusion plasma, and the quasi-neutrality are discussed, and the inverse bremsstrahlung heating is discussed in detail.

A typical laser experiment involving a high power laser consists of three key elements. First, we need a high power laser,[26,27] about which I tried to give a detailed description in Chapter 3. Our primary laser for the main experiments was the Texas Petawatt Laser (TPW),[26] but we also used the Texas High-Intensity Optical Research (THOR) laser[27] for some preliminary experiments and for the calibration[28] of neutron detectors.

Secondly, we need a target. Solid targets and gas targets are the two most commonly used targets for the laser experiments although liquid targets[29] can be used as well. In our experiments, we used deuterium clusters,[16] deuterated methane clusters,[18,20] and a deuterium cluster + Helium-3 mixture[30] as our targets. In Chapter 4, I will show how we prepared the cluster targets for the experiments. I will start with describing what clusters are, and how one can generate the cluster targets. The design for the supersonic nozzle and the liquid nitrogen cooling lines are given in the same chapter. The characteristics of our cluster targets are investigated some detail. For the mixture cluster target, we measured the composition of our target using the Residual Gas Analyzer (RGA). I will also show some Rayleigh scattering measurements that

indicated similar cluster formation in the case of deuterium cluster + helium-4 mixture target.

Thirdly, we need a set of diagnostics to investigate the interaction between intense laser pulses and cluster targets. In Chapter 5, I will show how I calibrated the neutron detectors. Three types of neutron detectors (plastic scintillation detectors, indium activation detectors, and CR-39 track detectors) were calibrated for the measurement of 2.45 MeV DD fusion neutron yields from the deuterium cluster fusion experiment on the TPW. A Cf-252 neutron source and 2.45 MeV fusion neutrons generated from laser-cluster interaction were used as neutron sources. The scintillation detectors were calibrated such that they can detect up to 10^8 DD fusion neutrons per shot in current mode under high electromagnetic pulse environments. Indium activation detectors successfully measured neutron yields as low as 10^4 per shot and up to 10^{11} neutrons. The use of Cf-252 neutron source allowed cross calibration of CR-39 and indium activation detectors at high neutron yields (~10^{11}). The CR-39 detectors provided consistent measurements of the total neutron yield of Cf-252 when a modified detection efficiency of 4.6×10^{-4} was used. The combined use of all three detectors allowed for a detection range of 10^4 to 10^{11} neutrons per shot.

In Chapter 6, the recent experimental results on TPW with deuterium clusters and deuterated methane clusters are given in much detail.[31] The main goal during this experimental campaign was to increase the neutron yield from the fusion plasmas. Detailed analysis and discussion about the implications of the results are given. During this run, we used plasma mirrors[32,33] to investigate the effect of possible pre-pulses of TPW on the cluster fusion experiments. A detailed description of the setup for using plasma mirrors is described in Chapter 6 and Appendix E as well.

In Chapter 7, results from another recent experimental campaign using mixture cluster targets are given, whose main focus was to measure the ion temperature of fusion plasmas at the time of the fusion reactions. With cryo-cooled deuterated methane cluster + helium-3 mixture target, we observed deuterium ions with ion temperature as high as 28 keV. Using deuterium cluster + helium-3 mixture as the target, we successfully generated both DD fusion reactions and D-^{3}He fusion reactions in the fusion plasma. By comparing the neutron yield from DD reactions with the 14.7 MeV proton yield from D-^{3}He fusion reactions, we were able to calculate the temperature of the fusion plasma at the time of the fusion reactions. The underlying physics and discussion of the results are given in the same chapter.

Finally, a summary of the experimental results and discussions about the application of this work are given in Chapter 8, which concludes the dissertation.

Chapter 2. Physics of the intense laser-cluster interactions

This chapter is aimed to introduce some of the basic concepts that are necessary to understand the results of the cluster fusion experiments. As mentioned in the previous chapter, clusters absorb the laser pulse energy very efficiently.[4] The cluster heating mechanisms that are relevant to this efficient absorption will be briefly discussed in this chapter. Then, I will show our current understanding of the cluster fusion experiment. Some expansion dynamics of the fusion plasma will be examined.

2.1. FREE ELECTRON IN AN OSCILLATING ELECTRIC FIELD

A free electron in an oscillating laser field will accelerate due to the electromagnetic field of the laser. In this section, we want to calculate the average kinetic energy of an electron in a strong electric field with an oscillating laser frequency of ω_0 and a peak amplitude of E_0. Assuming no other ions or electrons around, the equation of motion of an electron under an electric field, $\overrightarrow{E(t)} = \mathrm{Re}[E_0 \exp(-i\omega_0 t)] = E_0 \cos\omega_0 t$, can be written as:

$$m_e \frac{d^2x(t)}{dt^2} = e\,\overrightarrow{E(t)} = e\,E_0 \cos\omega_0 t, \qquad (2.1)$$

where m_e is the mass of an electron, t is the time, $x(t)$ is the position of the electron at time t, and e is the charge of an electron.

Solving equation (2.1) for the position and velocity of the electron using the initial conditions of $x(t=0)=x_0=0$ and $v(t=0) = dx(t=0)/dt = v_0=0$, we get the following solutions for $v(t)$ and $x(t)$:

$$v(t) = \frac{eE_0}{m_e\omega_0}\sin\omega_0 t, \qquad (2.2.a)$$

$$x(t) = -\frac{eE_0}{m_e\omega_0^2}(\cos\omega_0 t - 1). \qquad (2.2.b)$$

Therefore, the kinetic energy of the electron can be expressed as a function of time, and the kinetic energy of the electron averaged over one laser cycle becomes

$$< K(t) > = \frac{1}{2} m_e < v(t)^2 > = \frac{e^2 E_0^2}{2 m_e \omega_0^2} < sin^2\, \omega_0 t > = \frac{e^2 E_0^2}{4 m_e \omega_0^2} = U_p, \qquad (2.3)$$

where < > indicates an average over one laser cycle, and $< \sin^2 \omega_0 t > = 1/2$ was used in the calculation. U_p is commonly called the quiver energy or the ponderomotive potential of the electron. U_p can also be expressed in terms of the laser intensity, $I(t)$, and the wavelength, λ, of the laser pulse. Using $I=1/2*c\varepsilon_0 E_0^2$ and $\omega_0=2\pi c/\lambda$, the ponderomotive potential is

$$U_p[eV] = \frac{e^2 E_0^2}{4 m_e \omega_0^2} = \frac{e^2}{4 m_e} \frac{2I}{c\varepsilon_0} \frac{\lambda^2}{4\pi^2 c^2} = 9.33 \times 10^{-14}\, I \left[\frac{W}{cm^2}\right] \lambda[\mu m]^2. \qquad (2.4)$$

Now is a good time to pause and think about what this value means in the laser-cluster experiments. Equation (2.4) shows the electron quiver energy as a function of the laser intensity. With very intense laser pulses, one can expect to observe very energetic electrons during the laser pulse. On the TPW, laser pulses with intensities higher than 10^{16} W/cm^2 are easily produced. Since the wavelength of the TPW is about 1.057 μm, the average kinetic energy of the electrons while they are subject to a laser field with intensity of 10^{16} W/cm^2 is about 1.0 keV. This energy is much greater than the incoming photon energy of 1.2 eV, and one might naturally think that the laser pulse energy was somehow transferred to the electrons very efficiently. However, this is not entirely true. It is correct to say that the average kinetic energy of the electrons under strong electric field is expressed with equation (2.4), but the oscillating electrons in this field eventually come to a rest as the intensity of the pulse becomes smaller after the laser pulse duration. In other words, the energy transfer from the laser pulse to the electrons is not a permanent one. Later in this chapter, I will show when the electrons can absorb the laser pulse energy and how clusters absorb the pulse energy efficiently.

Now that we calculated the cycle-averaged kinetic energy of an electron in a strong laser field, it would be worth comparing this with that of an ion in the same field. Following the same procedure, the quiver energy of an ion in the laser field becomes

$$U_{p,ion}[eV] = \frac{e^2 E_0^2}{4m_{ion}\omega_0^2} = \frac{e^2}{4m_{D\,ion}} \frac{2I}{c\varepsilon_0} \frac{\lambda^2}{4\pi^2 c^2} = 2.5 \times 10^{-17}\, I\left[\frac{W}{cm^2}\right] \lambda[\mu m]^2, \quad (2.5)$$

where the mass of an ion is used in the denominator instead of the much smaller mass of the electron. Note that the positive charge of an ion does not change the sign of the ponderomotive potential. For the purpose of comparison, the mass of a deuterium ion was used in the last step of equation (2.5). While the ponderomotive potential of an electron is about 1 keV at 10^{16} W/cm^2, the ponderomotive potential of a deuterium ion is only 0.25 eV. This is even smaller than the energy of one photon, and indicates that the laser pulse energy is not efficiently absorbed by the ions at this laser intensity. This is true in the case of cluster fusion experiments where the incoming laser intensity ranges from about 10^{15} W/cm^2 to about 10^{18} W/cm^2.

2.2. IONIZATION OF A CLUSTER

2.2.1. Inner-ionization and outer-ionization

The ionization of an atom can be considered as the process of converting a neutral atom into a positive ion and a free electron. Likewise, the ionization of a cluster can be thought as the process of freeing all the electrons from the cluster. This ionization process can be understood as a two-step process.

First, the individual atoms inside a cluster have to be ionized. This process is often called the inner-ionization, and is similar to the ionization process of an atom. After a complete inner-ionization, the cluster consists of positive ions and free electrons. The electrons are free to move within the cluster, but they are still bound to the cluster. Much more energy is required to free the electrons from the cluster, and this second process is often called the outer-ionization.[34] After the outer-ionization, the electrons are free and the cluster consists of positive ions only, which makes the cluster unstable.

2.2.2. IONIZATION OF INDIVIDUAL ATOMS INSIDE A CLUSTER

In this section, I will describe the ionization process of individual atoms inside a cluster. Various ionization mechanisms that are relevant to the laser-cluster fusion experiment will be discussed.

2.2.2.1. Multiphoton ionization

In section 2.1, we introduced the cycle-averaged kinetic energy of electrons, or the ponderomotive potential, U_p. We also mentioned the photon energy, $\hbar\omega_0$. Now, we can think of a net potential energy of an electron bound to an atom. The energy that has to be supplied to free a bound electron is called the ionization potential, I_p. Therefore, we have at least three different energy scales to consider in a laser-cluster experiment.[35]

If the ponderomotive potential is much smaller than the photon energy and the ionization potential, lowest order perturbation theory (LOPT) can be applied.[5,35] This corresponds to laser intensities much lower than 10^{13} W/cm^2 for 1 μm laser systems in deuterium cluster fusion experiments.

The multiphoton ionization (MPI) was accurately modeled by LOPT, and the *n*-photon ionization rate is given by[5]

$$\Gamma_n = \sigma_n I^n, \tag{2.6}$$

where n is the minimum number of photons required for ionization, σ_n is the generalized n-photon ionization cross section, and I is the laser intensity.

2.2.2.2. Above-threshold ionization (ATI)

In 1979, it was found that MPI by more photons than the minimum required photon number can happen.[36] This is called the above-threshold ionization (ATI). They reported that electrons sometimes carried more energy than one photon energy in

their experiments for laser intensities of around 10^{13} W/cm^2. Though this is a strong-field MPI, perturbation theory has been applied to ATI. The ionization rate follows similar form as equation (2.6), and it was experimentally verified by Fabre *et al*. in 1982:[37,38]

$$\Gamma_{n+s} \propto I^{n+s}, \tag{2.7}$$

where *s* is the number of excess photons absorbed by the electron. The kinetic energy carried by the electron after ATI can be written as

$$E=(n+s)\hbar\omega-I_p. \tag{2.8}$$

As we will see in section 2.3, ATI is important in the heating of a cluster since the electrons carry excess kinetic energy, and can escape from the cluster.

2.2.2.3. Tunneling ionization

Now, comparing the ponderomotive potential, U_p, and the ionization potential energy, I_p, the Keldysh parameter[39] is defined as

$$\gamma = \sqrt{\frac{I_p}{2U_p}}. \tag{2.9}$$

For $\gamma>1$, the ponderomotive potential is smaller than the ionization potential, and this regime is called the MPI regime. When $\gamma<1$, the electric field of a laser pulse is strong enough to distort the atomic potential energy. Therefore, the laser field affects the potential energy near the ion, and the electron tunneling rate changes due to the laser field. The tunneling ionization rate for hydrogen-like ions in a quasi-static electric field was first calculated by Landau, and is given by:[40]

$$W_{DC} = 4\omega_a\left(\frac{I_p}{I_H}\right)^{5/2}\frac{E_a}{|E(t)|}\exp\left[-\frac{2}{3}\left(\frac{I_p}{I_H}\right)^{3/2}\frac{E_a}{|E(t)|}\right], \tag{2.10}$$

where I_H=13.6 eV is the ionization potential of hydrogen, ω_a=4.13x10^{16} /s is the atomic unit of frequency, E_a=5.14x10^9 V/cm is the atomic unit of electric field, and *E(t)* is the instantaneous applied electric field at time *t*.

To calculate the tunnel ionization rate of a complex atom or ion, the ionization model developed by Ammosov, Delone, and Krainov (ADK) is often used.[41] Augst *et al*. found that the ADK ionization rate agreed with their experimental results using He, Ar, Ne, Kr, and Xe over a wide range of intensities.[42] They also proposed using the term barrier-suppression ionization (BSI) for ionization at high enough intensities.

The BSI model predicts that there is a threshold intensity, above which the electron can freely escape from the atom because the strong field completely suppressed the Coulomb potential of the ion. The ionization threshold intensity can be estimated as:

$$I_{BSI}[\frac{W}{cm^2}] = 4.0 \times 10^9 I_p^4[eV]/Z^2, \quad (2.11)$$

where I_p is the ionization potential energy of the atom or ion in eV and Z is the charge state of the ion. For a deuterium molecule, this threshold intensity is estimated as 2.3×10^{14} W/cm^2 using the ionization potential energy of 15.47 eV. Therefore, a complete inner-ionization of a deuterium cluster is expected when the incoming laser intensity exceeds 10^{15} W/cm^2, which is true for laser cluster fusion experiments.

2.3. CLUSTER HEATING MECHANISMS

In this section, I will describe how the electrons inside a cluster further gain energy from the laser pulse and escape from the cluster. Even after a complete inner ionization, most of the electrons are still bound to the cluster. As the electrons escape from the cluster, there is a potential buildup on the surface of the cluster. Therefore, the electrons need to absorb more energy to overcome this potential barrier to escape from the cluster.

As was introduced in section 2.2.1, this ionization process is called outer ionization. For a deuterium cluster with a diameter less than 10 nm, the potential barrier

at the surface can easily become a few keV. A few heating mechanisms are known to be relevant in this stage, and these will be briefly discussed.

The first well known heating mechanism is the above-threshold-ionization (ATI). As described earlier, this is a multi-photon ionization process. This time, the electron carries excess photon energy when it overcomes the outer-ionization potential barrier.

A resonant heating becomes very important when a cluster expands and the local density of the cluster drops to the point when resonant absorption can occur. The electric field inside the cluster becomes huge, and the electrons collectively gain very high kinetic energy from the strong electric field. Since this process is not adiabatic, there is a net gain in the kinetic energy of electrons.

A vacuum heating[43] can also contribute to the heating at the interface. After some electrons are pulled out of a cluster by the laser field, some of them are driven back to the cluster and lose their kinetic energy to less energetic electrons. A stochastic heating[44] can happen for a large cluster, but it is not important in our experiments because the average size of our deuterium cluster is not large enough.

Finally, inverse bremsstrahlung (IB) heating[45-47] is a very important heating mechanism in a cluster. Resonant heating does not occur inside a cluster initially because the local density of a cluster is near solid density, which is too high for an efficient resonant absorption. However, the IB heating becomes a very efficient heating mechanism at higher densities, and it can be considered as the most important heating mechanism during the early stage of the laser-cluster interaction.

2.4. COULOMB EXPLOSION OF A CLUSTER

As the electrons escape from the cluster, the ions inside the cluster start expanding due to their own repulsive Coulomb force. Because of much bigger mass of the ions,

the expansion rate is very small compared with the time scale that the electrons escape from the cluster. Therefore, the ions can be considered nearly stationary during the outer ionization process for the sake of a simple model. Then, the expansion rate of the cluster or the kinetic energy of the ions can be calculated using the Coulomb explosion model. I will start by describing the Coulomb explosion model for further analysis.

Let's assume that the intensity of the laser pulse was high enough to strip all of the electrons out of the cluster, and that all of the electrons escaped from the cluster at time t=0. If N electrons escaped from the cluster, the charge build-up on the cluster is Q=+Ne. For a cluster with radius R and atomic number density n, the total number of ions inside a fully stripped cluster becomes:

$$N = n \times \frac{4\pi}{3} R^3. \tag{2.12}$$

For deuterium clusters, the Coulomb potential energy of the outermost deuterium ions can be calculated as [17],

$$E_{max}(r = R) = \frac{Qe}{4\pi\varepsilon_0 R} = \frac{Ne^2}{4\pi\varepsilon_0 R} = \frac{\frac{4\pi R^3}{3} ne^2}{4\pi\varepsilon_0 R} = \frac{ne^2 R^2}{3\varepsilon_0}, \tag{2.13}$$

where Q=Ne is the total charge inside a cluster of radius R, e is the charge of the deuterium ion, n is the density of the cluster, and ε_0 is the vacuum permittivity.

Similarly, the Coulomb potential energy of i-th ion located at distance r away from the center can be expressed as

$$E_i(r) = E(r) = \frac{Q(r)e}{4\pi\varepsilon_0 r} = \frac{\frac{4\pi r^3}{3} ne^2}{4\pi\varepsilon_0 r} = \frac{ne^2 r^2}{3\varepsilon_0}, \tag{2.14}$$

where $Q(r)$ is the total charge inside a ball of radius r within the cluster. Then, the average potential energy of the ions becomes [17]:

$$< E >= \frac{\sum_{i=1}^{N} E_i(r)}{N} = \frac{\int_0^R E(r) dN(r)}{N} = \frac{\int_0^R \frac{ne^2 r^2}{3\varepsilon_0} (n 4\pi r^2 dr)}{n\frac{4\pi R^3}{3}} = \frac{ne^2 R^2}{5\varepsilon_0} \ \left(= \frac{3E_{max}}{5}\right). \tag{2.15}$$

Upon Coulomb explosion, the potential energy of each ion is transferred into the kinetic energy of each ion. Therefore, the average kinetic energy of the ions becomes $< E >= \frac{ne^2R^2}{5\varepsilon_0}$ according to the Coulomb model, and the maximum kinetic energy of the ions would be $E_{max} = \frac{ne^2R^2}{3\varepsilon_0}$. In our experiments, the ion energy spectrum was very similar to that from a Maxwellian distribution, and we defined the ion temperature of the fusion plasma as $kT = 2/3 <E>$, where $<E>$ is the average kinetic energy of the ions from ion time-of-flight (TOF) measurements.

Now, a time scale for this explosion can be estimated in considering the requirements for the laser. The expansion time of a cluster is often defined as the time it takes for the cluster to expand to twice the initial size.[48] This characteristic explosion time is roughly estimated as about 20 fs, if an instant outer-ionization is assumed.[48]

In describing the Coulomb explosion model, we assumed the laser intensity was high enough to strip all the electrons out of the cluster. This threshold intensity is often called the critical intensity. At the critical intensity, an electron at the surface of a nearly fully stripped cluster has a total energy higher than 0. The potential energy of an electron at the surface of the cluster is expressed as

$$E_p(r = R) = \frac{Qe}{4\pi\varepsilon_0 R} = \frac{-\frac{4\pi R^3}{3}n_0 e^2}{4\pi\varepsilon_0 R} = -\frac{n_0 e^2 R^2}{3\varepsilon_0}, \quad (2.16)$$

where Q is the total charge of the fully stripped cluster, n_0 is the liquid density of deuterium, and R is the radius of the cluster. The kinetic energy of this electron can be approximated as the ponderomotive potential energy. Therefore, the condition to have a total energy higher than 0 gives a condition for the laser intensity as follows

(Total energy of an electron at the surface of the cluster) = $E_p + U_p = -\frac{n_0 e^2 R^2}{3\varepsilon_0} + 9.33 \times 10^{-14}\, I\left[\frac{W}{cm^2}\right]\lambda[\mu m]^2\,[eV] > 0,$ (2.17)

Solving the inequality, we have an expression for the critical intensity, above which the clusters can be fully stripped by the laser pulse. The critical intensity, I_{crit}, in W/cm^2 for clusters with radius R in nm, and wavelength of the laser in μm becomes

$$I_{crit}\left[\frac{W}{cm^2}\right] > 3.14 \times 10^{15}\frac{R[nm]^2}{\lambda[\mu m]^2}. \quad (2.18)$$

For a cluster with a radius of 7.9 nm, the critical intensity of a 1.06 μm laser is about 1.7x10^{17} W/cm^2.

2.5. CLUSTER FUSION MODEL

2.5.1. Expression for the neutron yield

Sometimes, the kinetic energy of the deuterium ions from the Coulomb explosion of deuterium clusters becomes high enough to generate nuclear fusion reactions when one ion from one cluster collides with another ion from a different cluster. DD fusion can also occur when an energetic ion from a cluster collides with a cold atom in the background gas jet. As a result of the DD fusion reactions, 2.45 MeV neutrons are produced 50% of the time, and we are interested in utilizing these quasi-monoenergetic neutrons.

Previous studies show that the DD fusion neutron yield in a cluster fusion experiment can be expressed as [18]

$$Y = \frac{1}{2}\int n_D^2 < \sigma v > dVdt + N_{ion}\int n_D < \sigma_v > dl \approx \frac{\tau_d}{2}\int n_D^2 < \sigma v > dV + N_{ion}\int n_D < \sigma_v > dl, \quad (2.19)$$

where, τ_d is the disassembly time of the fusion plasma, n_D is the average deuterium density, σ is the fusion cross section, v is the velocity of the ion, $< \sigma v >$ is the fusion reactivity, dV is the volume element of the fusion plasma, N_{ion} is the total number of hot ions, $<\sigma_v>$ is the velocity averaged fusion cross section, and dl is the length element of

the gas jet. The first term on the right is often called the beam-beam contribution. The second term is usually called the beam-target contribution.

Looking at the expression for the fusion neutron yield, we can think of a few ways to increase the neutron yields. First, we might increase the disassembly time of the fusion plasma. Efforts to create a high magnetic field to confine the fusion plasma will be a good example of this. Secondly, we might try to increase the overall gas density of the deuterium target. In our experiments, the density was about 10^{19} atoms/cm^3, but increase in the density will result in higher neutron yield. Next, we can increase the ion temperature of the fusion plasma to have higher fusion reactivity. The DD fusion reactivity increases very fast as the ion temperature increases in the energy ranges that we observe during cluster fusion experiments. This can be seen from the following figure. If the ion temperature increases from 2 keV to 8 keV, the fusion reactivity increases about 100 times.

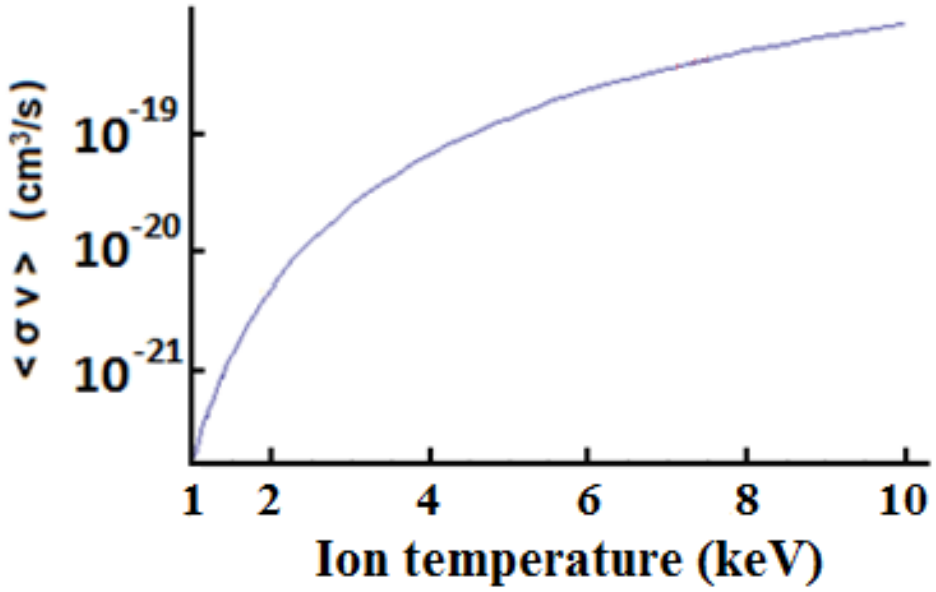

Figure 1. DD fusion reactivity is shown as a function of the ion temperature.

Another way to increase the neutron yield would be to increase the volume of the fusion plasma, or increase the total number of hot ions. We actually used this approach to enhance the neutron yield from the TPW cluster fusion experiments. In Chapter 6, I will describe how we increased the interaction volume and increased the total number of energetic ions on the TPW while keeping the laser intensities high enough to have high ion temperature.

Finally, an increase in the *dl* can enhance the neutron yield. A good example of this approach would be to have more background target deuterium atoms. For example, we can place a deuterated plastic around the gas jet for this purpose. Increasing the gas jet dimension itself does not help usually because the overall atomic density often drops if one just increases the gas jet size.

2.5.2. Disassembly time of the fusion plasma

In equation (2.19), the physical meaning of the plasma disassembly time is rather unclear. In this section, I will show how it is related with other gas jet parameters. For the purpose of this section, let's focus on the beam-beam contribution only. We will assume a cylindrical fusion plasma with an initial radius of R_0 and length of L_0. As the plasma expands, the density n_D will drop as well. This is not accounted for in the previous equation (2.19). Let's further assume that the expansion speed of the ions is the mean speed of the ions, $\langle v \rangle$. At time t, the radius of the plasma and length of the plasma becomes

$$R(t)=R_0 + \langle v \rangle t, \qquad L(t)=L_0 + 2\langle v \rangle t \tag{2.20}$$

Then, the volume of the plasma $V(t)$ can be calculated, and the density of the hot ions can be expressed as a function of time as follows

$$n_D(t) = \frac{N_0}{V(t)} = \frac{N_0}{\pi R(t)^2 L(t)}, \tag{2.21}$$

where the total number of the hot ions, N_0, does not change in time, and one can write $N_0 = \int n_D(t) dV(t)$.

Therefore, the beam-beam contribution becomes

$$Y_{bb} = \frac{1}{2}\int n_D^2 < \sigma v > dVdt = \frac{1}{2}\int n_D(t) < \sigma v > N_0 dt = \frac{1}{2}\int \frac{N_0}{\pi R(t)^2 L(t)} < \sigma v > N_0 dt \approx \frac{N_0^2}{2\pi} < \sigma v > \int_0^\infty \frac{1}{R(t)^2 L(t)} dt, \quad (2.22)$$

where $<\sigma v>$ is assumed to be constant in time in the last step.

Since we know the radius and length of the plasma as a function of time, we can calculate the integral term explicitly as follows

$$\int_0^\infty \frac{1}{R(t)^2 L(t)} dt = \frac{1}{2}\int_0^\infty \frac{dt}{(R_0 + <v>t)^2 (L_0/2 + <v>t)} = \frac{1}{2<v>}\left[\frac{1}{\left(\frac{L_0}{2} - R_0\right) R_0} - \frac{1}{\left(\frac{L_0}{2} - R_0\right)^2} \ln\left(\frac{L_0}{2R_0}\right)\right]. \quad (2.23)$$

Inserting this result into the equation (2.22), we get the following expression for the neutron yield from the beam-beam contribution,

$$Y_{bb} \approx \frac{N_0^2}{2} < \sigma v > \frac{1}{\pi R_0^2 L_0} \tau_d = \frac{1}{2} n_D^2 < \sigma v > V_0 \tau_d, \quad (2.24)$$

where τ_d is calculated using the following formula for $R_0 = \alpha L_0$,

$$\tau_d = \frac{R_0}{<v>}\left[\frac{1}{1-2\alpha} + \frac{2\alpha \ln 2\alpha}{(1-2\alpha)^2}\right]. \quad (2.25)$$

This analysis indicates that the disassembly time of the plasma is equivalent to the effective confinement time assuming a uniform density of n_D in the expression for the beam-beam contribution. The physical meaning of the equation (2.25) is surprisingly simple. The disassembly time is equal to 0.5–1.0 times the time it takes for an ion to travel the initial radius of the cylindrical fusion plasma. In the limit α goes to zero, the disassembly time is $R_0/<v>$. In the opposite case, when α goes to 1/2, the disassembly time becomes $R_0/(2*<v>)$. As an example, the disassembly time becomes $0.747* R_0/<v>$ if $R_0 = 0.1 L_0$.

2.6. EXPANSION OF THE FUSION PLASMA

2.6.1. Expansion of a quasi-neutral plasma sphere

In this section, we will consider a simplified model of an expanding plasma to understand the expansion of the fusion plasma. Let's imagine a big neutral plasma sphere with an initial radius of 300 μm that consists of hot ions and relatively cold electrons after the Coulomb explosion. After complete outer ionization of the deuterium clusters, the ions gain high kinetic energy after Coulomb explosion as we saw in detail from the previous section. The average kinetic energy of these ions can be several keV according to previous experiments[20,48] using deuterium clusters or deuterated methane clusters. To simplify our model, we will assume the electrons remain cold inside the plasma while the ions have an ion temperature of 10 keV. We define the ion temperature as 2/3 times the average kinetic energy of ions; 10 keV was chosen to reflect our measurements on the TPW. With this model, I want to show that quasi-neutrality of the plasma is kept during the expansion. I will also show that the temperature drop in the remaining plasma after very hot ions leave the sphere is insignificant according to this model.

Figure 2 shows the schematic diagram of an expanding plasma sphere with radius $a(t)$ after N_i ions escaped from the plasma leaving a negative net charge in the surface. Ions that do not have sufficient kinetic energy to overcome this potential energy are assumed to bounce off of the virtual boundary formed by the electron shell. The validity of this assumption will be checked in section 2.6.3.

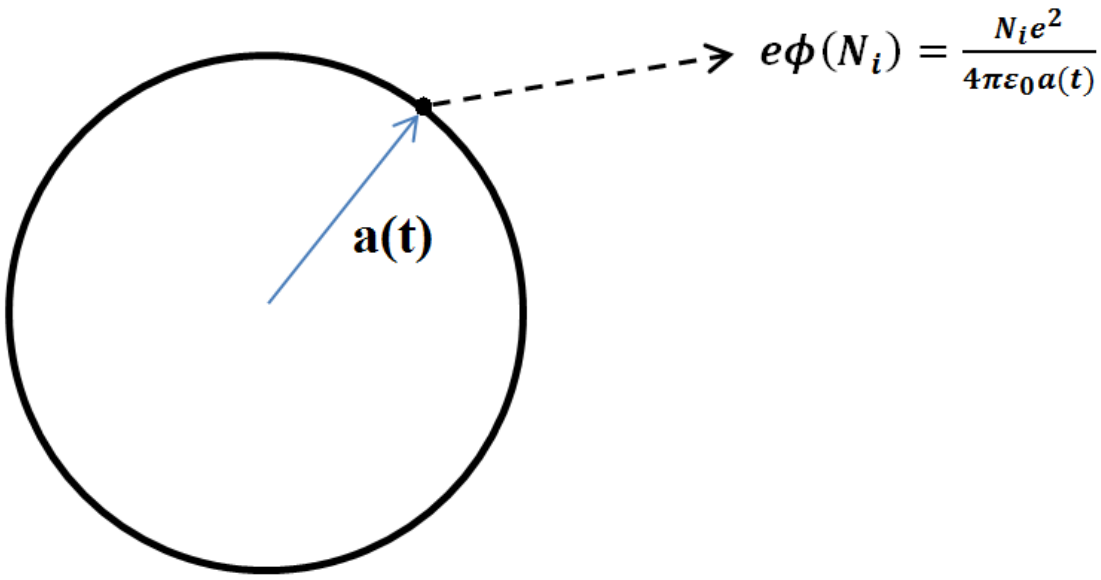

Figure 2. A neutral plasma sphere with radius *a(t)* is shown in this diagram. If very hot N_i ions leave the neutral plasma, the remaining plasma sphere is negatively charged. This charge imbalance creates a surface potential that acts like a barrier for ions with less kinetic energy.

For the subsequent simulations, I made a few assumptions:

- $\int_{E_i}^{\infty} f_{kT}(E)dE = N_i$
- $e\phi(N_i) = \frac{N_i e^2}{4\pi\varepsilon_0 a(t)} = E_i$
- $\phi(N_i)$ = Potential build-up after N_i ions escaped from the hot plasma
- E_i = minimum required kinetic energy to leave the hot plasma
- $f_{kT}(E)$ = distribution function of the ions (Maxwellian)
- Hot plasma: sphere with an initial radius of *a(t=0)* = 300 μm, w/ kT_{ion}= 10 keV
- The sphere expands with a mean speed $\langle v \rangle_{kT'}$, where *kT'* is the approximate ion temperature after N_i ions escaped from the region.

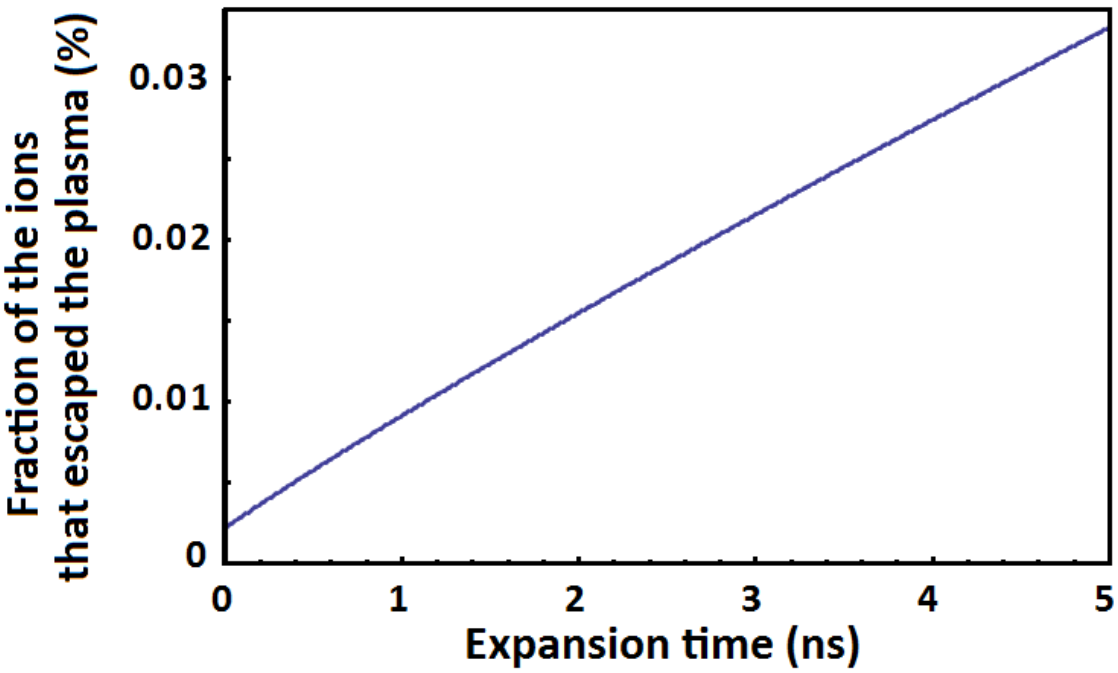

Figure 3. Fraction of ions that escaped the plasma is shown as a function of time.

As the plasma sphere expands, the potential barrier becomes lower since the denominator increases, and more ions can escape from the plasma. The fraction of the ions that escaped from the plasma sphere is plotted as a function of time in Figure 3.

This simulation result shows that only a very small fraction of the total ions escaped from the plasma during the expansion. After 5 ns, 3.8×10^{11} ions escaped from the hot plasma sphere according to the simulation. At 5 ns, the radius of the sphere is already 5.8 mm, which is more than twice the radius of the gas jet. Therefore, a simulation from 0 ns to 5 ns is sufficient in our case.

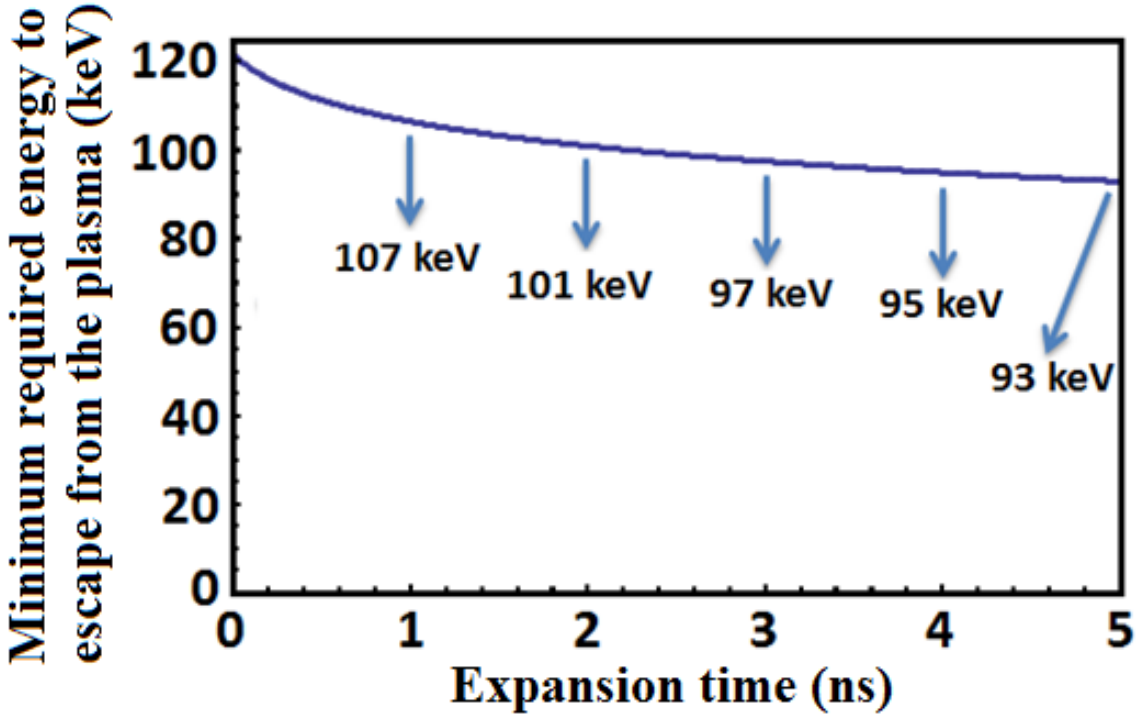

Figure 4. The minimum required kinetic energy of an ion at the surface to escape the plasma is plotted as a function of time.

In Figure 4, the potential barrier, or the minimum required energy to escape the plasma, is plotted as a function of time. This required energy becomes smaller because of the expansion. After 5 ns, all of the ions that have kinetic energy higher than 93 keV can escape from the plasma. As the hot ions leave the plasma, the remaining plasma will have ions with less kinetic energy.

We wanted to see how big this effect might be, and performed a simulation whose result is shown in Figure 5. As can be seen from the plot, the drop in the ion temperature of the remaining plasma is very small. Based on this simulation result, we conclude that the temperature drop due to the expansion of the plasma itself is very insignificant. In section 2.7, we will consider the loss in the average ion kinetic energy while the ions pass through the cold background gas jet layer.

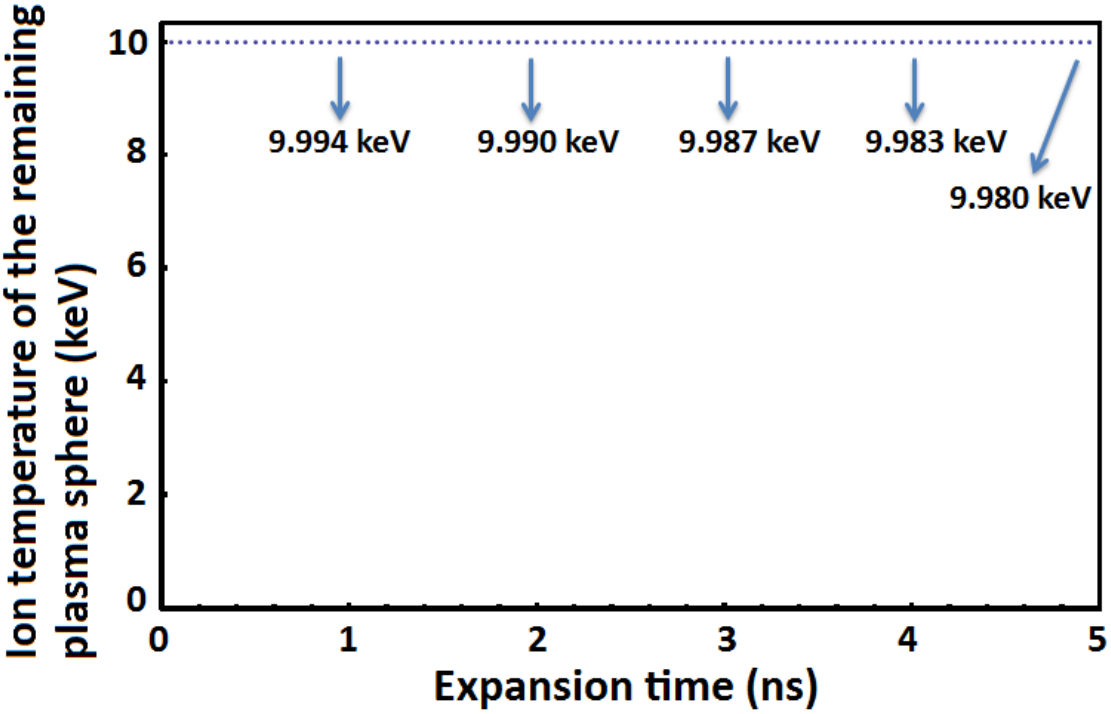

Figure 5. The approximate ion temperature of the remaining ions in the plasma sphere after some ions escaped from the plasma is shown in this figure as a function of time.

2.6.2. Acceleration of an electron due to the motion of a much heavier ion

In this section, we will examine the motion of an electron-ion pair. In the first example, the electron is nearly stationary while the ion moves to the right with a certain kinetic energy. They are separated by 1 nm, and we want to see how the electron behaves as the ion tries to leave the electron behind.

This situation is shown in Figure 6. If a deuterium ion at x=1 nm starts moving in the positive x direction with a kinetic energy of 3 keV, the electron is attracted toward the deuterium ion by the Coulomb force.

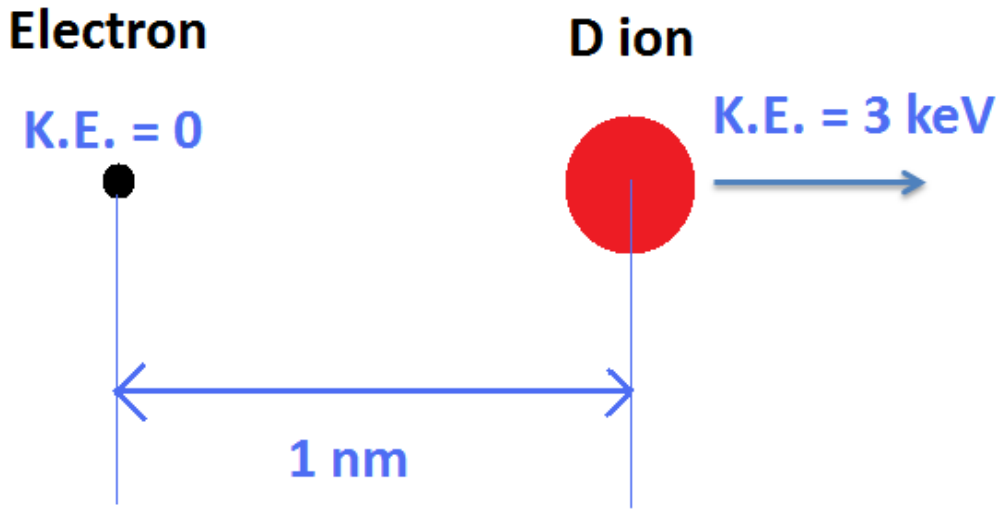

Figure 6. A simple model to see the energy transfer from a hot ion to a cold electron. An electron is stationary at x=0 at time=0, while the deuterium ion moves with a kinetic energy of 3 keV.

Figure 7 (a) and (b) show the trajectory of the ion and the electron, respectively. Due to the attractive Coulomb force between the electron and the deuterium ion, the electron accelerates very quickly. As can be seen from Figure 7 (b), this happens in a fs time scale. Then, the speed of the electron becomes larger than the speed of a 3 keV deuterium ion, and it passes the ion. From that moment, the electron gets accelerated backward and loses its speed. In other words, the electron can catch up to the deuterium ion very easily, and it oscillates around the ion. Because of the much bigger mass of the deuterium ion, the trajectory of the ion is not very much disturbed by the light electron. This can be seen in Figure 7 (a), which looks almost linear.

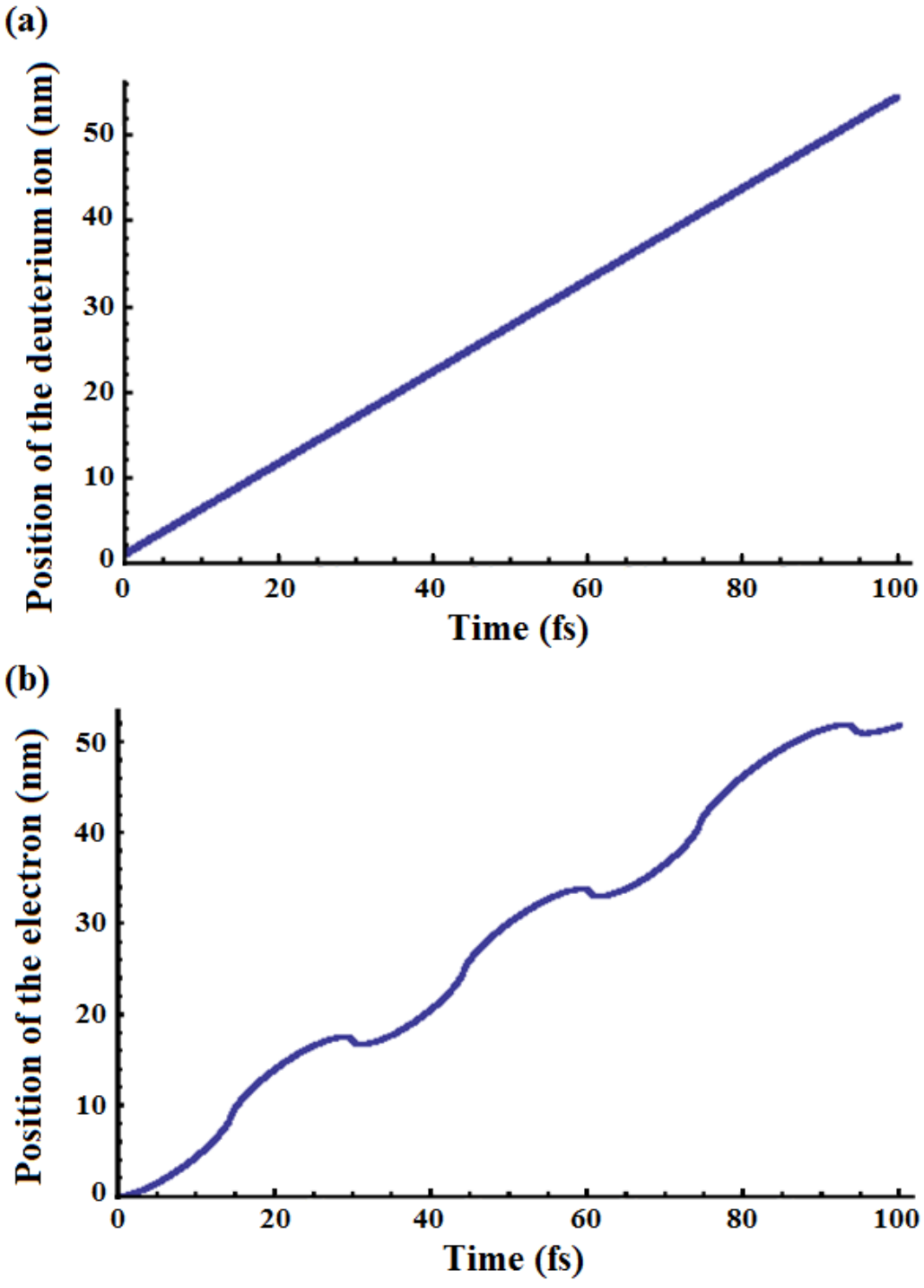

Figure 7. (a) The trajectory of a deuterium ion with initial kinetic energy of 3 keV, and (b) the trajectory of an electron are shown in the lab frame as a function of time from 0 fs to 100 fs.

The instant velocity of the electron and the distance between the electron and the ion are shown in Figure 8 and Figure 9, respectively. To avoid divergence in the speed of the electron when the distance between the electron and the ion gets very small, no attractive Coulomb force was assumed when the distance between them became smaller than 0.1 nm.

The choice of 0.1 nm is based on the rough size of a neutral atom. This keeps the electron speed much less than the speed of light, and justifies our non-relativistic treatment of the electron motion. The resolution of the time step for this simulation was 1 as. The velocity of the electron shown in Figure 8 confirms the oscillatory behavior of the electron. Note that the plot is not symmetric because the electron follows the ion that moves in the positive x direction while oscillating back and forth.

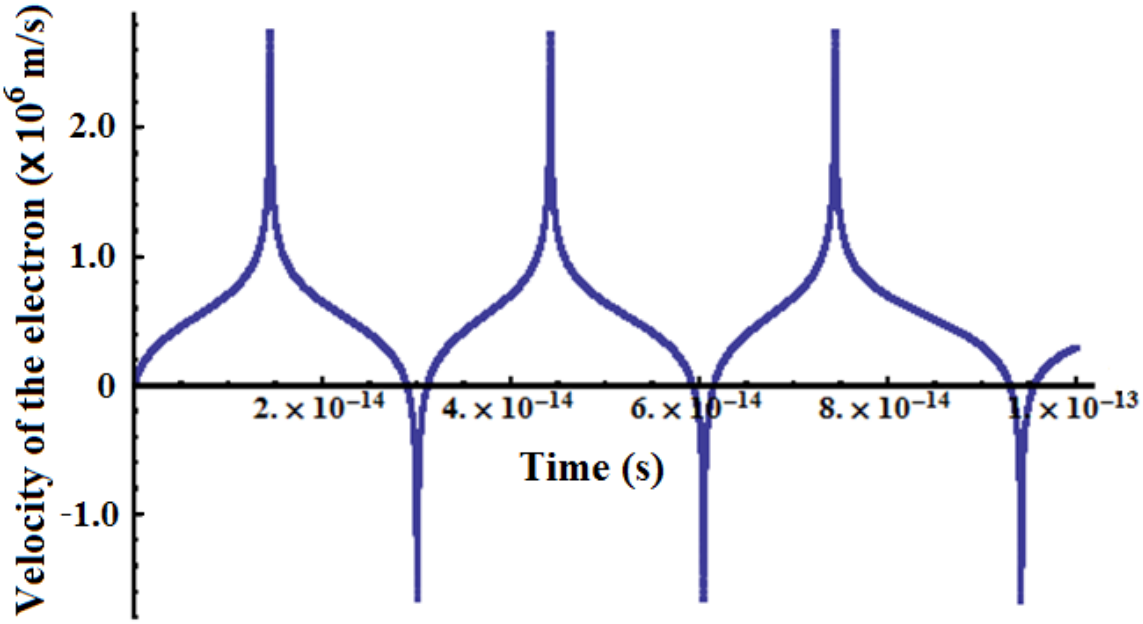

Figure 8. The velocity of the electron is plotted as a function of time from 0 fs to 100 fs.

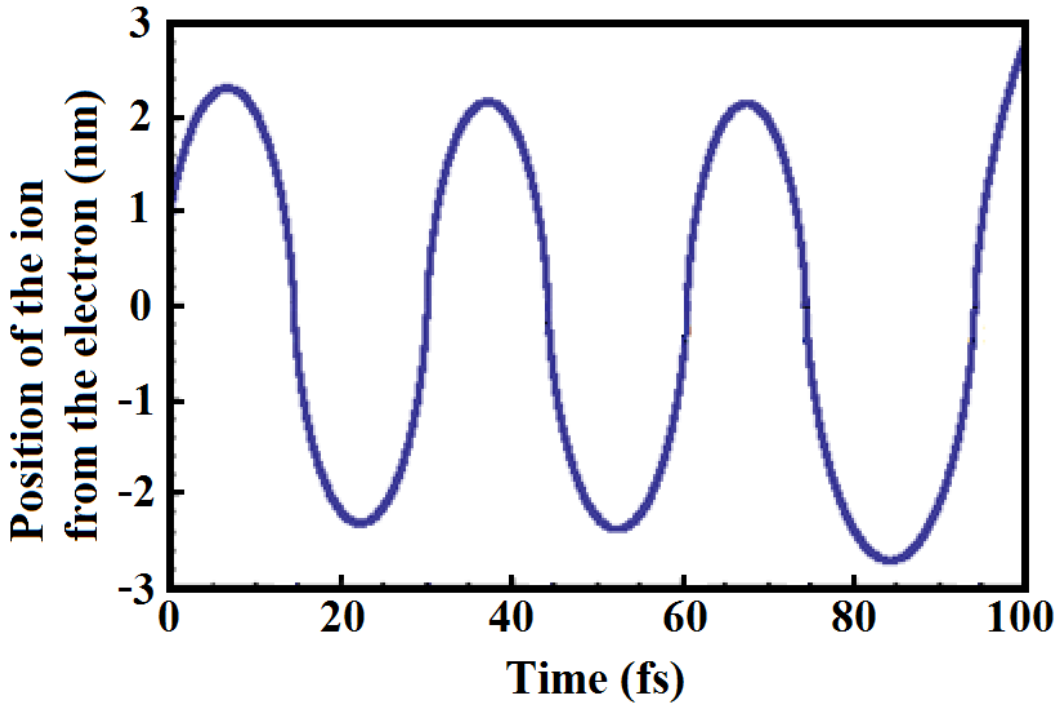

Figure 9. The position of the ion relative to the electron is plotted as a function of time from 0 fs to 100 fs.

In Figure 9, the distance between the two particles is plotted as a function of time, from which we can tell that the maximum distance between them is only about 2 nm. This implies that the electron indeed goes along with the ion. When the kinetic energy of the ion is 3 keV, the initially stationary electron is not left behind, but it follows the ion and moves together.

To check the validity of the simulation, Figure 10 shows the conservation of the energy of the system. As expected, the sum of the kinetic energy of the ion and the electron and the potential energy of the system is nearly constant in time. There are periodic small spikes because we had singularities when the distance becomes 0. This can be improved by treating the electron relativistically, and imposing a constraint that the distance cannot be exactly zero for the potential energy.

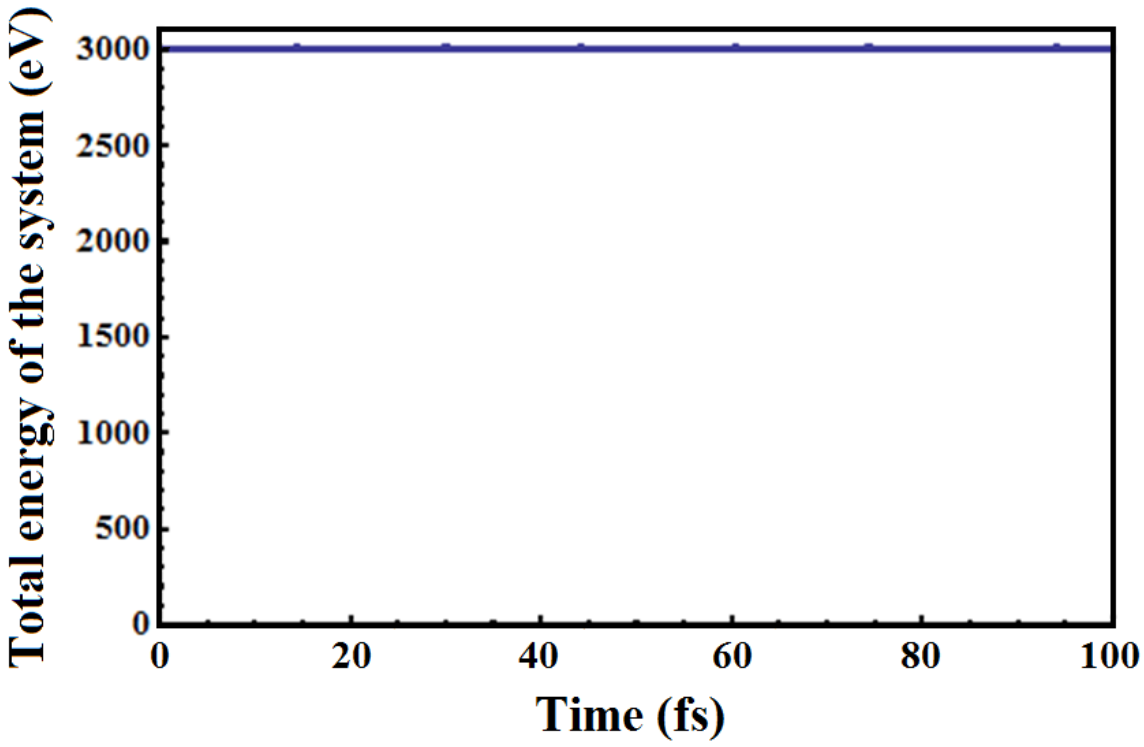

Figure 10. Total energy of the combined system is shown as a function of time from 0 fs to 100 fs.

Now, let's imagine a different situation. If an electron has an initial kinetic energy of 1 keV, and the ion is stationary, the motion of the ion is not very much affected by the electron as can be seen from Figure 11. Under this situation, the ion only gains a speed of 25 m/s due to the 1 keV electron. This simple simulation shows why the ions do not expand much while the electrons escape from the cluster.

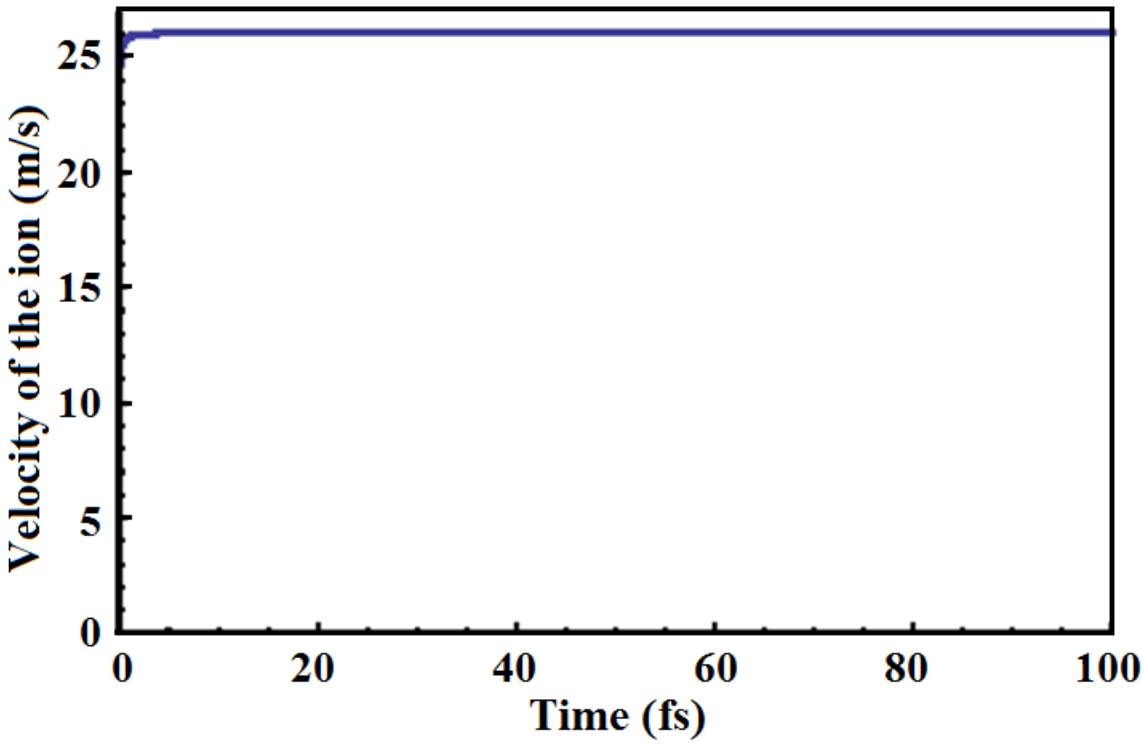

Figure 11. The velocity of the ion is shown in the plot as a function of time. The 1 keV electron starts moving in the positive x direction at time 0.

In Figure 12 (a) and (b), the position of the electron and the position of the ion are shown as a function of time, respectively. Comparing these two plots, we can conclude that the ions are almost left behind when the energetic electron moves away from the ion.

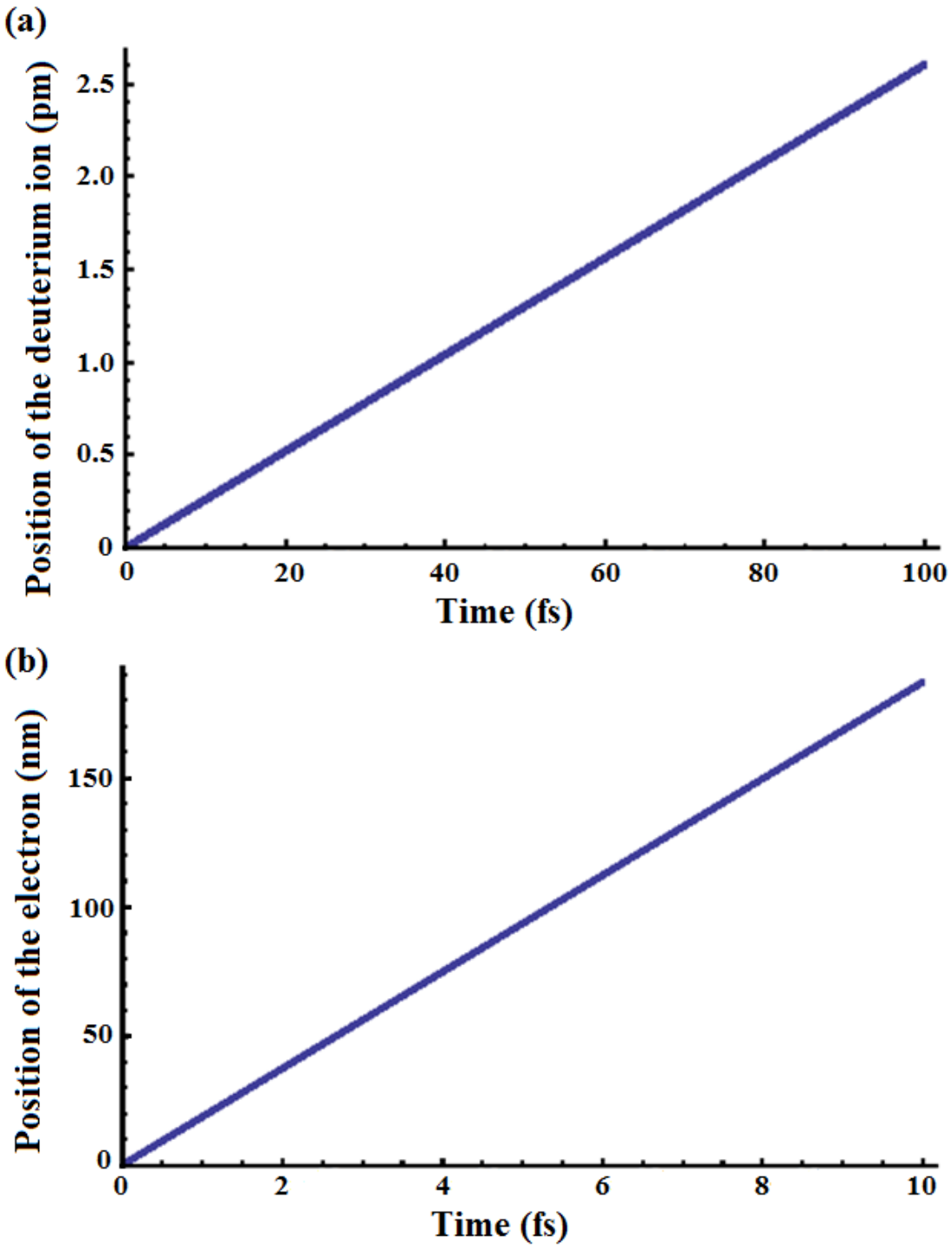

Figure 12. (a) The position of the escaping electron is plotted as a function of time from 0 fs to 10 fs. (b) The position of the deuterium ion is plotted as a function of time from 0 fs to 100 fs.

In addition to the above simulations, I performed a simple 1D hydrodynamics simulation using HYADES[49] codes, which showed that most of the kinetic energy of the ions stayed with the ions after 2 ns of expansion. According to the simulation, about 5.6% of the initial energy went from the ions to the electrons. This energy loss is big enough to make the electrons escape together with the ions. At least, we see that the electrons are not left behind as the ions expand.

The parameters for the simulation are as follows:

1. Deuterium ion temperature = 2 keV, electron temperature = 10 eV.
2. Cylindrical plasma filament with radius R=100 μm, density = 10^{19} atoms/cm^3.
3. Cold background gas density = small (~1/1000 x10^{19} atoms/cm^3).

Energy (erg)	Kinetic	Electron	Ion	Radiation
Initial	0.000	7.492×10^4	1.508×10^7	1.694×10^2
Electron-ion coupling		8.501×10^5	-8.501×10^5	
Radiation-electron coupling		-7.796×10^3		7.796×10^3
Hydro	1.115×10^7	-8.072×10^5	-1.034×10^7	-4.091

Table 1. Distribution of the energy after 2 ns of expansion.

The above table summarizes the simulation results from HYADES, and we find a few things from this:

1. Total initial energy of hot ions = 1.508×10^7 erg (= 1.508 J)
2. Energy loss of ions due to slow electrons = 8.5×10^5 erg (5.6%)

3. Most of the ion energy went into the kinetic energy term. (hydrodynamic expansion) This kinetic energy still belongs to the ions for the fusion reaction.

In this section, we saw that the electrons are not just left behind when the ions try to escape. This is related to the quasi-neutrality of the plasma, and we will further investigate this in the next example.

2.6.3. Quasi-neutrality of the expanding plasma

In section 2.6.1, we considered an expanding plasma sphere with an ion temperature of 10 keV. In that model, we simply assumed ions with high enough kinetic energy would escape from the plasma, and the relatively cold electrons would form a shell. In this section, we will have a closer look at what should happen to the electrons if the ions escape from the plasma suddenly. A schematic diagram to calculate the self-stored potential energy of a negatively charged spherical shell is shown in Figure 13.

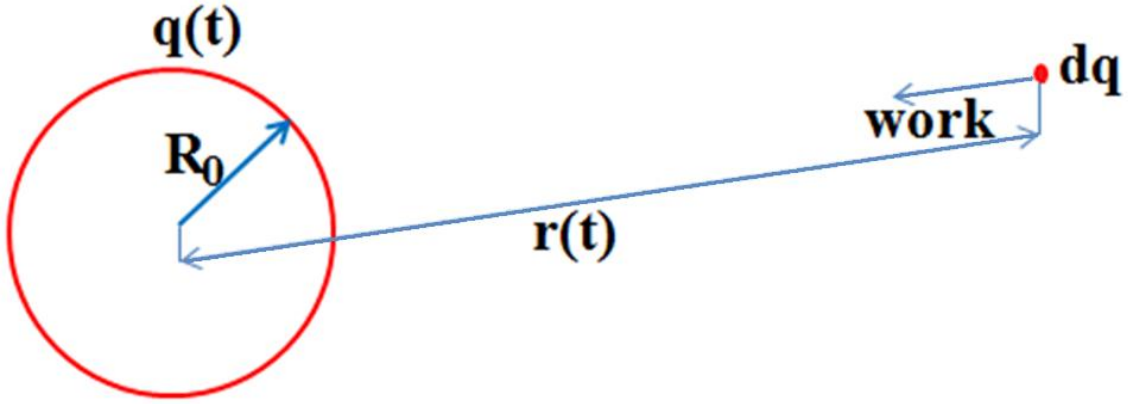

Figure 13. A schematic diagram to calculate the self-potential energy of a negatively charged electron spherical shell with radius R_0 and total charge $N_i e$ is shown. The work done to bring the charge element dq to the electron shell with radius R_0 and charge $q(t)$ is added until the total charge becomes $N_i e$.

Summing the work done to the charge element *dq*, the potential energy becomes:

Potential energy = $\int_{q=0}^{q=N_i e} \int_{\infty}^{R_0} \frac{qdq}{4\pi\varepsilon_0 r^2}(-dr) = \int_0^{N_i e} \frac{qdq}{4\pi\varepsilon_0 R_0} = \frac{(N_i e)^2}{8\pi\varepsilon_0 R_0}$. (2.26)

After N_i ions leave the neutral plasma sphere with radius R_0, the electrons on the surface of the plasma explode due to their own repulsive Coulomb forces. The above potential energy now becomes the kinetic energy of the electrons.

Therefore, $\frac{(N_i e)^2}{8\pi\varepsilon_0 R_0} = N_i(\frac{1}{2}mv^2)$. v = 1.46x10^8 m/s.

(Relativistic correction, $N_i(\gamma\text{-}1)mc^2$, gives v=1.34x10^8 m/s)

This calculation shows two things. First, it shows that the electrons on the surface cannot form a stable shell structure and expand together with the plasma. Secondly, the electrons on the surface of the sphere move outward faster than the ions inside the neutral plasma sphere. Therefore, the ions inside the sphere cannot really see the boundary, and they do not bounce off of the boundary formed by the electron shell.

2.7. TEMPERATURE DROP OF THE FUSION PLASMA

2.7.1. Shock formation at the boundary

In this section, we will first examine the possibility of the shock formation at the boundary of the expanding plasma sphere. With an initial temperature of *kT*=10 keV, the ion temperature inside the neutral plasma sphere after N_i ions left was still very close to 10 keV according to our previous model. Calculation of the mean free path shows that the shock formation must be due to very slow ions with kinetic energies (K.E.). Table 2 summarizes the possibility of the shock formation at the boundary due to ions with specific energies. Whether the shock formation is possible due to energetic ions is very important in the cluster fusion experiment because estimation of the beam-target contribution needs information about the density of the cold background targets. If a shock forms at the boundary, and sweeps the cold background atoms, the hot ions inside

the plasma sphere do not see the cold atoms. Therefore, the beam-target contribution will be only due to the very hot ions at the boundary of the sphere in this scenario. On the other hand, if no shock forms due to the energetic ions, the hot ions inside the boundary can interact with the cold deuterium atoms or ions, and DD fusion can occur.

Ion energy (eV)	Mean free path (μm)	Shock formation at the boundary?
50	44	Probable
100	82	Probable
120	97.5	Probable
200	161	Maybe?
300	243	Maybe?
400	326	Unlikely
500	409	Unlikely
1000	807	Unlikely
1300	1030	Unlikely
2000	1510	Impossible
3000 (=3 keV)	2120 (=2.12 mm)	Impossible
10000 (=10 keV)	5140 (=5.14 mm)	Impossible

Table 2**.** Mean free path of the ion and the possibility of shock formation.

Calculations in Table 2 show that the background cold atoms (or ions) are not pushed away due to the shock until slow ions with K.E. ≤ 100 eV arrive. The cold background atoms will interact with 1–100 keV ions to produce DD fusion neutrons through beam-target reaction.

2.7.2. Beam-target fusion reactions at different energy ranges

In section 2.7.1, it was shown that the background cold deuterium atoms or ions in the gas jet would not be swept away by the hottest ions from the fusion plasma. They remain as targets even for ions with a few keV kinetic energies. In this section, the beam-target contribution is calculated for a plasma sphere with a total number of hot ions = 10^{16} ions, and kT =10 keV. Then, the beam-target contribution can be expressed as follows

$$10^{16} \times \int_{E1}^{E2} n_D \sigma(E) f_{\frac{kT}{2}=5keV}(E) dE \times (2.5 \text{ mm}), \quad (2.27)$$

where E1 is the lower limit of the energy range, E2 is the upper limit of the energy range, and the radius of the gas jet is 2.5 mm.

Energy range (E1–E2 keV)	Number of ions	Beam-target DD fusion reactions (n/shot)
0~1000	10^{16}	1.16×10^{7}
90~1000	4.4×10^{12}	1.8×10^{5}
50~90	1.8×10^{14}	3.1×10^{6}
20~50	2.4×10^{15}	7.6×10^{6}
10~20	3.1×10^{15}	6.7×10^{5}
0~10	4.3×10^{15}	1.3×10^{4}

Table 3. Contribution to the beam-target fusion reactions for ions in the certain energy ranges.

Calculations in Table 3 show that the beam-target contribution from ions with their kinetic energy less than 90 keV gives a significant number of fusion neutrons.

2.7.3. Energy loss of the ions in the cold gas jet layer – SRIM calculation

In this section, I calculated how much energy was lost after deuterium ions passed through 2.5 mm thick gas jet using SRIM[50] code. The results show that the measured ion temperature from the ion time-of-flight (TOF) measurements could be 4–8 keV lower than the actual temperature of the plasma when a uniform 10^{19} atoms/cm^3 average gas density was used throughout the gas jet. In Table 4, some of the calculation results using SRIM code for the energy loss of deuterium ions after passing through 2.5 mm thick gas jet are shown, whereas a complete table can be found in Appendix A. A uniform deuterium gas density of 10^{19} atoms/cm^3 was assumed throughout the gas jet layer of 2.5 mm.

Incident particle energy (keV)	Average kinetic energy after transmission (keV)	Standard deviation (keV)
1	0.00	0.00
2	0.23	0.18
3	0.38	0.30
4	0.60	0.40
5	0.97	0.52
6	1.47	0.62
7	2.03	0.67
8	2.64	0.70
9	3.27	0.72
10	3.92	0.74
11	4.58	0.75
12	5.27	0.75
13	5.97	0.77
14	6.68	0.76
15	7.38	0.79
16	8.12	0.79
17	8.87	0.79
18	9.62	0.78

Table 4. Kinetic energy of the transmitted ions for incident ions with different initial kinetic energy.

19	10.37	0.81
20	11.14	0.83
30	19.17	0.82
40	27.73	0.85
50	36.60	0.94
60	45.81	1.04
70	55.18	0.80
80	64.71	0.88
90	74.40	0.84
100	84.23	0.80
110	94.13	0.82
120	104.13	0.82
130	114.18	0.83
140	124.31	0.84
150	134.46	0.82
160	144.66	0.82
170	154.87	0.86
180	165.10	0.90
190	175.37	0.82
200	185.62	0.86
250	236.97	0.82
300	288.20	0.82
1000	995.14	0.78

Table 4 (continued).

Using the results of Table 4 and Maxwellian distribution of ions, we can estimate the temperature drop of the fusion plasma. Figure 14 shows the ion temperature of the transmitted ions versus the ion temperature of the incident ions in keV. The graph shows that the energy loss of an ion after passing through 2.5 mm of deuterium gas jet was about 6.3 keV for ions with an initial temperature of 20 keV (Maxwellian).

The vertical axis on the plot corresponds to the measured ion temperature from the ion TOF measurements, and the horizontal axis indicates the actual ion temperature inside the plasma filament. A solid blue line is added to the figure as a reference to indicate a situation when no energy is lost to the cold gas jet background.

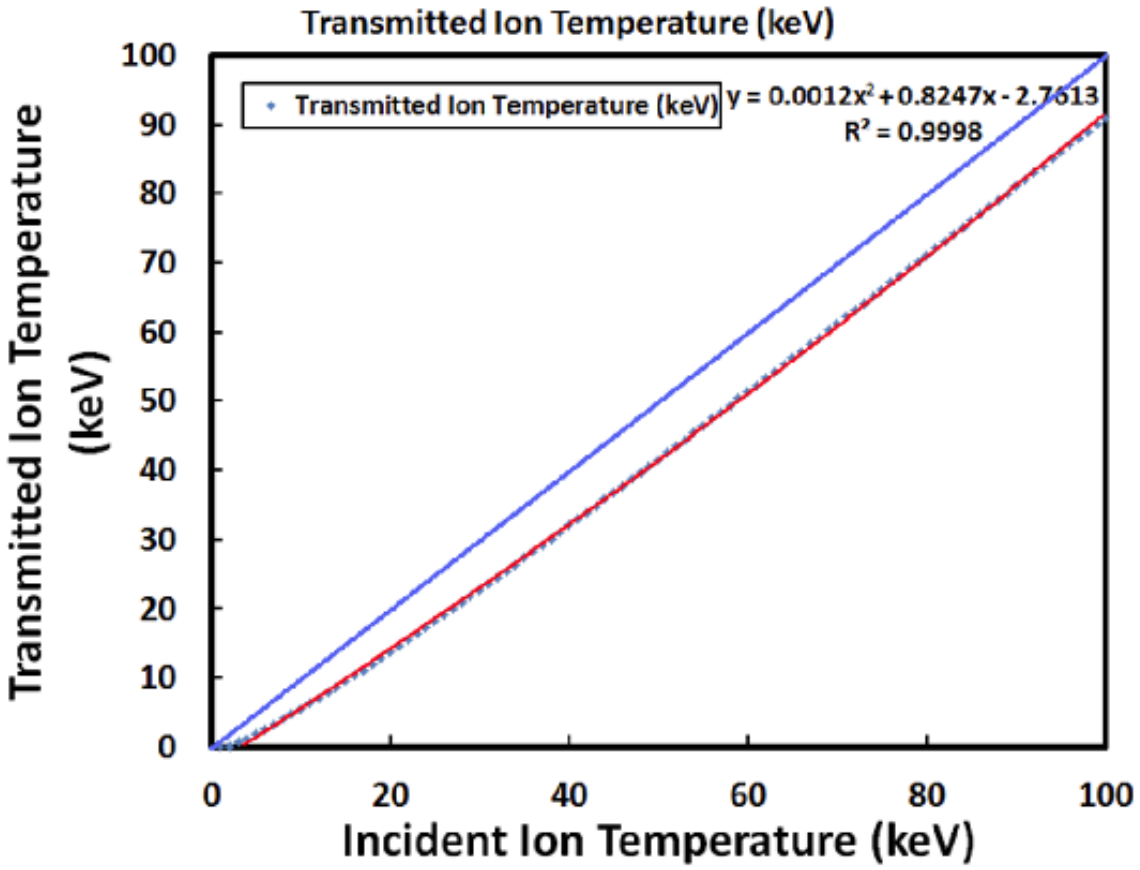

Figure 14. Ion temperature of the transmitted ions as a function of the temperature of the incident ions. A solid blue line is added as a reference, and indicates when there is no loss in the ion temperature.

2.7.4. Expansion of the plasma filament – Free expansion with dE/dx

In section 2.7.3, we saw that the energetic deuterium ions would lose their kinetic energy as they pass the cold gas jet layer. This is implemented in a simulation code to estimate the ion temperature drop of the deuterium fusion plasma as a function of time. A stopping power (keV/cm) was used to estimate the temperature drop. Also, a uniform gas density of $n_D = 10^{19}$ cm^{-3} was assumed, which is certainly an over-estimation near the edge of the gas jet. In an actual experiment, the gas density peaks at the center of the

gas jet, and drops near the edge. Therefore, the assumption of a uniform gas density would result in somewhat bigger drop in the ion temperature.

Figure 15 shows the simulation result with an initial condition of $N_{ion}=10^{16}$ ions, kT=10 keV, and gas jet radius of 2.5 mm. The shape of the fusion plasma is assumed to be a 5 mm long cylindrical filament. The radius of the filament is calculated using the total number of hot ions, N_{ion}, and the gas density of n_D. It is assumed that there are no cold atoms inside the fusion plasma.

As the fusion plasma expands, the hot ions at the boundary of the plasma would collide with the cold background atoms, and transfer some of their kinetic energy to the atoms in the surrounding gas jet. This causes an overall temperature drop of the hot fusion plasma, and the following figure shows the ion temperature as a function of time.

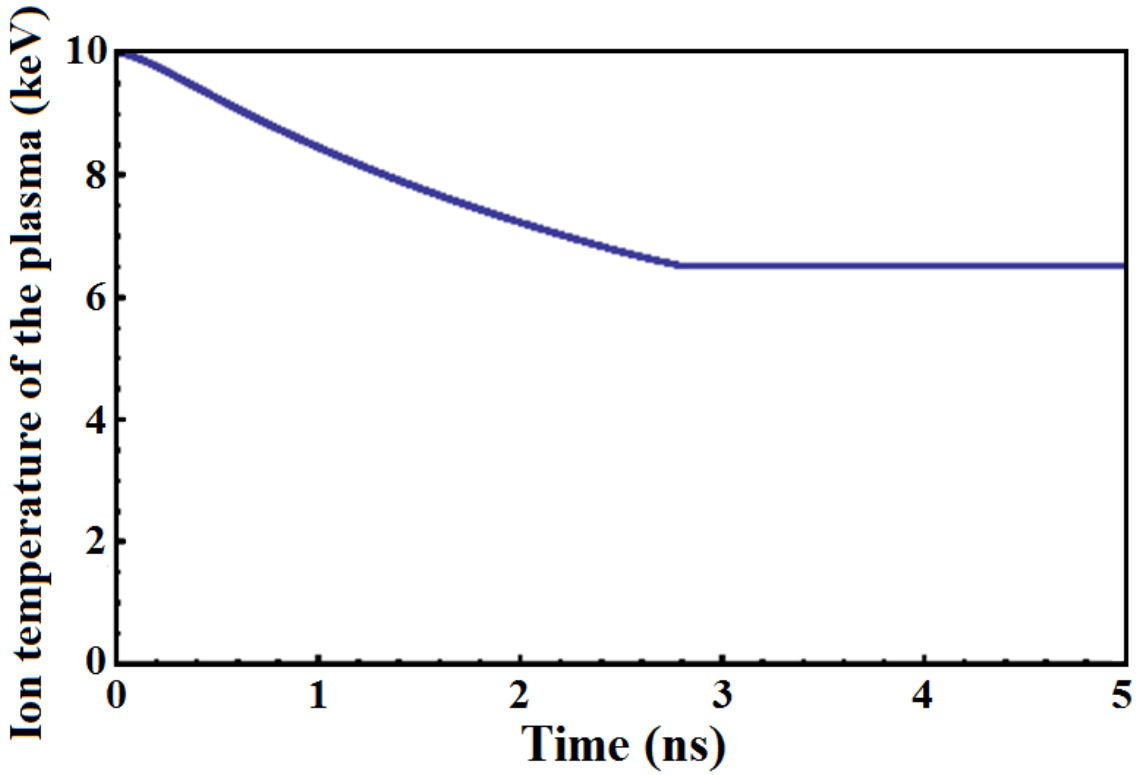

Figure 15. Drop in the ion temperature as a function of time.

The temperature of the fusion plasma dropped from 10 keV to about 6 keV after about 3 ns according to the figure. If we detected 6 keV ions from ion TOF measurements, the original ion temperature of those ions could have been up to 10 keV. Since we used a uniform gas density of 10^{19} atoms/cm^3, the real ion temperature would be somewhere between these two temperatures.

Figure 16 shows the stopping power of the deuterium gas from SRIM code that we used for the simulation. For a simpler calculation, I used SRIM code to calculate a few data points in the plot, then used OriginPro 8.5 to find a fit curve for the data. Then, I used this fit curve in the simulation code to find the temperature drop as the plasma expands.

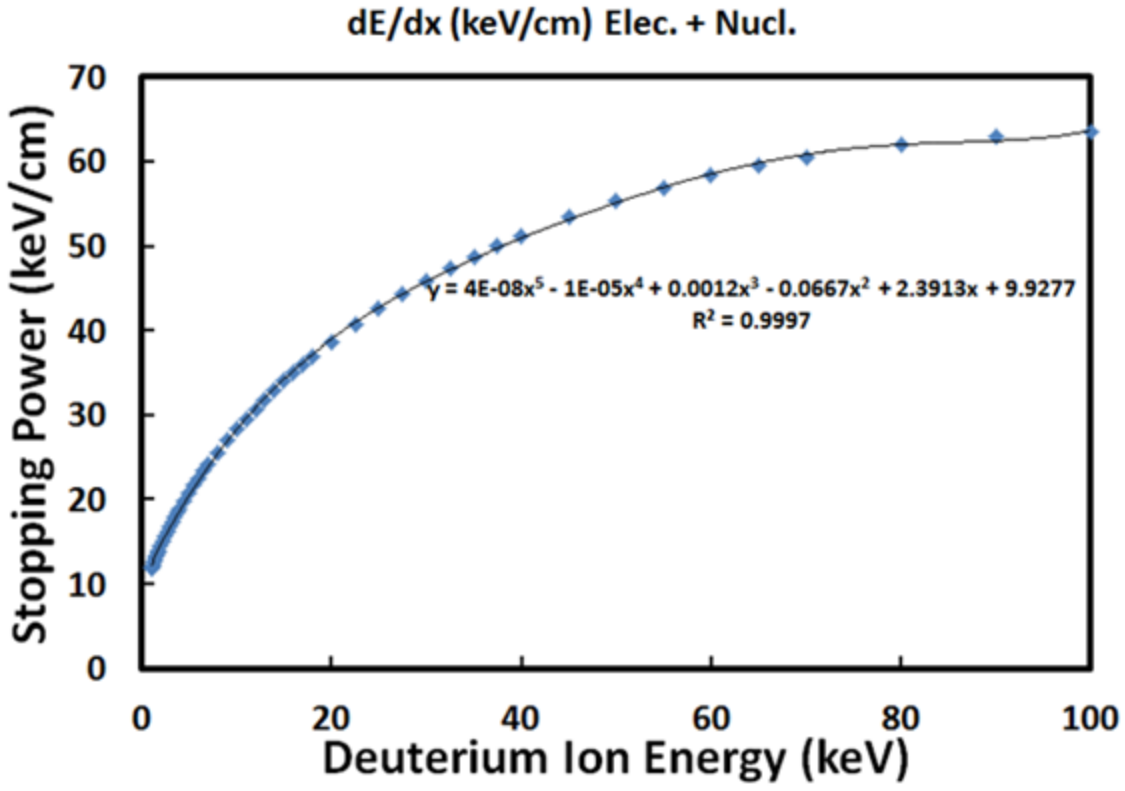

Figure 16. Stopping power is shown in keV/cm as a function of the kinetic energy of the incident deuterium ion.

2.8. ESTIMATION OF THE NEUTRON YIELD (BEAM-BEAM OR BEAM-TARGET) AS A FUNCTION OF TIME

Now that we have a model for the expansion of the fusion plasma, we will implement this to estimate the number of fusion reactions happening inside the deuterium plasma. For this purpose, we need to know the DD fusion cross section, the total number of hot ions, the initial temperature of the plasma, and the density of the background targets. For simplicity, we assumed a uniform gas density of 10^{19} atoms/cm^3. The ion temperature and the number of hot ions are based on the actual measurements during the cluster fusion experiments on the TPW described in detail in Chapter 6. For the simulation, we used kT=10 keV, N_{ion} = 10^{16}, and Bosch's parameterization[51] for the DD fusion cross section. Figure 2.16 shows the neutron yield as a function of time from 0 ns to 5 ns. Figure 17 (a) shows the neutron yield from the beam-target contribution, where Figure 17 (b) shows the neutron yield from the beam-beam contribution. In Figure 17 (c), the total estimated fusion neutron yields as well as the yields from each contribution are shown together in a linear plot. The estimated neutron yield is about 9x10^6 neutrons per shot, which is comparable to the actual neutron yields measured during the experiments on the TPW. It is interesting to see that the beam-target contribution is about the same order as the beam-beam contribution. The essential parts of the simulation code for the fusion neutron yield calculation are added in Appendix B.

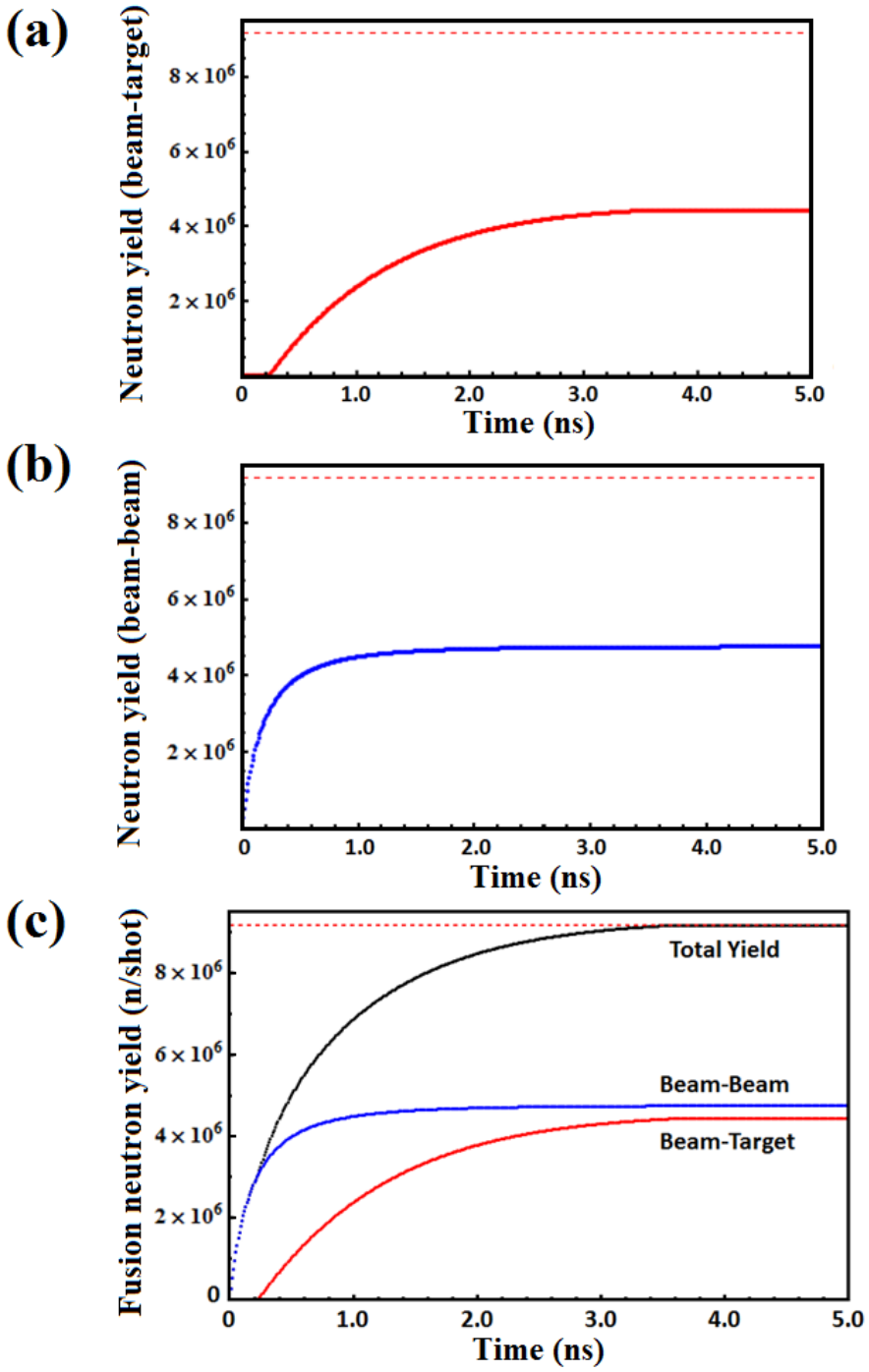

Figure 17. (a) Beam-target contribution as a function of time, (b) beam-beam contribution as a function of time, (c) total neutron yield as a function of time along with the beam-beam contribution and the beam-target contribution.

2.9. ESTIMATION OF THE MAXIMUM ACHIEVABLE NEUTRON YIELD ON THE TPW

2.9.1. Fusion neutron yield without B field

In this section, we want to have a rough estimate of the maximum achievable neutron yield on the TPW without any magnetic confinement. For the simulation, I assumed kT<20 keV, and the total energy of the hot ions < 100 J, from which the number of hot ions can be calculated as:

$$N_{ion} < 100 \text{ J}/30 \text{ keV} = 2.08\text{x}10^{16} \text{ ions.} \quad (2.28)$$

A uniform atomic density of $n_D = 10^{19}$ cm^{-3} was used for the simulation. Based on the simulation results, I think the highest neutron yield we can expect from the TPW without any type of confinement of the plasma would be $1.1\text{x}10^{8}$ n/shot.

Figure 18 (a) shows the total neutron yield as a function of time, and (b) shows the ion temperature as a function of time. Without any confinement, the neutron production seems to be practically over at around 2 ns. The ions would have an ion temperature of 16 keV after passing through the gas jet according to the simulation.

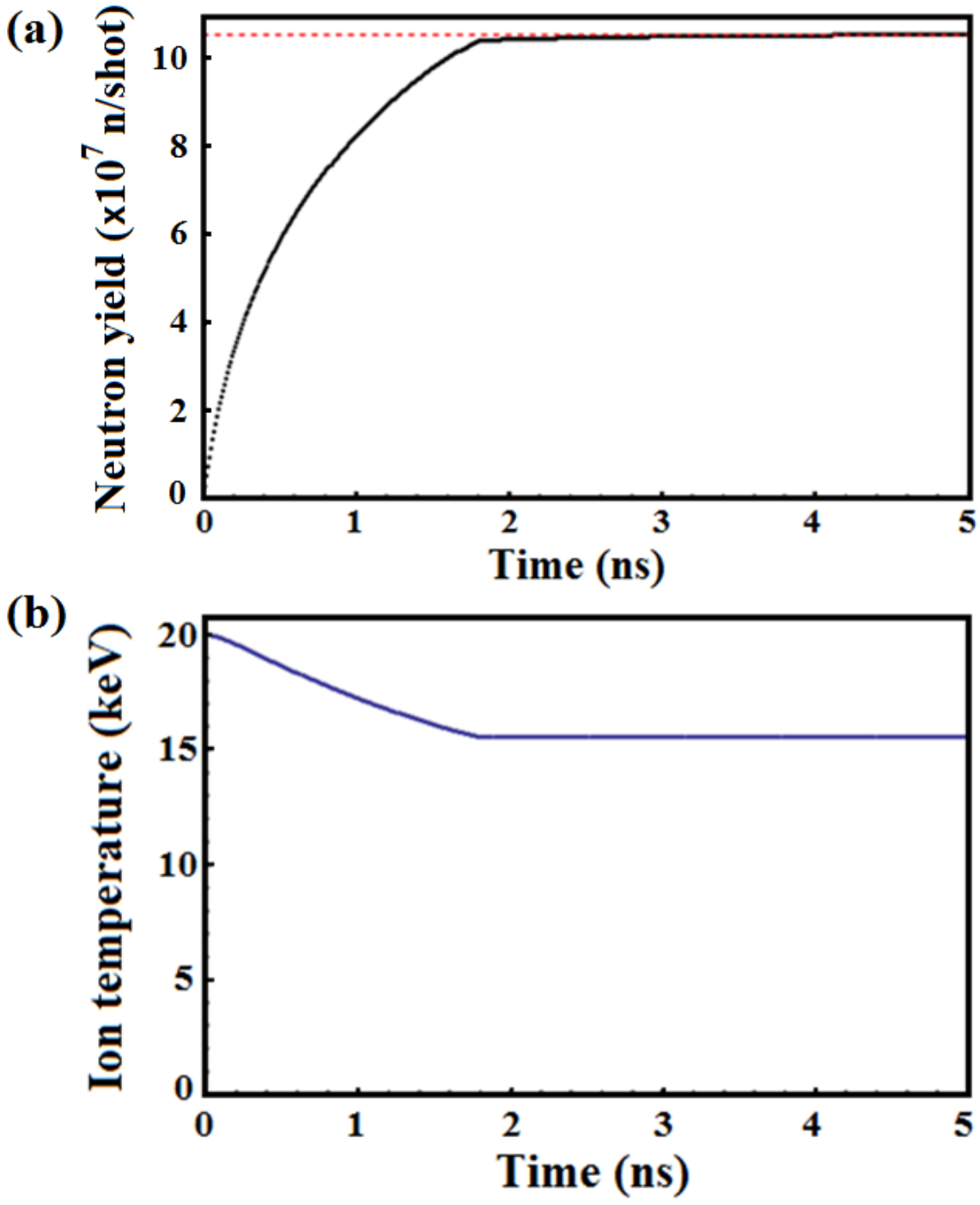

Figure 18. (a) Neutron yield on the TPW as a function of time, (b) ion temperature of the fusion plasma as a function of time. No magnetic confinement is assumed for these simulations.

2.9.2. Fusion neutron yield with B field

In this section, I want show a rough estimate of the maximum achievable neutron yield on the TPW with magnetic confinement in the radial direction. For the simulation, I assumed kT=10 keV, and the total energy of the hot ions < 100 J, from which the number of hot ions can be calculated as:

$$N_{ion} < 100 \text{ J}/15 \text{ keV} = 4.17\text{x}10^{16} \text{ ions.} \quad (2.29)$$

Once again, a uniform atomic density of $n_D = 10^{19}$ cm^{-3} was used for the simulation. Also, the length of the filament is assumed to be $L(t)$=5 mm + 2*<v>*t, where 5 mm is the initial length of the plasma filament, <v> is the mean speed of the ions in the plasma, and t is the time. The radius of the filament is assumed to be constant from 0 ns to 10 ns. We did not assume any confinement in the laser propagation direction.

Figure 19 shows the neutron yield as a function of time. In this figure, the neutron yield keeps increasing because of the confinement of the plasma in the radial direction. After 10 ns, the total neutron yield is about 5x10^8 n/shot, which I think is the reasonably achievable maximum neutron yield on the TPW with magnetically confined deuterium plasmas. However, this does not represent a physical limit because we can still improve the neutron yield by increasing the density of the gas jet, for example. Therefore, this simulation result can be considered as an upper limit if only the gas jet conditions are similar to those used on the TPW cluster fusion experiments described in Chapter 6.

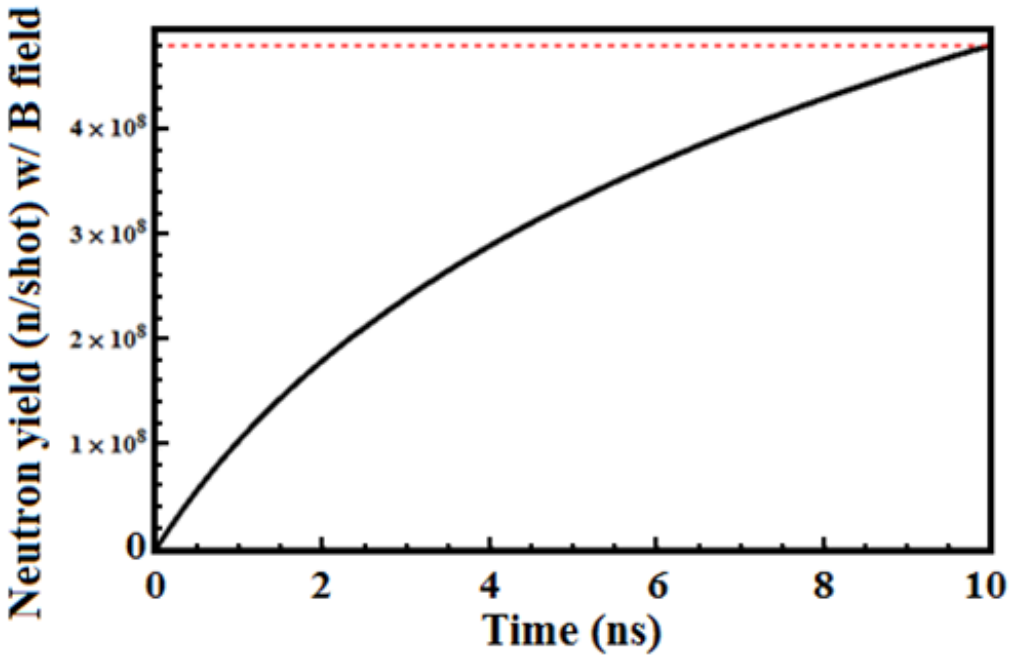

Figure 19. Neutron yield from the beam-beam contribution is shown as a function of time. The fusion plasma is confined in the radial direction. The dashed red line indicates 4.8×10^8 n/shot.

The density of hot ions is plotted as a function of time in Figure 20. Since the fusion plasma is not confined in the laser propagation direction, the density drops after its creation at t=0 ns. Due to the confinement in the radial direction, the overall atomic density of the hot plasma only drops down to about 2×10^{18} atoms/cm^3 after 10 ns according to the simulation. The drop in the number density accounts for the decrease in the slope in Figure 19.

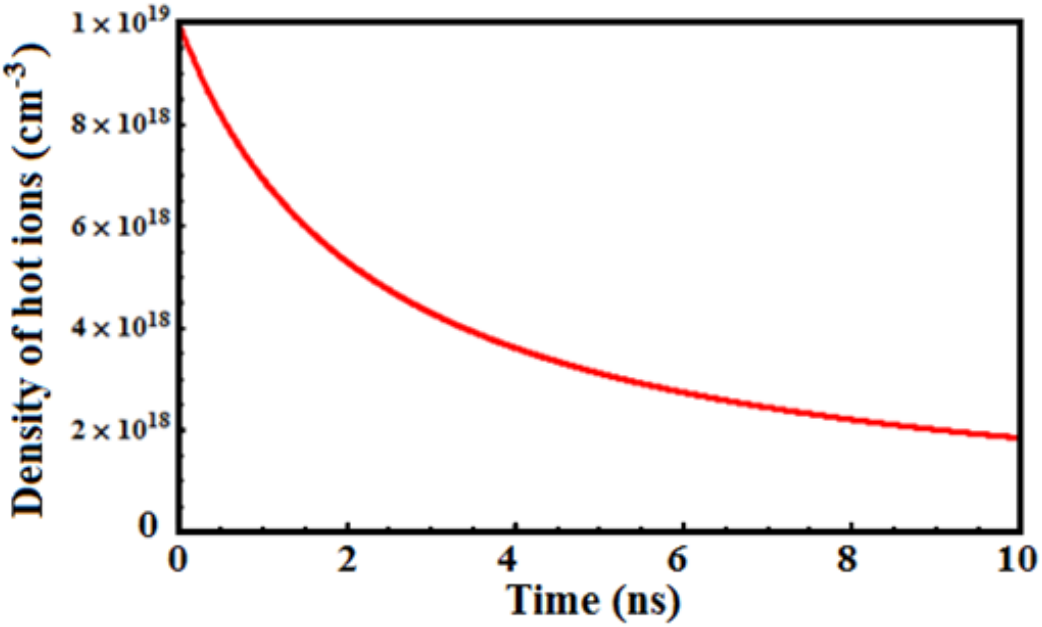

Figure 20. The density of the energetic deuterium ions decreases in time because the filament is not confined in the longitudinal direction.

2.9.3. Neutron production rate (w/o magnetic field)

The number of neutrons produced from the source during a 10 ps time interval is plotted from 0 ns to 1 ns in Figure 21 for two different situations. In Figure 21.(a), the plasma is assumed to be a 1 mm long filament, and the temperature is assumed to be 8 keV. About 0.1 J of the laser pulse energy is assumed to be absorbed by the energetic ions. This situation can be realized in small laser systems such as THOR. On the other hand, Figure 21.(b) shows the same result for a 5 mm long filament with kT=10 keV ion temperature. 24 J of the pulse energy is assumed to be absorbed by the hot ions. In both cases, the atomic density of deuterium, $n_D = 10^{19}$ cm^{-3}, is assumed to be uniform throughout the gas jet.

Both figures look similar in shape, but there is certainly a noticeable difference between Figure 21 (a) and (b). In both cases, the neutron production rate is highest in

the earliest moment, when the beam-beam contribution is most important. However, we see a much steeper drop in the rate in Figure 21 (a). The main reason for this difference is due to the lower ion temperature assumed in Figure 21 (a). When the temperature of the plasma is on the order of a few keV, the DD fusion cross section increases very fast with the ion temperature. For the beam-target contribution, this gets more severe because the effective ion temperature becomes $kT/2$. Therefore, the fraction of neutrons generated from the beam-target reactions is less important in the kT=8 keV case than in the kT=10 keV case.

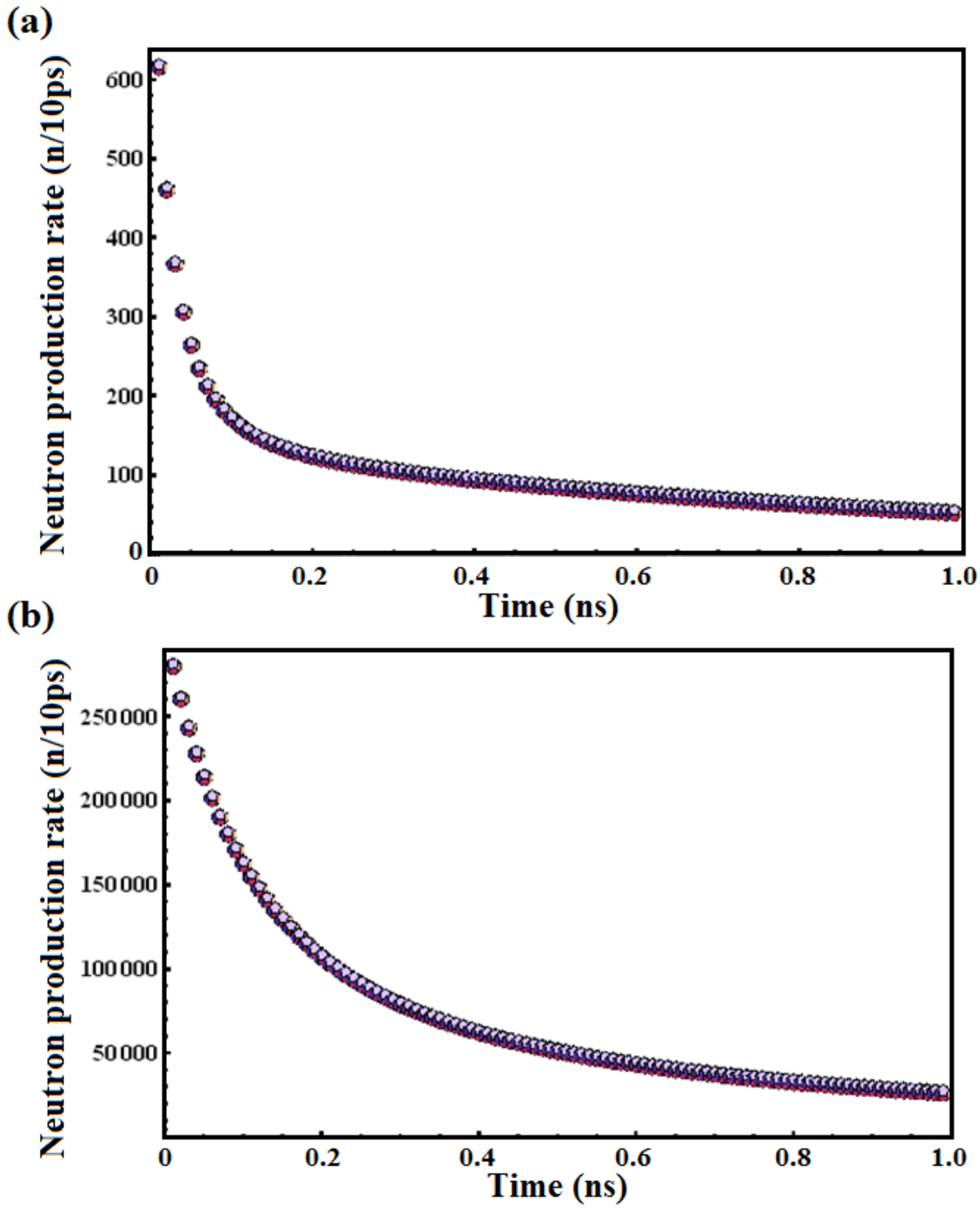

Figure 21. Neutron production rate (neutrons per 10 ps) is shown as a function of time from 0 ns to 1 ns for a (a) 1 mm long filament, 0.1 J into hot ions with kT=8 keV case, and for a (b) 5 mm long filament, 24 J into hot ions with kT=10 keV.

Chapter 3. Laser systems (TPW, THOR)

3.1. TEXAS PETAWATT LASER (TPW)

Intense laser pulses (> I_{crit} ~ 10^{17} W/cm^2) are required for the generation of fusion neutrons from laser driven deuterium cluster fusion experiments. The Texas Petawatt Laser (TPW)[26] is the first laser system that produced a laser pulse with power over 1 PW and pulse duration as short as 150 fs. TPW delivers nearly 200 J per pulse with 150–180 fs duration.

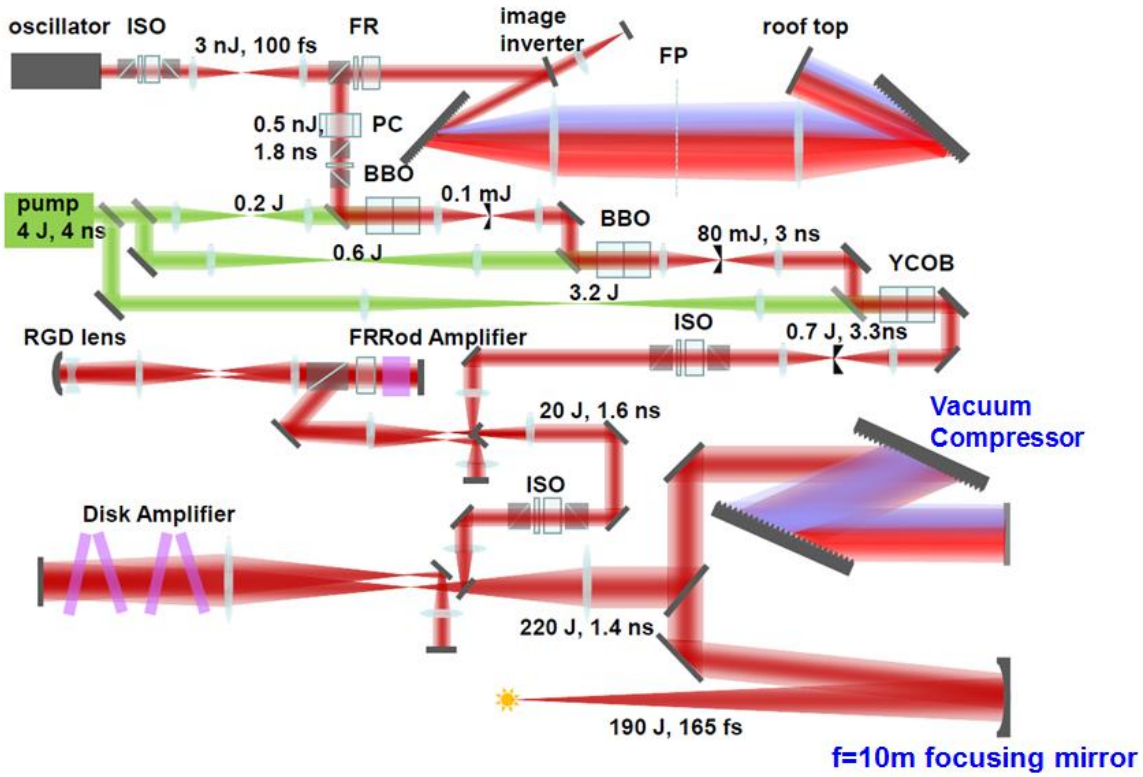

Figure 22. Schematic layout of the TPW.

It utilizes f/40 focusing geometry for the cluster fusion experiments, and the intensity at the focus exceeds 10^{18} W/cm^2. The very long 10 m focal length of the focusing mirror is beneficial for the cluster fusion experiment, which is discussed in

detail in Chapter 6. The f/40 focusing mirror is used to maximize the interaction volume while keeping the laser intensity over the critical intensity for the Coulomb explosion of the deuterium clusters. The schematic layout of the TPW[26] is shown in Figure 22.

The oscillator, model Tsunami from Spectra Physics, produces a 3 nJ, 100 fs pulse with its wavelength centered at 1058 nm and a full width at half maximum (FWHM) of 16 nm. This pulse enters the stretcher, which is aimed to stretch the pulse in time so that the pulse can be safely amplified in the laser amplifier chains afterwards.

This technique is called chirped pulse amplification (CPA)[52,53], and is a basic technique that has been used to build numerous TW to PW class lasers.[3,54,55] In combination with the CPA technique, the optical parametric amplification (OPA)[56] can be used to produce ultrashort intense laser pulses, and the TPW uses the optical parametric chirped pulse amplification (OPCPA) technique.

After the stretcher, a Pockels cell is used to select the oscillator pulses at 2.5 Hz.[26] The 2.5 Hz pulses then go through the three broadband OPCPA stages. The OPCPA stages are pumped by a 4 J, 4 ns custom laser from Continuum. After two BBO stages and one YCOB stage, the pulse energy becomes 300–700 mJ. Since the seed pulse energy injected into the OPCPA stages is only about 270 pJ[26], the combined total gain in the three OPCPA stages amounts to over 10^9.

The amplified pulse after the OPCPA stages still has broad bandwidth because the amplifier crystals do not suffer from gain narrowing in OPCPA. If we started using Nd:glass amplifiers from the beginning, maintaining the spectrum would have been extremely difficult due to the gain narrowing.

After the three OPCPA stages, the pulse goes through two different Nd:glass amplifier stages. The pulse gains the majority of the pulse energy from these two

stages. The first stage called rod amplifier uses a 64 mm flashlamp pumped Nd:silicate glass rod whose peak gain occurs at 1061.5 nm.[26] The second stage called the main amplifier uses four 315 mm flashlamp pumped Nd:phosphate glass disk amplifiers from the NOVA laser whose peak gain occur at 1053 nm.[26]

The combined use of Nd:silicate glass and Nd:phosphate glass results in broader gain bandwidth as a whole amplifier stage, and enables recompression of the pulse duration down to 150 fs at the compressor. Though the majority of the pulse energy comes from the Nd:glass amplifier stages, the net gain is only a few hundred, and the gain narrowing is minimied by the use of mixed Nd:glass amplifiers.

After leaving the main amplifier stage, the pulse enters the vacuum compressor, where the pulse gets recompressed down to 150 fs. The transmission efficiency (85%) of the compressor is quite high due to the multi-layer dielectric grating pair that a ~190 J, 150 fs pulse exits the compressor. Then the laser pulse arrives at the cluster fusion target chamber after reflecting from the f/40 focusing mirror whose focal length is 10 m.

The focused intensity at the gas jet target chamber can easily exceed 10^{18} W/cm^2 after the implementation of the deformable mirror (DFM) and the radial group delay (RGD) correction lens package. A more detailed description of the DFM and RGD lens can be found in Ref. [26,57].

The pulse energy of the laser beam can be controlled by adjusting the charging voltage of the rod amplifier or the main amplifier or both. The full energy shots are called as system shots, and their energy in the cluster fusion experiments varies from 80 J to 190 J. If only the rod amplifier fires, it is called a rod shot and the pulse energy at the target chamber varies from 5 J to 15 J. An OPA shot is when just the OPCPA stages work. The pulse energy at the target chamber can be adjusted by rotating a waveplate, and can be up to a few hundred mJ.

The repetition rate for an OPA shot is 2.5 Hz. The rod shot can be fired every 15 minutes, and the system shot can be fired every hour.

3.2. TEXAS HIGH-INTENSITY OPTICAL RESEARCH (THOR) LASER

The Texas High-Intensity Optical Research (THOR) laser also uses CPA technique to produce intense ultrashort laser pulses. It is a 10 Hz Ti:sapphire system, and delivers up to 700 mJ per pulse on target with a 35 fs pulse duration. The schematic layout of THOR is shown in Figure 23.[27]

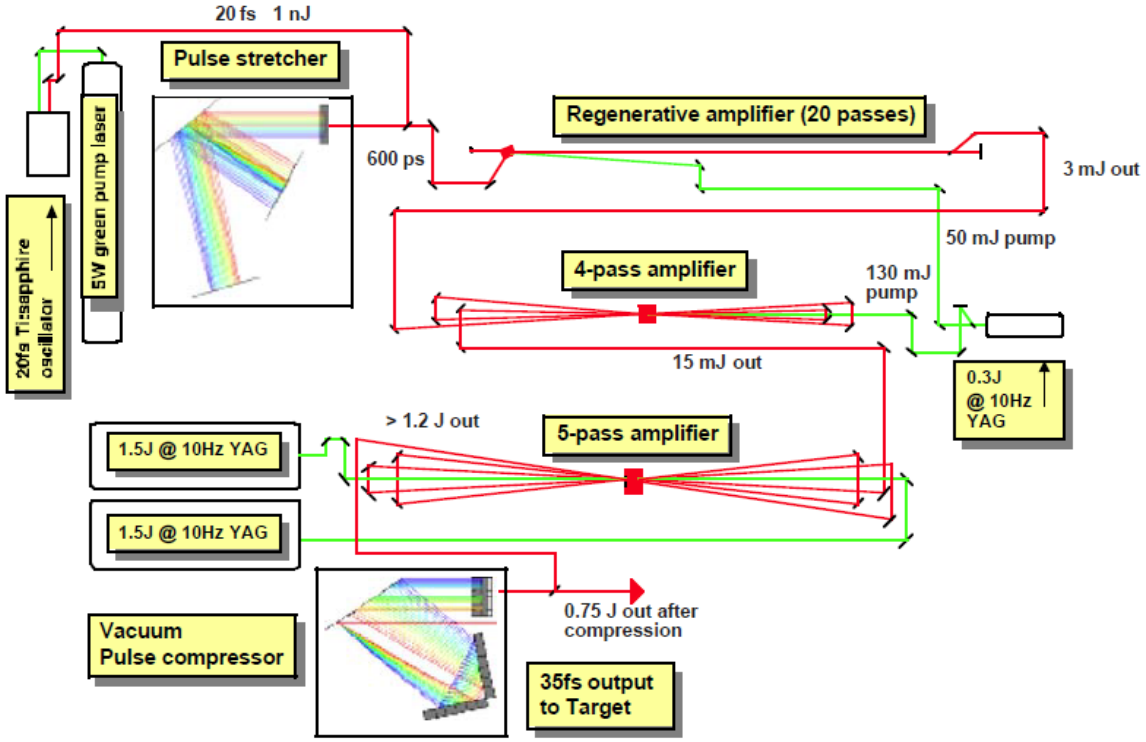

Figure 23. Schematic layout of the THOR laser.

The Kerr lens mode-locked[58] Ti:sapphire oscillator, Femtosource Scientific S20 pumped by a 4.5 W Spectra Physics Millennia Vs DPSS laser, produces 8 nJ, 20 fs, 800 nm pulses at 75 MHz. Then, a Pockels cell is used to select the oscillator pulses at

10 Hz. The 10 Hz seed pulse enters the stretcher, where the pulse duration becomes 600 ps.

After the stretcher, the pulse is sent to a polarization maintaining fiber, where the dispersions are pre-compensated so that the pulse can later be recompressed down to 35 fs at the vacuum compressor.

Then, the pulse gets amplified in the regenerative amplifier, where the pulse gains its energy up to 1–3 mJ while maintaining its broad bandwidth. The 5 mm x 10 mm x 10 mm Brewster-cut Ti:sapphire crystal in the regenerative amplifier is pumped by about 45 mJ from the output of a frequency doubled Q-switched Nd:YAG laser, BigSky CFR 400. A flashlamp pumping is not adequate for the Ti:sapphire laser system because of the short fluorescence lifetime (= 3.2 μs) of Ti:sapphire.

The second amplifier stage consists of a 10 mm diameter, 20 mm long, Brewster-cut Ti:sapphire crystal with an absorption coefficient of 1.05 cm^{-1}. The same BigSky CFR 400 laser is used to pump the Ti:sapphire crystal, and about 100 mJ is absorbed in the crystal. After 4 pass, the pulse energy goes as high as 20 mJ, and the pulse goes through a spatial filter before entering the third amplifier stage.

The final amplifier stage is pumped by two frequency doubled Q-switched Nd:YAG lasers, Spectra Physics PRO 350 YAG lasers. Each laser delivers 1.4 J pulse at 10 Hz on each side of the 2 cm diameter, 2 cm long Ti:sapphire crystal. The absorption coefficient of the crystal is 2.3 cm^{-1}, so most of the pump energy should be absorbed in the first pass. However, about 90% of the pump energy is absorbed in the first pass on THOR, and the transmitted pump beams are sent back to the crystal.

After 5 pass through the 2 cm thick Ti:sapphire crystal, the pulse energy becomes over 1 J, and enters the vacuum compressor before going to the target chamber. The pulse gets recompressed down to 35 fs at the compressor, which can be routinely

measured using the second order autocorrelation setup installed inside the vacuum chamber.

The fluence of the laser beam on the surface of the grating is always kept under 100 mJ/cm^2 on THOR. This value already assumes a safety factor of at least two, and is based on a number of damage threshold measurements of a gold grating.[59,60]

The intensity of the compressed pulse can be measured as a function of time using a third order autocorrelation measurement setup. Figure 24 shows the measurement of various pre-pulses and post-pulses using the setup in 2010. Though the regenerative amplifier maintains the bandwidth very well and the amplified pulse can be recompressed down to 35–40 fs without difficulty, it is known that the optics such as a polarizer inside the regenerative amplifier often serves as the origin of many pre-pulses.[12,61]

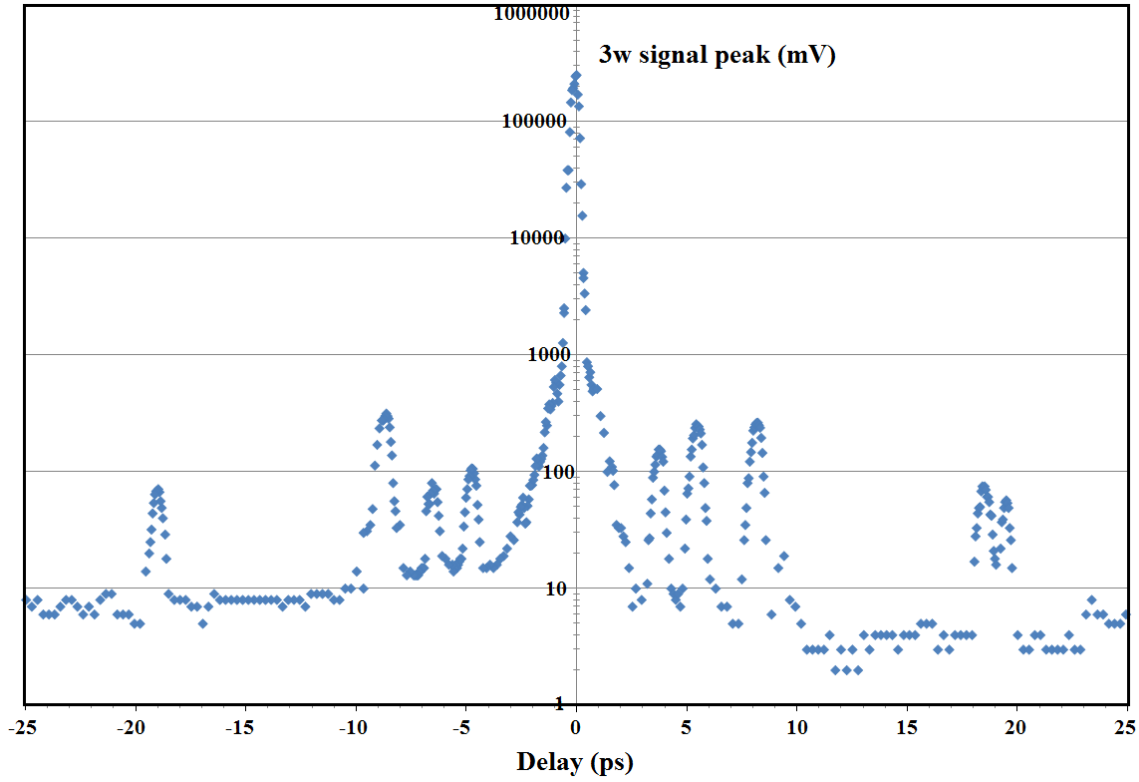

Figure 24. Third order autocorrelation measurements on THOR (on 2/5/2010).

As can be seen in Figure 24, the intensities of the pre-pulses were as high as 1/1000 during the measurements. This contrast ratio is acceptable for the cluster fusion experiments on THOR. However, much higher contrast ratio is desirable for the solid target experiments. THOR laser is currently undergoing a major upgrade, and we replaced the regenerative amplifier to an OPA stage for these reasons.

3.3. THOR PW UPGRADE – LARGE PUMP LASER

Recently, we started upgrading the THOR laser to a higher power laser. To upgrade the 20 TW laser to a 1 PW laser, we decided to use much bigger Ti:Sa crystal with a diameter of 10 cm and a thickness of 2.5 cm. We expect to extract about 45 J of energy from this crystal without deteriorating the beam quality. The uncompressed amplified beam will then enter the compressor, and 30 J, 30 fs pulse will exit the compressor.

To produce a 45 J, 800 nm uncompressed pulse after the power amplifier stage, we designed a large pump laser that can send a total of 100 J of green light onto the Ti:Sa crystal. To avoid damaging the crystal, the green beam will be split into two and each surface of the Ti:Sa crystal will be hit by a 50 J, 20 ns pulse. The schematic layout of the large pump laser is shown in Figure 25.

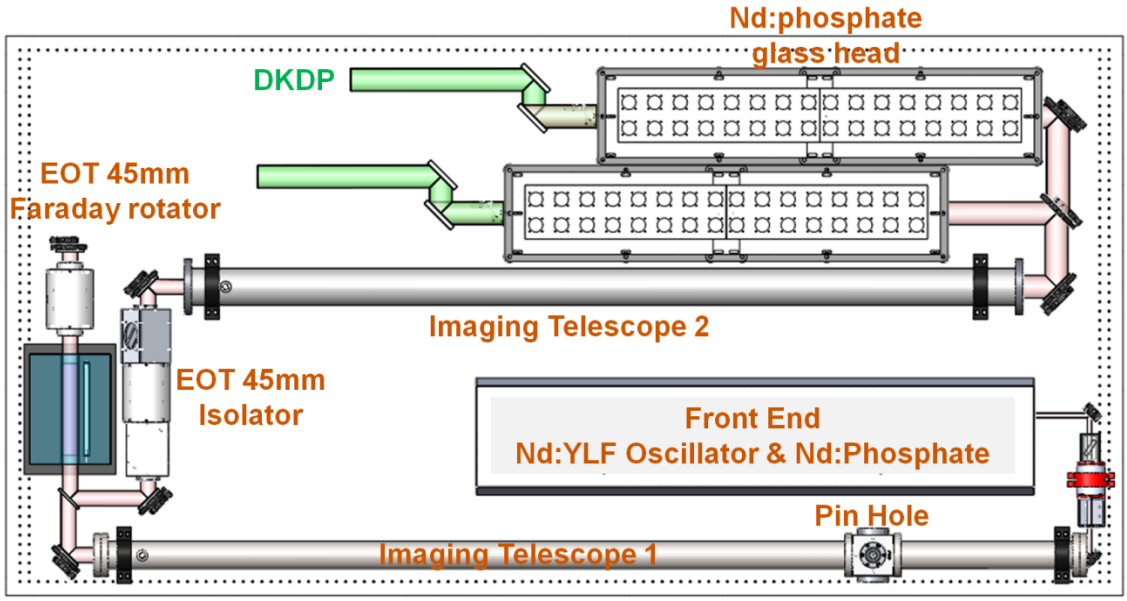

Figure 25. Schematic layout of the large pump laser. (Courtesy of Donghoon Kuk)

3.3.1 Energetics design principle

The goal of our pump laser energetics design is to produce 120 J of 527 nm light after the two DKDP crystals. We decided to use two legs of final amplification stages, each of which will produce 120 J of IR. Then, we will have two DKDP crystals for frequency doubling. We expect to achieve 50% conversion efficiency. In order to model our amplifier chain, we used MIRO software, Mathematica 8, and Excel spreadsheet. We decided to use Nd:phosphate glass heads as our main gain material since we need over 100 J of IR from each chain. Although glass has generally poor thermal properties compared with crystals, they can be produced in bigger volumes relatively easily. We decided to use 50 mm diameter Nd:phosphate glass heads in our final amplification stage, and a 50 mm glass rod would be big enough to produce the required pulse energy. Since we are using a glass rod as our gain material, the repetition rate is limited to about 1 shot per 10 minutes. The pulse duration of our pump beam

would be about 20 ns, and we chose this value after considering the damage thresholds of our optics. As we increase the pulse duration, the damage threshold gets higher; however, the frequency doubling gets less efficient if we use too long of a pulse and too low intensity. Starting from the required energy of 120 J and using Frantz-Nodvik equation[62] for a few types of Nd:glass amplifier heads, we were able to find the requirements for the front end laser. The following table shows some of the specifications of the amplifier heads that we plan to use for the big glass pump laser of the THOR PW laser.

Specification	7 mm Nd:YLF Head	12 mm Nd:Phosphate Head	32 mm Nd:Phosphate head	50 mm Nd:Phosphate head
Rod Dimension (Dia. x length in mm)	7 × 100	12.7 × 120	31.75 × 235	50 × 240
Clear Aperture	90 %	90 %	95 %	98 %
Peak Emission Wavelength (nm)	1053 ± 1	1054 ± 1	1054 ± 1	1054 ± 1
Single Pass Gain	≥ 8	≥ 8	≥ 7	≥ 7
Saturation Fluence (J/cm^2)	1.5	5.5	5.5	5.5
Transmission	≥ 97 % at 1053 nm	≥ 95 % at 1054 nm	≥ 95 % at 1054 nm	≥ 95 % at 1054 nm
Wavefront Distortion (632.8 nm)	≤ λ/4	≤ λ/4	≤ λ/4	≤ λ/4
Edge Bevel	30° ± 5°	30° ± 5°	30° ± 5°	30° ± 5°
End Face Parallelism Angle	1°, Antiparallel	1°, Parallel	1°, Parallel	1°, Parallel

Table 5**.** Specifications of the required laser heads.

3.3.1.1. Front end

(a). Q-switched Unstable Resonator

A 7 mm diameter Nd:YLF rod will be used as our gain material for the oscillator. Our 7 mm Nd:YLF head will produce 1053 nm laser light that matches the location of the peak gain of Nd-doped phosphate glass rod at 1054 nm. Nd:YLF can be pumped by flashlamps due to its relatively long fluorescence lifetime. With a small signal gain of 8, the Nd:YLF oscillator can produce 80 mJ, 20 ns FWHM pulse at 10 Hz. Figure 26 shows the basic design of our Q-switched unstable oscillator using 7 mm Nd:YLF head. We will use a variable reflectivity mirror for the generation of third order super-Gaussian beam profile.

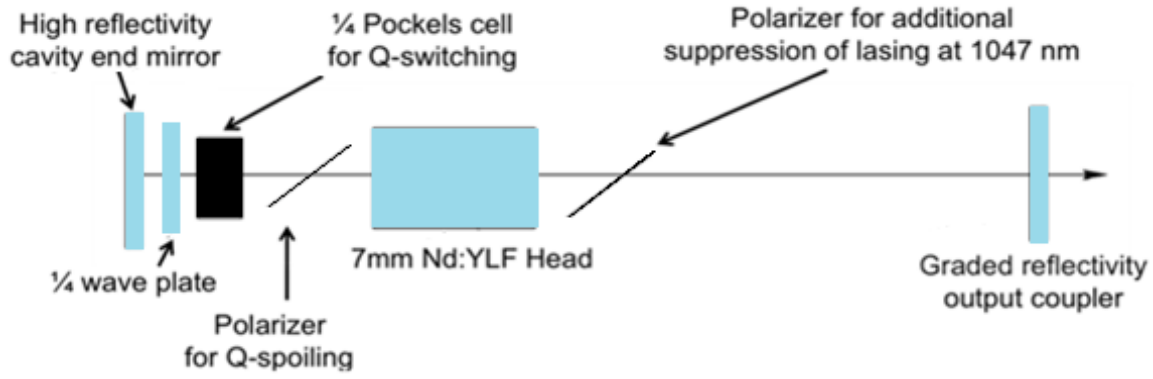

Figure 26. Q-swithched unstable resonator design block diagram.

The intensity of the output pulse from the Nd:YLF oscillator is shown as a function of time, the beam profile is shown in a 128 pixels by 128 pixels plane, and the fluence of the output beam is shown as a function of position in Figure 27 (a), (b), (c), respectively. A peak reflectivity of 8% is assumed for the graded reflectivity mirror. After 30 round trips, the pulse energy becomes about 80 mJ according to the simulation.

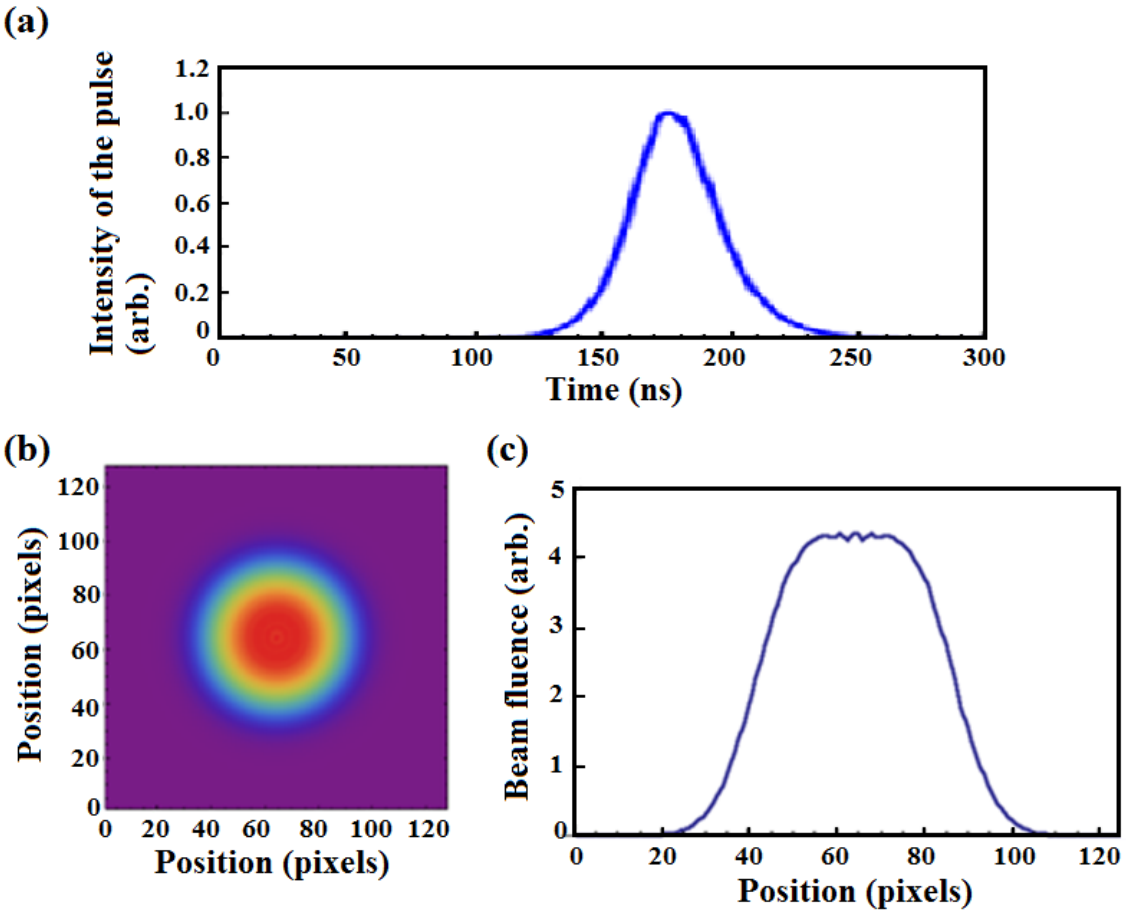

Figure 27. Analysis of the 80 mJ, 20 ns FWHM pulse from the Nd:YLF oscillator. (a) The intensity of the pulse is shown as a function of time, (b) the beam profile of the output pulse is shown in a 2D plane, and (c) the beam fluence is shown as a function of position. (Courtesy of Todd Ditmire)

(b). Booster

A 12 mm Nd:phosphate glass head is used to amplify the 60 mJ output pulse energy from the Nd:YLF oscillator to 1.5 J. With 20 ns, 1.5 J input beam from the front end, we expect to achieve 120 J of 527 nm light after the final amplification and frequency doubling. A single pass gain of 8 is assumed for the 12 mm head. The schematic layout of the booster amplifier is shown in Figure 28.

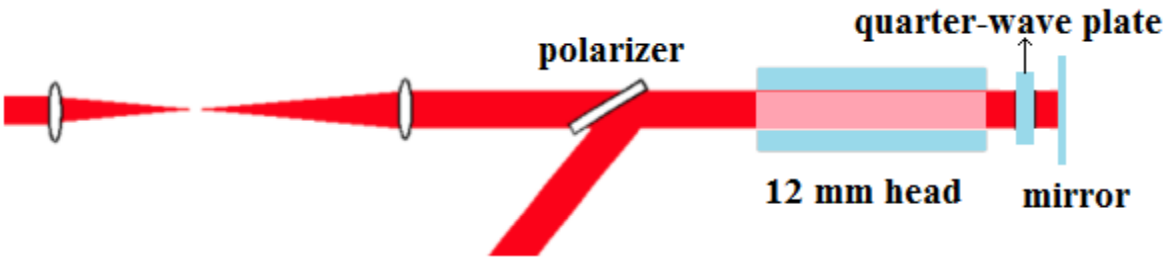

Figure 28. Double pass amplification through 12 mm head produces 2 J output level.

3.3.1.2. Pre-amplification

Pre-Amplification stage amplifies the 1.5 J, 1054 nm, 20 ns laser beam relayed from the front end to 23 J output level. A 32 mm Nd:Phosphate laser head is employed for this stage and double pass amplification is going to be used. A small signal gain of 6.5 or greater is assumed for the 32 mm head. The beam size entering the 32 mm head is going to be 25 mm FWHM while the outgoing beam size would be 27.5 mm after double-passing the 32 mm head due to some gain saturation. For the MIRO calculation, we assumed 15% less gain at the center as shown in Figure 29.

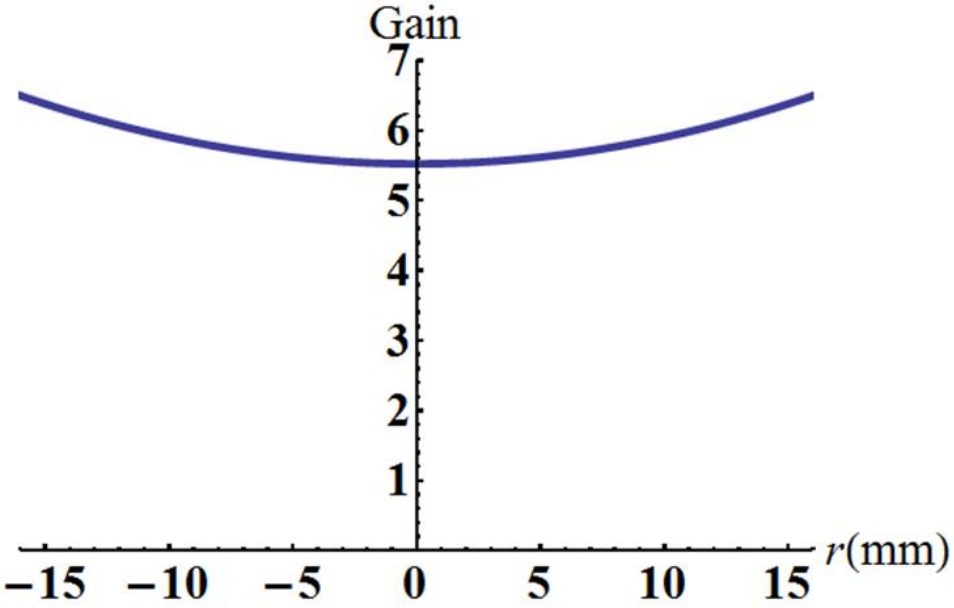

Figure 29. Assumed radial gain profile of the 32 mm head.

3.3.1.3. Main amplification

Main amplification stage is the most important part of our big glass pump laser system. Again, we plan to use Nd:phosphate glass as our gain medium, and this limits the repetition rate of our system down to 1 shot per 10 minutes. A small signal gain of 6.5 or higher is assumed, and the following radial gain profile in Figure 30 is assumed for the 50 mm heads in our MIRO calculation. We cannot put all the 50 mm heads in series and produce 240 J of 1054 nm light because this would damage our optics. Instead, we will use one 50 mm head to amplify the energy up to 77 J, and will split the beam into two legs. Each leg will have one 50 mm head, and we expect to get 120 J of IR from each leg. After this final amplification, we will have a total of 240 J of IR. We expect 50% conversion efficiency from the 55 mm x 55 mm x 25 mm DKDP crystal, so we will have two beams of 60 J, 527 nm, 18 ns pulse as our final output.

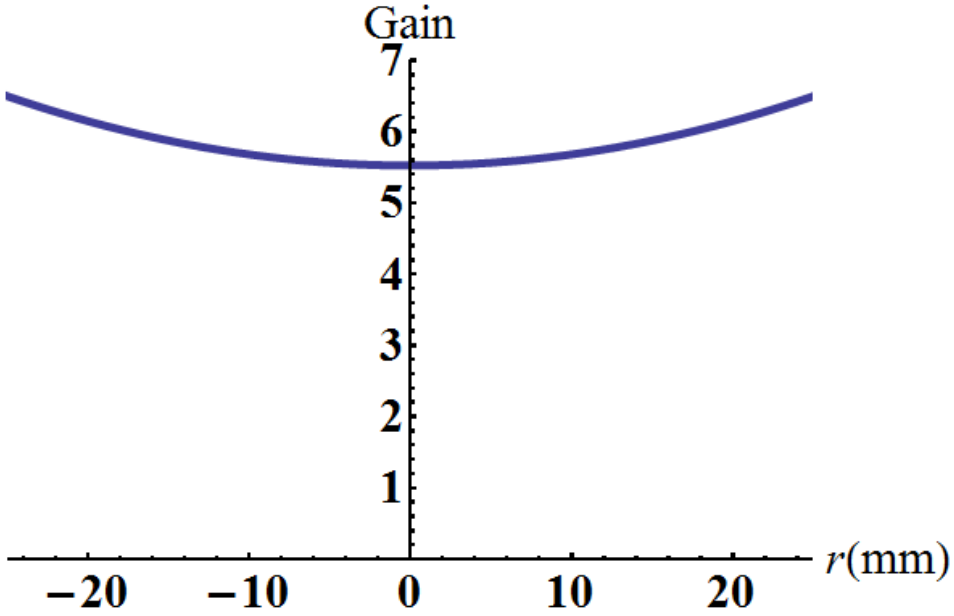

Figure 30. Assumed radial gain profile of the 50 mm head.

3.3.1.4. Frequency doubling crystal

After the final amplification stage, we expect to get a 1054 nm, 120 J, 20 ns pulse in each leg. Then, we plan to use DKDP crystal for frequency doubling. For the selection of the crystal, we focused on two things. First, the beam diameter after the final amplification stage is expected to be about 50 mm. Therefore, we need to have a pretty big crystal. This narrows down our selection to a few crystals such as YCOB, DKDP, KDP, etc. Although crystals such as BBO or KTP have larger effective nonlinear coefficients than these crystals, the growth of BBO or KTP is known to be very difficult. Secondly, we need to achieve 50% conversion efficiency. For this, we want to use a crystal with higher effective nonlinear coefficient. At the same time, we want to have long enough nonlinear length L_{NL} compared with the crystal thickness required for 50% conversion efficiency.

For the final selection of the crystal, we used both SNLO program, and Mathematica. The simulation results can be seen in the next section. After these simulation results, we decided to use 55 mm x 55 mm x 25 mm DKDP crystal with Type II phase matching. In the case of a DKDP crystal, we get larger effective nonlinear coefficient d_{eff} with Type II phase matching. To determine the dimensions of the DKDP crystal, we used MIRO software. We were able to avoid modulations in the beam when we used 70 mm clear aperture DKDP crystals.

After we decided to use DKDP crystal, we also took into account the AR coating damage threshold of the crystal. Many vendors failed to provide us a reliable damage threshold value in the beginning, and we had to put a lot of effort into finding out those numbers. The expected peak fluence on the DKDP crystal is 8.3 J/cm^2. Since we want to have a minimum safety factor of 2, we require the vendors to provide AR coating damage threshold higher than 17 J/cm^2.

3.3.1.5. Beam homogenization (optional)

After the DKDP crystal, we want to have a uniform pump beam for the Ti:sapphire crystal. However, some researchers reported how much their pump beam got distorted after passing through a series of thick Nd:glass amplifiers.[63] We looked into how we could improve the 2ω pump beam quality before sending the pump beam to our 10 cm diameter Ti:sapphire crystal. Tanaka *et al.* and Ertel *et al.* reported substantial improvements in their pump beam quality when they used diffractive homogenizers.[63,64] We will leave this beam homogenization technique as an option.

3.3.2. Simulation

3.3.2.1. MIRO simulation for the energetics design

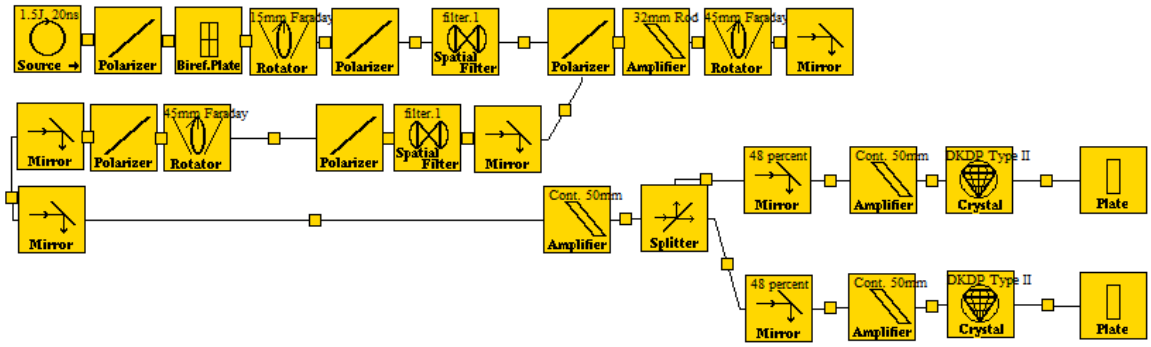

Figure 31. Layout of the big glass pump laser for the MIRO simulation.

The layout shown in Figure 31 was used for the MIRO simulation. For the front end, we assumed 1.5 J, 20 ns pulse with 10 mm beam diameter. We expect the beam to be Gaussian in time, and third order super-Gaussian in space. The assumed beam profile for the front end of the MIRO simulation is shown in Figure 32.

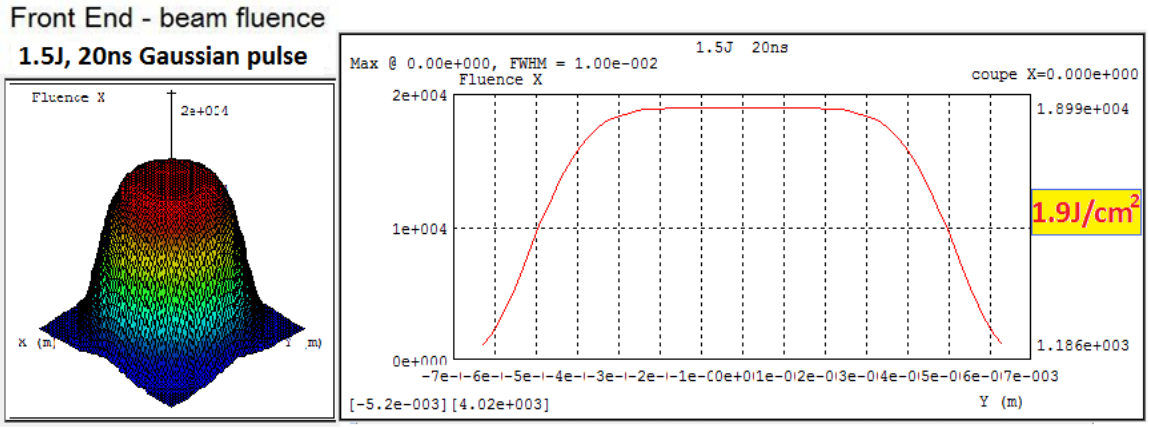

Figure 32. Assumed beam profile of the front end for the MIRO simulation.

We initially planned to use four 64 mm diameter Nd:phosphate glass heads in our final amplification stage. However, we had some challenges in procuring the 64 mm Nd:glass rods. Alternatively, we decided to use three 50 mm diameter Nd:phosphate glass heads in the final amplification stage of the big glass pump laser system. The smaller beam diameter caused by this change in the design inevitably increased the beam fluence at each stage.

The following diagram in Figure 33 shows the peak fluence on major optical components. MIRO simulation program was used to get the energy, FWHM beam diameter, pulse duration, and the peak fluence. We expect to get a peak fluence of 8.3 J/cm^2 in an 18 ns pulse on the front surface of the DKDP crystal. This implies that we need to have a very high damage threshold (>20 J/cm^2) for the AR coating of the DKDP crystal.

The damage threshold of the Faraday rotator crystal is about 3 J/cm^2 for a 1 μm, 20 ns pulse. So, we intentionally lowered the gain of the 32 mm diameter Nd:glass head down to 6.5 for the MIRO simulation shown below. After double-passing the 32 mm diameter Nd:glass head, the beam will be relay-imaged onto the surface of the Faraday

rotator. This will minimize the possible modulations in the beam inside the Faraday rotator, and help us to keep the peak beam fluence lower than the damage threshold of the Faraday rotator.

All the subsequent optical components have AR coating damage thresholds higher than 10 J/cm^2. We decided not to expand the beam after the 45 mm diameter Faraday rotator since this requires another telescope. We will have a 40 mm FWHM beam on the first 50 mm diameter Nd:glass head. After the amplification, the beam energy will be as high as 77 J.

Then, we will split the beam into two legs, each of which consists of one 50 mm head and a 25 mm thick DKDP crystal. We expect to get 60 J of 527 nm light from each leg in an 18 ns pulse with a FWHM diameter of 44 mm. Therefore, we will have 120 J of 527 nm light after the frequency doubling. Type II phase matching will be used for the frequency doubling.

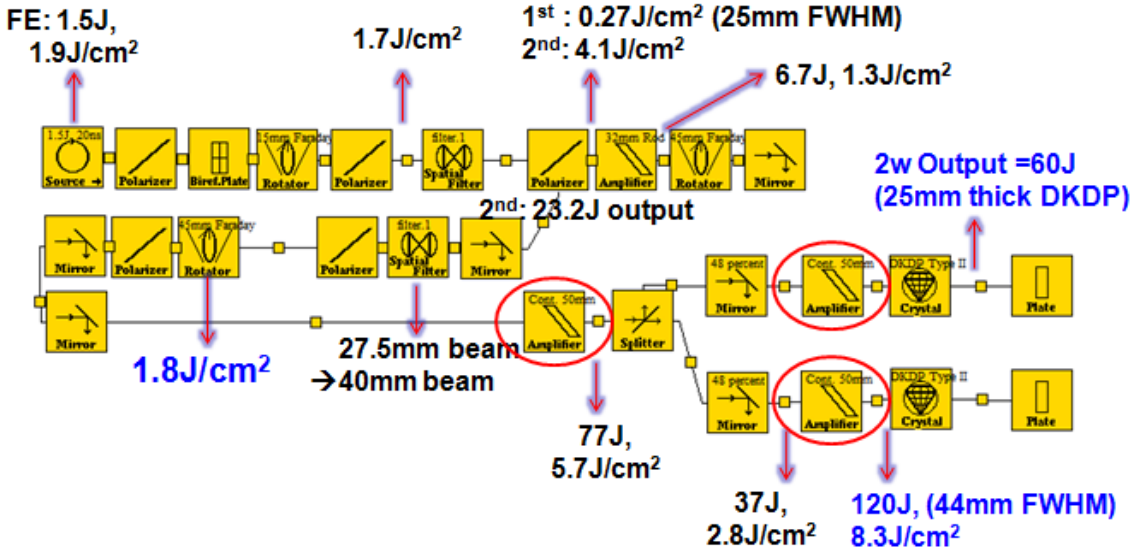

Figure 33. Peak fluence and the pulse energy on major optical components.

3.3.2.2. SNLO for the frequency doubling

Using SNLO software, we were able to find the effective nonlinear coefficient d_{eff} for various crystals. Of the few crystals that can be grown as large as 55 mm, DKDP and YCOB were our final two candidates for the SHG material. YCOB with type I phase matching has slightly higher d_{eff} than that of DKDP with type II phase matching. However, YCOB also has larger index of refraction, which results in smaller nonlinear length L_{NL}. When we assumed the same phase mismatch of 0.6 cm^{-1}, and 60 mm input beam diameter with 120 J pulse energy, we can expect slightly better performance with DKDP crystal as is shown in Figure 34. The calculations were done using Mathematica 8.0.

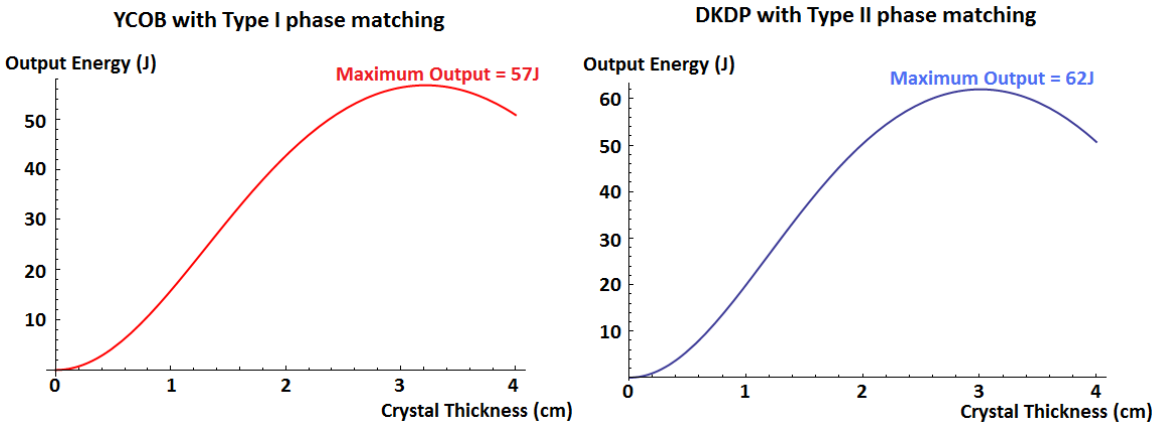

(a) (b)

Figure 34. (a) Expected output energy from YCOB, and (b) DKDP after the frequency doubling.

Based on Figure 34 (a), we expect to get a maximum of 57 J output energy using YCOB crystal. When DKDP crystal was used, a maximum output energy of 62 J at 2ω light is produced according to the SNLO calculations. This was also confirmed by the SNLO software as one can see from the result shown in Figure 35.

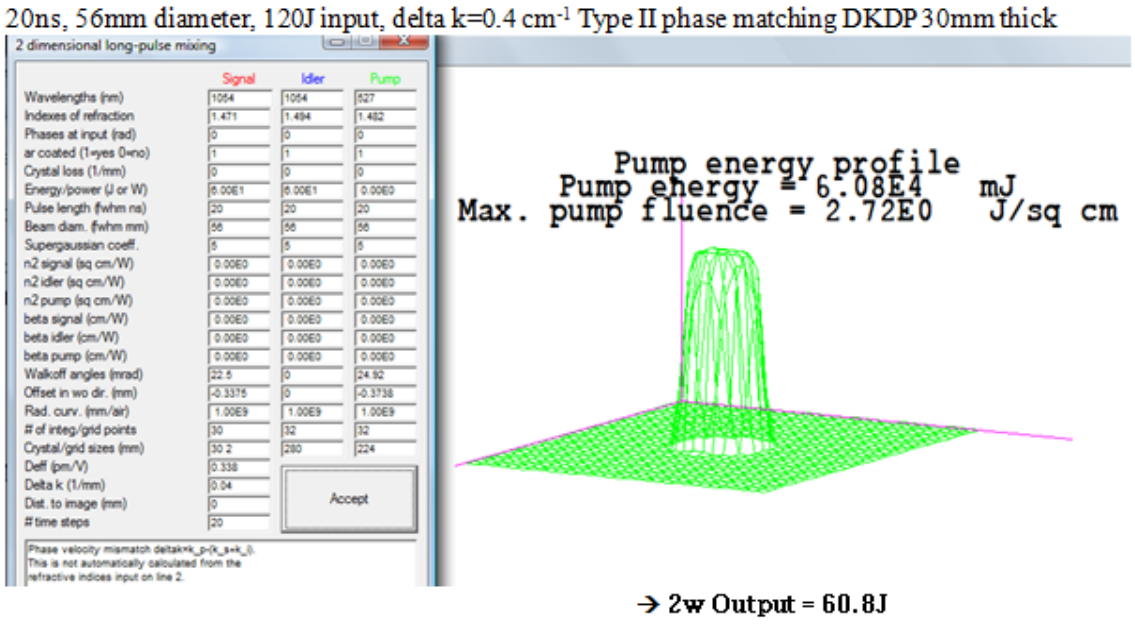

Figure 35. 2ω energy output from the 30 mm thick DKDP crystal using SNLO software.

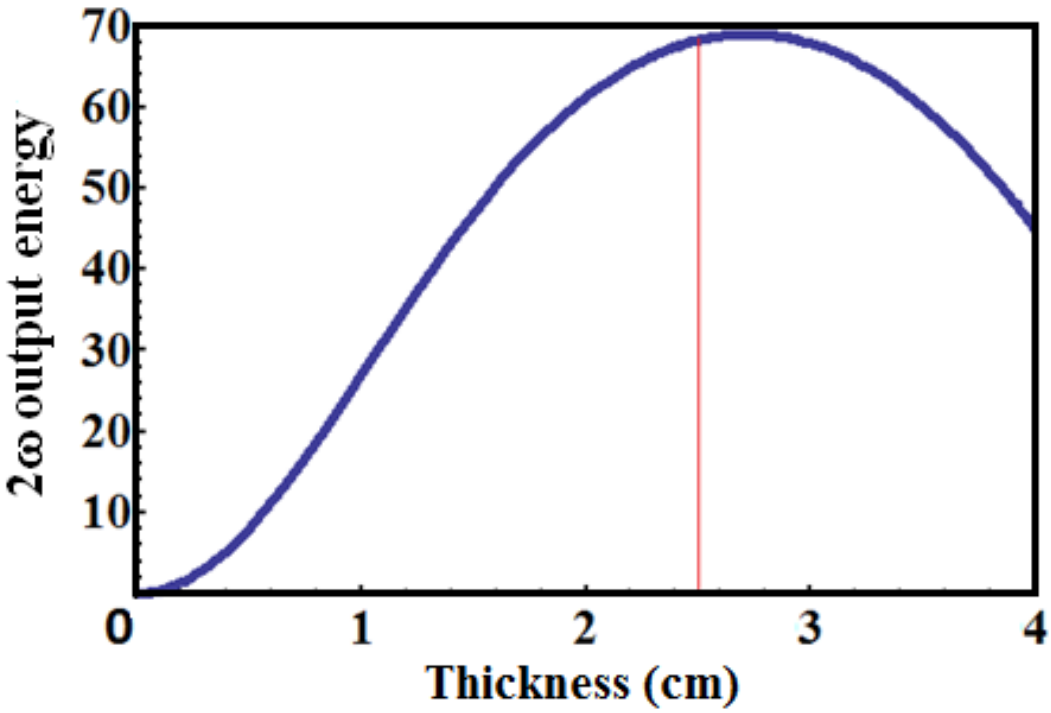

Figure 36. 2ω output energy from the 25mm thick DKDP crystal using Mathematica.

Calculations using Mathematica 8.0 also confirmed that we can get 60 J of 527 nm light from the DKDP crystal. As can be seen from Figure 36, we can use 25–27 mm thick DKDP crystals instead of 30 mm thick DKDP crystals because the expected laser intensity on the crystal became much higher after we decided to use 50 mm glass heads instead of the 64 mm glass heads. Based on these simulation results, we decided to use DKDP crystal with type II phase matching for the SHG of our 1054 nm, 20 ns, 120 J pulse. We will have two DKDP crystals of size 55 mm x 55 mm x 25 mm. The final layout of the crystal is shown in Figure 37. Red arrow indicates the 1054 nm, 20 ns, 120 J input beam, and the green arrow indicates the 2ω output beam. We plan to tilt the crystal by 3 degrees to avoid the reflected light hitting the 50 mm amplifier head.

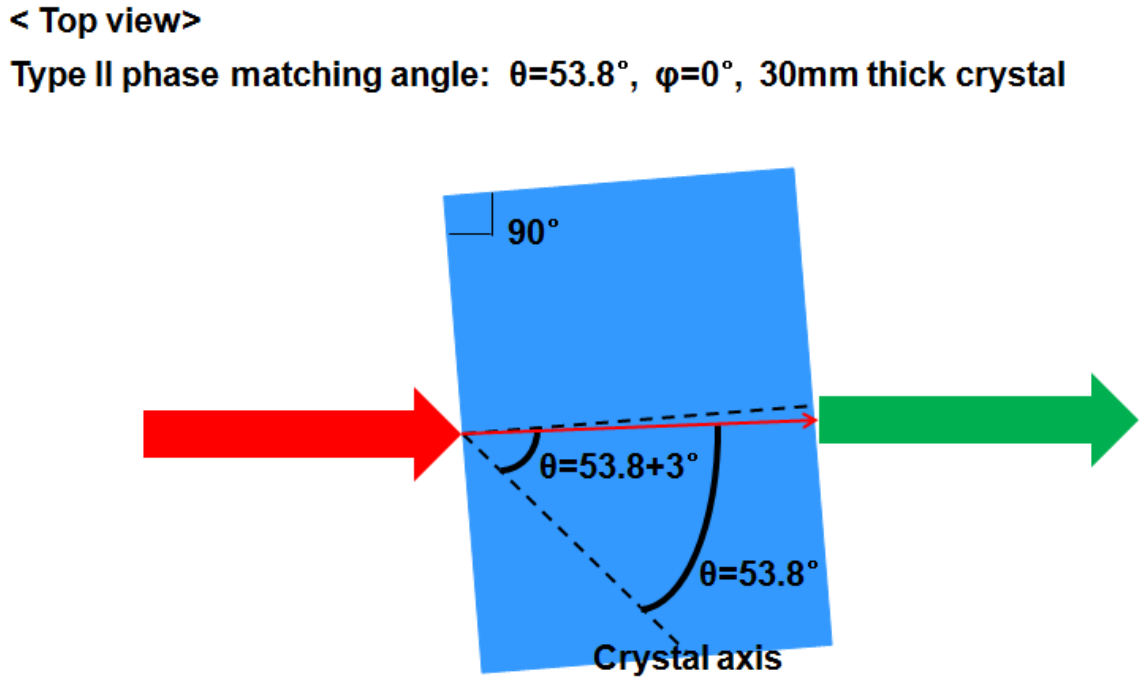

Figure 37. Layout of the DKDP crystal with Type II phase matching.

3.3.2.3. Radial gain profile of Nd:phosphate glass rod

We assumed 15% less gain at the center of the rod, r=0, than at the boundary of the rod, r=R, in the MIRO modeling for the Nd:phosphate glass rod. To justify this radial gain profile, we wrote a short Mathematica code that calculates the stored energy density at a particular location as a function of the distance from the center to that location. This simulation will tell us what concentration of Nd doping is good for the pump laser. For the calculation, we assumed a surface element of the rod that acts like a Lambertian radiator, then integrated the contribution from each element. Since the side surface of each rod is going to be grounded, this assumption is valid. If the rough grounded surface is not taken into account, the simulation shows a hot spot at the center as in Figure 38. These simulation results are for a 50 mm diameter, 24 cm long Nd:phosphate glass rod with a flashlamp energy of 400 J.

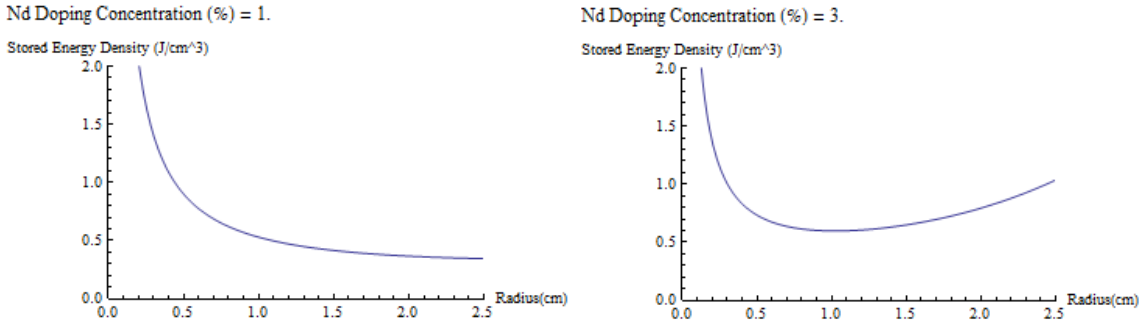

Figure 38. Mathematica simulation of the stored energy density for a 50 mm diameter Nd:phosphate glass rod with Nd doping concentration of 1% (left) and 3% (right) by weight.

These hot spots can be avoided by considering the surface elements as Lambertian radiators.[65,66] With this taken into account, the modified simulation results show that the stored energy density becomes smaller at the center, which agrees with the functional form that was used in the MIRO modeling. Though the exact value of the stored energy is hard to predict, the simulation results for a 50 mm diameter Nd:glass rod shows that

the stored energy density with Nd doping concentration higher than 1% is not adequate for the pump laser. At 1.0% Nd doping, the stored energy density at the center is 47% less than that at 2.5 cm from the center as can be seen in Figure 39. The stored energy density with 0.5% Nd doping for the same diameter glass rod is also shown in the figure for comparison.

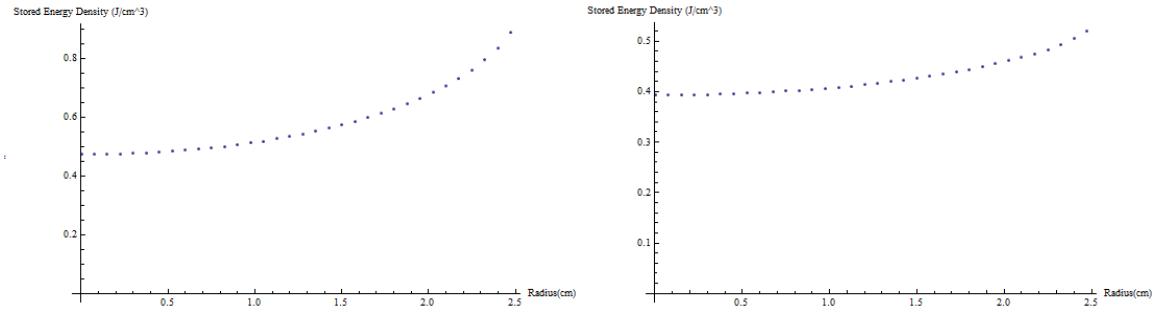

Figure 39**.** Modified Mathematica simulation of the stored energy density for a 50 mm diameter Nd:phosphate glass rod with Nd doping concentration of 1% (left) and 0.5% (right) by weight.

Above 1% Nd doping concentration, the difference gets bigger, and we cannot expect a uniform radial gain profile. Since the beam size is about 40 mm at the first 50 mm rod, the difference in the stored energy density would be smaller, though. Moreover, the surface elements are not perfect Lambertian radiators in reality, and we think that the gain at the center would be higher than the modified simulation shown above. In other words, the actual stored energy density will be somewhat similar to Figure 39, but will be a combination of Figure 38 and Figure 39. Based on these simulation results, we think that the Nd doping concentration of 0.5–1.0% can be used for the 50 mm Nd:phosphate glass rods.

Chapter 4. Generation of cluster targets

In this chapter, I will talk about our targets. I showed the design of our supersonic nozzle, and measurements of the cluster size using Rayleigh scattering. A mixing process of deuterium and Helium-3 is shown along with the residual gas analyzer data.

4.1. PHYSICS BACKGROUNDS

4.1.1. Joule-Thomson effect

When deuterium gas expands, the average distance between the deuterium molecules becomes larger. Since the molecules are bonded together with van der Waals potential, a change in the average distance between two molecules is equivalent to a change in the potential energy between them.

Due to the small intermolecular attractive force between the deuterium molecules, the net potential energy of the deuterium gas increases when the gas expands. Since the total energy has to be conserved and the total energy of the deuterium gas is the sum of the kinetic energy and the potential energy of the molecules, the overall increase in the potential energy implies the decrease in the kinetic energy of the molecules. Therefore, an expansion of deuterium gas causes a drop in the temperature of the gas.

Note that this is only true if the initial temperature of the expanding gas is lower than the Joule-Thomson inversion temperature.[67] If the initial temperature is higher than the inversion temperature, the expansion of gas actually causes an increase in the temperature. This happens because of the drop in the collision rate between the gas molecules as the gas expands, where fewer collisions lead to a decrease in the potential energy.

Sometimes, the initial temperature of the gas in the reservoir is sufficiently low that the gas liquefies as it expands. The result of this expansion is a mixture of cluster and a gas in the sense that the overall density is still that of a gas, but there are aggregates of many atoms, whose local density is near solid density. In other words, clusters are formed after the expansion if the initial temperature of the gas is low enough.

4.1.2. Supersonic nozzle

A supersonic nozzle changes some portion of the random thermal energy of molecules into a directional kinetic energy. The temperature of a gas can be thought of in terms of the average kinetic energy of the constituent molecules. These motions are usually randomly directed.

However, a supersonic nozzle has a small throat diameter, and lets through only molecules that move in a specific direction. If an observer watches the gas molecules in the frame that moves in the same direction as the gas (i.e. in the center of mass frame), the observer will see that the average kinetic energy in his frame became much less after the gas passed through the nozzle.

Before the molecules passed through the nozzle, all the kinetic energy was random thermal energy, and the temperature could be defined as two thirds of the average kinetic energy of a molecule. However, after passing through the nozzle, the gas molecules collectively move outward. This motion has to be considered separately from the random thermal motion, and the temperature in the frame that moves along with the expanding gas becomes much smaller than the original temperature.

In addition to the temperature drop due to the Joule-Thomson effect, this creates further temperature drop in the center of mass frame. This is the main reason we used a

conical supersonic nozzle in our cluster fusion experiments. Studies about the dependence of the cluster size on nozzle geometry can be found in the literature.[68-70]

The design of the supersonic nozzle can vary widely across experiments, but we consistently used the following nozzle design shown in Figure 40 during the cluster fusion experiments. Though the drawing says a throat diameter of 0.032", the correct throat diameter of the nozzle was about 790 μm, and the cone angle was about 5 degrees.

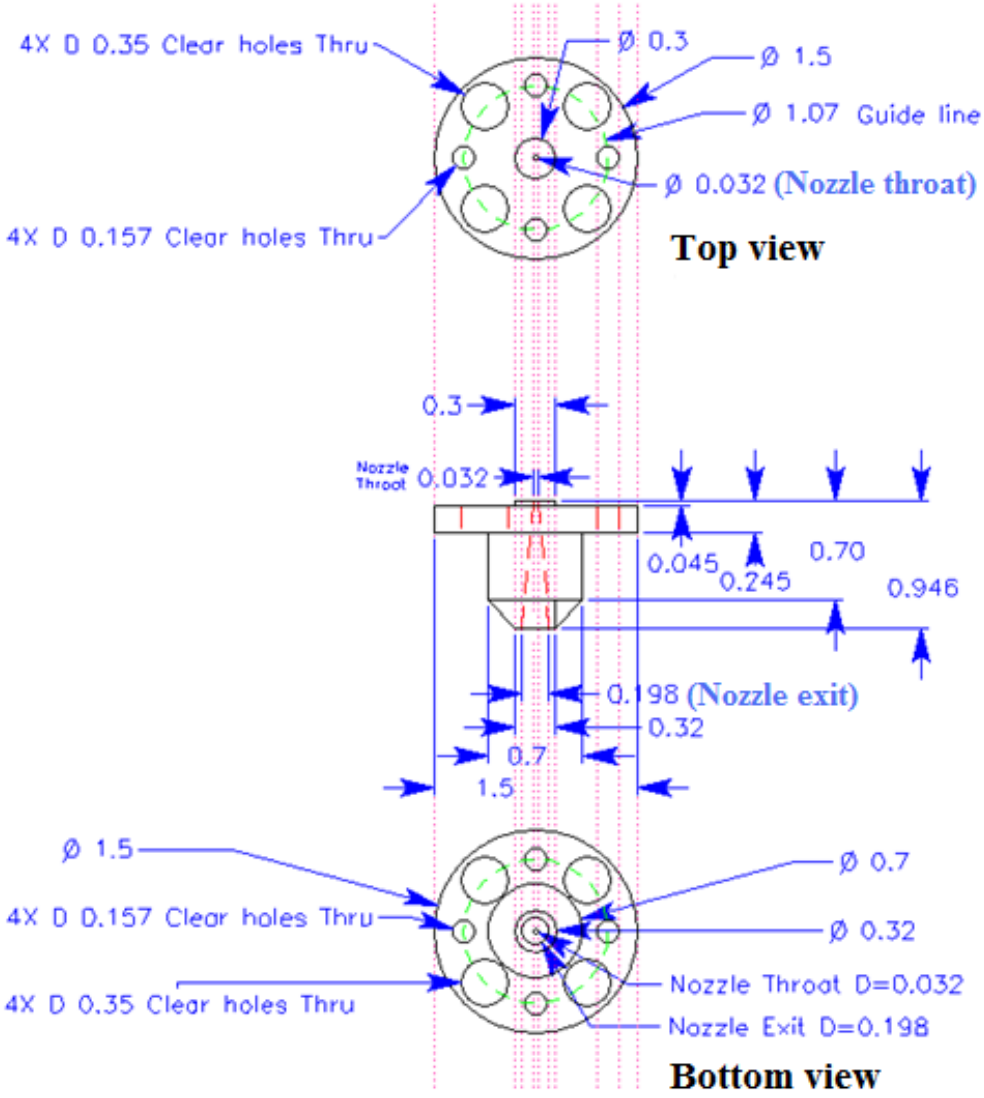

Figure 40. Design of the supersonic nozzle that was used in the cluster fusion experiments on the TPW. The units are shown in inches in the figure.

We had a cooling jacket above the nozzle and around the pulse valve to cool the deuterium gas down to liquid nitrogen temperature, and the design of the cooling jacket is shown in Figure 41. Liquid nitrogen was flowed through the channels in the copper cooling jacket, cooling the deuterium gas to about -187 ºC. The gas was typically under 700–1000 psi backing pressure.

Inside the cooling jacket was a Parker pulse valve (series 99, 99S1-A2-P1-99B05), with a Vespel poppet. Vespel poppet seemed to be more durable than the normal Teflon poppet in our applications. The valve was held open for 1 ms, and produced deuterium clusters with an average radius of a few nanometers.

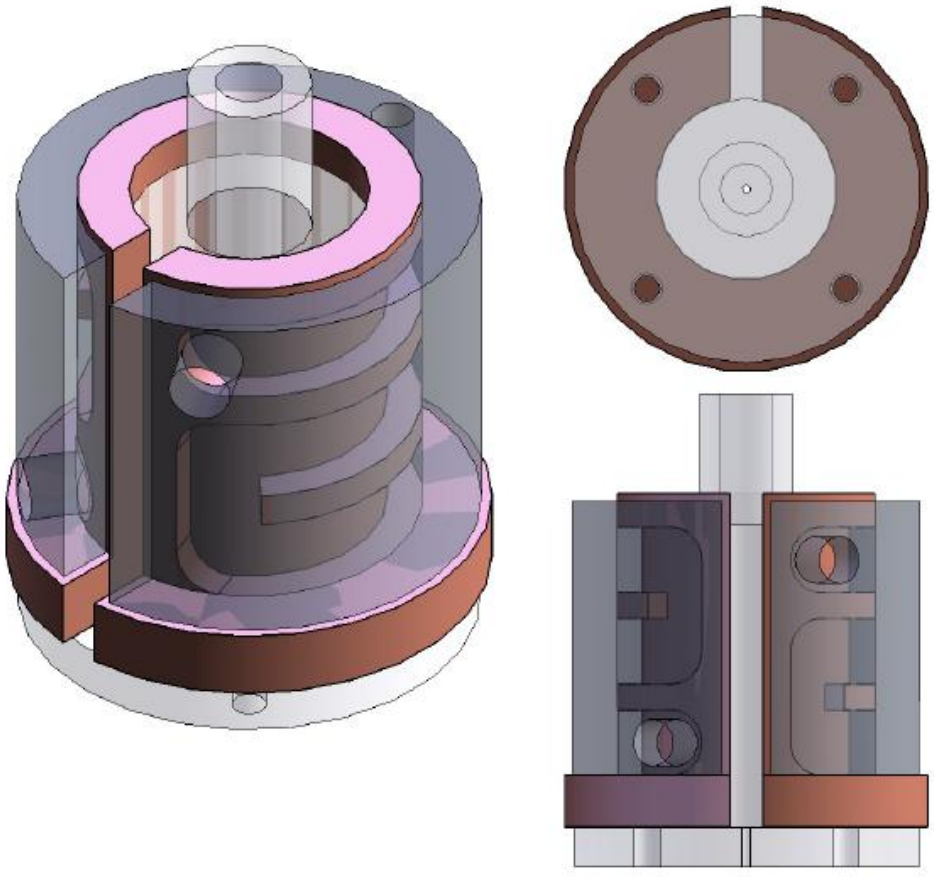

Figure 41. Design of the cooling jacket surrounding the pulse valve.

4.1.3. Hagena parameter

In the previous section, I mentioned the importance of a supersonic nozzle in the generation of cluster targets. Previous studies have shown that the average cluster size can be expressed in terms of the dimensions of the nozzle and the parameters of the gas jet. The so-called Hagena parameter is the most commonly used measure for that purpose.[68] If different experimental conditions give the same Hagena parameter, similar cluster sizes are expected.

The Hagena parameter is defined as:[34,68,70]

$$\Gamma^* = k \frac{(\frac{d}{\tan\alpha})^{0.85}}{T^{2.29}} P, \quad (4.1)$$

where P is the backing pressure in units of mbar, T is the temperature of the gas in the reservoir in units of K, d is the nozzle throat diameter in units of μm, α is the expansion half angle, and k is a constant specific to a gas. For example, k=181 can be used for deuterium.[70]

The number of atoms in a cluster is related to the Hagena parameter as

$$N_c = 33(\frac{\Gamma^*}{1000})^{2.35}, \quad (4.2)$$

for Hagena parameter less than 10^4. When Γ* is in the range from 10^4 to 10^6, the following formula can be used.[69]

$$N_c = 100(\frac{\Gamma^*}{1000})^{1.8}. \quad (4.3)$$

A more detailed summary of the relationship between the Hagena parameter and the cluster size based on numerous experimental measurements can be found in Table 1 of Ref. [71].

4.1.4. Rayleigh scattering measurements to determine the average cluster size

The average size of the atomic or molecular clusters can be measured from a series of Rayleigh scattering measurements. The size of the cluster targets usually

ranges from a few nanometers to a few tens of nanometers. Since the wavelength of visible light is much bigger than this, Rayleigh scattering is the dominant scattering effect when a laser pulse is incident on the cluster targets. The intensity of the incident laser should be kept sufficiently low to avoid ionizing the clusters.

The OPA light from the TPW is not a good light source for this measurement because the intensity at the focus is already too high for the Rayleigh scattering measurements due to the short pulse duration. Instead, we used a much weaker 17 mW He-Ne laser to acquire the following measurements.

The scattered light signal is proportional to the number density of scattering objects, which in our case is the number density of cluster targets. It is also proportional to the scattering cross section. This can be summarized as follows:[34,70,72,73]

$$S_{RS} \propto n_c \sigma_c, \tag{4.4a}$$

$$\sigma_c = \frac{128\pi^5 r^6}{3\lambda^4}\left(\frac{n^2-1}{n^2+2}\right)^2, \tag{4.4b}$$

where n_c is the number density of the clusters, and σ_c is the Rayleigh scattering cross section of a cluster with a radius r, λ is the wavelength of the light source, and n is the index of refraction. For hydrogen or deuterium clusters, the index of refraction is about 1.10.[18,74,75] Assuming each cluster with radius r consists of N_c atoms, one can express the radius in terms of the number of atoms, N_c, in a cluster:

$$r \propto \left(\frac{3}{4\pi n_0}\right)^{1/3} N_c^{1/3} \propto N_c^{1/3}, \tag{4.5}$$

where n_0 is the solid or liquid density of the cluster. For example, the radius of a deuterium cluster can be written as

$$r[\text{Å}] = 1.7 \times N_c^{1/3}. \tag{4.5a}$$

Also, the number density of the cluster can be written as

$$n_c = \frac{n_D}{N_c} \propto \frac{P}{k_B T}\frac{1}{N_c} \propto \frac{P}{N_c}, \tag{4.6}$$

where n_D is the atomic density of the deuterium cluster, P is the backing pressure of the gas jet, k_B is the Boltzmann constant, and T is the temperature of the gas.

Using equation (4.4a), (4.4b), (4.5), and (4.6) the scattered light signal is expressed as[72]

$$S_{RS} \propto n_c \sigma_c \propto \frac{P}{N_c} r^6 \propto \frac{P}{N_c} N_c^2 = P N_c. \quad (4.7)$$

Let's assume that the onset of Rayleigh scattering corresponds to 100 atoms per cluster (i.e. N_c=100).[34] This is equivalent to saying that the cluster formation starts when N_c gets bigger than 100. Then, we can relate the measured minimum scattering signal height to the number of particles in a cluster:

$$V_{min} = A^* P_{min}^* 100, \quad (4.8)$$

where V_{min} is the measured minimum scattering signal for a gas jet backing pressure of P_{min}. To obtain equation (4.8) from equation (4.7), N_c=100 and a proportionality constant of A were used.

From equation (4.8), the value of the constant can be written as A = (V_{min}/P_{min})/100, and we can express the relation between the measured scattering signal and the backing pressure as follows:

$$V = A^* P^* N_c = (V_{min}/P_{min})^* P^* N_c/100, \quad (4.9)$$

where V is the measured Rayleigh scattering signal, and N_c is the number of atoms per cluster with a backing pressure of P.

Therefore, the number of atoms per cluster can be expressed in terms of the backing pressure and the scattering signal as

$$N_c = 100 \times \frac{V}{V_{min}} \times \frac{P_{min}}{P} \ . \quad (4.10)$$

Plugging equation (4.10) into equation (4.5a), we have the following formula for the radius of a cluster:

$$r = (100 \times \frac{V}{V_{min}} \times \frac{P_{min}}{P})^{1/3} \times 0.170 \text{ [nm]}. \quad (4.11)$$

Therefore, the average radius of the clusters can be quantitatively measured from the scattered signal height and the backing pressure of the gas jet.

4.2. MEASUREMENT OF THE CLUSTER SIZE

4.2.1. Experimental setup for the Rayleigh scattering measurements

Rayleigh scattering measurements were used for the measurement of the deuterium cluster size. A 17 mW He-Ne laser was used as the light source, and the spot size of the beam was about 1 mm. The diameter of the gas jet was about 5 mm, and the gas jet was open for about 1 ms.

To collect the scattered light, we had a two inch lens between the gas jet and a Hamamatsu R928 photomultiplier tube (PMT). The scattered light was then imaged onto the photocathode of the PMT. The selection of Hamamatsu R928 PMT was based on the relatively high quantum efficiency at 628 nm, and high gain. A table that shows the characteristics of a few other PMTs is shown in Appendix C.

Several ND filters were used to adjust the overall signal strength, and two laser line filters (632.8 nm, 3 nm FWHM) filtered out the ambient light. Tektronix TDS 5054 A 500 MHz oscilloscope was connected to the PMT, and measured the scattered light signal. An input impedance of 1 MΩ was used to maximize the signal on the oscilloscope. The trigger signal for the oscilloscope was synchronized with the opening of the pulse valve. The temperature and pressure of the gas jet were varied during the measurements. The schematic setup for this measurement is shown in Figure 42.

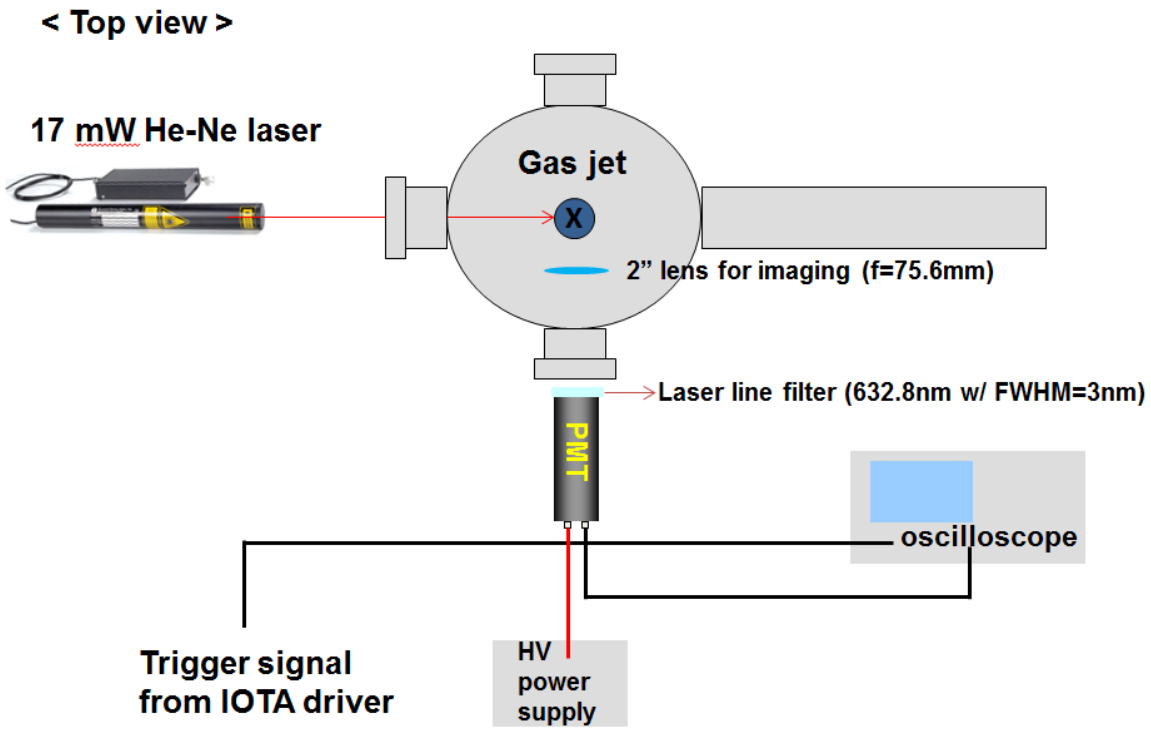

Figure 42. Schematic diagram of the experimental setup for the cluster size measurements.

4.2.2. Rough estimation of the Rayleigh scattering signal

A rough estimation of the scattered signal height is possible with a known PMT gain and the light source. For example, a 17 mW He-Ne laser emits 5.4×10^{16} photons per second. If the gas jet is open for 1 ms, a total of 5.4×10^{13} photons are incident on the gas jet.

To calculate how many photons are scattered, we still need to know the scattering cross section. If we know this number, we can assume that 1% of these photons are collected from the 2-inch lens, and imaged onto the photocathode. This is summarized in Figure 43.

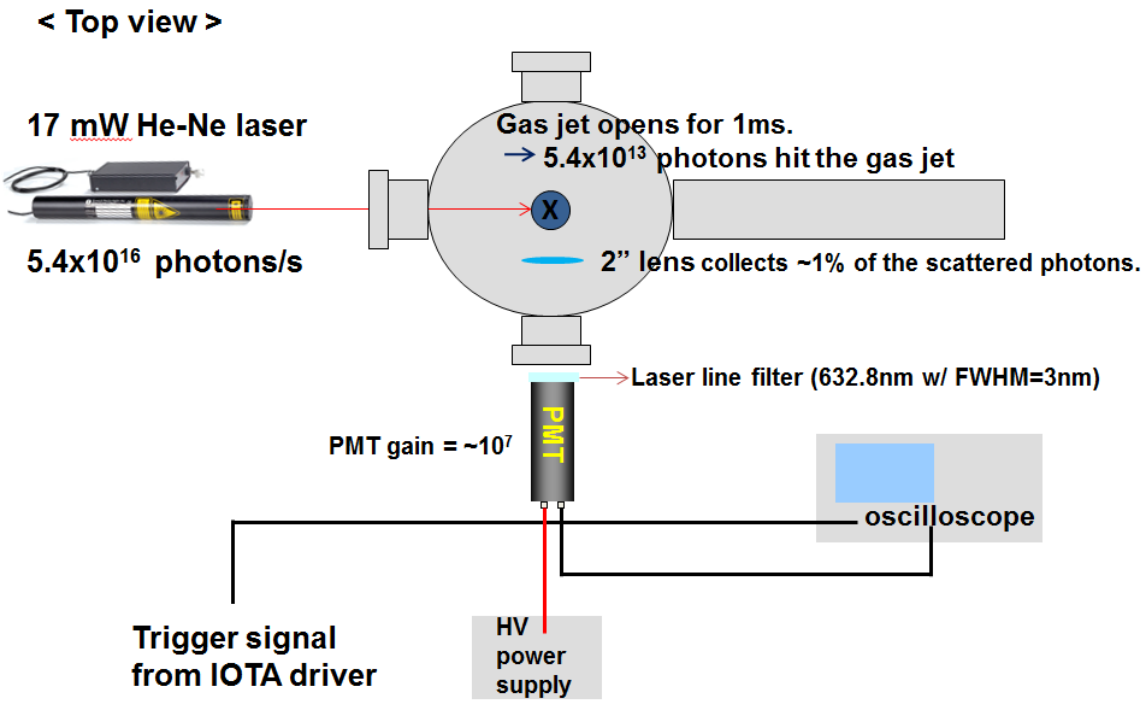

Figure 43. Rough estimation of the Rayleigh scattering signal I.

The Rayleigh scattering cross section from a dielectric sphere can be calculated using equation (4.4b). Putting R=5.00 nm, λ=632.8 nm, and n=1.10 for deuterium into the formula, the scattering cross section of a single cluster becomes $\sigma_c = 5.45\text{x}10^{-24}$ m^2. Then, I assumed a cluster density of $n_c=1.0\text{x}10^{15}$ clusters/cm^3, and a gas jet length of z=3.0 mm in the laser propagation direction. This gives $n_c*\sigma_c*z=1.63\text{x}10^{-5}\sim1.6\text{x}10^{-5}$ and results in a total scattered photon number of $5.4\text{x}10^{13} *n_c*\sigma_c*z = 8.8\text{x}10^{8}$.

Let's assume that 1% of these photons are collected from the 2" lens, all of which hit the photocathode of the PMT. Using the quantum efficiency of 8% of the photocathode, approximately $7\text{x}10^5$ electrons are generated due to the scattered light. With a gain of 10^7, $7\text{x}10^{12}$ electrons are produced after the PMT. This is summarized in Figure 44.

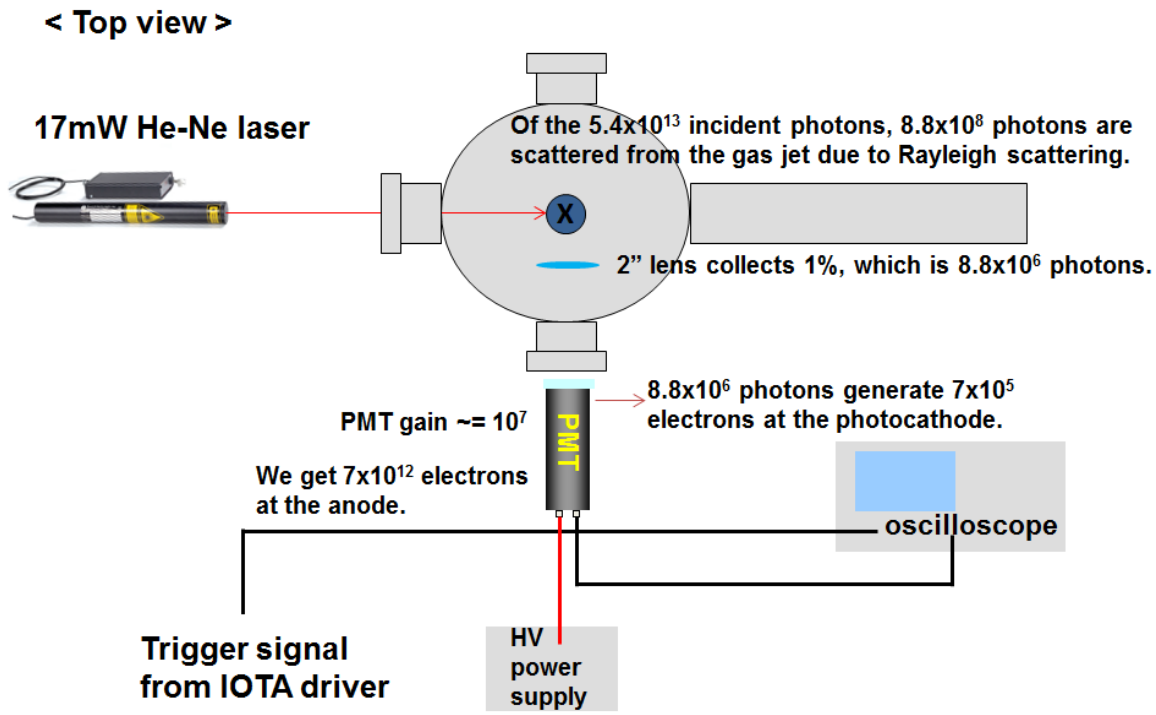

Figure 44. Rough estimation of the Rayleigh scattering signal II.

Finally, the signal on the oscilloscope can be approximated from the estimated number of electrons. To calculate the current, the charge of 7×10^{12} electrons is divided by the opening time of the nozzle, which gives 1.6×10^{-19} C * 7×10^{12} /(1 ms) = 1.1 mA. Note that this estimate of the current is not exact because the electrons do not arrive continuously and the angular distribution of Rayleigh scattering was not considered when the collection efficiency of the lens was estimated as 1%.

With 50 ohm impedance, 1.1 mA corresponds to 55 mV. During the actual Rayleigh scattering signal measurements, voltage peaks of a few mV were observed instead of 55 mV. This calculation is summarized in Figure 45.

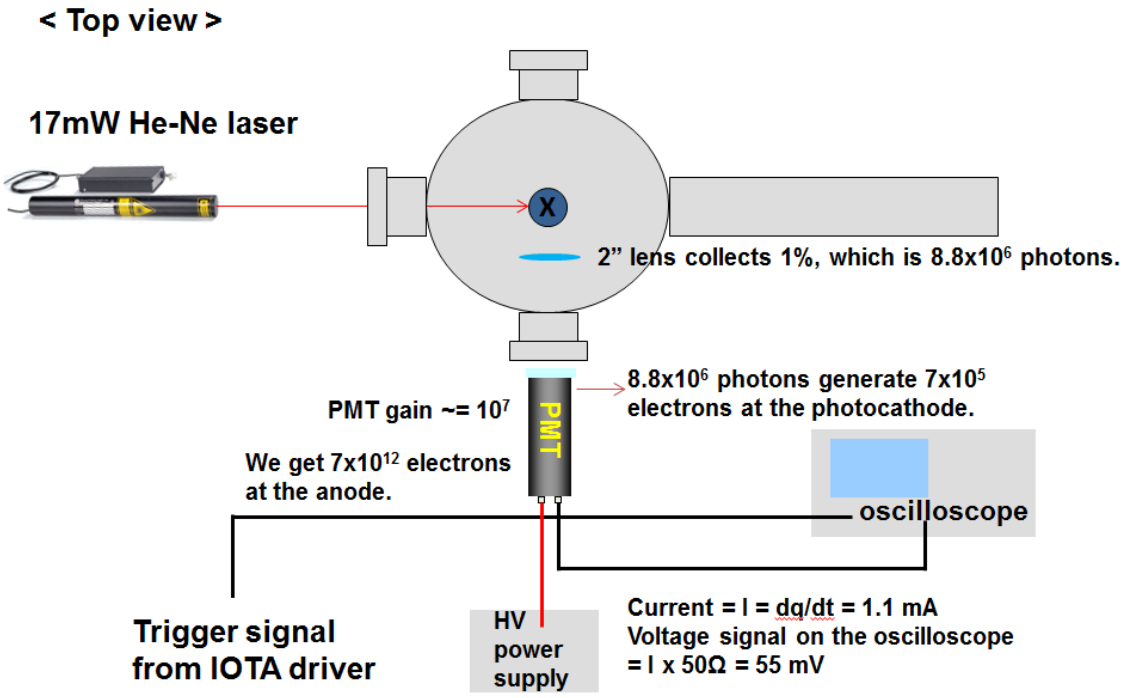

Figure 45. Rough estimation of the Rayleigh scattering signal III.

4.3. RAYLEIGH SCATTERING MEASUREMENTS

4.3.1. Temperature scan with D_2 target

With the Rayleigh scattering measurement setup, we measured the scattered light varying the temperature of the deuterium gas from 87 K to 150 K. The pressure of the gas jet was about 770 psi. The scattered signal in mV is shown as a function of time in Figure 46 (a), and the diameter of the deuterium cluster is shown as a function of the gas jet temperature in Figure 46 (b). The solid red curve in Figure 46 (a) indicates a fit to the data.

The Rayleigh scattering signal was strongest at the lowest temperature we used with deuterium cluster targets. The calculation indicates that we had deuterium clusters with a diameter of 16 nm, which is equivalent to about N=10^5 deuterium atoms at liquid density.

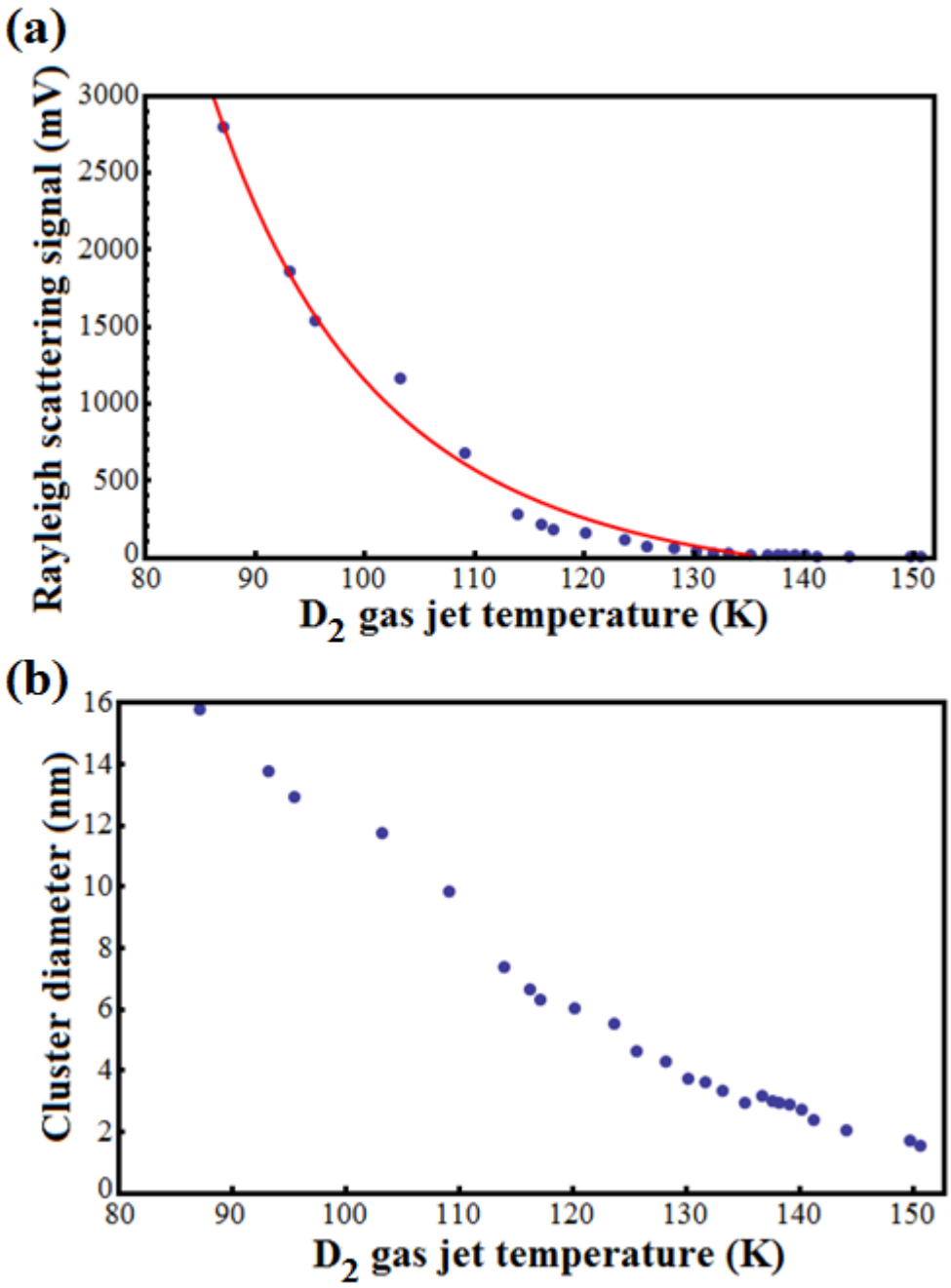

Figure 46. (a) Rayleigh scattering signal as a function of the deuterium gas jet temperature, (b) diameter of the deuterium clusters as a function of the gas jet temperature.

4.3.2. Temperature scan with D_2 + He-4 target

After mixing the deuterium gas and helium-4 gas, we performed similar Rayleigh scattering measurements. After mixing the gas, we waited for about an hour before starting the measurements. This wait time is based on the RGA measurements discussed in section 4.4, and is necessary to give sufficient time for the two gases to be mixed uniformly.

The mixture rate was 50% deuterium and 50% helium-4, and the total pressure was about 770 – 800 psi. The scattered signal in mV is shown as a function of time in Figure 47 (a), and the diameter of the deuterium cluster is shown as a function of the gas jet temperature in Figure 47 (b).

Comparing with the previous result for the deuterium clusters, we find that the cluster formation did not change much after we added helium-4 gas. While we had about 16 nm diameter clusters with deuterium clusters, we had about 15 nm diameter clusters with deuterium clusters + helium-4 mixture. We think that this difference is insignificant, and expect that the cluster formation of the deuterium molecules is not going to be affected when helium-3 gas is added in the mixture cluster fusion experiments described in detail in Chapter 7.

We did not perform these scattering measurements with deuterium + helium-3 because helium-3 is very difficult to obtain and is prohibitively expensive. However, we expected that the chemical properties of deuterium + helium-4 would be very similar to the helium-3 mixture in terms of clusterization. Moreover, we expect that only deuterium molecules will form clusters while helium-3 or helium-4 atoms are present in the background.

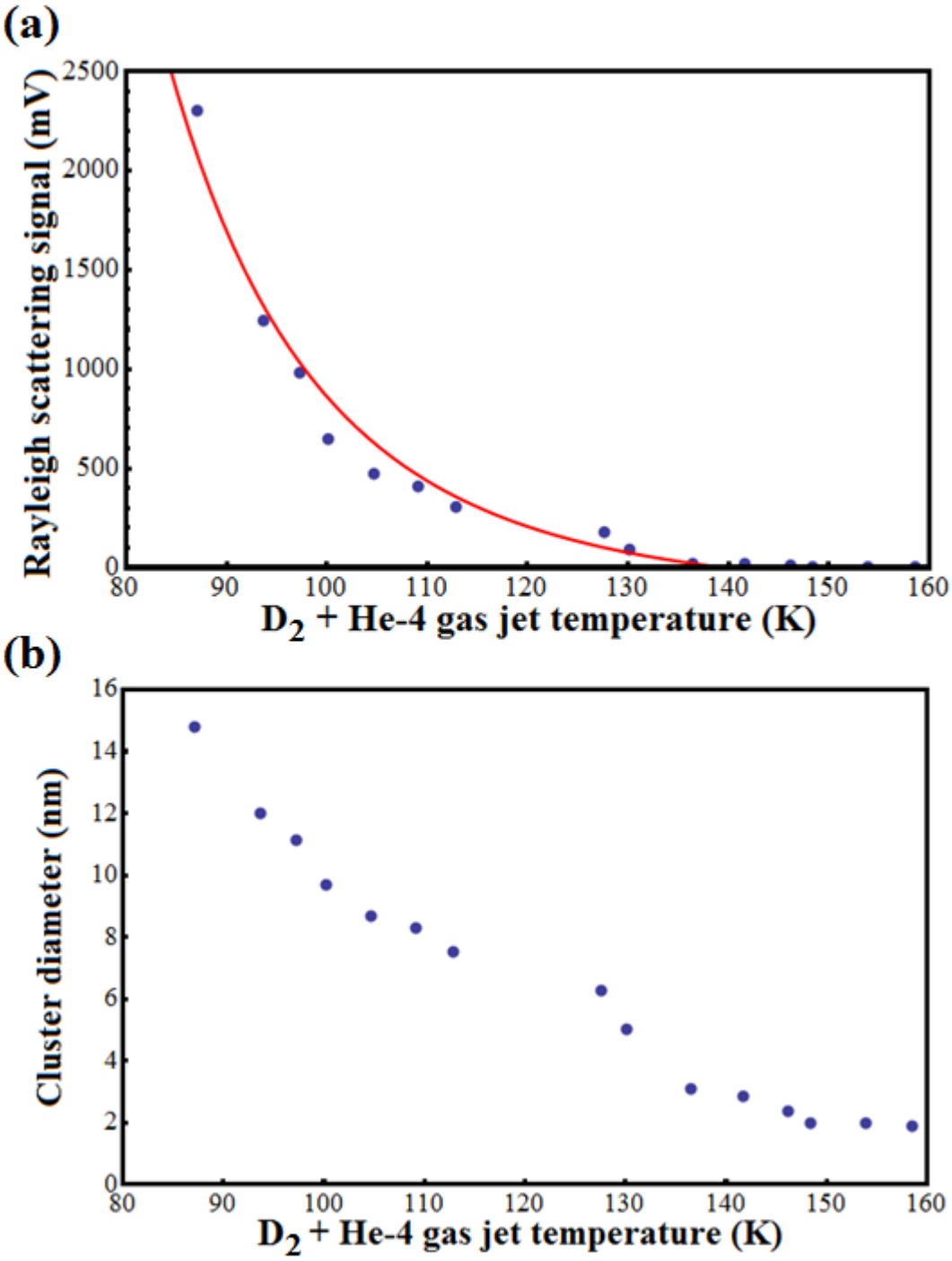

Figure 47. (a) Rayleigh scattering signal as a function of the mixture gas jet temperature, (b) diameter of the mixture cluster as a function of the gas jet temperature.

4.3.3. Pressure scan with D_2 target

In this section, the scattering signal measurements are shown as a function of the backing pressure of deuterium gas while keeping the temperature at 87 K. In Figure 48 (a), we see the signal increases as the pressure approaches 500 psi. This is what we expected based on previous experimental measurements.[70]

Above 500 psi, though, we observed the signal no longer increased with pressure. We found that this was related to the performance of the nozzle at higher pressures. The pulse valve suffered when the pressure got above 500 psi, and the total amount of gas released did not increase as much as it should have. Because of this issue, the results shown in the Figure 48 (b) do not represent the actual size of the deuterium clusters.

After the scattering measurements, we were able to improve nozzle performance by adjusting the duration of the driving pulse from the IOTA driver to the pulse valve. We also changed the drive pulse amplitude to make the valve behave more consistently. Aware of this problem, we tried to keep the valve at a fixed pressure of 770 psi and temperature of 87 K, where we observed biggest cluster size for deuterium.

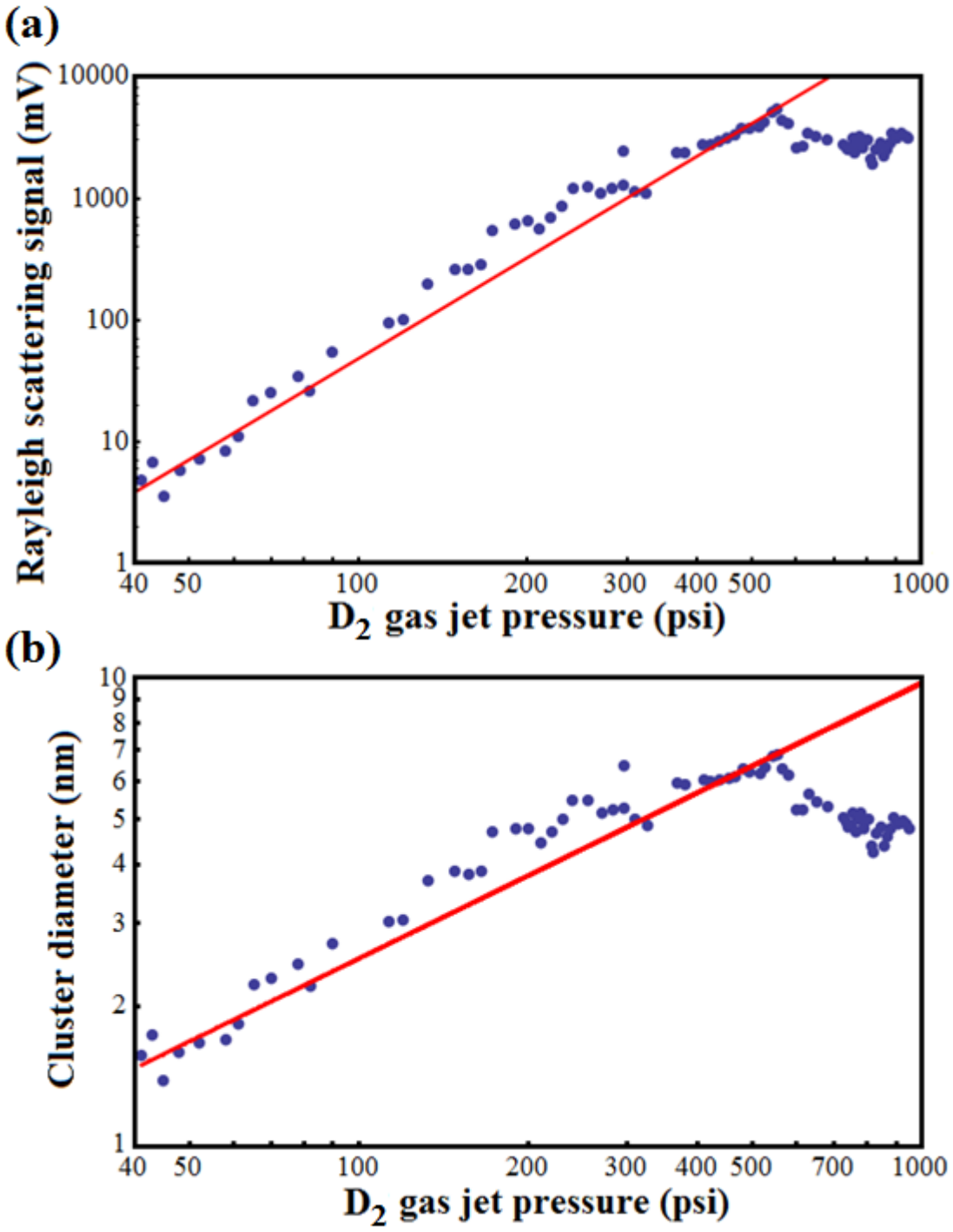

Figure 48. (a) Rayleigh scattering signal as a function of the deuterium gas jet backing pressure, (b) diameter of the deuterium cluster as a function of the gas jet backing pressure.

4.3.4. Pressure scan with D_2 + He-4 target

We also performed a similar pressure scan with deuterium gas + helium-4 mixture targets. The results in Figure 49 indicate that we had a similar performance issue with the pulse valve during these measurements. Also, we find that the measurements show a similar trend when compared with Figure 48. Again, this implies that the addition of helium-4 did not affect the cluster formation of deuterium molecules.

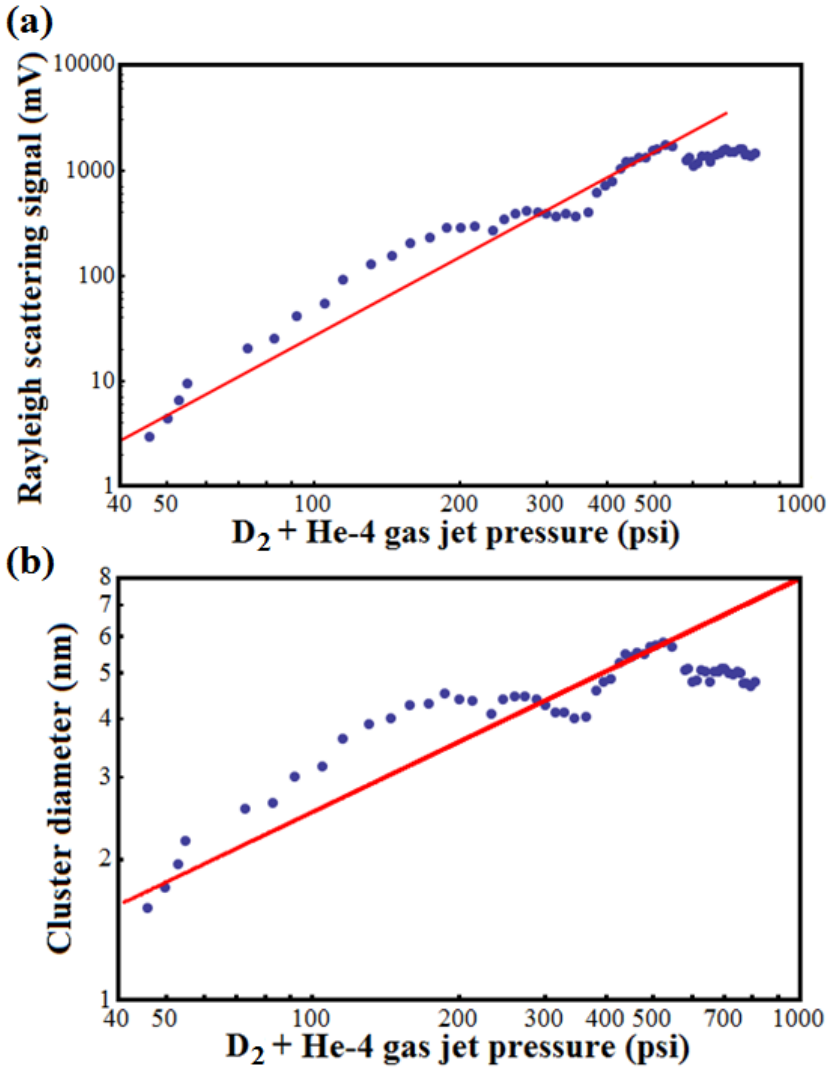

Figure 49. (a) Rayleigh scattering signal as a function of the mixture gas jet backing pressure, (b) diameter of the mixture cluster as a function of the gas jet backing pressure.

4.4. RGA MEASUREMENTS OF $D_2 + CD_4$ MIXTURE

4.4.1. RGA measurements 1

The RGA measures the partial pressure of each gas species when there are different gas molecules present in the vacuum chamber. Therefore, one can tell the composition of the gas mixture by analyzing the RGA data.

In our first RGA measurement, a test tube was initially filled with deuterium gas (D_2 = 220 psi), and deuterated methane (CD_4 = 90 psi) gas was added at t = 0 min from the top. The temperature of the gases was room temperature (20 ºC).

As shown in Figure 50 (a), the partial pressure of D_2 drops as a function of time, which is expected because the composition of the target should change from 100% deuterium to about 70% deuterium. In Figure 50 (b), the partial pressure of CD_4 gas increases with time. Obviously, the mixing process takes longer than one hour based on this RGA measurement.

In Figure 51 (a), the partial pressures of both gas species are shown in a log scale, which clearly shows the aforementioned trend. The partial pressures changed very quickly in the first thirty minutes, and somewhat quickly during the first hour. The ratio of the two partial pressures is shown as a function of time in Figure 51 (b) and (c). Figure 51 (b) shows the ratio from 0 min to 74 min, while Figure 51 (c) shows the ratio from 20 min to 74 min only.

After one hour, the pressure change slowed, and we decided to start another complementary RGA measurement. The second RGA measurement just consists of adding more CD_4 gas to the existing $D_2 + CD_4$ mixture. The CD_4 gas was added at t = 80 min.

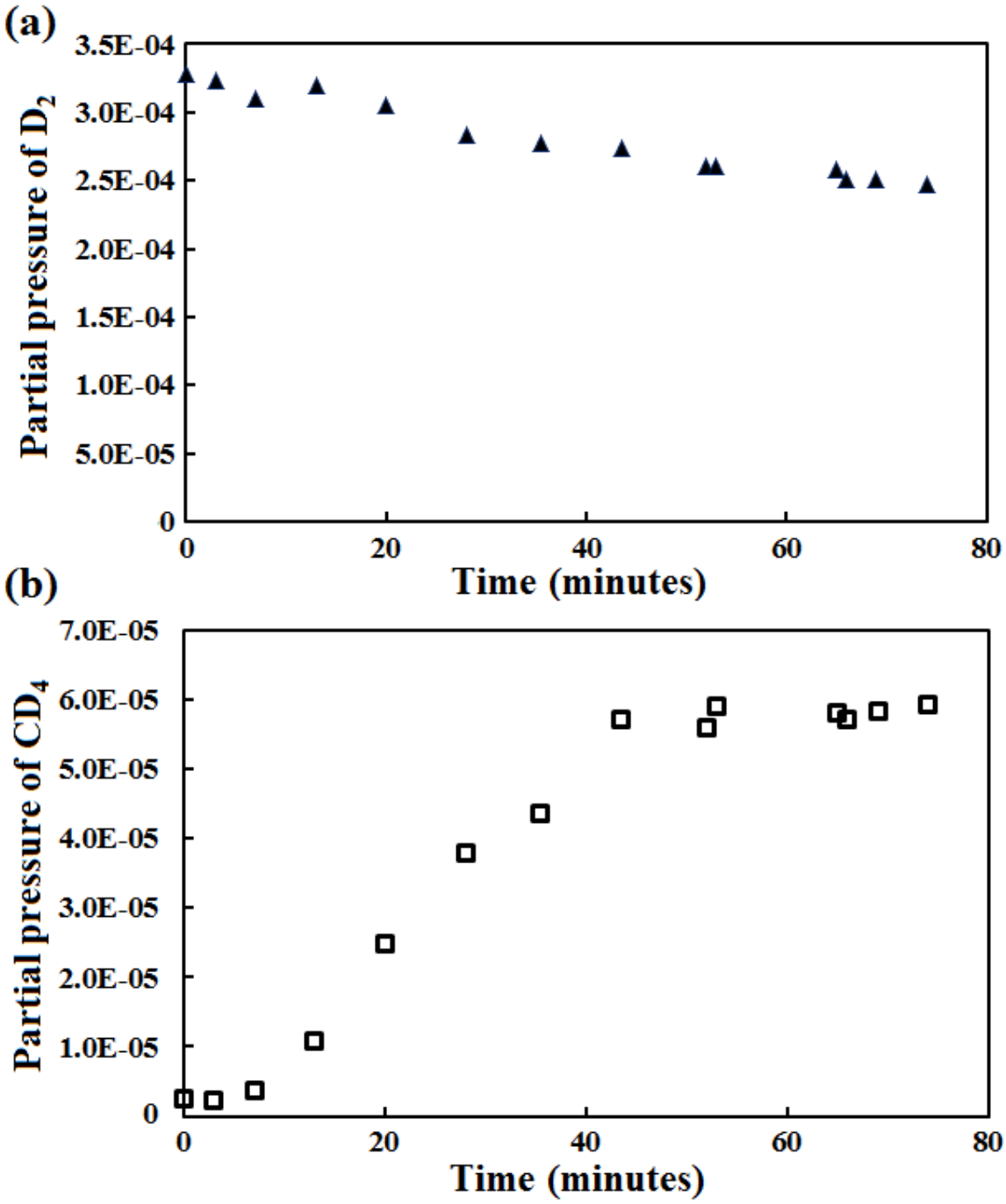

Figure 50. (a) The partial pressures of D_2 gas and (b) CD_4 gas are shown as functions of time.

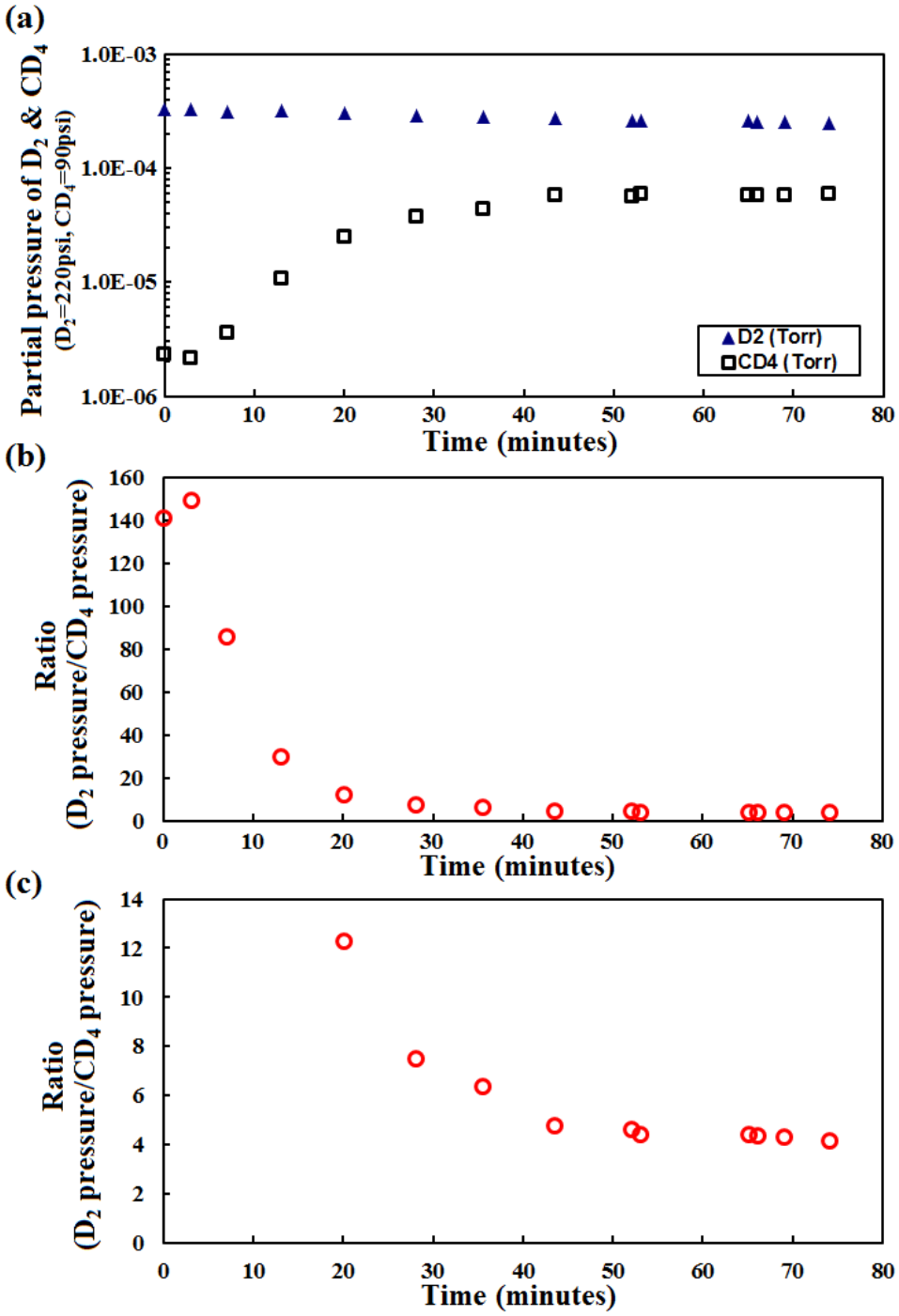

Figure 51. (a) The partial pressures of D_2 (solid triangle) and CD_4 (hollow square) gases are shown as functions of time in a log scale. (b) The ratio of D_2 pressure and CD_4 pressure is shown from 0 min to 74 min, and (c) a magnified image shows the ratio from 20 min to 74 min.

4.4.2. RGA measurements 2

Initially, the test tube was filled with 220 psi of D_2 gas, and we added 90 psi of CD_4 gas at time= 0 min. Then, additional CD_4 (= 130psi) gas was added to the tube at *t* = 80 min. In summary, the test tube was filled with 220 psi of D_2 gas and 220 psi of CD_4 gas after *t* = 80 min.

Therefore, we expected a 1 to 1 ratio when the mixing process was complete. Again, in Figure 52 (a), the partial pressure of D_2 gas decreases in time, and the pressure of CD_4 increases in time in Figure 52 (b). The change in the pressure seemed to be slowing, but it was difficult to determine when the mixing process was complete based on these figures.

Both Figure 52 (a) and (b) show abrupt changes in the partial pressure at *t* = 80 min, at which point the second RGA measurements started. It is interesting to see that the partial pressures change very quickly right after the addition of CD_4 then slows down in both cases.

Figure 53 (a) shows the partial pressures of D_2 and CD_4 in one graph in a log scale, and Figure 53 (b) shows the ratio of the two pressures as a function of time. The ratio clearly approaches 1.0 in Figure 53 (b), and the mixing process seems to be complete one hour after adding 130 psi of CD_4 gas. In both figures, the plots start from *t* = 80 min.

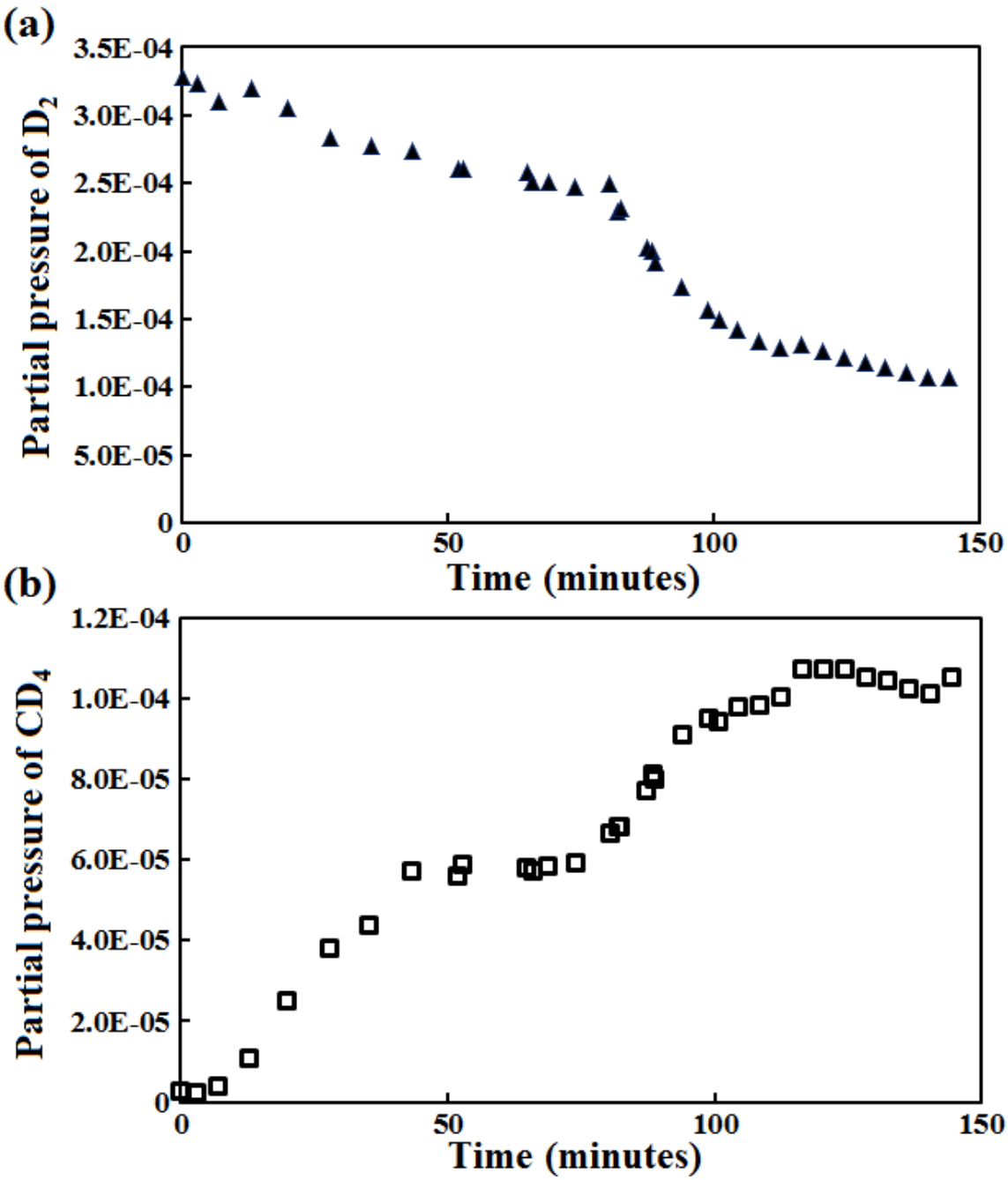

Figure 52. (a) The partial pressure of D_2 gas and (b) CD_4 gas are shown as functions of time. Additional CD_4 gas was supplied to the tube at t = 80 min.

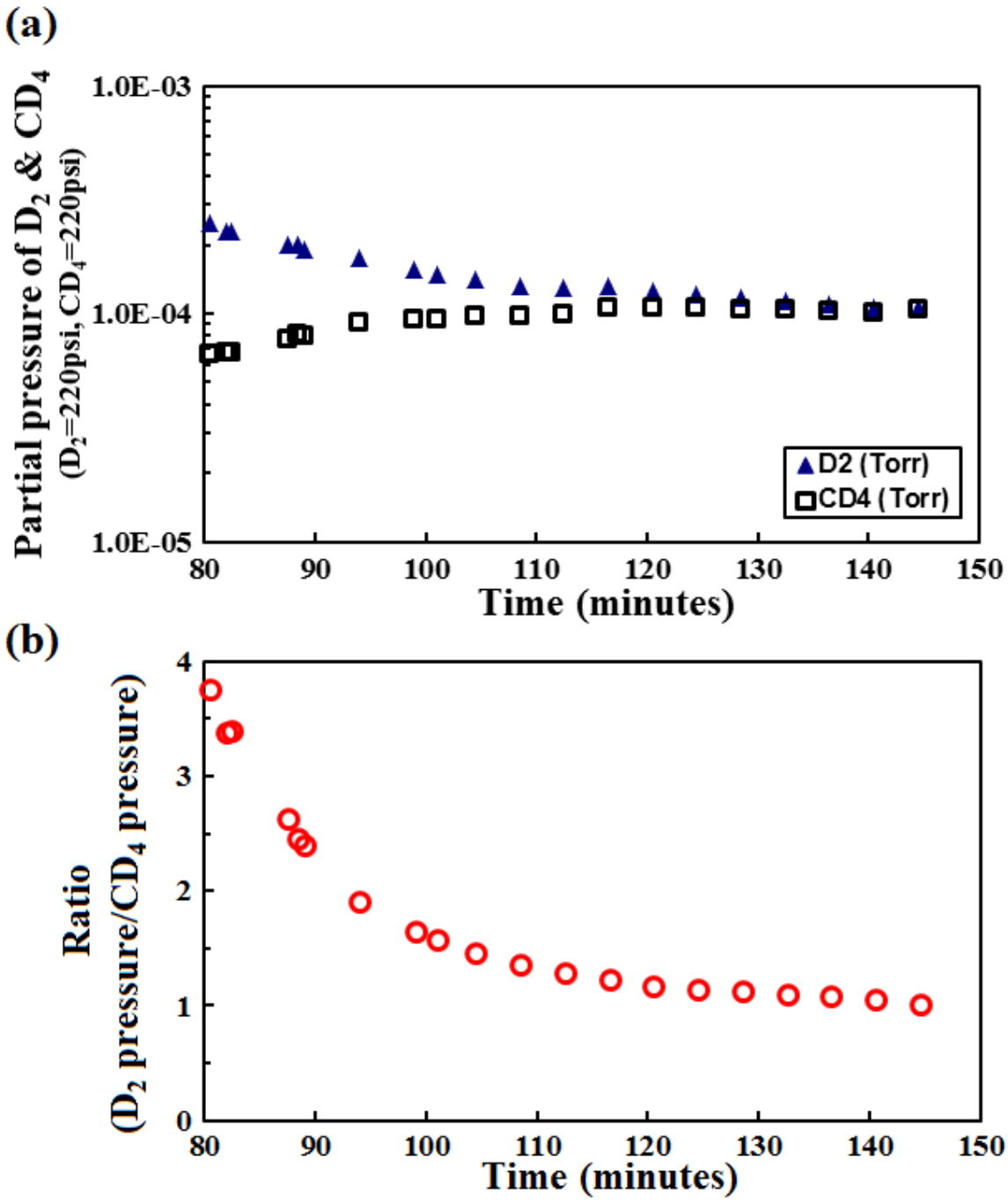

Figure 53. (a) Partial pressure of D_2 and CD_4 gas vs. time in a log scale, (b) the ratio of D_2 pressure and CD_4 pressure vs. time.

4.5. PREPARATION OF D_2 CLUSTER + ^{3}HE OR CD_4 + ^{3}HE MIXTURE TARGET

The measurements of target composition are very important in the mixture cluster fusion experiments because the ratio of fusion yields defined in equation (7.4) requires the knowledge of the atomic density of both deuterium and helium-3 in the gas jet.

Based on the RGA measurements using deuterium gas and deuterated methane gas at room temperature, we knew that the mixing process took at least one hour to stabilize. Therefore, during the mixture cluster fusion experiments, we kept the RGA on to measure the composition of the target on each system shot. We turned off the RGA just before the shot for safety purposes.

Analyzing the RGA data from many system shots during the mixture cluster fusion experiments, we found that the mixing process took much longer for the mixture target at 87 K than at room temperature. This gives us another reason to keep record of the target composition on each shot. Instead of waiting to have a certain mixture ratio, we measured the composition of the target before the shot, and fired a system shot immediately thereafter.

Figure 54 shows an RGA measurement taken before the system shot 2751. The plot shows the partial pressures of nitrogen, deuterium, helium-3, and water vapor. At 827 seconds, the gas jet was fired while the RGA was still on. From that test fire, we found that the small leak from the nozzle had similar target composition when compared with the target composition of the gas jet during the test shot.

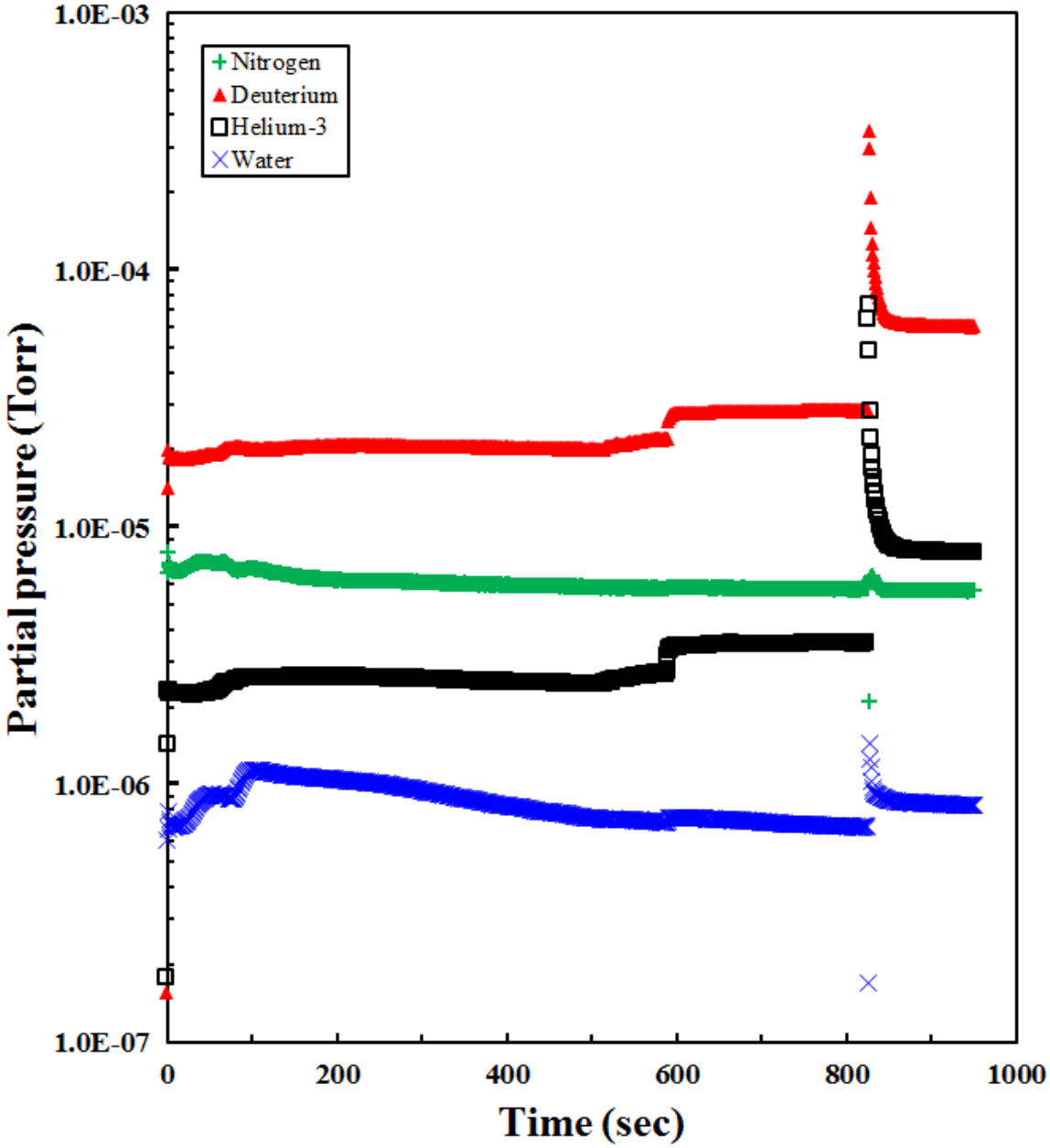

Figure 54. (a) Partial pressure of nitrogen, deuterium, helium-3, and water vapor as a function of time.

Chapter 5. Calibration of neutron detectors

In this chapter, I want to show our diagnostics for the neutron yield measurement. The figures and contents of this chapter are based on the recently published paper (W. Bang, H. J. Quevedo, G. Dyer, J. Rougk, I. Kim, M. McCormick, A. C. Bernstein, and T. Ditmire, "Calibration of the neutron detectors for the cluster fusion experiment on the Texas Petawatt Laser," Rev. Sci. Instrum. **83**, 063504 (2012).) about the calibration of our neutron detectors.[28] For the calibration of scintillation detectors, Dr. G. Dyer, J. Rougk, I. Kim, and M. McCormick helped me with collecting the oscilloscope data on THOR. Dr. H. J. Quevedo helped me with the LabView data acquisition program. I also thank Dr. A. C. Bernstein and Dr. T. Ditmire for useful discussions.

5.1. INTRODUCTION

Neutron detection is a very important diagnostic in the area of fusion science. Through the measurement of neutron yields and energy spectrum, one can calculate fusion power, plasma temperature, and areal density of the target.[76-78] Because of its importance in fusion research, many types of neutron detectors and techniques have been developed. Scintillation detectors are one example of the most commonly used neutron detectors in inertial confinement fusion (ICF) and tokamak[78] experiments. In addition, activation techniques, CR-39 track detectors, and gas proportional detectors are also widely used to measure the total neutron yield.[79-84] These detectors have their own working ranges and are affected differently by the experimental environment. For example, scintillation detectors are well suited for measuring low neutron yields, but suffer from saturation under high neutron flux. Also, strong electromagnetic pulse (EMP) noise or x-rays can severely affect the measurements. On the other hand, activation techniques and CR-39 detectors require that the total neutron yield or the

fluence be higher than a certain minimum detection range while not surpassing an upper limit. Therefore, researchers must choose the appropriate set of detectors for the particular conditions in their experiments.

A table-top short pulse laser system can generate nuclear fusion from explosions of laser-heated deuterium clusters.[16] In Ref. [16], they achieved 10^4 DD fusion neutrons per shot by focusing a 35 fs, 120 mJ laser pulse into cryo-cooled deuterium cluster targets. The electrons in the nanometer-scale deuterium clusters efficiently absorb the laser pulse energy and are removed from the clusters. This occurs in a very short time period, during which the ions are nearly stationary. The remaining cluster of highly charged ions undergoes a Coulomb explosion, causing the ions to obtain high kinetic energy.[17] The collision of two energetic deuterium ions from different clusters can result in a DD fusion reaction that generates a 2.45 MeV neutron. Since those initial experiments, there have been improvements in the energy that can be delivered by short pulse laser systems. Previous studies showed that the DD fusion neutron yield scales as the square of the laser pulse energy after optimization of all other parameters,[85,86] and up to 5.5×10^6 neutrons per shot has been achieved using cluster targets.[87] With the TPW that delivers near 200 J per pulse with 170 fs duration,[26] we can expect to achieve a maximum of 10^8 neutrons per shot in a nanosecond burst.

In this chapter, I will present the calibration results of 6 plastic scintillation detectors, the indium activation detectors, and CR-39 track detectors to be used in the TPW cluster fusion experiments. Two neutron sources were used to generate the expected range of neutron yield. A 15 TW laser system generated 10^4 DD fusion neutrons per shot for the calibration of the scintillation detectors, and a total of 2.4×10^8 neutrons were produced during the 10 hour irradiation time to calibrate the indium activation detectors. The activation technique was used to measure the activity of a Cf-

252 neutron source, and this source was used to produce a total of 10^{11} neutrons for the calibration of CR-39. The calibration method used for the scintillation detectors, which is described below, ensures that neutron yields between 10^5–10^8 n/shot can be measured under the high noise environment on the TPW, where a very strong EMP noise is expected from the laser-cluster interaction. In performing the calibration with indium, we successfully applied the activation technique for the measurement of very low yields of ~10^4 n/shot in deuterated methane cluster-fusion experiments. While calibrating the CR-39 detectors, we also found that averaging the neutron-proton cross section over the neutron spectrum of the Cf-252 source is an appropriate procedure for calibration.

5.2. EXPERIMENTAL SETUP

5.2.1. Neutron source

Two independent neutron sources were used to calibrate the scintillation detectors, indium activation detectors, and the CR-39 track detectors in the range of 10^5–10^9 neutrons per shot expected in the TPW experiments. A laser system generating DD fusion neutrons provided quasi-monoenergetic neutrons in sub-nanosecond bursts, which is ideal for the precise calibration of the detectors because it simulates the experimental environment that we would face on the TPW. However, the low neutron yield of 10^4 n/shot is not adequate to test the upper limit of the detectors. Though having a broad energy spectrum, a Cf-252 neutron source can easily produce 10^{11} total neutron yield. A Cf-252 source was used to generate neutron yields higher than 10^8 and up to 10^{11} for the calibration of the detectors.

DD fusion neutrons were generated on the THOR laser using deuterated methane (CD_4) cluster targets as performed in Ref. [88]. The THOR laser is a 10 Hz Ti:sapphire CPA system that delivers up to 600 mJ per pulse on target with a 35 fs pulse duration.

Figure 55 shows a schematic diagram of the cluster fusion source along with the three types of neutron detectors we calibrated. The CD_4 clusters were produced in a vacuum chamber using a supersonic nozzle with an input diameter of 790 μm, a half angle of 5 degrees, and a nozzle opening diameter of 5 mm. The backing pressure of the CD_4 gas before the nozzle was between 600 psi and 800 psi throughout the calibration process. We fired the gas jet into vacuum and focused the laser beam into the cluster jet at an intensity of ~10^{17} W/cm^2, producing multi-keV deuterium ions that can generate nuclear fusion reactions.[88] The laser-cluster interaction produced DD fusion neutrons at a repetition rate of 0.64 Hz, which was limited by the pumping speed of the turbo pump attached to the target chamber.

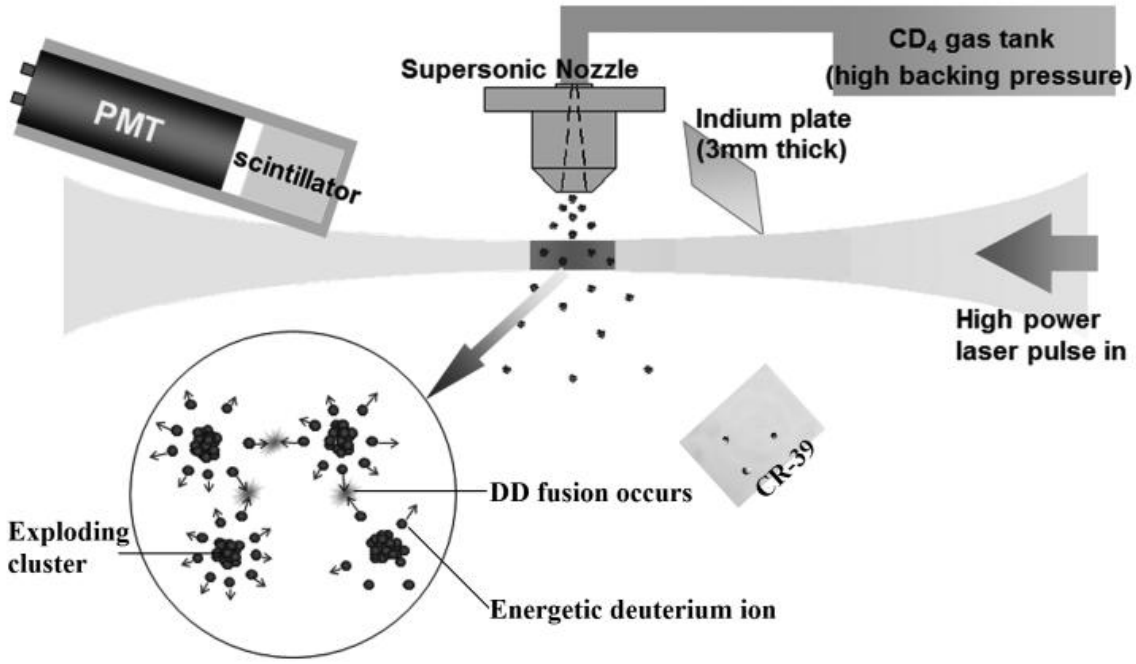

Figure 55. Nuclear fusion from ultrashort laser-cluster interaction on THOR with 3 types of neutron detectors for the DD fusion neutron yield measurement.

Up to 10^4 neutrons per shot were generated at the target chamber center (TCC) on THOR, which were emitted nearly isotropically.[88] The volume of the fusion plasma generated by the laser-cluster interaction was less than 1 mm^3, which lasted less than a nanosecond before the plasma disassembled. These localized bursts of neutrons were used in calibrating the plastic scintillation detectors and activating the 3.2 mm thick indium plate placed inside the experimental chamber.

The kinetic energy of the neutrons from the CD_4 cluster fusion is around 2.45 MeV, which correctly simulates the DD neutrons from the deuterium cluster fusion experiment on the TPW. The nanometer-scale CD_4 clusters interact with the incoming laser pulse whose peak intensity is about 10^{17} W/cm^2, producing energetic deuterium ions with an ion temperature of several keV.[88]

Cf-252 is a strong neutron emitter whose average neutron energy is about 2.1 MeV. This source was provided by the Nuclear Engineering Teaching Laboratory (NETL) at the University of Texas at Austin, where all subsequent measurements involving the use of Cf-252 were performed. Using the known activation cross section of Indium-115 for Cf-252,[89] we measured the activity of the source prior to the calibration.

The activity of this source was 8×10^7 Bq, and 9.3×10^6 neutrons per second were emitted isotropically. Though the neutrons emitted from Cf-252 have a broad energy spectrum ranging from below 0.003 MeV up to about 15 MeV, the CR-39 detectors can be calibrated using the known spectrum[90] of Cf-252 and the neutron-proton cross sections.[91]

5.2.2. Scintillation detectors

We built 6 plastic scintillation detectors using two types of scintillators to expand the detection range of the neutron yield. These detectors provide real time measurements that can be performed outside of the vacuum chamber without the need of venting and pumping the target chamber between each system shot. Moreover, the specific time of flight (TOF) of quasi-monoenergetic 2.45 MeV neutrons allows for the identification of scattered neutrons in the signal.

Four of the detectors used 4.0 cm diameter, 2.0 cm long EJ-232Q (a BC-422Q equivalent version from ELJEN Technology) scintillators with 1% quenching, which had very fast rise and decay times of 100 ps and 700 ps, respectively. The fast rise and decay time of these scintillators are adequate for the precise TOF measurements of the DD fusion neutrons produced in the cluster fusion experiment.[25] The remaining 2 detectors used 4.6 cm diameter, 4.9 cm long EJ-200 (a BC408 equivalent version from ELJEN Technology) scintillators for a higher detection sensitivity along with sufficiently fast rise and decay times of 0.9 ns and 2.1 ns, respectively.

One of the two EJ-200 detectors is shown in Figure 56 with its mu-metal shield and aluminum housing. Each scintillation crystal was coupled to a Photonis XP2020 photomultiplier tube (PMT). Three detectors were connected to a 500 MHz, 5 GSa/s, 4 ch Tektronix TDS5054 oscilloscope, and the other three detectors were connected to a 1 GHz, 5 GSa/s, 4 ch Tektronix TDS 684A oscilloscope. The remaining channel of each oscilloscope received a photodiode trigger signal from the laser that indicated the arrival time of the laser pulse at the cluster targets.

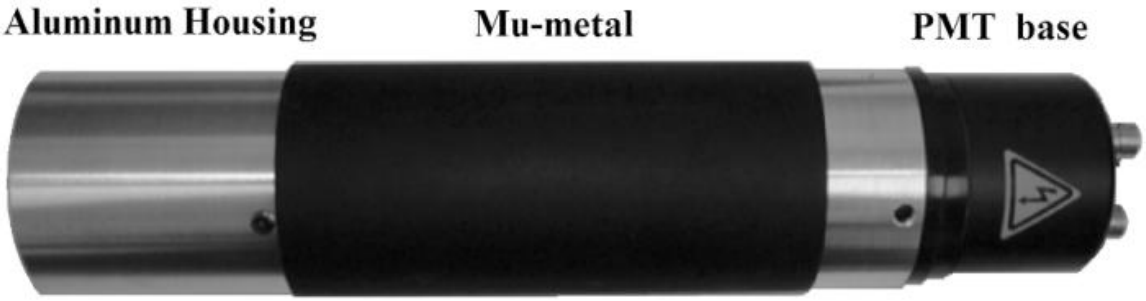

Figure 56. EJ-200 detector consists of a Photonis XP2020 PMT, an EJ-200 plastic scintillator (4.6 cm dia. × 4.9 cm long), a magnetic shield, and an aluminum housing.

Only the neutron signals that appeared at the expected TOF of around 90 ns from the arrival of the pulse were considered as DD fusion neutrons. Occasionally, the oscilloscopes showed x-ray peaks, whose locations were consistent with the photodiode trigger signal. A pre-calibrated reference plastic scintillation detector[92] monitored the neutron yield during the calibration process. We calibrated the scintillation detectors so that they could operate in current mode[93] on the TPW.

The scintillation detectors were installed ~2 m away from the TCC outside of the vacuum chamber, and operated in pulse counting mode. The neutron yield was intentionally lowered by decreasing either the laser pulse energy or the backing pressure of CD_4, and at most one neutron was detected out of 10 laser shots by each scintillation detector. This procedure ensured that a two-neutron event was less than 5% of the total neutron events recorded by each detector.

We defined a single neutron event area as the area underneath the signal peak on the oscilloscope that corresponds to the detection of one neutron in units of V×ns. This area is proportional to the total electron charge amplified by the PMT due to a single neutron hitting the scintillator. For a fixed gain at the PMT, the total amplified charge is a linearly increasing function of the light output at the scintillator, which is statistically

proportional to the detected number of neutrons. Therefore, multiple neutron events will show a larger peak area (current mode operation). The detected number of neutrons is calculated by dividing this area in the current mode operation by the single neutron event area defined previously. When the detectors are used in current mode at a location 2–10 m away from TCC, the detection range is 10^5–10^8 n/shot in the TPW experiments.

5.2.3. Indium activation

Neutron activation[80,81] is often used for the measurement of neutron yields above 10^8. For the detection of the 2.45 MeV neutrons on the TPW, indium activation serves our purposes very well. The activation cross section of indium is relatively large for DD fusion neutrons, so it is more sensitive to 2.45 MeV neutrons. Since the reaction ^{115}In(n,n')^{115m}In requires a threshold energy of 0.339 MeV for activation, it is less sensitive to low energy scattered neutrons. More importantly, it is not affected by the EMP noise or x-rays.

Indium-115m decays with a half-life of 4.5 hours emitting 336 keV gamma rays. A half-life on the order of a few hours is advantageous in the TPW cluster fusion experiment because the indium targets are going to be inside the vacuum target chamber. After each laser shot, the indium targets irradiated by DD fusion neutrons are removed from the chamber and placed on a high purity germanium (HPGe) detector for the 336 keV gamma ray counting.

The relatively long half-life of 4.5 hours also opens the possibility of using the indium activation for a low neutron yield measurement by integrating many shots. Indium activation technique is typically used to measure neutron yields above 10^8–10^{10} neutrons,[80,81] but we demonstrated that it can also be used for neutron yield

measurements as low as 10^4 neutrons per shot. For this application, we used a 99.99% pure indium target with a diameter of 7.6 cm and thickness of 3.2 mm. While the scintillation detectors were set up outside of the target chamber, the indium target was installed close (~5 cm) to the nozzle inside the vacuum chamber to increase the neutron fluence. A 25 μm thick aluminum filter prevented any charged particles from hitting the indium target, which was irradiated by the DD fusion neutrons generated on THOR.

The half-life of 4.5 hours, however, also implies that comparable amount of time is required for the measurement of gamma rays. This is an obvious disadvantage over the scintillation detectors, with which real time measurements are possible. For gamma counting, an Ortec HPGe detector with a relative detection efficiency of 30% and Genie 2000 software were used for the measurement and acquisition, respectively. Standard efficiency curves were used to find the detector efficiency at 336 keV. Prior to the calibration of the thick indium plate, 38.1 mm × 25.4 mm × 0.3 mm indium foils were used to measure the source activity of Cf-252.

5.2.4. CR-39 track detectors

CR-39 track detectors can measure neutron yields higher than the practical detection limit (~10^8 n/shot) of the scintillation detectors on TPW. They are not affected by EMP or x-rays, and the neutron yield can be measured by counting the neutron tracks on the surface of the detectors after etching them. The characteristics of CR-39 track detector for DD neutrons are well known,[83,94,95] making it unnecessary to calibrate them with the cluster fusion source.

For the calibration at higher neutron yields using the Cf-252 source, we used 25 mm × 25 mm × 1.1 mm TASTRAK CR-39 track detectors. After exposure to a Cf-252 source for 3 hours, they were etched in 6N NaOH solution at 80 °C ± 2 °C for 6 hours.[83]

After the chemical wet etching of the CR-39 detectors, we took the front and back surface images using a Zeiss model AxioCam MRc 5 optical microscope. Each CR-39 detector had a unique number engraved at the corner of the front surface for identification. Several CR-39 plates were placed at various distances from the Cf-252 source to simulate different neutron fluence on the detector.

Due to the intrinsic noise density of several hundred tracks per cm^2, CR-39 requires the measured track density to be much higher than this value.[95] When the measured track density is comparable to the noise density, a technique called coincidence counting[96] can be used to distinguish the neutron tracks from the background noise tracks for low neutron yield measurements.

5.3. RESULTS AND DISCUSSION

5.3.1. Calibration of scintillation detectors using cluster fusion neutron source

Nearly monoenergetic 2.45 MeV DD fusion neutrons produced from the laser-heated deuterated methane clusters on THOR served as a sub-nanosecond compact neutron source for the calibration of the scintillation detectors. The main objective was to determine a single neutron event area of each detector at several different high voltage (HV) biases applied to its PMT base, and the benefit of this particular calibration method is discussed below.

The calibration result of one of the two EJ-200 detectors is shown in Figure 57 (a) along with a power law fit to the data. Each point in the graph represents the average of a single neutron event area at each HV bias out of several thousand laser shots. The statistical averaging process is very important because the amount of energy transferred from the detected neutron to the scintillator is different every time.

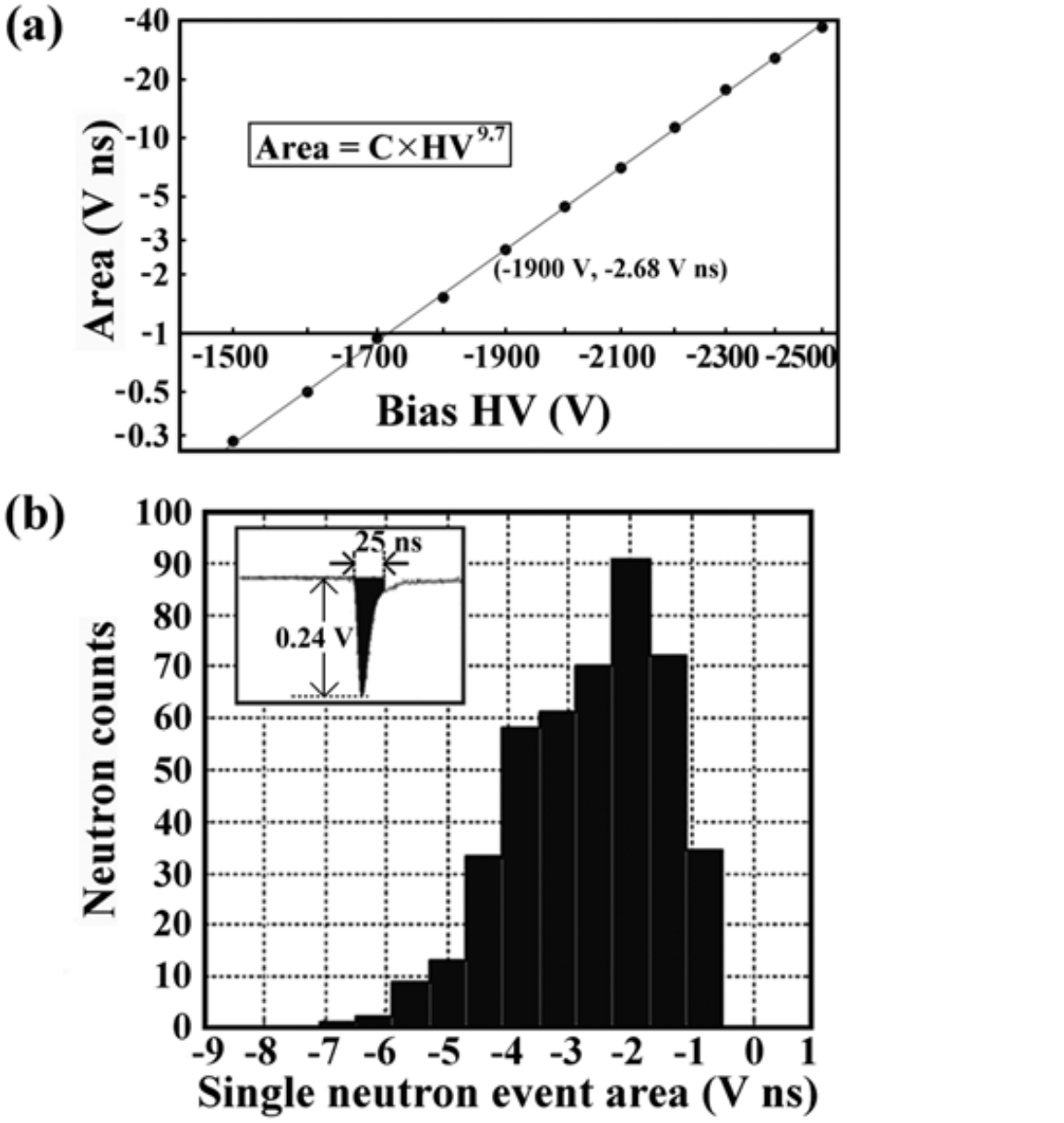

Figure 57. (a) Calibration of one of the two EJ-200 neutron detectors on THOR with a power law fit. The average single neutron event area is plotted versus high voltage (HV) bias of the PMT, showing a scaling of $C \times HV^{9.7}$ with a constant coefficient, C. (b) The distribution of a single neutron event area for a HV bias of -1900V applied to the EJ-200 detector. 444 neutron events are shown in the histogram out of 6125 laser shots fired on THOR. The oscilloscope trace of the average neutron signal is shown in the inset of the histogram.

As an example, Figure 57 (b) shows the distribution of a single neutron event area for the HV bias of -1900V, which corresponds to the data point (-1900 V, -2.68 Vns) in Figure 57 (a). The histogram shows a maximum at -2 Vns, but the average value is -2.68 Vns at this HV bias. The inset in Figure 57 (b) shows the average oscilloscope trace of a single neutron event at this specific HV bias with the grayed area representing how we defined the area. We set a time window of 25 ns, and measured the area of the neutron signal within this interval. In most cases, the neutron signal became less than 10% of its peak height at the end of the time window.

The single neutron event area was proportional to $(HV)^{9.7}$, which is consistent with a 12 stage PMT design. Each individual Photonis XP2020 came with a manufacturer's calibration slip showing the required high voltage bias for the same gain of 3×10^7. Therefore, all six PMTs had quite different gains at the same HV bias. Also, the experimental value of the exponent in the power law fit was observed to be a characteristic of each detector, and the other 5 scintillation detectors showed a single neutron event area proportional to $(HV)^{9.4}$–$(HV)^{11.2}$. The calibration results of the other 5 detectors are summarized in Appendix D.

This calibration method is particularly useful if we want to extend the detection range of the scintillation detectors without saturating the PMT when a large background noise is expected. A HV bias of -2100 V or higher is appropriate for a neutron yield lower than 10^6 n/shot on TPW. This has an advantage in the detection of DD fusion neutrons in the harsh environment that we expect to encounter on the TPW because the EMP noise can be up to 1 V in the vicinity of the target chamber. When the detectors are located at 2 m from TCC, the 2.45 MeV neutrons arrive 85 ns after the x-rays and we estimate the EMP noise can still be up to several hundred mV on the oscilloscope. By having a larger gain on the PMT, we expect a distinguishable neutron peak for neutron

yields as low as 10^5 n/shot with a signal to noise ratio greater than one even with 800 mV EMP noise level.

For neutron yields ranging from 10^6 to 10^7 n/shot, the HV bias can be reduced such that the PMT does not become saturated while keeping the neutron signal on the oscilloscope above the EMP noise level. With the detectors set up at 10 m from TCC and HV bias less than -1700 V, the scintillation detectors can measure a total neutron yield as high as 10^8 n/shot. Therefore, the scintillation detectors can measure neutron yields ranging from 10^5 n/shot to 10^8 n/shot in the TPW cluster fusion experiments.

5.3.2. Application of indium activation for the low neutron yield measurement of the cluster fusion neutron source

At 5 cm away from the source, the neutron fluence with a total yield of 10^4 n/shot is only 32 n/cm^2/shot, which has too low of a probability of activating the indium disk target with one laser shot. However, the activation detector can still measure the average neutron yield per shot by accumulating many shots over several times the half-life.

For each gas jet fire, the number of neutrons that arrive within the surface area of the target is $Y_0 \frac{\Omega}{4\pi}$, where Y_0 is the neutron yield per shot at the source and Ω is the solid angle of the indium disk from the source. These neutrons activate the In-115 atoms with an activation cross section σ. Then, the number of activated In-115m atoms per shot becomes $N_{act}=(Y_0 \frac{\Omega}{4\pi}) \frac{N\sigma}{A}$, where A is the surface area of the target and N is the number of In-115 atoms in the target.

Therefore, the rate equation for the number of In-115m atoms at time t, $N_{act}(t)$, can be expressed as

$$\frac{dN_{act}(t)}{dt} = (fY_0)\frac{\Omega}{4\pi}\frac{N\sigma}{A} - \lambda N_{act}(t) \quad \text{(for } 0 \le t \le T_0\text{)}, \tag{5.1}$$

where f is the frequency of the nozzle fire, λ=4.292×10^{-5} s^{-1} is the time constant of In-115m, and T_0 is the total exposure time. After the irradiation, the indium target is immediately removed from the source until T_1, at which point 336 keV gamma rays are measured until T_2. Then, the number of disintegrations of In-115m atoms, ΔN, during the time interval T_2-T_1 becomes

$$\Delta N = N_{act}(T_1) - N_{act}(T_2) = fY_0 \frac{\Omega}{4\pi}\frac{N\sigma}{A\lambda}(1 - e^{-\lambda T_0})[e^{-\lambda(T_1 - T_0)} - e^{-\lambda(T_2 - T_0)}]. \quad (5.2)$$

Therefore, the number of 336 keV gamma rays registered at the HPGe detector is

$$N_\gamma = \varepsilon p\, \Delta N = \varepsilon p f Y_0 \frac{\Omega}{4\pi}\frac{N\sigma}{A\lambda}\left(1 - e^{-\lambda T_0}\right)e^{-\lambda(T_1 - T_0)}[1 - e^{-\lambda(T_2 - T_1)}], \quad (5.3)$$

and the total neutron yield during time T_0 becomes

$$Y = (f\, Y_0) \times T_0 = \frac{4\pi A N_\gamma \lambda T_0}{\varepsilon p N \sigma \Omega} \frac{e^{\lambda(T_1 - T_0)}}{\left(1 - e^{-\lambda T_0}\right)[1 - e^{-\lambda(T_2 - T_1)}]}, \quad (5.4)$$

where, ε=0.039 is the detection efficiency of the HPGe detector for the cylindrical plate with 7.6 cm diameter, p=0.458 is the probability of emitting a 336 keV photon per disintegration of In-115m, and σ=326 mb is the neutron activation cross section of In-115 for 2.45 MeV neutrons.[91]

Using the cluster fusion source, we integrated 23,000 shots during 10 hours at 0.64 Hz, and obtained the gamma ray spectrum shown in Figure 58. The area under the peak at 336 keV contains 362 (±22) counts, from which the calculated total neutron yield was 2.4 (±0.15) ×10^8 neutrons during the 10 hour period. This result agrees within 6% error with the independently measured average neutron yield of 1.0×10^4 n/shot using the scintillation detectors.

Two scintillation detectors operated in pulse counting mode for this measurement, and counted neutron events during the irradiation process. Applying the detection efficiency and solid angle of each detector, the neutron yields from EJ-200 and EJ-232Q detectors were 9.05×10^3 n/shot and 1.13×10^4 n/shot, respectively.

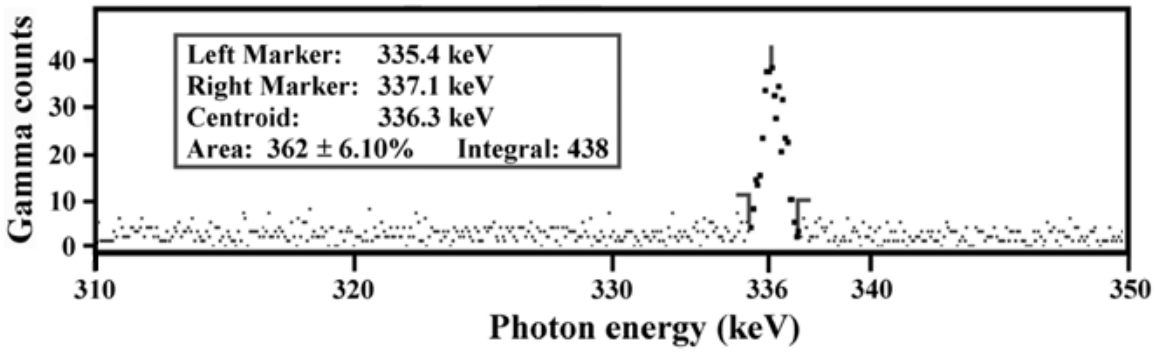

Figure 58. Gamma ray spectrum of indium plate after 10 hours of irradiation on THOR (Total neutron yield ~2.4×10^8 n).

In equation (5.4), we did not account for the self-absorption of gammas, which is not significant for the 3.2 mm thick disk target and 0.3 mm thick foil target that we used. The absorption cross section of indium for 336 keV photons was neglected for the purpose of this calibration. Also, the mean free path of 2.45 MeV neutrons inside the indium target is significantly longer than the thickness of 3.2 mm.

Using 3.2 mm thick disk target and accumulating 23,000 shots, we demonstrated that the indium activation technique can be used for the average neutron yield measurement as low as 10^4 n/shot. The successful measurement of low neutron yield in the cluster fusion experiment on THOR ensures that this technique can be properly used for the fusion yield measurement on TPW for neutron yields higher than 10^7 n/shot.

5.3.3. Calibration of CR-39 and indium activation using Cf-252 neutron source

A Cf-252 neutron source was used to cross calibrate CR-39 detectors and the indium activation detectors. Several indium foils set up at various distances from the source measured the activity of the Cf-252 using the indium activation technique. Based on previous studies, the total neutron yield at the source is given by the following formula,[79-81]

$$Y = \frac{N_\gamma}{\varepsilon p N \langle\sigma\varphi\rangle} \frac{exp(\lambda \Delta t_1)}{1 - exp(-\lambda \Delta t_2)}, \quad (5.5)$$

where N_γ is the number of gamma counts measured by the HPGe detector during the time interval Δt_2, ε=0.058 is the measured HPGe detection efficiency for a rectangular foil geometry using 344 keV gamma rays from a calibrated Eu-152 source, N=1.057×10^{22} is the total number of In-115 nuclei in the 2.106 g indium foil, and Δt_1 is the time interval between the end of neutron irradiation and the start of gamma count. $\langle\sigma\varphi\rangle$ is the activation coefficient, where the fluence, φ, is $1/4\pi R^2$ for a point source with R being the distance from the source to the indium atom and the Cf-252 spectrum-averaged neutron activation cross section of In-115 is σ=199.4 mb.[89]

The measured gamma ray spectrum from an indium foil that was placed 10.4 cm from the Cf-252 source is shown in Figure 59, which shows 354 (±21) counts of 336 keV gamma rays. In this measurement, Δt_1 was 134 minutes and Δt_2 was 60 minutes while the foil was irradiated for 180 minutes. A background noise of 73 counts was subtracted from the total event count of 427 for the photon energy ranging from 334.1 keV to 339.2 keV. A magnified spectrum image shows the peak at 336 keV. The measured value of 354 (±21) photons corresponds to 1.08 (±0.07) ×10^{11} neutrons emitted from the source, which is consistent with the measured source activity of 9.3×10^6 n/shot or 8×10^7 Bq.

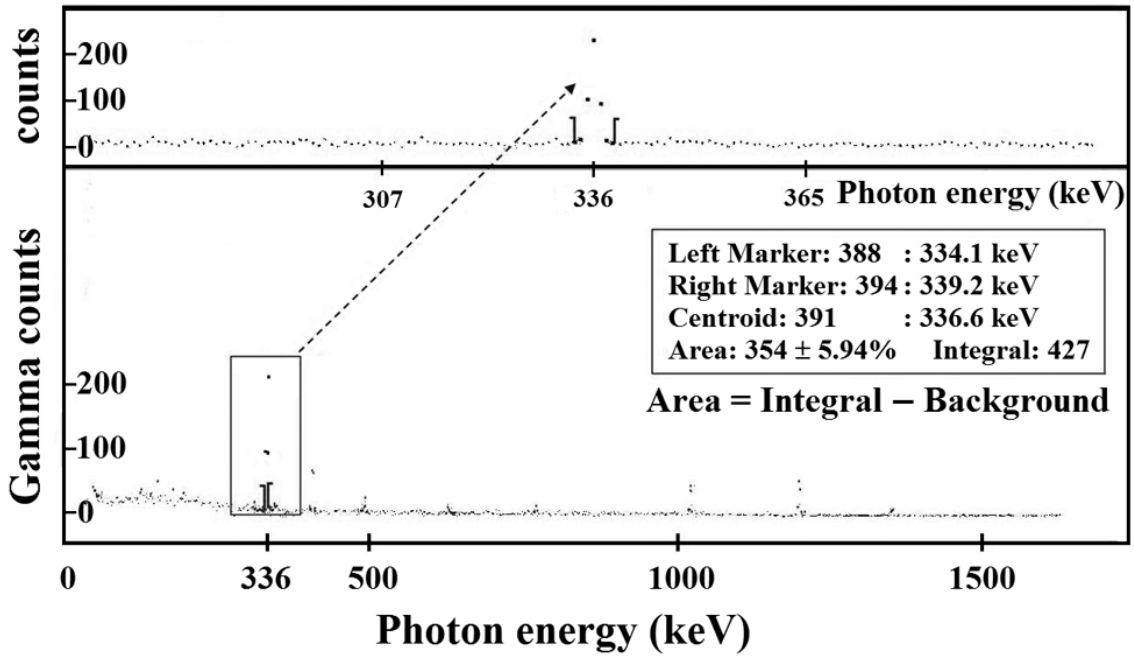

Figure 59. Measured gamma ray spectrum of an indium foil after 1 hour counting. The foil was exposed to a total of $Y=1.1\times10^{11}$ neutrons, and was placed at 10.4 cm from Cf-252 source.

Figure 60 (a) and (b) show sample images of the CR-39 detectors located at 5.2 cm and 12.2 cm from the source, respectively. The back surface images in the figures contain 28 and 3 neutron tracks, respectively, with dashed circles indicating the location of those tracks. On average, the CR-39 located at 5.2 cm from the source showed 29.8 tracks per image, while the one located at 12.2 cm from the source showed 5.5 tracks per image.

To calculate the neutron yield from the measured number of tracks on the back surface, a calculated detection efficiency of 4.6×10^{-4} was used. Since the detection efficiency of CR-39 for 2.45 MeV neutrons is known to be 3.3×10^{-4} on the back surface of CR-39,[83] we calculated the Cf-252 spectrum-averaged neutron-proton elastic cross section (=3.6 b) and divided it by the cross section (=2.5 b) for DD fusion neutrons.[90,91]

Then, we multiplied this ratio by the known detection efficiency, which resulted in the efficiency of 4.6×10^{-4} on the back surface for the Cf-252 neutron source. Based on the measured number of neutron tracks, the neutron yields were 0.97×10^{11} and 1.01×10^{11} for the detectors at 5.2 cm and 12.2 cm, respectively.

These values agree with the yield measurements from the indium activation detectors irradiated by the same Cf-252 neutron source for the same time duration. Therefore, the method that we used to calculate the detection efficiency of CR-39 for the Cf-252 source is an appropriate procedure to calibrate the CR-39 detectors. Both indium and CR-39 detectors would be suitable for the measurement of neutron yields as high as 10^{11} n/shot.

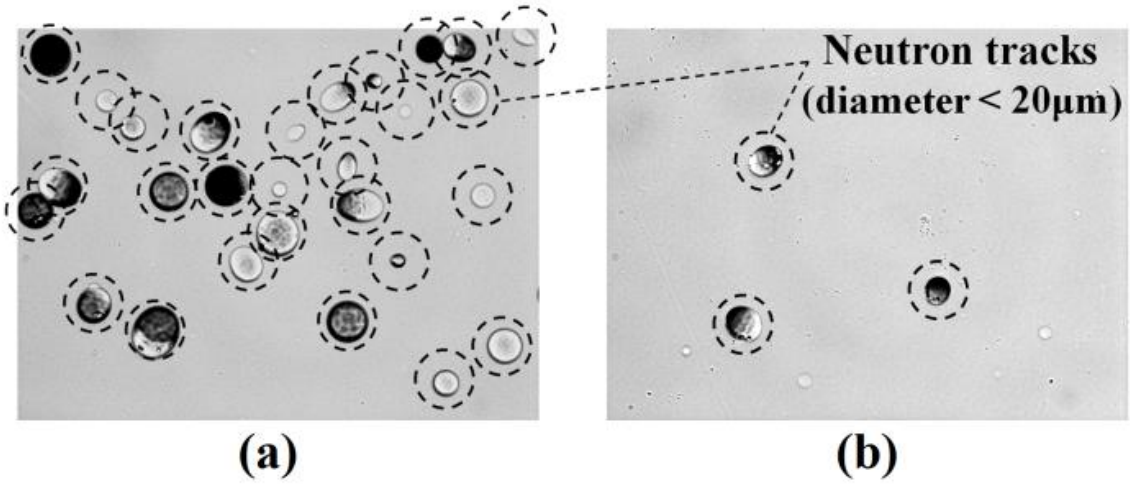

Figure 60. Optical microscope images of CR-39 track detectors after 6 hours of chemical etching. The CR-39 plates at various distances were exposed to a Cf-252 source, which emitted a total of 1.1×10^{11} neutrons during the calibration period. The distance from the Cf-252 source to the plate was (a) 5.2 cm, and (b) 12.2 cm.

5.4. CONCLUSION

We have calibrated three types of neutron detectors for use in the deuterium cluster fusion experiment on the TPW. DD fusion neutrons from a cluster fusion

experiment on the 15 TW THOR laser and Cf-252 were used as neutron sources. For the calibration, the neutron detectors were exposed to the expected total number of neutrons from the cluster fusion experiment on the TPW.

The plastic scintillation detectors operated in a pulse counting mode during calibration, and single neutron event areas were measured at various HV biases. This method allows us to expand the dynamic range of the scintillation detectors under high EMP noise environment, and they would work in current mode to detect 10^5–10^8 n/shot.

We demonstrated that the indium activation technique, frequently used in high neutron yield measurements, could also be used for low neutron yields of 10^4 n/shot in cluster fusion experiments on small scale table-top laser systems. The calibration result from a 7.6 cm diameter, 3.2 mm thick indium target agreed with the yield measurements from scintillation detectors within the measurement error of 6% during gamma counts. This indicates that the indium activation detectors can measure the fusion neutron yield when the yield on the TPW is over 10^7 n/shot.

We also used the indium activation technique to calibrate the Cf-252 source with several indium foils. This allowed cross calibration of CR-39 detectors, which showed clear neutron tracks when irradiated by the same source with $Y=1.1\times10^{11}$ neutrons. When a neutron detection efficiency of 4.6×10^{-4} was used, the total neutron yield measured from CR-39 detectors agreed with the yield measurement from indium activation.

Chapter 6. TPW cluster fusion experiment

The dependence of the hot (multi-keV) ion temperature from Coulomb explosion of deuterium clusters on the incident laser intensity has been investigated at the TPW facility.[31] After optimization, deuterium plasmas with up to 10 keV ion temperature were observed. The substantial increase in the volume (1–10 mm^3) of the deuterium plasma at the TPW enabled the production of 1.6×10^7 neutrons in a single shot with a 120 J, 170 fs laser pulse. The possible effects of the pre-pulses were examined by implementing a pair of plasma mirrors. Ion energy measurements with and without plasma mirrors both show a drop in the deuterium ion temperature for laser intensities above an optimum intensity. Qualitative agreement of this feature with a computer simulation is presented for the case without plasma mirrors.

6.1. INTRODUCTION

Nuclear fusion from laser-heated deuterium clusters has been studied since 1999.[16] Liquid-density, nanometer scale deuterium clusters are commonly used as targets, which form when cold deuterium gas is forced under high pressure through a supersonic nozzle.[70] In these experiments, deuterium ions were observed with energies up to a few keV, which is energetic enough for collision of those ions to result in DD fusion and produce a burst of 2.45 MeV neutrons.

Neutron fluxes greater than 10^9 n/cm^2/shot would enable sub-ns time-resolved pump-probe experiments of neutron damage studies.[25] The petawatt lasers currently operating and being built with pulse durations below 200 fs have the potential to drive such sources. Therefore, the laser-cluster generated fusion plasma is attractive as a bright, short, and localized neutron source which is potentially useful for neutron radiography or material damage studies.

Since the initial experiments, there has been much research on the details of the laser-cluster interactions.[48,97] The process by which the ions attain their energies has been well explained by the Coulomb explosion model.[17,97] In this model, the electrons in the atomic cluster first absorb the laser pulse energy and the atoms are ionized, which is often referred to as the inner-ionization. The electrons further gain energy through other absorption mechanisms such as above-threshold ionization[5], inverse bremsstrahlung heating[98], resonant heating[43], and stochastic heating[44], then escape from the cluster. At high enough laser intensity, almost all of the electrons are removed from the cluster. This occurs on a time scale short relative to the ion motion, so what remains is a highly charged cluster of ions at liquid density, which promptly explodes by Coulomb repulsion.

There are two important time scales in the Coulomb explosion model. The first is the ionization time, or the time interval between the start of the inner-ionization and the moment at which all the electrons escape from the cluster, and the second is the cluster expansion time, characterized by the time it takes to expand to twice the initial size.

Since the DD fusion cross section rapidly increases with ion temperature in the keV energy range, generating more energetic deuterium ions is crucial in achieving higher neutron yields. To maximize the ion energies, previous studies have shown that the cluster ionization time should be less than the expansion time.[86] Up to about 7 keV ion temperature has been observed with a peak laser intensity of $10^{16} – 10^{20}$ W/cm^2 using deuterium cluster targets.[18,48,85,86]

Besides requiring an ultra-short pulse, a very high contrast ratio between the main pulse and the pre-pulse is desirable. If ionization takes place due to pre-pulses, the ions in the cluster start expanding before the main pulse arrives, effectively decreasing the overall atomic density of the deuterium cluster, and resulting in less ion kinetic energies after the Coulomb explosion.

The DD fusion neutron yield in a cluster fusion experiment can be expressed as follows[18]:

$$Y \approx \frac{\tau_d}{2} \int n_D^2 < \sigma v > dV + N_{ion} \int n_D < \sigma_v > dl. \quad (6.1)$$

The disassembly time of the plasma filament, τ_d, can be estimated as $\tau_d \sim r/<v>$, where the mean speed of the hot deuterium ions within the filament, $<v>$, is $\sqrt{16\overline{E_D}/3\pi m_D}$ for a Maxwellian distribution, and r is the radius of the cylindrical filament. The average deuterium density n_D can be measured experimentally, and its approximate value was $7\ (\pm 4)\times 10^{18}$ cm^{-3} for similar gas jet conditions [99]. We assumed $n_D = 1\times 10^{19}$ atoms/cm^3 for the subsequent calculations considering the lower gas jet temperature and slightly higher backing pressure. Given the velocity distribution $f(v)$ of the hot ions, we can calculate the fusion reactivity, $<\sigma v>$. The first integration is over the volume element dV within the plasma filament. N_{ion} is the total number of energetic deuterium ions originating from the plasma, and $<\sigma_v>$ is the velocity averaged fusion cross-section. The second integration is over the length element dl over the entire gas jet, where l varies from r to the radius of the gas jet, R. The first term accounts for the total DD fusion reactions within the hot plasma. The second term is the beam-target contribution, which accounts for the fusion reactions between hot deuterium ions originating from the exploding clusters and the cold background deuterium ions or atoms in the gas jet.

Two side camera images of the plasma filament are shown in Figure 61. Figure 61 (a) shows the typical side image of the deuterium plasma filament at the focus, and Figure 61 (b) shows the side image of the filament at 10 cm away from the focus. Assuming a uniform density n_D of the deuterium ions inside the plasma filament and throughout the gas jet, the theoretical neutron yield can be calculated using the Faraday cup TOF measurements and a simple model for the filament.

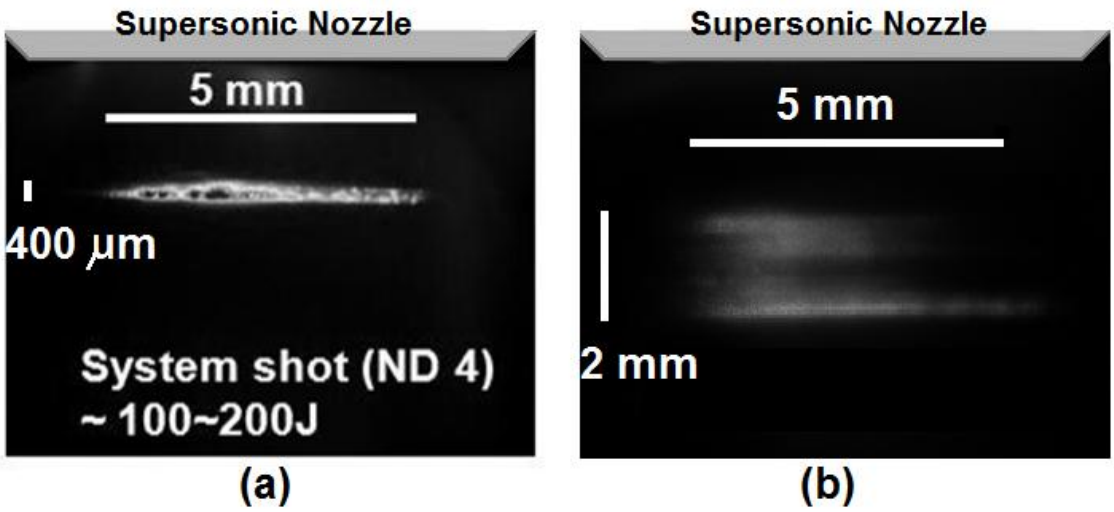

Figure 61. Side images of the deuterium plasma filament on a system shot (a) at focus (with 1ω suppressing filter) and (b) at 10 cm away from the focus

The deuterium plasma filament in each figure can be approximated as a 5 mm long cylindrical filament. The length of the filament was about the same dimension as the diameter of the nozzle opening, and was l=5 mm. Then, the total number of hot ions can be expressed as $N_{ion} = n_D V = n_D \times \pi r^2 \times 5\, mm$, and the volume of the filament, V, and the radius r can be calculated using the experimentally measured value of N_{ion} from the Faraday cup and the assumed ion density of n_D.

The calculated radius of the filament from this cylindrical model is smaller than the apparent size of the plasma in the side camera image because only the regions where the intensity of the laser is high enough to induce Coulomb explosion are the sources of hot ions. Instead, the diameters of 400 μm and 2 mm in Figure 61 (a) and (b), respectively, were consistent with the measured focal spot sizes according to the images of the laser beam in the mid-field.

A color image of the deuterium plasma filament along with the supersonic nozzle and the pulse valve is shown in Figure 62. A mirror installed for the bottom-view

camera is also shown in Figure 62 under the plasma filament. The OPA pulse energy was a few hundred mJ on this shot.

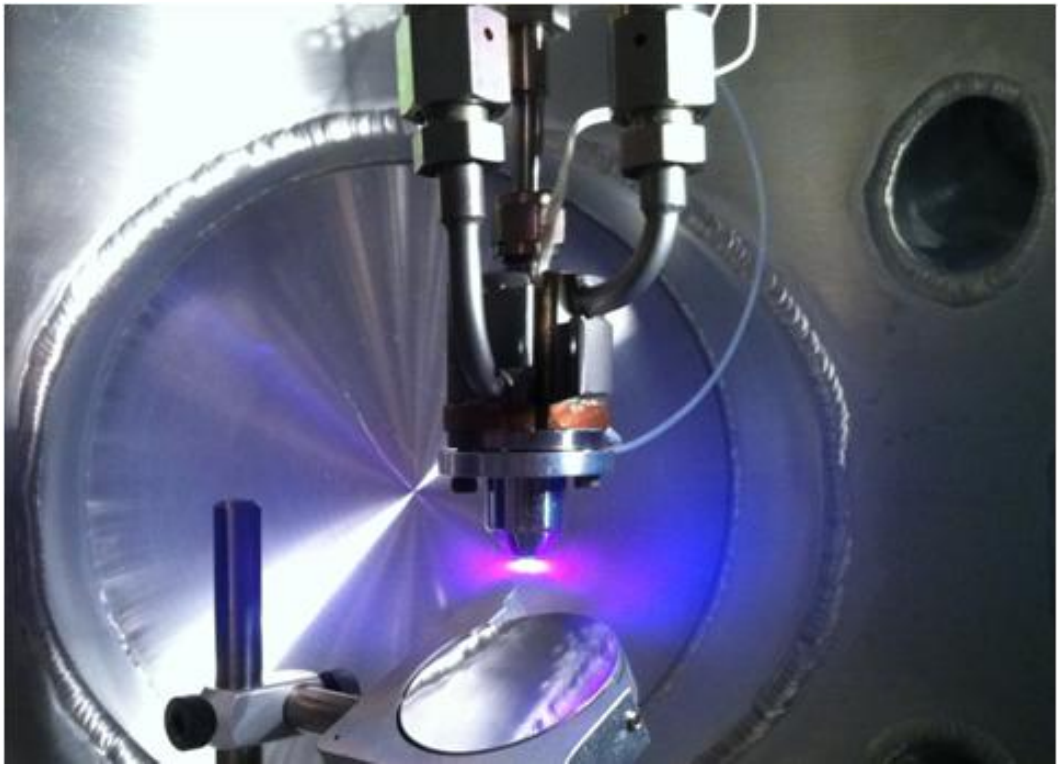

Figure 62. An image of the deuterium plasma filament with an OPA shot

In this chapter, a cluster fusion experiment using a petawatt laser system is described in detail. For this experiment, we used the TPW[26]. The greater energy of this laser over those previously used enabled a much greater volume for the laser-cluster interaction enabling the production of 1.6×10^{7} neutrons in a single shot. We look at the neutron yield and the ion temperature as a function of laser parameters such as the pulse energy, the pulse duration, the power, and the intensity of the laser. We also investigate possible pre-pulse effects of our system by comparing the neutron yields with and without plasma mirrors. For this work, we used laser pulses of 10 to 120 J pulse energy, and varied the pulse duration from 170 fs to 550 fs.

6.2. EXPERIMENTAL SETUP

The TPW has, as part of its beam-delivery options, an f/40 focusing spherical mirror with 10 m focal length. This creates a much bigger interaction area, and higher neutron yields are expected from the increase in the volume of the plasma filament. The TPW is a chirped pulse amplified laser that can deliver 200 J pulses of 1057 nm wavelength, with 170 fs duration [26].

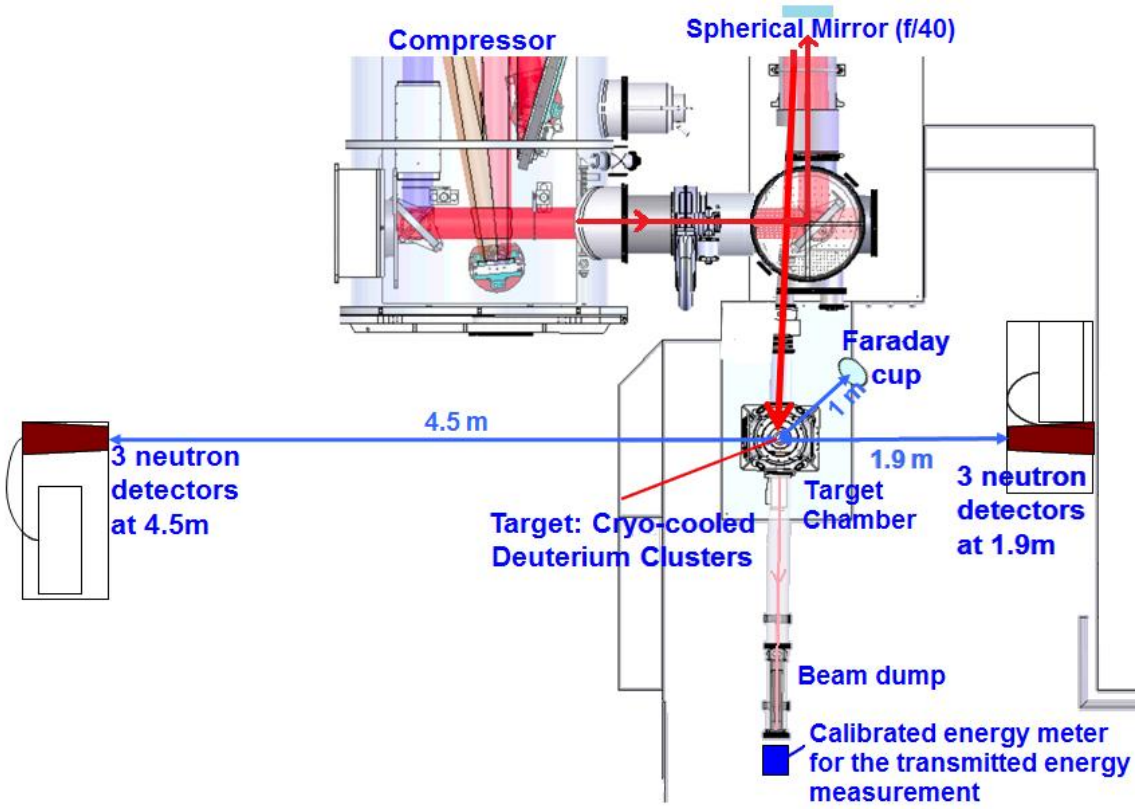

Figure 63. The layout of the Texas Petawatt target area for this experiment

Figure 63 shows the experimental layout of the system and the detector locations in the TPW target area. After being compressed to 170 fs by the compressor, the pulse continues in vacuum, reflecting off of a 45 degree turning mirror to the f/40 spherical mirror, then the 22 cm diameter beam is focused to a 200 μm diameter focal spot in the

target chamber. The spherical mirror was fixed on a translation stage with a 20 cm travel distance in the laser propagation direction, which allowed us to adjust the relative distance between the focus and the cluster producing nozzle. The peak laser intensity at the focus was on the order of 10^{18} W/cm^2, and the average incident laser intensity on the cluster target was varied from 10^{15} W/cm^2 to 10^{18} W/cm^2 either by translating the spherical mirror or by adjusting the location of the nozzle.

To maximize the neutron yield by optimizing the laser intensity, we used the following setup shown in Figure 64. Neutron yield was measured varying the distance from the nozzle to the focus in the laser propagation direction.

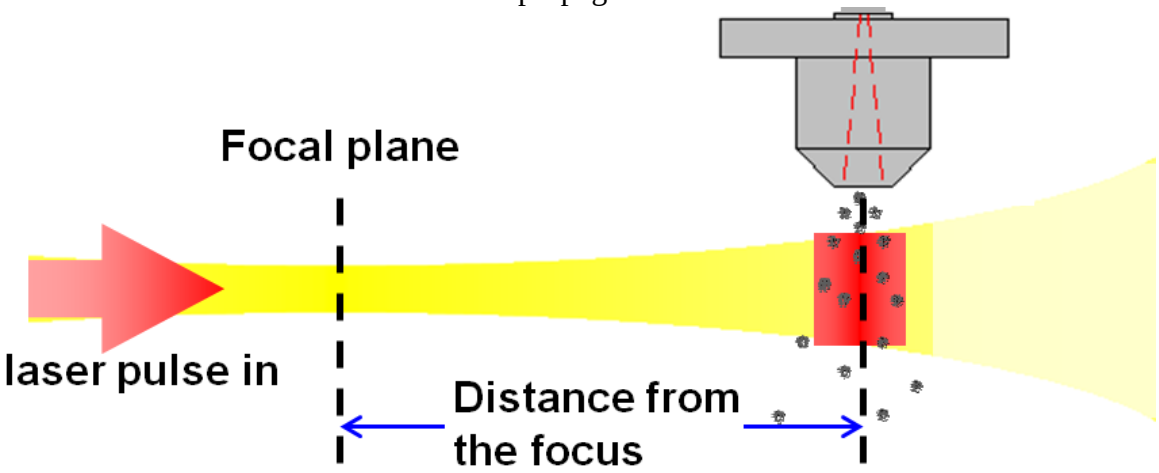

Figure 64. Schematic diagram for the neutron yield measurement as a function of the distance from the nozzle to the focus

To produce cluster targets, deuterium gas was cryo-cooled to 86 K, and forced through a supersonic nozzle at a pressure of 770 psi. The conic nozzle had an input diameter of 790 μm, a half-angle opening of 5 degrees, and an exit diameter of 5 mm. The nozzle was attached to an XYZ manipulator with 5 cm travel distance in each direction. At 86 K, clusters with average diameter around 15 nm were produced (about 100,000 atoms), which was confirmed using a series of Rayleigh scattering

measurements with a 17 mW HeNe laser. The peak intensity of the TPW was high enough to fully ionize deuterium clusters of this size.

Six plastic scintillation detectors that had been calibrated using the cluster fusion neutron sources on the THOR laser prior to this experiment detected the DD fusion neutrons [28]. Four of the six scintillation detectors used 4.0 cm diameter, 2.0 cm long EJ-232Q scintillators with very fast rise time and decay time for accurate TOF measurement along with neutron yield measurement, and the other two detectors used 4.6 cm diameter, 4.9 cm long EJ-200 scintillators for a higher detection sensitivity. Each scintillator was coupled to a Photonis XP2020 PMT. Three scintillation detectors were located at 1.9 m away from the nozzle, and the other three detectors were 4.5 m away. All the detectors were placed at 90 degrees from the laser direction.

To measure the total number of deuterium ions and determine the ion temperature, a Faraday cup 0.96 m away from the interaction region measured the deuterium ions in a TOF configuration. An electric field of 80 V/mm was applied over the last 5 mm of this flight path to repell slow electrons without affecting the time measurement.

Laser energy not absorbed by the cluster target was attenuated and directed onto a calibrated energy meter. Together with a calibrated on-shot measurement of pulse energy before the cluster jet, this allowed us to measure the absorption in the cluster gas jet plume. Two cameras took images at orthogonal views of the plasma filament during the shot. A camera measured an equivalent mid-field image plane that represented the actual beam profile on the cluster target. The pulse duration, through autocorrelation, and energy was also measured on each shot.

In order to examine the effect of the TPW pre-pulses on the cluster fusion experiment, some shots were taken using a pair of plasma mirrors to increase the relative

size of the main pulse over any pre-pulses. Plasma mirrors can increase this contrast ratio without modifying the system significantly [33]. For this experiment, a pair of uncoated BK7 glass windows was inserted at 45 degrees between the target and the f/40 focusing mirror. Therefore, the combined reflectivity of the double plasma mirrors will be 1% for pre-pulses, while 50% reflectivity is expected for the main pulse.

Previous studies showed that the reflectivity of one plasma mirror goes as high as 70% when the fluence on the mirror exceeds 50 J/cm^2 [32,33]. On the TPW, the s-polarized laser beam fluence on the first mirror was about 100 J/cm^2, and the beam fluence on the second mirror was estimated to be about 70 J/cm^2. The double plasma mirrors reduced the energy of the main pulse by a factor of 2, while reducing the pre-pulse energy by two orders of magnitude, for a 50x contrast ratio improvement. A few pictures of the plasma mirror setup are added in Appendix E.

6.3. RESULTS AND ANALYSIS

The neutron yield (neutrons per shot) averaged over all 6 plastic scintillation detectors on each system shot is plotted in Figure 65 as a function of the nozzle distance relative to the focus, where the distance from the focus is described in Figure 64. The blue squares are data taken with delivered laser energies of 90 to 115 J. The neutron yield peaked at a distance of 11 cm, where we achieved 1.6×10^7 n/shot. A similar nozzle position scan while using two plasma mirrors, shown as red triangles, had an optimum distance of 5 cm, achieving a neutron yield of 7.2×10^6 n/shot using the post-plasma mirror energies of about 45 to 60 J. Interestingly, we did not see higher neutron yield with plasma mirrors, which we believe is due to the decrease in the number of energetic deuterium ions since only 50% of the pulse energy went into the target. The ion temperature in both cases was as high as 10 keV.

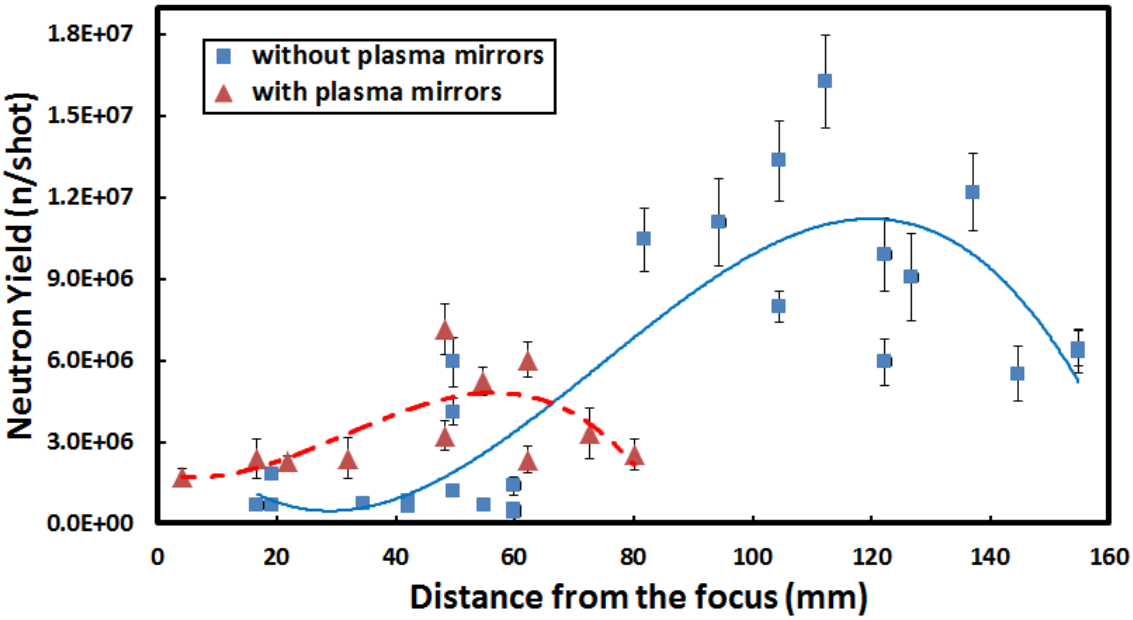

Figure 65. Neutron yield (neutrons per shot) on system shots with (triangle) and without (square) plasma mirrors as a function of the distance from the nozzle to the focus. The solid line indicates the third order polynomial fit to the no plasma mirror data, and the dashed line indicates the third order polynomial fit to the data with plasma mirrors. The error bars indicate one standard deviation of the mean.

The TOF measurements indicated that the hot deuterium ions had a nearly Maxwellian velocity distribution. Two examples of the Faraday cup data with Maxwellian fits are shown in Figure 66. Initial x-ray peaks are followed by the energetic deuterium ion peaks, the delay of which is used to deduce the ion temperature of the plasma. The number of deuterium ions, N_{ion}, generated within the interaction region was estimated by scaling the solid-angle detection of the Faraday cup data to a full 4π distribution [18].

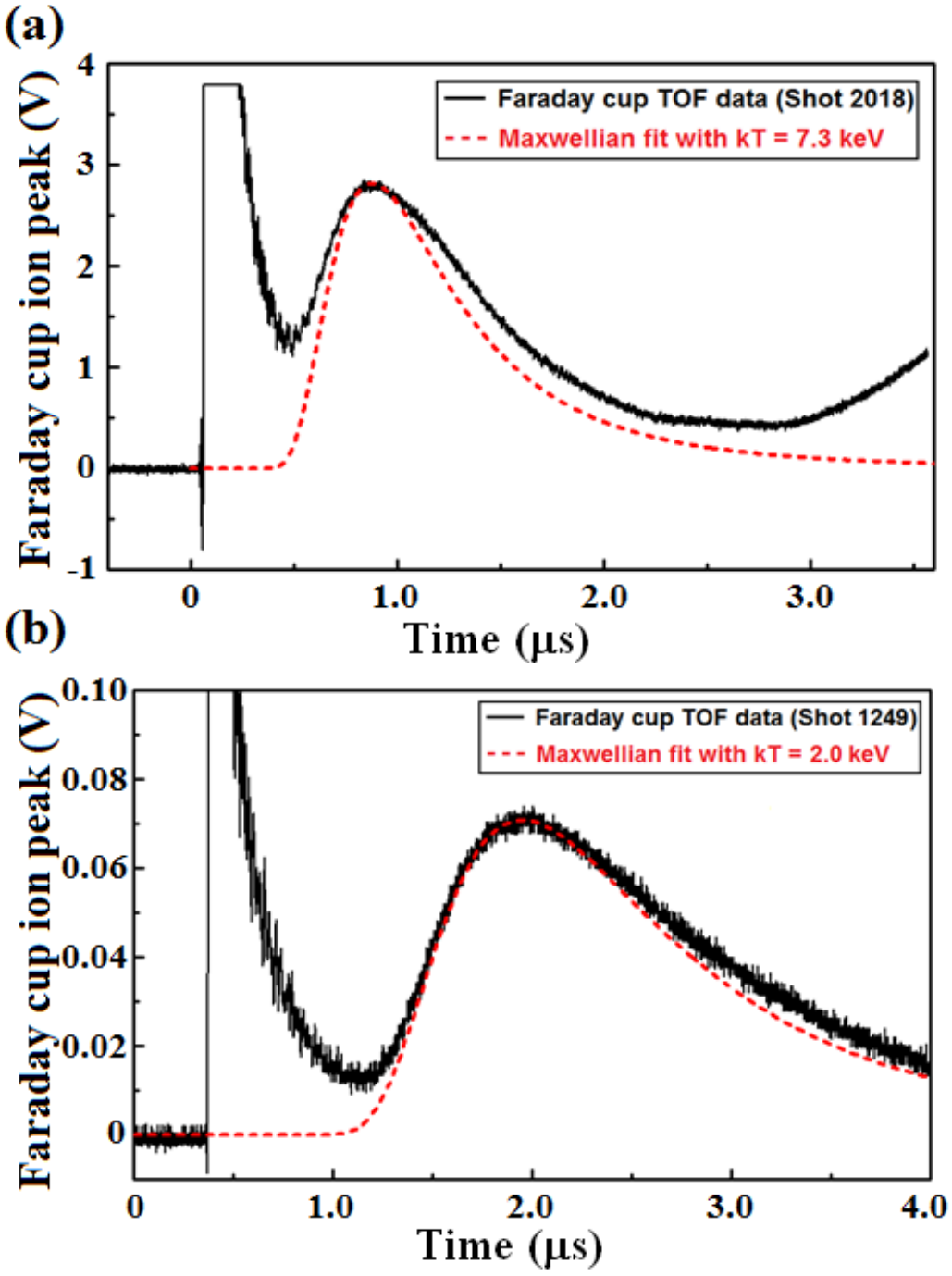

Figure 66. (a) Faraday cup trace of a system shot with a Maxwellian fit with ion temperature of 7.3 keV. (b) Typical Faraday cup trace of a 10 J shot with a Maxwellian fit with ion temperature of 2 keV. A huge initial x-ray peak is followed by the deuterium ion peak in each figure.

The beam-target contribution and the beam-beam contribution in equation (6.1) can be evaluated if we know r (or N_{ion}) and the ion temperature, kT, both of which can be calculated from the Faraday cup TOF measurements. The beam-beam contribution can be directly calculated using the assumed uniform atomic density of n_D, the fusion reactivity for the measured ion temperature, and the total number of ions deduced from the Faraday cup measurements. The plasma disassembly time in equation (6.1) is also known since r can be calculated using the measured value of N_{ion} and applying the cylindrical filament model with density n_D.

The beam-target contribution can be estimated approximating the velocity averaged fusion cross-section $<\sigma_v>$ as $<\sigma>_{kT/2}$. This approximation is legitimate since the overall ion energy distribution of the energetic ions from Coulomb explosion closely followed a Maxwellian distribution, and the background ions can be considered stationary.

Previous studies suggest that the Maxwellian distribution of the hot ions originates from the log-normal size distribution of the clusters, and not from the thermalization of the energetic ions [18,100]. This is consistent with the fact that the mean free path of the hot deuterium ions for ion temperatures ranging from 2 keV to 10 keV is 2–7 mm according to the SRIM simulations [18,50], which is greater than the radius r in this experiment.

As a special case, $< \sigma_v >_{kT/2} = \frac{<\sigma v>_{kT/2}}{<v>_{kT/2}}$ when the energy distribution of hot ions follows a delta function distribution. Though an exact value of $<\sigma>_{kT/2}$ can be calculated using the known DD fusion cross section and the Maxwellian distribution, a rough approximation, $< \sigma >_{kT/2} \approx \frac{<\sigma v>_{kT/2}}{<v>}$, can be used for ion temperatures ranging from 5 keV to 100 keV [18]. Note that this approximation gives up to about 30% errors for low ion temperatures.

Therefore, the ratio of the two contributions in equation (6.1) is approximately

$$\beta = \frac{N_{ion}\int_r^R n_D<\sigma_v>dl}{\frac{\tau_d}{2}\int n_D^2<\sigma v>dV} \approx \frac{N_{ion}n_D\frac{<\sigma v>_{kT/2}}{<v>}(R-r)}{\frac{r}{2<v>}N_{ion}n_D<\sigma v>_{kT}} = 2\left(\frac{R}{r}-1\right)\frac{<\sigma v>_{kT/2}}{<\sigma v>_{kT}}, \quad (6.2)$$

where, R=2.5 mm is the radius of the gas jet and $r = \sqrt{\frac{N_{ion}}{\pi\, n_D(5\ mm)}}$ is the radius of the filament. Knowing N_{ion} and kT from the TOF Faraday cup measurements and assuming a constant n_D=10^{19} cm^{-3} inside the whole gas jet whose radius is 2.5 mm, we have an independent way to calculate the total DD fusion neutron yield, Y, theoretically using the simplified cylindrical filament model.

$$Y \approx \frac{\tau_d}{2}\int n_D^2 < \sigma v > dV + N_{ion}\int n_D < \sigma_v > dl = (1+\beta)\frac{\tau_d}{2}\int n_D^2 < \sigma v > dV = (1+\beta)\frac{r}{2<v>}n_D^2 < \sigma v >_{kT} V = (1+\beta)\frac{r}{2<v>}n_D < \sigma v >_{kT} N_{ion}. \quad (6.3)$$

From equation (6.2), β is a function of r and kT. Since r is a function of N_{ion}, and both $<v>$ and $<\sigma v>_{kT}$ are functions of kT, the total neutron yield is a function of N_{ion} and kT only in equation (6.3). Figure 67 (a) shows the relationship between the measured average neutron yield and the fusion reactivity in a log-linear scale. Figure 67 (b) shows measured average neutron yield versus $<\sigma v>\times N_{ion}$ in a log-log scale. System shots with plasma mirrors (red triangle) and without plasma mirrors (blue square) are plotted together in each graph.

Figure 67 (a) does not exhibit a linear relationship because Y also depends on N_{ion}. Since we changed the focal spot size by moving the nozzle away from the focus in the laser propagation direction, N_{ion} was very different on each shot. Also, N_{ion} dropped considerably when we used plasma mirrors due to the less available energy, which resulted in smaller neutron yields in general with plasma mirrors.

From equation (6.3), Y is an increasing function of $<\sigma v>_{kT}N_{ion}$. Figure 67 (b) shows the relationship between the measured neutron yield and this parameter along with a linear fit (solid line). Approximately linear relationship between the neutron yield and

$<\sigma v>_{kT} N_{ion}$ is shown in this figure. However, the deviation from the linear fit was rather large when the value of $<\sigma v>_{kT} N_{ion}$ was small. This is likely related to the fact that the plastic scintillation detectors were located far away from the chamber, and their detection limits were on the order of 10^5 neutrons per shot. There were some shots that did not trigger any neutron detectors with similar ion temperatures, and those shots with no measured neutron yields are not shown in the figure. Consequently, there were not many neutron yield data with low ion temperatures, which resulted in larger statistical errors in this region.

Finally, Figure 67 (c) shows the plot of the experimentally measured average neutron yield (neutrons per shot) from the 6 plastic scintillation detectors on each shot versus the calculated neutron yield using the cylindrical filament model and the ion TOF measurements data.

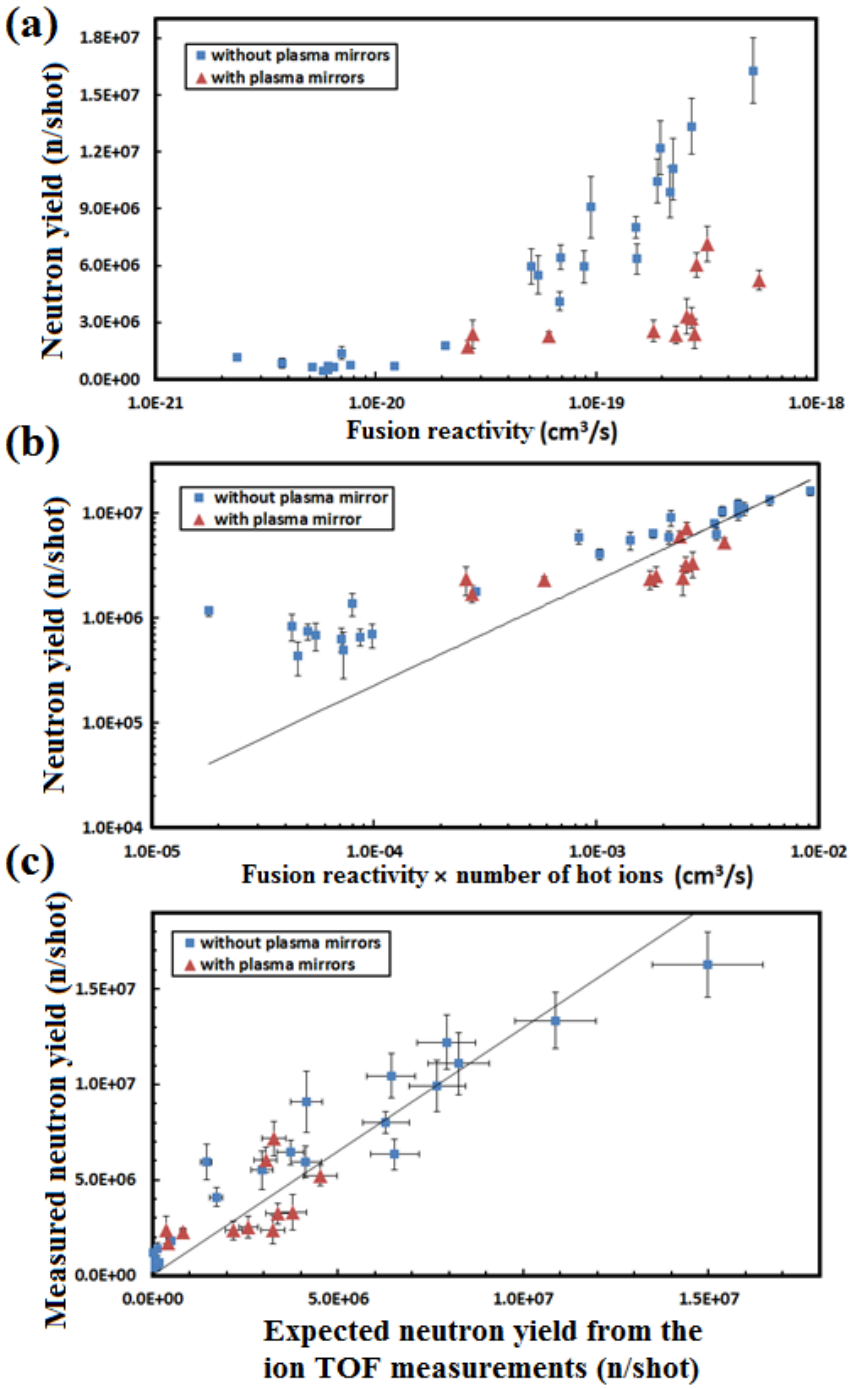

Figure 67. Experimentally measured neutron yield from 6 plastic scintillation detectors versus (a) the fusion reactivity, (b) the fusion reactivity times the number of hot ions, (c) and the calculated neutron yield. The solid black lines are linear fits to the data.

After finding the focus, and firing several 100 J ~ 180 J system shots and 10 J rod shots near the focus, we found that the highest possible intensity laser beam on the cluster target did not produce the most energetic deuterium ions or the most number of DD fusion neutrons. Even with a very soft focusing, the TPW reaches several times 10^{18} W/cm^2 at peak intensity. However, we have not seen any neutron peaks with the plastic scintillation detectors at this high peak intensity when the filament was located at the focus or near the focus. When the targets were close to the focus, we generally had very strong x-ray peaks with the 100 J ~ 180 J system shots.

Due to the huge x-ray signal near the focus, the minimum detection range was limited to about 10^4 ~ 10^5 n/shot for the system shots. It took more than 50 ns for the saturating x-ray signals to decay low enough to distinguish TOF neutron signals even for the plastic scintillators with very fast decay constant, and we could not place the detectors close enough for low neutron yield measurement. Therefore, the estimated neutron yield at the focus was lower than 10^4 n/shot.

Interestingly, the scintillation detectors occasionally detected fusion neutrons with much lower energy shots, or with 10 J rod shots. This was quite unexpected because it was shown that the neutron yield scaled as square of the laser pulse energy as a result of the increase in the volume and the ion temperature [48,85,86]. Though the exact cause of this behavior is unclear, this brings up a question of how the ion temperature depends on the laser intensity. There are at least two different approaches to investigate this dependence and the cause of that.

The first approach is to send the nozzle further away from the focus so that the laser intensity on the target gets smaller with same pulse energy and similar pulse duration. This is equivalent to varying the intensity of the laser for a fixed pulse energy, and measuring the neutron yield and ion temperature, etc. The measurements of the

pulse energy, pulse duration, and the beam profile on the target enabled us to calculate the average laser intensity incident on the deuterium cluster target. To the best of the authors' knowledge, there has not been an experimental scan of the average laser intensity in relation to the DD fusion neutron yield or the ion temperature of the deuterium plasma. Instead, researchers have normally performed a series of nozzle position scan to optimize the neutron yield for a fixed laser pulse energy [48,85].

For the laser intensity scan, the focal spot area should be kept similar throughout the entire filament length of 5 mm. Without the depletion of the incident laser pulse energy, this means that each cluster experiences similar laser intensity throughout the filament. When the pulse energy is efficiently absorbed by the clusters, we can still examine the collective behavior of the hot ions in terms of the average incident laser intensity. Due to the big f-number of TPW focusing optics, the Rayleigh length of TPW laser beam was over 2 cm, and this allowed us to perform a scan of the laser intensity by moving the nozzle away from the focus. Even at 15 cm away from the focus, the beam size almost did not change throughout the entire filament length, which we verified by looking at the side images of the filament on each shot.

The second approach involves implementing a pair of plasma mirrors. The installation of plasma mirrors did not require any major design change in the amplifier chain of TPW, so all the characteristics of the laser pulse remained unchanged during the system shots with plasma mirrors. The contrast ratio of the TPW laser beam was better than 10^7 outside 1 ns time window based on a series of photodiode measurements. However, we have not identified all the pre-pulses within 1 ns time window from the main pulse. So, there was a possibility that the cluster targets were destroyed by possible pre-pulses before the main pulse arrived. It is estimated that as low as 10^{11} W/cm^2 pre-pulse could destroy the cryo-cooled deuterium clusters [101,102]. If that

actually happened, we would have had much smaller clusters left by the time the main pulse arrived, and less energetic ions would have been produced from the laser-cluster interaction. The second approach is based on the assumption that if the pre-pulses started destroying the deuterium clusters at certain intensity, we could possibly avoid that by reducing the pre-pulse intensity by 50 times while keeping the main pulse intensity the same utilizing a pair of plasma mirrors.

Figure 68 (a) shows the neutron yield versus the spatially averaged incident laser intensity for the system shots without plasma mirrors. Clearly, there was an optimum average laser intensity, after which the neutron yield started getting lower. The spatial average of the incident laser intensity was calculated by dividing the pulse energy by the pulse duration and the focal spot size of the beam at the target, all of which were measured from the TPW on-shot diagnostics. The peak intensity was up to 4 times the average intensity in this experiment, and the perimeter of the beam was more intense than the center according to the mid-field images.

Figure 68 (b) shows the fusion reactivity versus average laser intensity for system shots without plasma mirrors. The fusion reactivity was calculated using the ion temperature for each shot measured on the Faraday cup [18,51,86]. Both system shots with and without plasma mirrors are shown together in Figure 68 (c). Interestingly, both curves lie very close without showing distinct features. The fact that the fusion reactivity did not become larger when we used plasma mirrors at high laser intensity seems to indicate that either we failed to filter out the relevant pre-pulses completely or this intensity dependence is not a result of pre-pulses. With 50 times contrast ratio improvement, we expected to see a saturating behavior when double plasma mirrors were implemented. Instead, we observed similar dependence of the fusion reactivity on the average laser intensity.

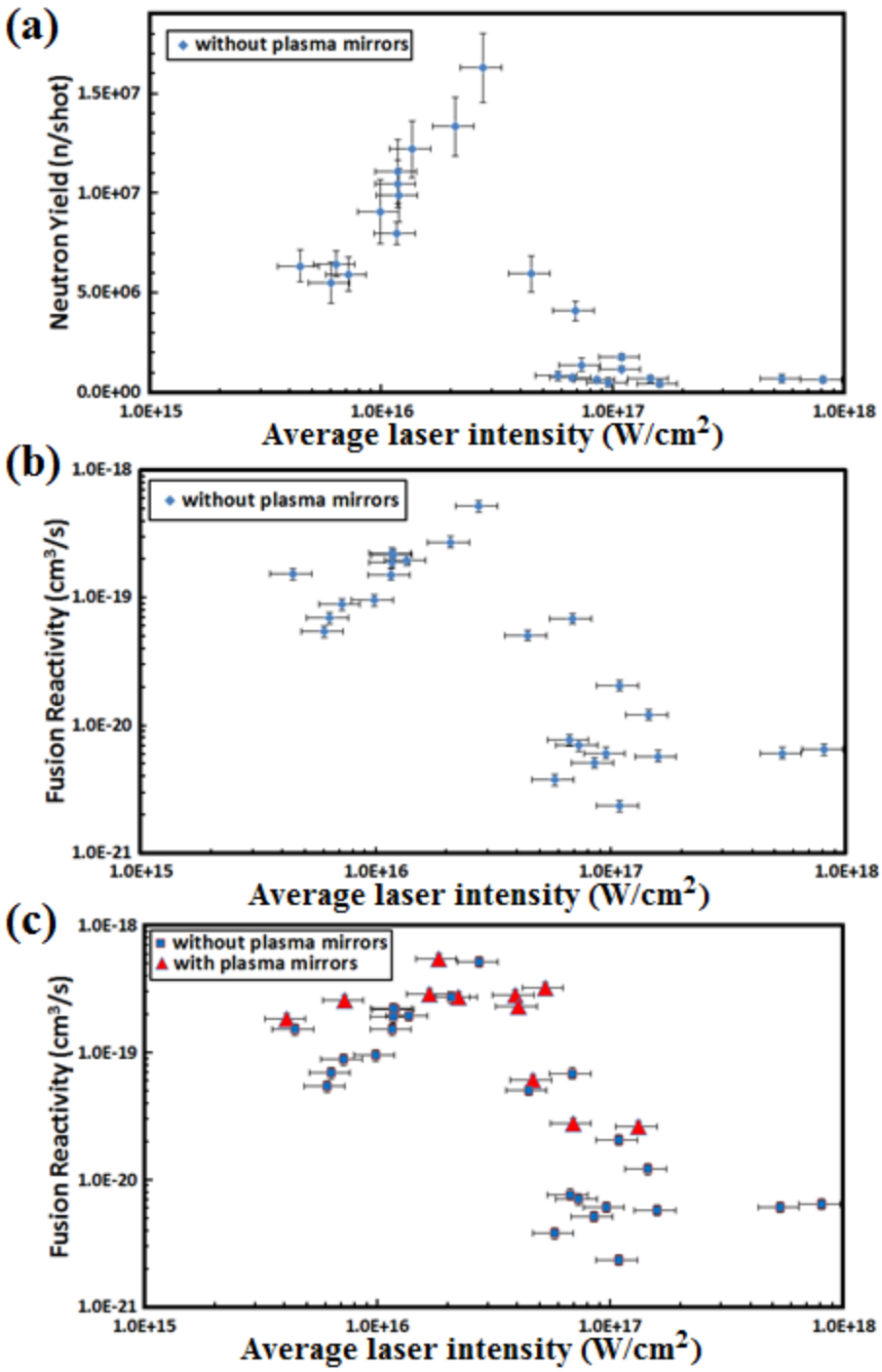

Figure 68. (a) The average neutron yield, (b) the fusion reactivity without the plasma mirrors, (c) the fusion reactivity with and without the plasma mirrors versus the average laser intensity

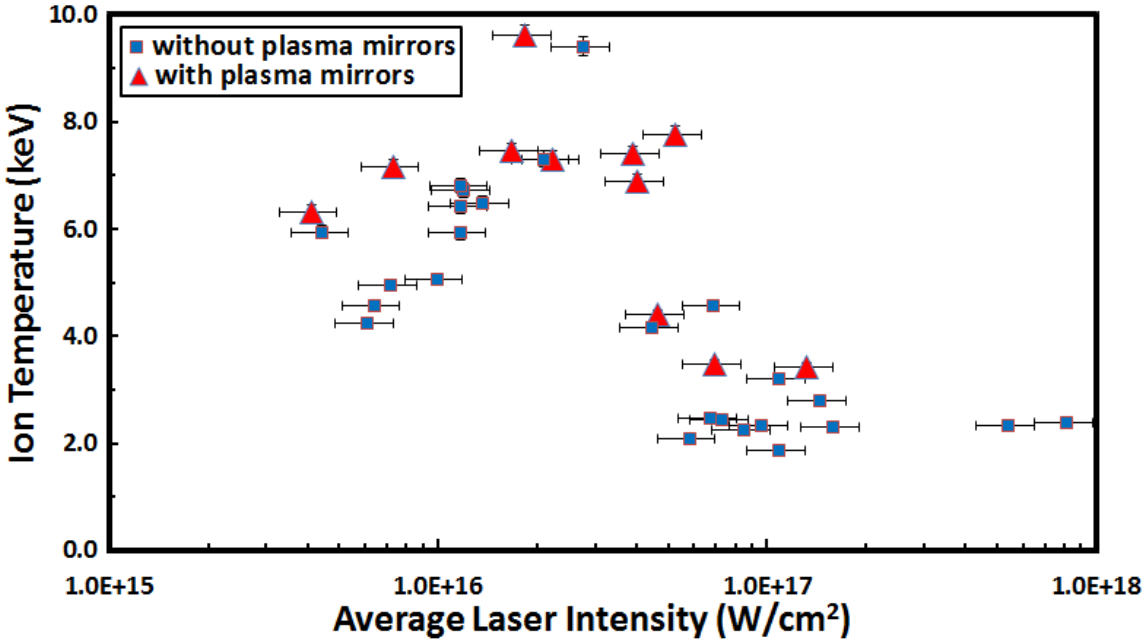

Figure 69. The dependence of the ion temperature on the average laser intensity for system shots with and without plasma mirrors. The error bars indicate 20% uncertainty in the measurement of the average laser intensity and 2% error in the measurement of the ion temperature.

The dependence of the ion temperature on the average laser intensity is shown in Figure 69. The ion temperature decreases as the laser intensity becomes higher than the optimum intensity. Below the optimum intensity, the ion temperature increases as the laser intensity increases. The latter trend has been observed before, and was shown to agree with the numerical simulations [100,103].

The deuterium atoms inside each cluster experience inner-ionization within a femtosecond once the laser intensity rises above 10^{14} W/cm^2. In this state, the atoms inside the cluster are fully ionized, but the electrons are still bound to the cluster. They can only escape from the cluster after gaining further energy from the laser pulse. This process is often called the outer-ionization [104]. For this outer-ionization, the electrons should gain kinetic energy larger than the potential energy at the surface of the cluster.

At the surface of the cluster, the average kinetic energy of an electron is roughly the ponderomotive potential inside the laser field, which increases linearly with the laser intensity. Therefore, more electrons will escape from the cluster as the laser intensity increases. This would be true until the laser intensity becomes high enough to strip all the electrons out of a given cluster, whose intensity is called the critical intensity. So, higher laser intensity results in higher charge state of the cluster, and the higher ion temperature and neutron yield that we see in Figure 68 can be understood as the results of this.

Above the critical intensity, it was thought that the clusters would be still fully outer-ionized, producing equally hot ions [85]. In this experiment, this was not the case, and we saw much less energetic ions at the highest laser intensity above 10^{18} W/cm^2. We successfully produced very energetic ions. The ion temperature reached almost 10 keV at optimum laser intensity, which implies that these ions originated from a very big deuterium cluster. The measured ion temperature in the range of 2 keV ~ 10 keV is also consistent with other experiments with deuterium cluster targets [18,48,85].

Assuming liquid density of deuterium atoms inside the cluster, we can estimate the average size of a cluster from the measured ion temperature. Using the number density of liquid deuterium, n=4.86×10^{22} atoms/cm^3, a deuterium cluster with N atoms has a radius of R (Å)=1.7×$N^{1/3}$. After complete outer-ionization, the potential energy of the outermost ions can be calculated as [17],

$$E_{max}(r = R) = \frac{Qe}{4\pi\varepsilon_0 r} = \frac{Ne^2}{4\pi\varepsilon_0 R} = \frac{\frac{4\pi R^3}{3} ne^2}{4\pi\varepsilon_0 R} = \frac{ne^2 R^2}{3\varepsilon_0}, \quad (4)$$

where Q is the total charge inside a cluster of radius R, n is the liquid density of deuterium, e is the charge of the deuterium ion, and ε_0 is the vacuum permittivity.

Similarly, the potential energy of i-th ion located at distance r away from the center can be expressed as $E_i(r) = E(r) = \frac{Q(r)e}{4\pi\varepsilon_0 r} = \frac{\frac{4\pi r^3}{3}ne^2}{4\pi\varepsilon_0 r} = \frac{ne^2r^2}{3\varepsilon_0}$, (5)

where *Q(r)* is the total charge inside a ball of radius r within the cluster. Then, the average potential energy of the ions is [17]:

$$< E >= \frac{\sum_{i=1}^{N} E_i(r)}{N} = \frac{\int_0^R E(r)dN(r)}{N} = \frac{\int_0^R \frac{ne^2r^2}{3\varepsilon_0}(n4\pi r^2 dr)}{n\frac{4\pi R^3}{3}} = \frac{ne^2R^2}{5\varepsilon_0} \quad (= \frac{3E_{max}}{5}). \quad (6)$$

Upon Coulomb explosion, the potential energy of each ion is transferred into the kinetic energy of each ion, which we can measure using the Faraday cup. Using $< E >= \frac{ne^2R^2}{5\varepsilon_0} = \frac{3}{2}kT \approx 14$ keV at the optimum intensity, we can estimate the approximate average size of the clusters, R=8.9 nm, or equivalently, $N = n \times \frac{4\pi R^3}{3} = 1.4 \times 10^5$ atoms. This cluster size is quite large for deuterium, and we believe that this indicates how successful the shot was in terms of generating hot ions. If pre-pulse caused the ion temperature drop in the high intensity regime, it certainly did not affect appreciably at the optimum intensity.

We also looked at the relationship between the pulse duration and the ion temperature in two different intensity regimes. For system shots without plasma mirrors, the ion temperature at higher than the optimum intensity was around 2–4 keV, which shots are shown with a linear fit in Figure 70.

Normally, higher ion temperature is expected at shorter pulse duration according to the Coulomb model. However, in this experiment, the ion temperature decreased as we further increased the laser intensity beyond the optimum intensity. Similarly in Figure 70, the ion temperature drops as the pulse duration becomes shorter in this high intensity regime.

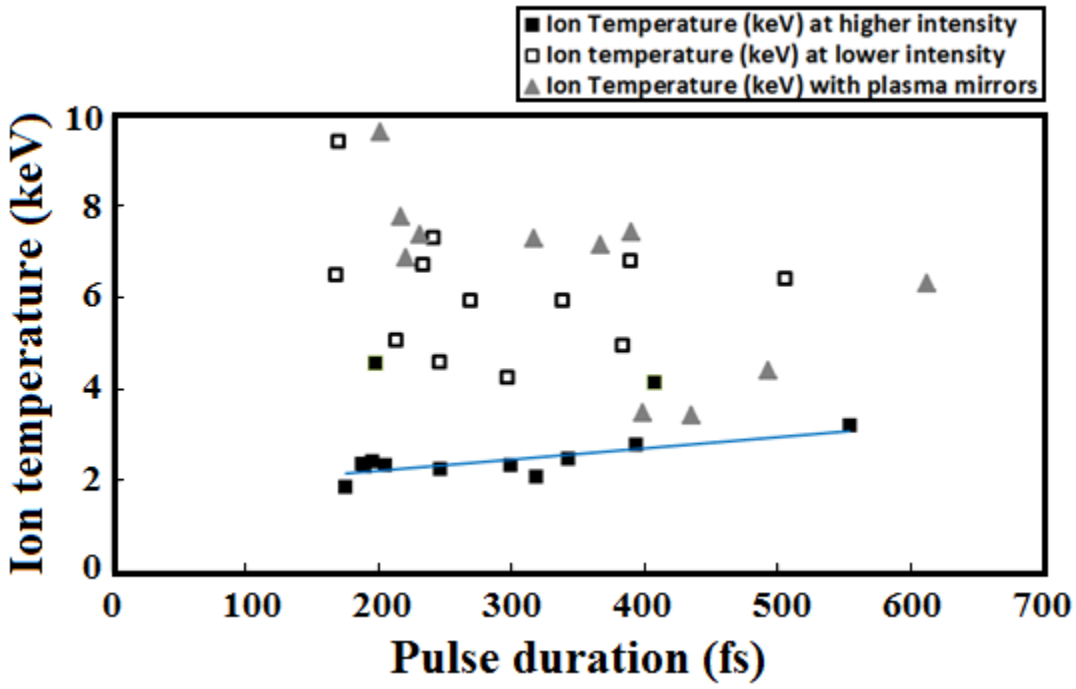

Figure 70. The ion temperatures on system shots measured from the ion TOF data are shown for different pulse durations at various laser intensities.

In Figure 70, solid triangles represent the ion temperature on system shots with plasma mirrors. It is quite surprising to see that we can get 6 keV ion temperature with a 600 fs pulse. The ion temperature with plasma mirrors was slightly higher than or comparable to the ion temperature without plasma mirrors. The hollow square marks represent system shots without plasma mirrors when the intensity was lower than the optimum intensity. The ion temperature is not a function of the pulse duration alone in this regime, and there is no clear trend. Again, a 500 fs pulse generated energetic ions with ion temperature higher than 6 keV. This suggests that we can generate reasonable amount of fusion reactions with relatively longer pulse lasers than TPW.

6.4. DISCUSSION

When the nozzle was near the focus, the ion temperature was only about 2 keV and N_{ion} was small, which resulted in low neutron yield. With a simple model for the filament and the ion TOF Faraday cup data, we confirmed a good agreement between the theoretically calculated neutron yield and the measured neutron yield averaged over the 6 plastic scintillation detectors.

This demonstrates the validity of the simple model, and allows an estimation of the maximum achievable neutron yield with the current system and setup. The ion TOF measurements showed up to 10 keV deuterium ion temperature in this experiment, which agreed with the transmitted energy measurements showing up to 90% absorption of the 120 J pulse energy by the cluster targets. The TOF Faraday cup measurements also showed that the hot ions carried less than half of the total laser pulse energy. Given this information, we can estimate the maximum possible neutron yields on the TPW.

TPW can deliver 180 J laser pulse with up to 90 J carried by the energetic deuterium ions. Assuming a temperature of 10 keV ions at the optimum intensity, the total number of ions can be calculated using 90 J = 3/2 $kT \times N_{ion}$. With kT=10 keV and $N_{ion}=3.8\times10^{16}$, the DD fusion neutron yield was estimated using the same model presented in this paper. This sets the highest achievable neutron yield limit of 6.5×10^{7} n/shot with the current setup on TPW system although we can still improve the neutron yield either by optimizing the laser intensity and the gas jet condition to get hotter ions or by increasing the overall atomic density n_D with a modified supersonic nozzle. Since the maximum achievable ion temperature strongly depends on the cluster size[100], ion temperatures higher than 10 keV is achievable with a bigger deuterium cluster target or a bigger deuterated methane cluster target, too.

The dependence of the ion temperature on the laser intensity measured in this experiment is rather surprising. Although the cause of this discrepancy is not identified yet, we were able to reproduce similar features qualitatively with simulations assuming a pre-pulse with an intensity of 10^{-4} times the peak intensity of the main pulse. For the simulation, we made the following assumptions:

- Clusters experience Coulomb explosion as they interact with the laser pulse, the ions are not stationary during the duration of the pulse, and they start expanding as soon as the outer-ionization starts. The radius of a cluster at certain time *t*, *r(t)*, can be written as the distance from the center of the cluster to the outermost deuterium ions at the surface.

- The charge state for a given cluster at time *t* can be calculated by counting how many electrons escaped from the cluster surface due to the laser field until that time.

- At certain time *t*, an electron at the surface of the cluster has the electric potential, $\varphi(r(t))=-Q(t)e/4\pi\varepsilon_0 r(t)$, where -e is the charge of an electron, and $Q(t)$ is the total charge of a cluster.

- Due to the laser field, the free electron at the cluster surface (after inner-ionization) acquires an average kinetic energy equal to the ponderomotive potential, $9.33\times10^{-14}\times I(t)[\mathrm{W/cm^2}]\lambda[\mu\mathrm{m}]^2$, where $I(t)$ is the intensity of the laser at time *t*, and λ is the wavelength of the laser. If the sum of the ponderomotive potential and the electric potential $\varphi(r(t))$ is equal to or greater than 0, the electron escapes from the cluster immediately.

- The clusters expand symmetrically, and the outermost ions pick up the highest kinetic energies as is predicted by the Coulomb explosion model.

- The pre-pulse arrives 5 ps earlier than the main pulse with a peak intensity 10^{-4} times smaller than the peak intensity of the main pulse. The pulse duration of the main pulse and pre-pulse are both 200 fs. A deuterium cluster of 500,000 atoms at liquid density is irradiated by a λ=1.057 μm, Gaussian (temporally), flat-top (spatially) laser pulse.

Figure 71 shows the dependence of the maximum kinetic energy of the deuterium ion as a function of the main pulse peak intensity, which agrees well with the experimental data qualitatively. This suggests that pre-pulse might have been the cause for this ion temperature drop at higher intensities beyond the optimum intensity. However, this is not a definite proof, and needs further verifications since we had somewhat similar trend when we utilized the plasma mirrors. We think that this opens two possibilities: First, the plasma mirrors might have been triggered earlier than the arrival of the relevant pre-pulses that caused break-up of the deuterium clusters. This can happen if the relevant pre-pulses were too close to the main pulse to be filtered out by the plasma mirrors. Second, the similar trend is explained if the outer-ionization of the cluster becomes less efficient as the main pulse intensity exceeds the optimum intensity.

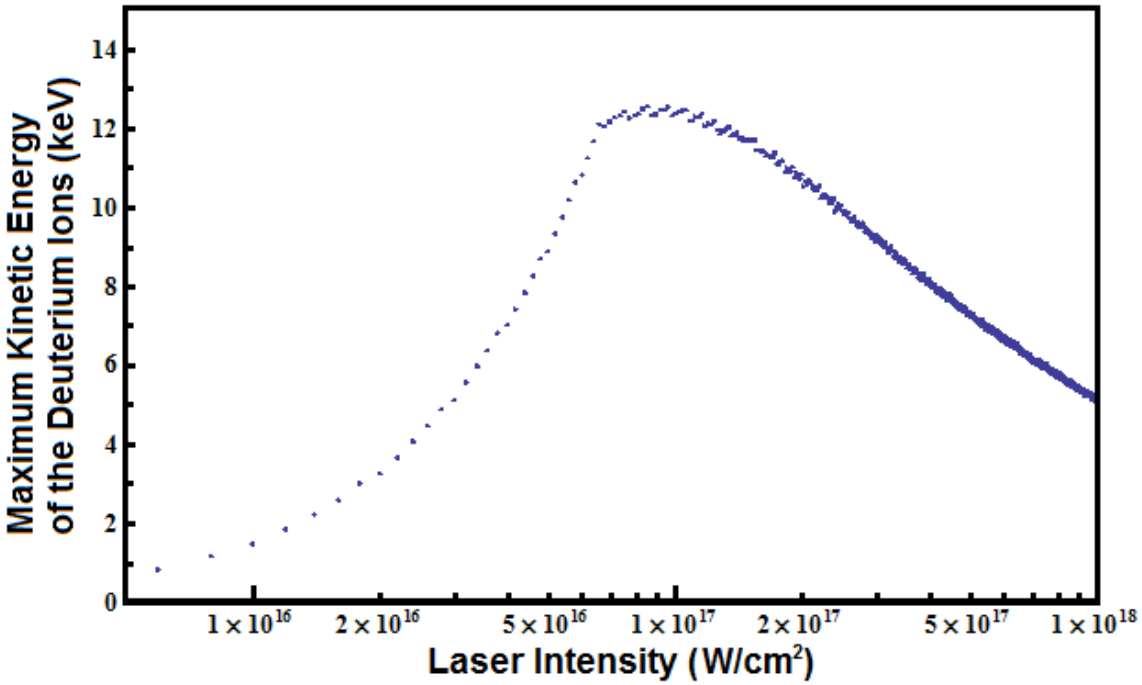

Figure 71. The maximum kinetic energy of the deuterium ions from an expanding deuterium cluster of 500,000 atoms is shown as a function of the peak intensity of the main pulse.

6.5. CONCLUSIONS

After optimization of the laser intensity, the gas jet condition, and the laser pulse duration, we achieved 1.6×10^7 neutrons per shot on TPW. Along with N_{ion}, the ion temperature is a very important quantity in the cluster fusion experiment, and we successfully produced energetic deuterium ions with ion temperature in the range from 5 keV to 10 keV on many system shots. For the first time, we showed the relationship between the laser intensity and the ion temperature experimentally. The big focal length of the TPW focusing mirror and high enough intensity of TPW allowed us to investigate this relationship. We also investigated the effect of pre-pulses on the cluster fusion experiment using a pair of plasma mirrors.

Although it may require further confirmation, we showed that higher intensity is not always good for the highest possible ion temperature for a fixed cluster size. The experimental results show that there can be an optimum laser intensity above which the ion temperature drops. This imposes a limit on the ion temperature, and implies that we need to increase the volume of the plasma after achieving the desired ion temperature if we want to increase the neutron yield further.

Chapter 7. Mixture cluster fusion experiment on the TPW

In this chapter, I will describe a novel way of determining the plasma temperature in a laser-cluster fusion experiment on the TPW using the ratio of the 2.45 MeV neutron and 14.7 MeV proton yields.[30]

7.1. INTRODUCTION

Nuclear fusion from explosions of laser-heated clusters has been an active research topic for over a decade.[16,17,20,21,25,48] Researchers have used either cryo-cooled deuterium (D_2) cluster targets, or near room temperature deuterated methane (CD_4) cluster targets for generating cluster fusion reactions. These cluster fusion experiments have been well explained by the Coulomb explosion model, which is particularly useful in explaining how we could get energetic deuterium ions from laser-cluster interaction.

The temperature of the energetic deuterium ions is very important in the cluster fusion experiment because the fusion cross-section strongly depends on the ion temperature.[51] To measure this ion temperature, researchers have used TOF diagnostics.[18] This ion temperature is believed to be close to the overall plasma temperature when the fusion reactions occurred.

However, the temperature as measured by a Faraday cup contains the entire time history of the ions, and it is possible that the ions measured result from additional interactions en route to detection and are not those directly responsible for the fusion. This point is illustrated in Figure 72 (a). As the ions undergo Coulomb explosion, they are accelerated outward. In Figure 72 (a), three particle locations are indicated. Let's assume that the deuterium ion at r_1 away from the cluster has a speed v_1, the ion at r_2 away from the cluster has a speed v_2, and the ion at r_3 (~1 m) away from the cluster has a speed v_3. Note that the figure is not to scale, and $r_1 < r_2 < 2.5$ mm $<< r_3 \sim 1$ m.

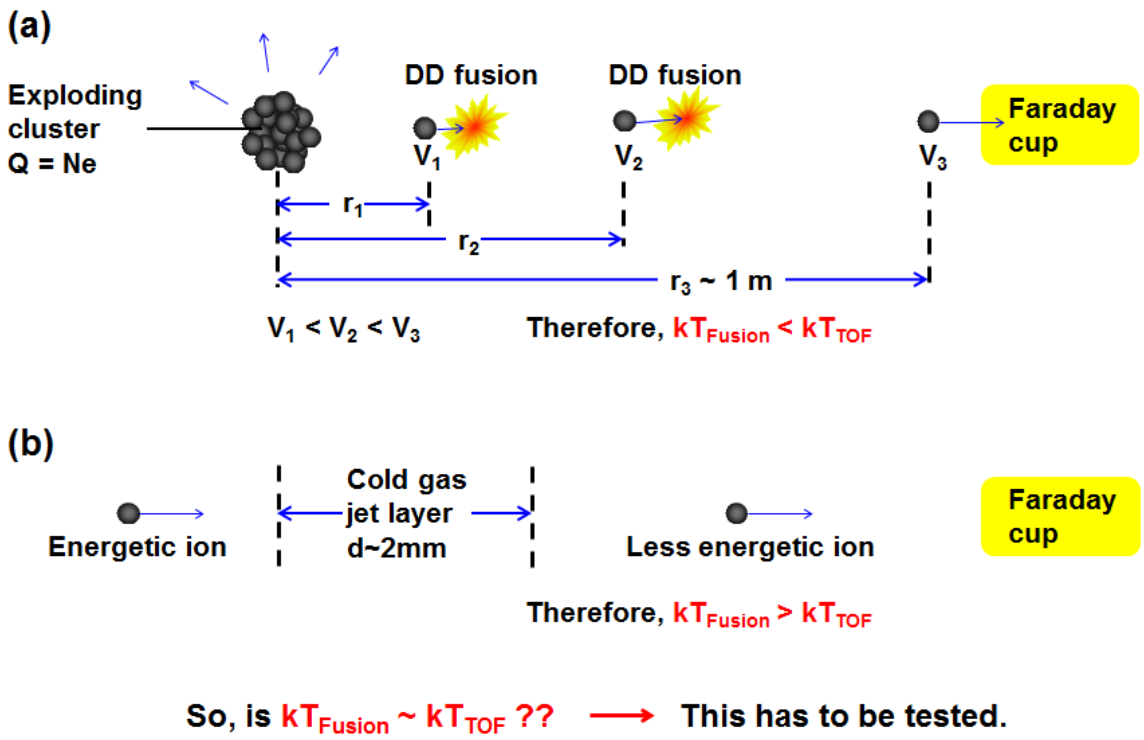

Figure 72. (a) A possible scenario that can result in higher ion temperature measurement (kT_{TOF}) than the actual ion temperature of the fusion plasma (kT_{Fusion}), and (b) a different scenario that can result in the opposite case are illustrated in the figure.

Since the ions are accelerated outward due to the repulsive Coulomb force of the ions, v_1 is smaller than v_2. For the same reason, v_2 is smaller than v_3. Since $v_1<v_2<v_3$ and the Faraday cup measures the average speed (~ v_3), the average kinetic energy of the ions seen by the Faraday cup will be always higher than the kinetic energy of the ion at r_1 or r_2.

In other words, we can summarize this as

$$kT_{Fusion} < kT_{TOF}, \tag{7.1}$$

where kT_{Fusion} corresponds to the relevant ion temperature of the fusion plasma and kT_{TOF} is the ion temperature measured from the ion TOF measurements.

In Figure 72 (b), a different scenario is illustrated. In cluster fusion experiments, the hot fusion plasma is surrounded by a cold gas jet background layer. This is discussed in earlier chapters, and we estimated the beam-target contribution in Chapter 2.

In this situation, an energetic deuterium ion coming from the hot plasma loses its kinetic energy while it penetrates the cold gas jet layer. This energy loss can be up to several keV as we have seen from SRIM calculations in Chapter 2.

Therefore, it would be legitimate to say that the average kinetic energy measured at the Faraday cup would be always smaller than the relevant ion temperature for the fusion reactions. In other words, we expect the opposite relation:

$$kT_{Fusion} > kT_{TOF}. \quad (7.2)$$

Based on the inequalities, (7.1) and (7.2), one might claim that kT_{Fusion} would be close to kT_{TOF}. However, this is improper reasoning, and the relationship has to be checked experimentally.

We therefore sought a temperature measurement that uses the fusion products themselves to directly determine the plasma temperature during the fusion reactions. This is possible by introducing a gas mixture of D_2 and ^{3}He. The resulting D(D, ^{3}He)n and ^{3}He(d, p)^{4}He fusion reactions generate 2.45 MeV neutrons and 14.7 MeV protons, respectively, which are energetic enough not to thermalize en-route to detection.

An illustration that describes this situation is shown in Figure 73. Since the ^{3}He does not form clusters at liquid nitrogen temperature, the ions would remain cold because the high kinetic energy gain from the laser-cluster interactions is not possible. In Chapter 4, a series of Rayleigh scattering measurements proved that the cluster formation of deuterium was not significantly affected when ^{4}He gas was added into the deuterium gas target. We concluded that the cluster formation of deuterium would not be affected by the addition of ^{3}He in the mixture cluster fusion experiment.

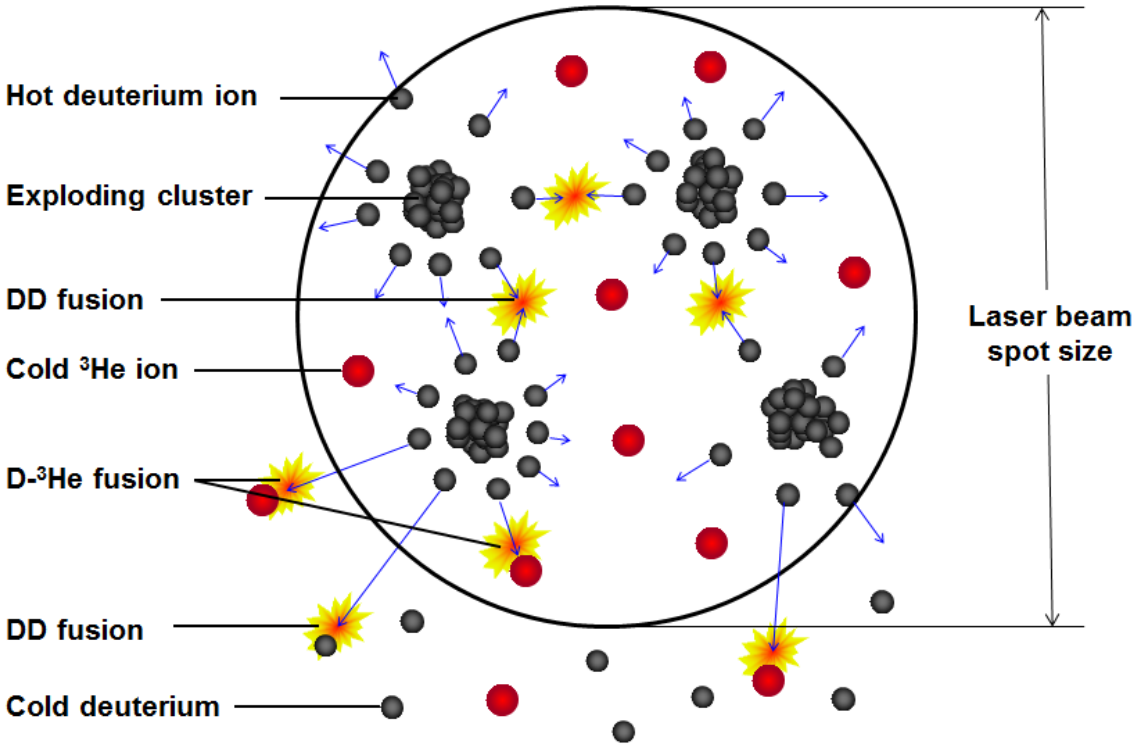

Figure 73. Possible fusion reactions between the constituent particles are shown in this illustration. The bigger red spheres indicate cold ^{3}He ions or atoms, and the smaller black spheres represent energetic deuterium ions or cold deuterium atoms.

Therefore, we assume that only the deuterium ions have high kinetic energies. In this chapter, the ion temperature of the fusion plasma always means the ion temperature of the deuterium ions, except in Figure 76. The ion temperature of the deuterium ions is defined as two thirds of their average kinetic energy in the hot plasma.

Possible fusion reactions in the gas jet are summarized in the following:

$$D + D \rightarrow T\ (1.01\ MeV) + p\ (3.02\ MeV)\ (50\%) \quad (7.3a)$$

$$D + D \rightarrow {}^3He\ (0.82\ MeV) + n\ (2.45\ MeV)\ (50\%) \quad (7.3b)$$

$$D + {}^3He \rightarrow {}^4He\ (3.6\ MeV) + p\ (14.69\ MeV)\ (100\%) \quad (7.3c)$$

$$D + T \rightarrow {}^4He\ (3.5\ MeV) + n\ (14.1\ MeV)\ (100\%) \quad (7.3d)$$

Among these possible fusion reactions, we are interested in (7.3b) and (7.3c), from which 2.45 MeV neutrons are generated and 14.7 MeV protons are generated, respectively. Because the two reactions have different cross-sectional dependence on the plasma temperature, their ratio can uniquely determine the plasma temperature at the critical moments when the fusion reactions occur.

This point is illustrated in Figure 74, and explains the benefit of adding ^{3}He gas into the deuterium cluster target. In Figure 74, only the fusion reactions inside the fusion plasma are considered. There can be fusion reactions between the ions inside the hot plasma and the ions at the surrounding background gas jet, and this has to be accounted for in a correct modeling.

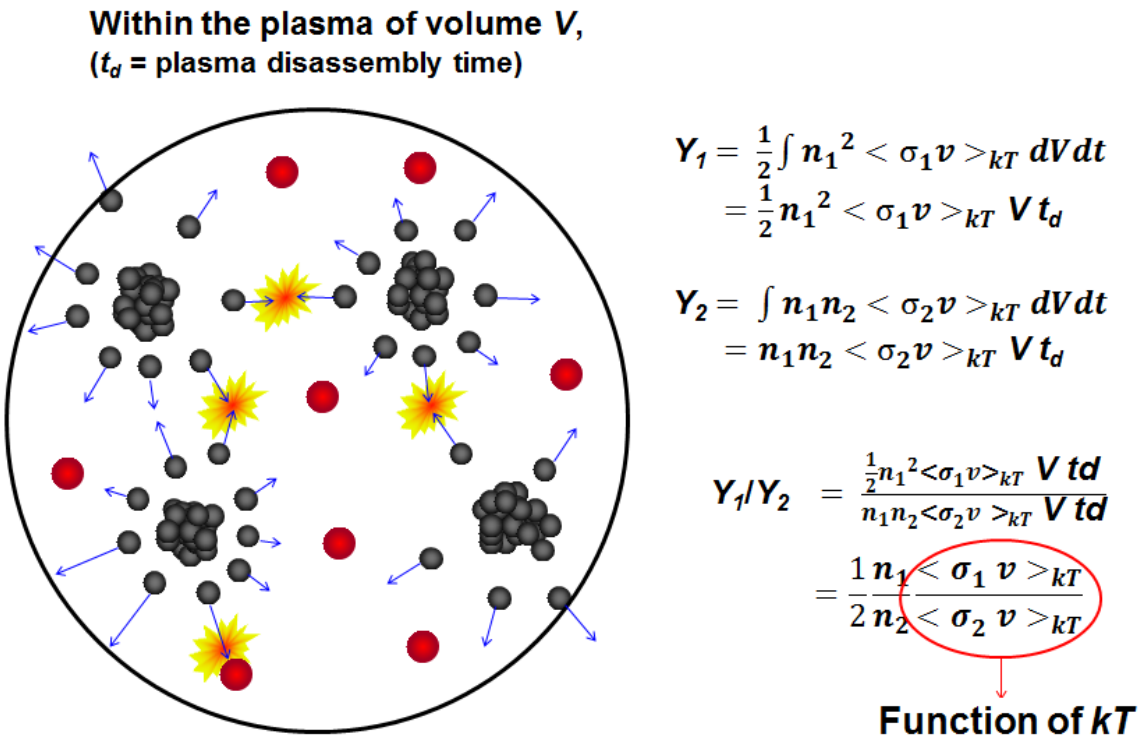

Figure 74. This illustration shows how one can measure the ion temperature of the fusion plasma from the measurements of fusion yields and number densities.

In Figure 74, Y_1 indicates the fusion yield from ion species 1, and Y_2 indicates the fusion yield between ion species 1 and 2. The ion temperature of the fusion plasma is kT, and the fusion reactivity at kT can be calculated for both ion species.

Therefore, by adding ^{3}He, we have two species, and kT is a function of the fusion yields and number density of each species. The ion temperature measured from this process is the relevant ion temperature for the fusion reactions exclusively.

7.2. EXPERIMENTAL SETUP

The laser pulse after the compressor reflects from an f/40 spherical mirror and arrives at the target chamber. The TPW delivered 10–180 J pulse energy during this experiment, and the pulse duration varied from 154 fs to 266 fs.[26] We used cryo-cooled deuterium gas (D_2) + ^{3}He mixture or cryo-cooled deuterated methane gas (CD_4) + ^{3}He mixture as our target.

We controlled the concentration of ^{3}He in the mixture, which was measured before each shot using the residual gas analyzer (RGA). The temperature of the D_2 + ^{3}He mixture target was 86 K, and that of the CD_4 + ^{3}He mixture target was 200–260 K. In both cases, the backing pressure was 770 psi.

We used the same supersonic nozzle with a throat diameter of 790 um described in Chapter 4. The half angle of the nozzle was 5 degrees, and the diameter of the opening was 5 mm. In addition to cooling down the D_2 + ^{3}He gas mixture, we also cooled down the CD_4 + ^{3}He gas mixture because the peak intensity from the TPW was high enough to strip all the electrons from our cluster targets.

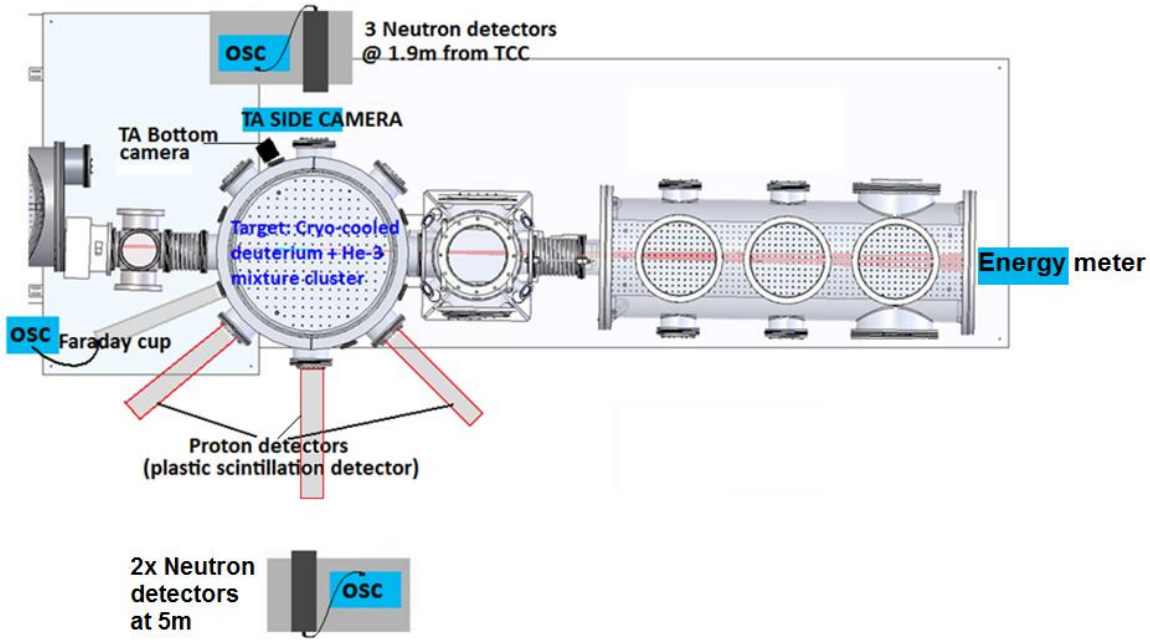

Figure 75. Layout of the target area. The laser comes from the left, and the nozzle is located near the center of the target chamber. Five plastic scintillation neutron detectors and three proton detectors are shown in the figure.

We used OPA shots (~300 m J @ ~0.1 Hz) and optimized the brightness of the filament by changing the backing pressure. We also optimized other timings using the 2.5 Hz OPA beams.

The experimental layout of the target area is shown in Figure 75. For the detection of the neutrons generated from DD fusion reactions, we used five plastic scintillation detectors, all of which were calibrated on THOR prior to this experiment.[28] Three of the five plastic scintillation detectors were located at 1.9 m away from the target chamber, and the other two detectors were located at 5.0 m away from the chamber.

The detectors at 1.9 m used EJ-232Q scintillators for a very fast rise time and accurate TOF measurement, and the other 2 detectors at 5.0 m used EJ-200 scintillators for a higher detection sensitivity along with a fast rise time. We also had 4 NE213

liquid scintillation detectors for low neutron yield measurements, all of which were calibrated on the Cyclotron Institute at Texas A&M University.

For the detection of 14.7 MeV protons from the $^{3}He(d,p)^{4}He$ fusion reactions, we also used plastic scintillation detectors with 1.10 mm thick aluminum degraders. The detectors were located at 1.06–1.20 m from the chamber. We had a total of three such detectors at 45º, 90º, and 135º. Each proton detector consists of a 4.18 cm diameter, 0.254 mm thick BC-400 plastic scintillator and two PMTs on the side of the scintillator.

The 1.1 mm thick aluminum degrader served two purposes. First, it blocked all the other charged particles including 3 MeV protons from DD fusion reactions, and functioned as a blocking filter. Second, it slowed down the 14.7 MeV protons to 4.0 MeV protons, so the protons with reduced kinetic energy transferred all their energy to the thin scintillator disk.

For the detection of 3 MeV protons from DD fusion reactions, we simply changed the degraders to thinner ones. The proton detectors were calibrated at the Cyclotron Institute at Texas A&M University prior to the experiment.

To collect the energetic deuterium ions or carbon ions coming from the plasma filament, we installed a Faraday cup at 1.07 m away from the bottom of the nozzle to perform ion TOF measurements. Assuming 4π radiation of the deuterium ions, we were able to calculate the total number of the deuterium ions generated at the source.

The ion temperature, kT_{TOF}, was calculated from the ion TOF measurements. A negative high voltage (HV) bias of 400 V was applied on the surface of the Faraday cup to repel slow electrons that could affect the ion TOF measurements. A ground mesh was inserted 5 mm before the cup, so the ions were not affected by the HV bias.

The TPW laser beam that was not absorbed by the cluster target went through a beam dump made of a pair of black glass plates. We installed an energy meter behind

this beam dump for a transmitted energy measurement, which was proportional to the actual pulse energy that was not absorbed or scattered.

Two cameras took the images of the plasma filament during the shot. Another camera acquired the mid-field image that represented the actual beam profile on the cluster target, and a fourth camera captured the far field image. We also had a pulse energy measurement and an autocorrelation measurement as our on-shot diagnostics.

Although we did not use it during the experimental campaign, we had another design for proton detectors using CR-39 stacks. This can be useful when the PMTs do not work as expected due to strong EMP noise. Some SRIM calculations concerning this design are shown in Appendix F.

7.3. CLUSTER FUSION MODEL WITH A MIXTURE TARGET

Measuring the 14.7 MeV proton yields as well as the DD fusion neutron yields, we can calculate the ratio of the two different fusion reactions. Because these two reactions have different cross sections, measuring the ratio of the yields of these two reactions allows a precise determination of the plasma temperature at the time when the reactions occurred.

In Figure 76, the fusion reactivity for each reaction is shown in a linear plot. Apparently, the DD fusion reactivity increases much more slowly than the D-^{3}He fusion reactivity as the ion temperature increases. At low ion temperatures (< 16 keV), the DD fusion reactivity is greater than the D-^{3}He fusion reactivity, which can be seen more easily in a log-scale plot.

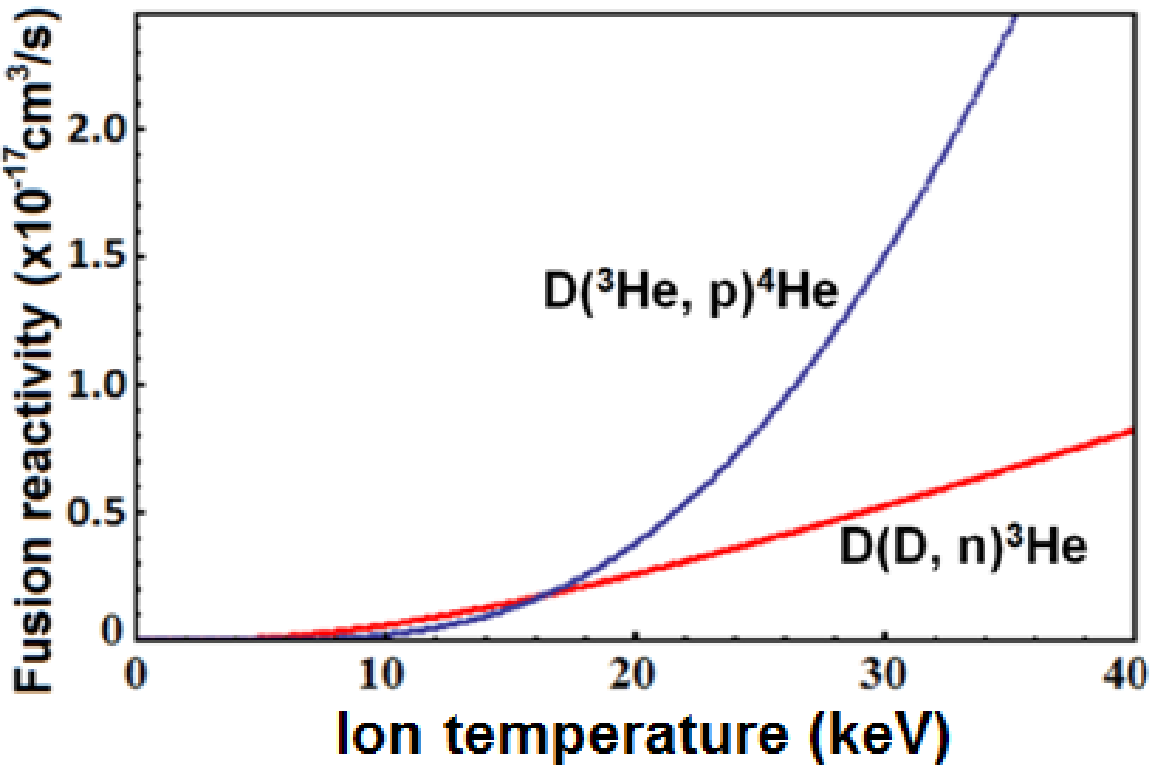

Figure 76. Fusion reactivity of DD fusion reactions and that of D-^{3}He reactions are shown as a function of the ion temperature. In this plot, both ions are assumed to be thermalized.

Let's consider an example: if we detected many more 14.7 MeV protons than 2.45 MeV neutrons with a 1:1 mixture of deuterium + ^{3}He target, it would mean the ion temperature at the time of the fusion reactions was much higher than 16 keV. If, on the other hand, we detected many more neutrons than the 14.7 MeV protons with 1:1 mixture ratio, it would mean that the ion temperature was low when the fusion reactions occurred.

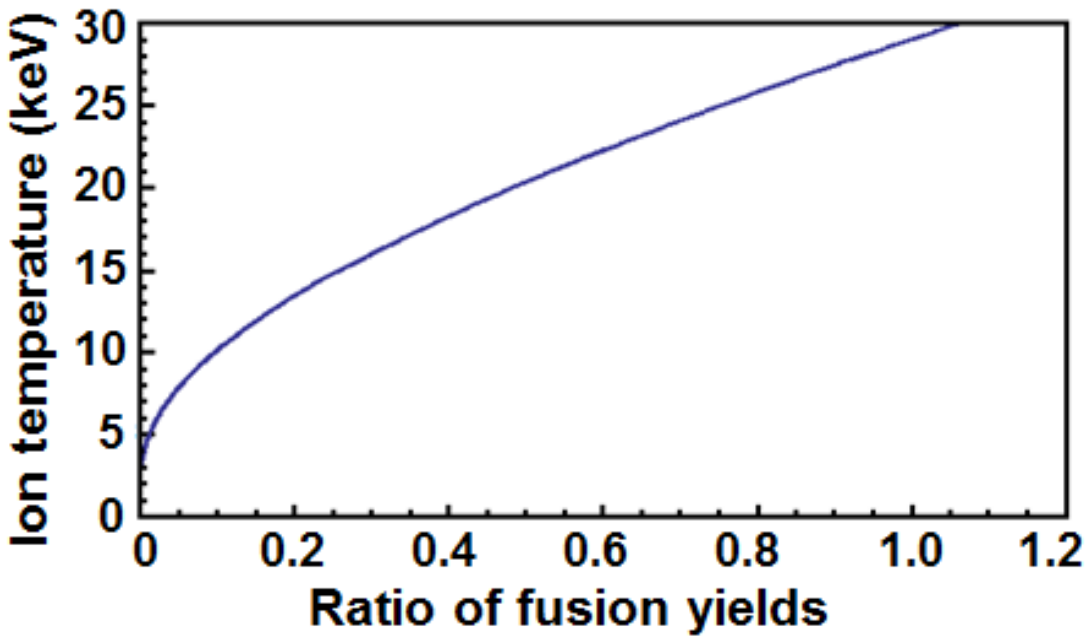

Figure 77. The deuterium ion temperature is plotted as a function of the ratio of fusion yields.

This can be generalized, and we have a plot for the ion temperature as a function of the fusion yields. Figure 77 shows the ion temperature as a function of the fusion yields, where the ratio of the fusion yields is defined as:

$$\text{Ratio of fusion yields} \equiv \frac{(14.7\text{ MeV proton yield})}{(2.45\text{ MeV neutron yield})} \times \frac{(\text{number density of D})}{(\text{number density of He}-3)}. \quad (7.4)$$

The number density of each species can be obtained from the RGA before each shot. Therefore, one can measure the ion temperature of the fusion plasma if one knows the neutron yield and the proton yield at the same time. In Figure 77, the ion temperature indicates only the ion temperature of the energetic deuterium ions. The ^{3}He ions are considered cold in our model.

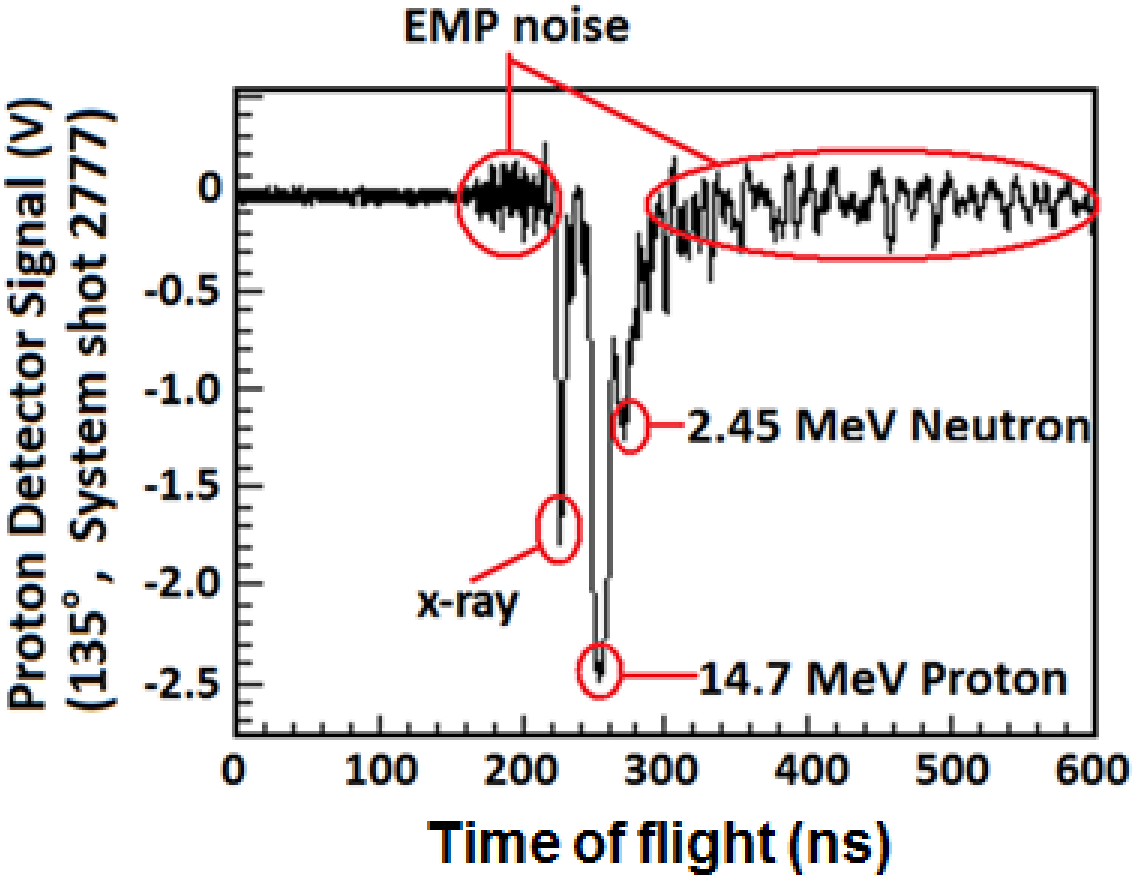

Figure 78. The oscilloscope trace from a proton detector at 135 degrees on system shot 2777.

We used mixture clusters as our target. With both the energetic deuterium ions from Coulomb explosion and cold background ^{3}He ions inside the filament, we observed ^{3}He(d,p)^{4}He fusion reactions as well as DD fusion reactions. The signature of the ^{3}He(d,p)^{4}He fusion reaction is one 14.7 MeV proton from each reaction.

In Figure 78, an example of the proton signal is shown. The initial ringing comes from the EMP noise, and the second peak indicates the initial x-ray peak. About 25 ns after the x-ray peak, a bigger 14.7 MeV proton peak is shown in the figure. The

3 MeV protons are blocked from the degrader. On this shot (system shot 2777), a distinguishable neutron peak was visible on the proton detector.

The detection of neutrons from a proton detector implies that we can use one scintillation detector setup to measure both proton yield and the neutron yield, in principle. Since we had calibrated neutron detectors installed at 1.9 m and 5.0 m already, we did not use this neutron signal for the neutron yield. However, this data definitely shows a possibility of designing a single detector for both proton and neutron yield measurements.

Before proceeding with the measurements of 14.7 MeV proton yields, we verified whether the proton detectors worked as expected. This time, the target was only deuterium clusters, and we knew from (7.3a) and (7.3b) that equal number of 2.45 MeV neutrons and 3 MeV protons were expected from the fusion reactions. Then, we compared the measured 3 MeV proton yield with the 2.45 MeV neutron yield.

Within our measurement errors, we observed a linear relationship between the two yields, and confirmed that the measured proton yields agreed with the neutron yields. The result is shown in Figure 79, where the red line indicates the expected result.

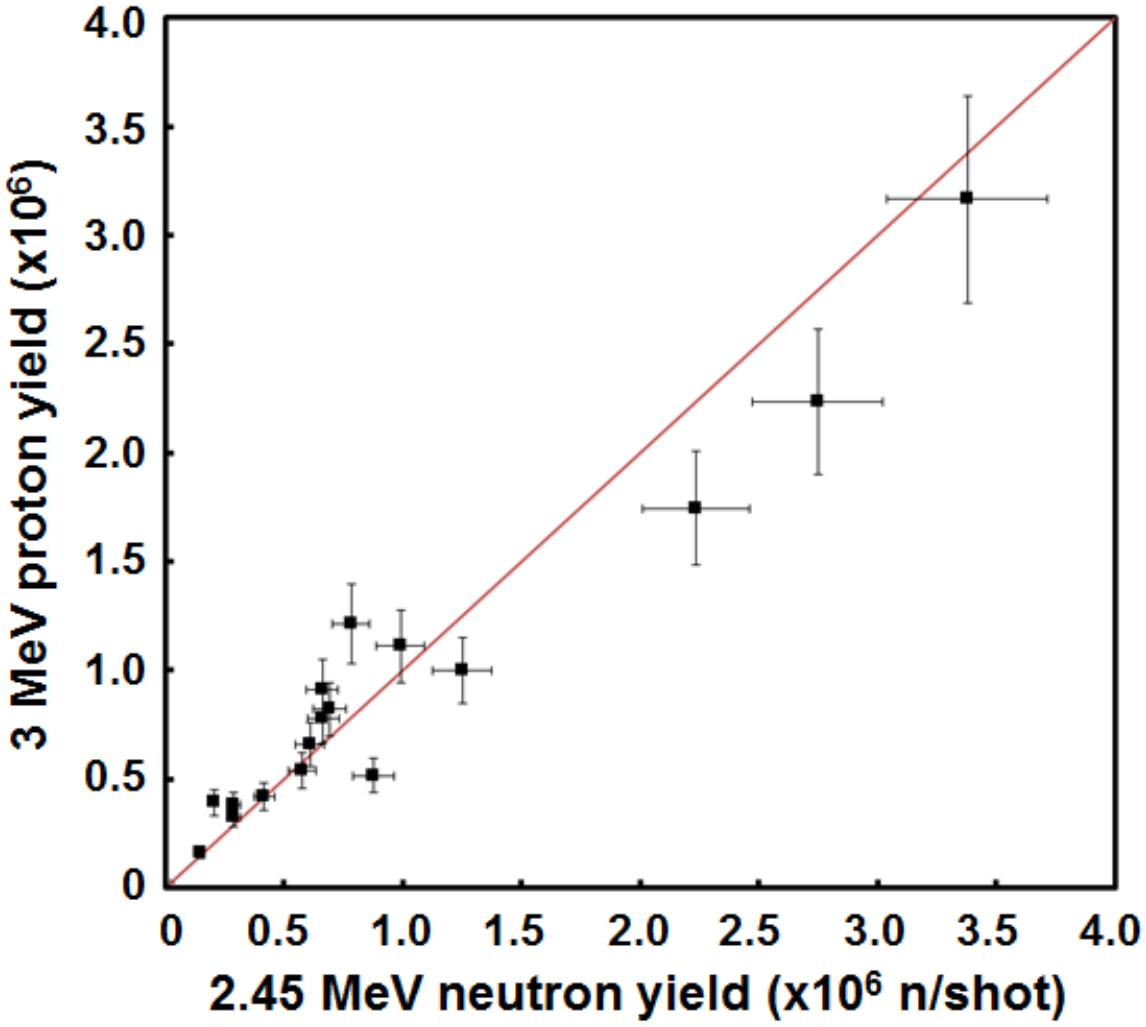

Figure 79. 3 MeV proton yield vs. 2.45 MeV neutron yield is shown. The straight red line indicates when both yields are the same.

In Figure 80, the ion temperature is plotted as a function of the ratio of fusion yields, where the ratio is defined as in equation (7.4). Solid blue circles indicate the ion temperature measurements with D_2 + ^{3}He mixture target while red triangles indicate the measurements with CD_4 + ^{3}He mixture target.

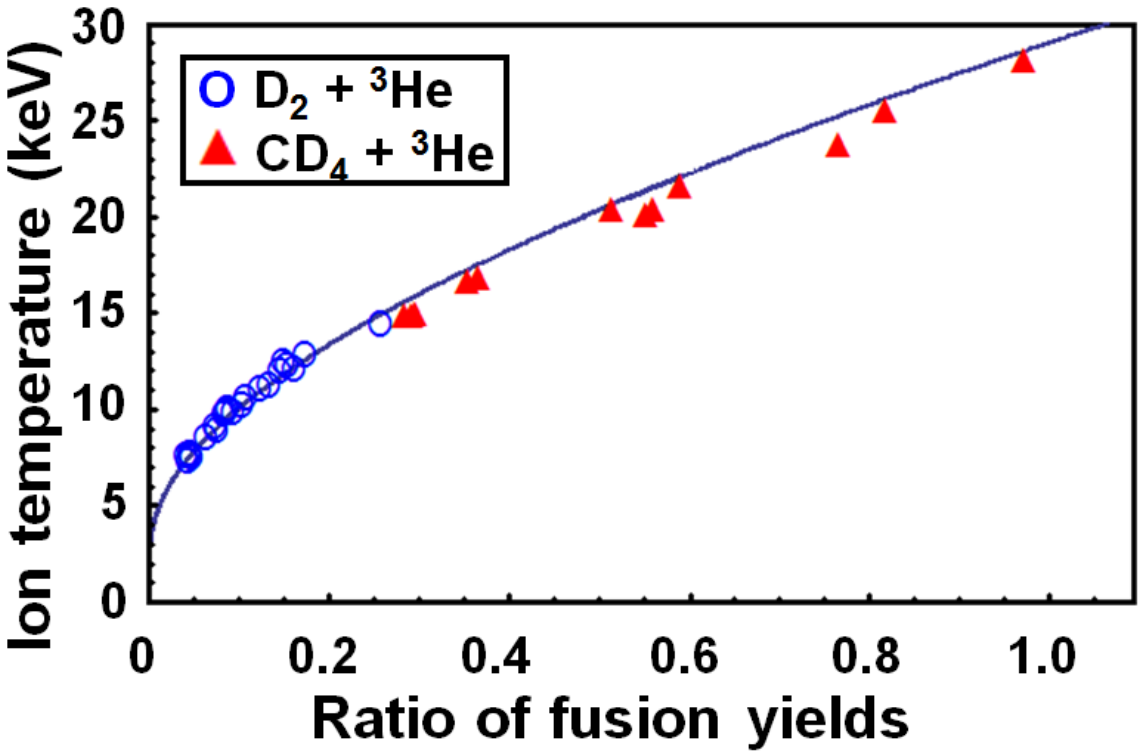

Figure 80. The ion temperature of deuterium, kT_{Fusion}, was measured from the ratio of fusion yields.

In Figure 80, the measured ion temperature lies slightly off the solid line because a different filament size, r, results in slightly different ion temperature. To calculate the ion temperature of deuterium, kT, from the measured fusion yields, I used the following formula.

$$\frac{(14.7\text{ MeV proton yield})}{(2.45\text{ MeV neutron yield})} = \frac{N_{ion}\times n_{He-3}\langle\sigma_v\rangle_{D(He-3,p)He-4,\ \frac{3}{5}kT}\times R}{N_{ion}\times n_D[\frac{1}{2}\langle\sigma v\rangle_{D(d,n)He-3,\ kT}\times\frac{r}{\langle v\rangle_{kT}}+\ \langle\sigma_v\rangle_{D(d,n)He-3,\ \frac{1}{2}kT}(R-r)\ ]} = \frac{\frac{n_{He-3}}{n_D}\langle\sigma_v\rangle_{\frac{3}{5}kT}R}{[\frac{1}{2}\langle\sigma v\rangle_{kT}\times\frac{r}{\langle v\rangle_{kT}}+\ \langle\sigma_v\rangle_{\frac{1}{2}kT}(R-r)\ ]}, \quad (7.5)$$

where N_{ion} is the total number of energetic deuterium ions, $n_{He\text{-}3}$ is the number density of ^{3}He, n_D is the number density of deuterium, R=2.5 mm is the radius of the gas jet, r is the

radius of the plasma filament, and $\langle v \rangle$ is the mean speed of the hot deuterium ions. A uniform atomic density was assumed throughout the gas jet for both ^{3}He and deuterium.

In this model, the size of the filament on each shot is used to get the beam-beam contribution and the beam-target contribution for the DD fusion. The plasma disassembly time is estimated as $r/\langle v \rangle_{kT}$, and the beam-target contribution happens only outside of the fusion plasma. This explains the length (R-r) instead of R in the denominator.

On a few system shots with cryo-cooled CD_4 + ^{3}He mixture target, deuterium ions with ion temperature higher than 20 keV were observed. We also observed that the deuterated methane cluster mixture showed higher ion temperature than the deuterium cluster mixture.

The deuterium ion temperature calculated using the equation (7.5), kT_{Fusion}, is shown in Figure 80 and corresponds to the actual ion temperature of the fusion plasma at the time of the fusion reactions. We compared this temperature with the ion temperature from the ion TOF measurements. Figure 81 shows the comparison between the two ion temperatures.

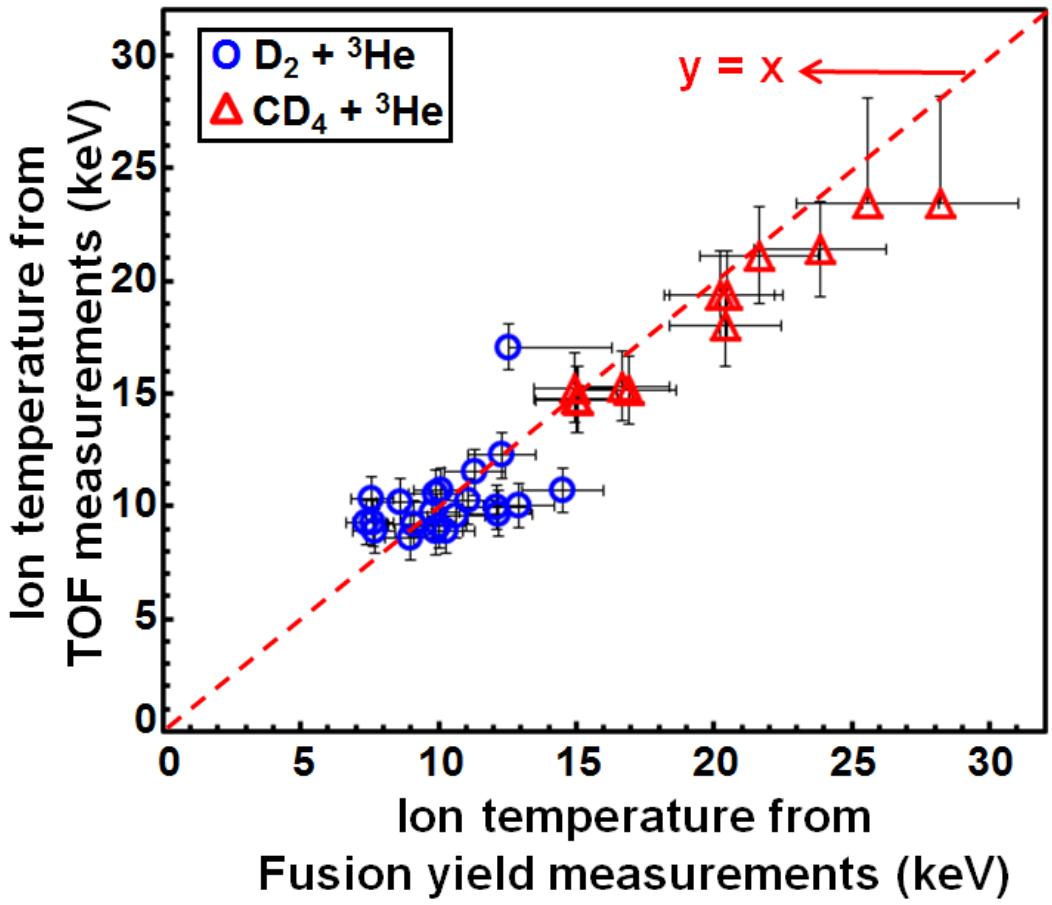

Figure 81. kT_{TOF} vs. kT_{Fusion}. The dashed red line indicates a line with y=x.

In general, the kT_{Fusion} was higher than the kT_{TOF}. However, we do see a linear relationship between the two independent temperature measurements. The fact that kT_{Fusion} is higher than the temperature from TOF measurements implies that the ions lost their kinetic energy while they passed through the cold background gas jet layer. This was discussed in section 7.1, and corresponds to the scenario described in Figure 72 (b).

The error bars are approximate. Ten percent errors were assumed on most of the data except for a few shots. The Faraday cup was capable of measuring ion temperatures only up to 23 keV because of the initial x-ray peak. For those shots, 20% positive errors were assumed in the vertical direction.

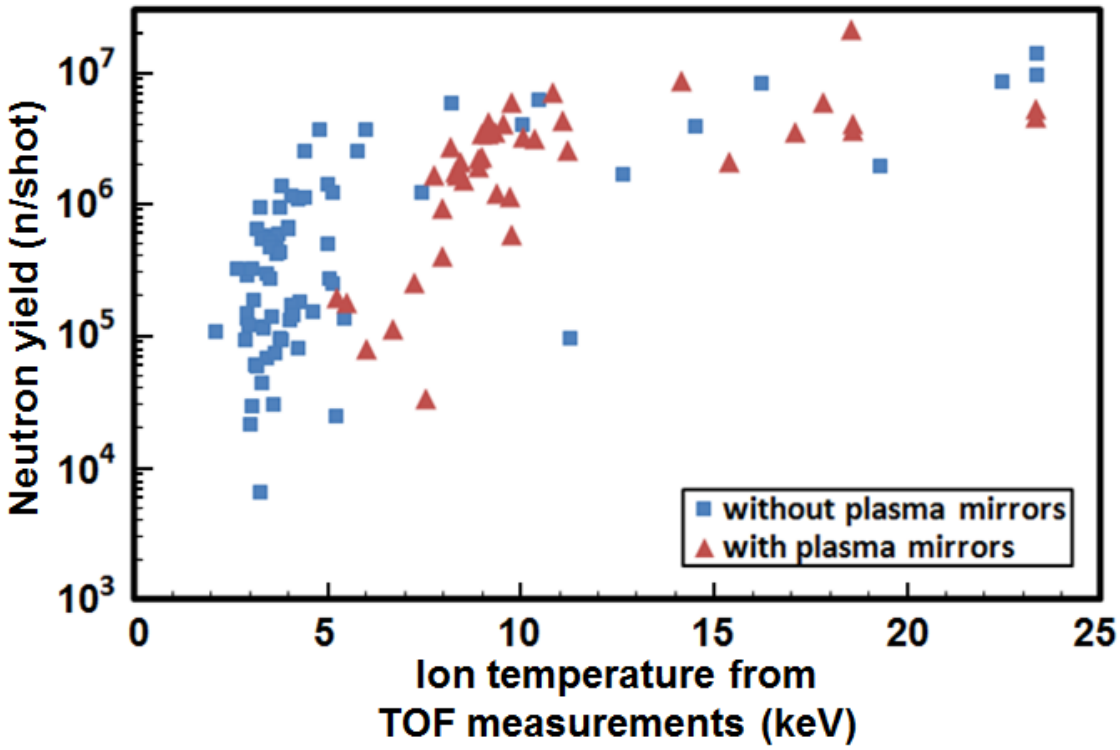

Figure 82. Neutron yield is plotted as a function of the deuterium ion temperature measured from the Faraday cup.

Now that we have a valid measurement of the ion temperature, and verified the temperature from ion TOF agreed with the temperature from the ratio of fusion yields, we can compare the neutron yield with the ion temperature from ion TOF measurements.

Figure 82 shows the neutron yield as a function of the deuterium ion temperature measured from the Faraday cup. System shots with plasma mirrors are shown as solid red triangles while system shots without plasma mirrors are shown as solid blue squares.

Though the neutron yield also depends on other gas jet parameters such as the radius of the plasma, the number of ions, and the number density of deuterium ions, the neutron yield in Figure 82 shows a strong dependence on the ion temperature from the TOF measurements.

Similar strong dependence was found when we plotted the neutron yield as a function of the ion temperature measured from the fusion yields. Figure 83 shows the relationship between the neutron yield and the ion temperature for system shots with mixture cluster targets.

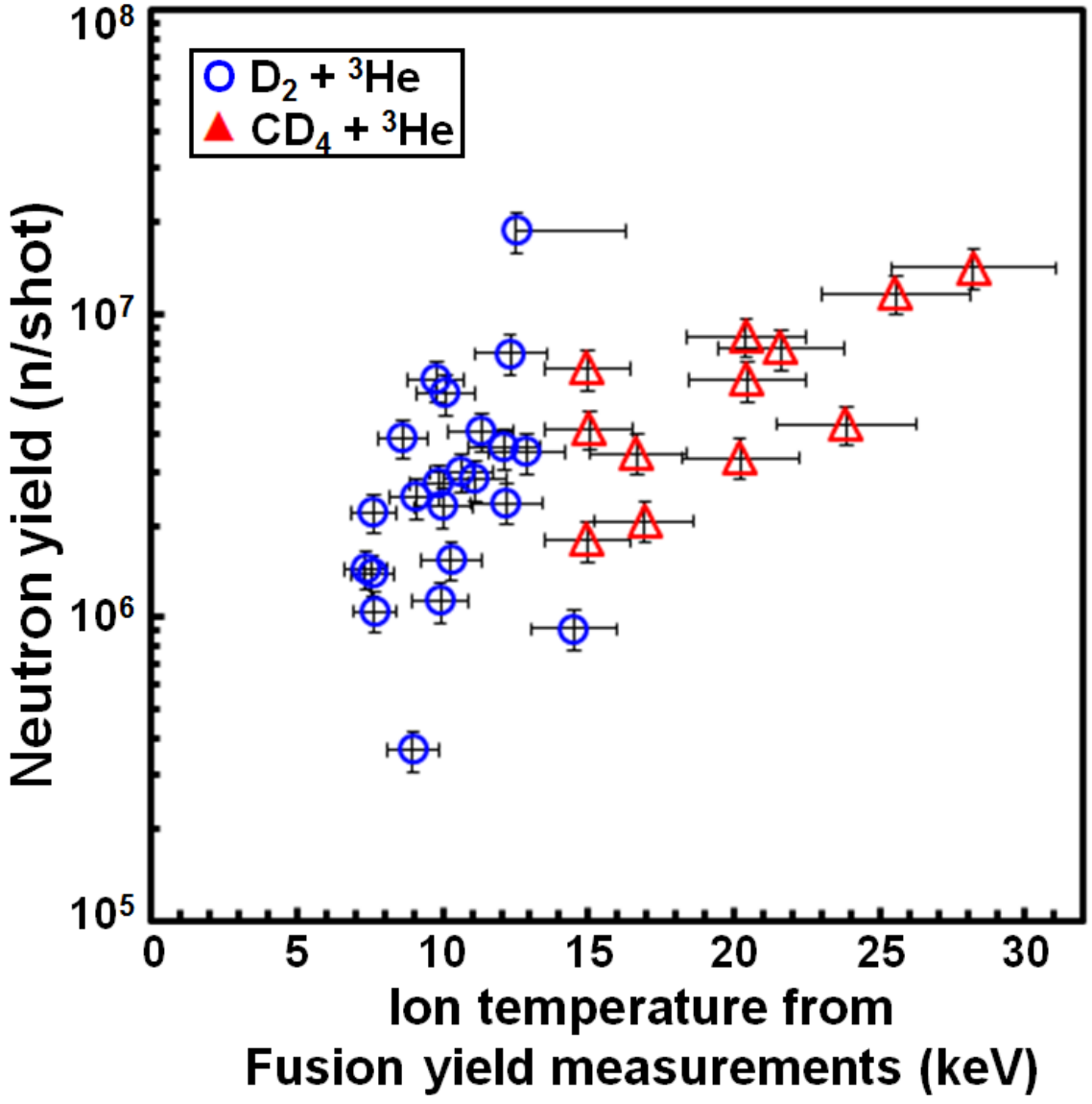

Figure 83. Neutron yield is plotted as a function of the ion temperature from the fusion yield measurements.

7.5. CONCLUSION

PW irradiation of a cryo-cooled CD_4 cluster + ^3He mixture gas jet has produced 28 keV deuterium ion temperatures and more than 10^7 fusion neutrons per shot. With mixture cluster targets, we successfully measured the ion temperature at the time of fusion reactions using the ratio of fusion yields. We observed a linear relationship between this temperature and the ion temperature measured from ion TOF measurements.

Chapter 8. Conclusion

The interaction of intense, femtosecond laser pulses with van der Waals bonded atomic clusters leads to very efficient energy absorption. This allows the laser to produce plasma with ion temperature higher than a few keV.

When an energetic deuterium ion collides with another deuterium ion, a nuclear fusion reaction can occur, generating a 2.45 MeV neutron. By shooting cryogenically cooled deuterium clusters with the TPW, we were able to observe nuclear fusion reactions happening inside our target chamber.

The most readily measured signature of DD fusion comes from one branch of the fusion reaction, $D + D \rightarrow He^3 + n$, in which a neutron carries 2.45MeV kinetic energy. The number of these monoenergetic neutrons produced at the source was measured using the plastic scintillation detectors that had been calibrated on THOR laser.

One of our driving goals of this research has been to produce a nanosecond quasi-monoenergetic neutron source that is strong enough to be used for radiography or material damage studies. By adjusting the distance from the focus to the cluster target, we produced deuterium ions with ion temperature higher than 25 keV, and achieved neutron yields as high as 2×10^7 neutrons per shot on the TPW.

The simulation results in Chapter 2 with observed parameters during the experimental campaign suggest that we can expect to achieve neutron yields as high as 10^8 neutrons per shot after some optimization process. This high flux of fast and nearly monoenergetic neutrons will allow us to do neutron-induced material damage studies in the future.

For the first time, time-resolved neutron damage experiments might be possible. There have been many molecular dynamics simulation results suggesting that neutron damage takes place on a 10 to 1000 ps time scale.

With our current understanding of the cluster fusion experiments, I showed the neutron production as a function of time in Chapter 2, which shows a fusion burn time on the order of 1 ns. With our nanosecond monoenergetic neutron source, we will be able to do pump-probe experiments and test if the simulation results match the experimental data.

In the future experiment, the nanosecond neutron pulse will drive damage in a material which will be probed by a synchronized laser pulse at a later time. By controlling the time delay between the neutron pulse and the probe laser beam, we can take snapshots of the neutron damage process and possibly subsequent annealing process. These damage studies have a broad importance including the study of materials to be used in future fusion reactors.

During the D_2 cluster + ^{3}He mixture fusion experiments, we observed D-^{3}He fusion reactions as well as DD fusion reactions. From the measurements of the 2.45 MeV neutron yields and 14.7 MeV proton yields, we were able to determine the ion temperature of the fusion plasma at the time of fusion reactions.

With cryo-cooled CD_4 cluster + ^{3}He mixture target, we observed deuterium ions with ion temperature as high as 28 keV. The ion temperature measured from TOF measurements agreed with the ion temperature measured from the ratio of fusion yields.

Appendices

APPENDIX A

In this table, the calculation results using SRIM[50] code for the energy loss of deuterium ions after passing through 2.5 mm thick gas jet are shown. The table shows the ion temperature of the transmitted ions as a function of the temperature of the incident ions. A uniform gas density of 10^{19} atoms/cm^3 was assumed throughout the gas jet layer of 2.5 mm.

Incident particle energy (keV)	Average kinetic energy after transmission (keV)	Standard deviation (keV)
1	0.00	0.00
2	0.23	0.18
3	0.38	0.30
4	0.60	0.40
5	0.97	0.52
6	1.47	0.62
7	2.03	0.67
8	2.64	0.70
9	3.27	0.72
10	3.92	0.74
11	4.58	0.75
12	5.27	0.75
13	5.97	0.77
14	6.68	0.76
15	7.38	0.79
16	8.12	0.79
17	8.87	0.79
18	9.62	0.78
19	10.37	0.81
20	11.14	0.83
21	11.91	0.80
22	12.70	0.81
23	13.48	0.82
24	14.28	0.81
25	15.08	0.82

26	15.89	0.82
27	16.71	0.82
28	17.53	0.82
29	18.34	0.87
30	19.17	0.82
31	20.02	0.83
32	20.87	0.81
33	21.69	0.88
34	22.56	0.89
35	23.40	0.84
36	24.27	0.83
37	25.11	0.90
38	26.00	0.82
39	26.87	0.84
40	27.73	0.85
41	28.59	0.86
42	29.47	0.86
43	30.35	0.81
44	31.25	0.82
45	32.13	0.83
46	33.03	0.86
47	33.91	0.80
48	34.80	0.92
49	35.71	0.87
50	36.60	0.94
51	37.51	0.81
52	38.41	0.88
53	39.30	0.88
54	40.22	0.88
55	41.13	0.98
56	42.04	0.89
57	43.06	0.82
58	43.96	0.91
59	44.90	0.94
60	45.81	1.04
61	46.75	0.88
62	47.67	0.94
63	48.60	0.95

64	49.54	0.85
65	50.46	0.82
66	51.40	0.93
67	52.36	0.86
68	53.29	0.86
69	54.24	0.95
70	55.18	0.80
71	56.11	0.83
72	57.08	0.81
73	58.03	0.82
74	58.98	0.80
75	59.93	0.85
76	60.90	0.83
77	61.83	0.88
78	62.80	0.80
79	63.74	1.06
80	64.71	0.88
81	65.68	0.95
82	66.63	0.86
83	67.61	0.81
84	68.56	0.92
85	69.53	0.92
86	70.53	0.81
87	71.49	0.95
88	72.46	0.81
89	73.43	0.87
90	74.40	0.84
91	75.38	0.85
92	76.36	0.81
93	77.34	0.84
94	78.33	0.81
95	79.30	0.84
96	80.28	0.87
97	81.26	0.85
98	82.26	0.86
99	83.23	0.80
100	84.23	0.80
110	94.13	0.82

120	104.13	0.82
130	114.18	0.83
140	124.31	0.84
150	134.46	0.82
160	144.66	0.82
170	154.87	0.86
180	165.10	0.90
190	175.37	0.82
200	185.62	0.86
250	236.97	0.82
300	288.20	0.82
1000	995.14	0.78

APPENDIX B

I modified the code a little bit, and considered the fraction of hot ions inside the cold background region. In Figure 84, the beam-target contribution starts from 0 ns because some of the hot ions at the bouFigure 84ndary of the plasma start interacting with the cold gas jet immediately.

```
NeutronProduction3[Nion_, kT_] :=
 Module[{N0 = Nion, N, T = kT, dY = 0, YieldBeamTarget = 0, dYieldBeamTarget = 0, Y = 0, nD, nD0 = 10^19,
   v, fs = 10^-15, n = 1, L0 = 0.5, R0, R, L, t = 0, S = 0, timeinterval, list1}, N = N0;
  R0 = Sqrt[N0 / (nD0 * Pi * L0)]; timeinterval = 10 000 fs; list1 = {{t, dY}};
  (* N0= number of total D ions in the filament, nD=average deuterium density in cm^3 at time t,
  nD0=initial average deuterium density in cm^3 at time 0,
  sigmavBOSCH is in cm^3/s,
  R=radius of the expanding filament at time t in cm, R0=initial radius of the filament at time 0 in cm,
  L=length of the expanding filament at time t in cm, L0=initial length of the filament at time 0 in cm,
  v=mean speed of D ions with kT [keV] in cm/s,
  dY= total number of neutrons produced until t,
  Mean free path of 10 keV ions with 10^19 cm^-3 density = 5.45mm *)
  While[n < 5*10^6*fs/timeinterval, t = n*timeinterval;
   (* I assumed uniform ion density with kT [keV] at t=0. *)
   S = StoppingPower[3/2*T];
   v = AVGv1[T]; (* mean speed [cm/s] of D ions with kT [keV]. *)
   L = L0 + 2*v*t; R = R0 + v*t;
   If[v*t < 0.25 - R0, T = T - S*2/3*v*timeinterval*(R^2*If[L > 0.5, 0.5, L] - R0^2*L0) / (R^2*L)];
   (* Energy loss due to background atoms, thickness=0.25 cm. For R0+vt<2.5mm,
   N*(R^2*If[L>0.5,0.5,L]-R0^2*L0)/(R^2*L) ions are in the background gas jet.  There are
    very few cold atoms inside the original filament volume of Pi*R0^2*L0. *)
   If[0.25 > v*t > 0.25 - R0, T = T - S*2/3*v*timeinterval*((0.25^2*0.5 - R0^2*L0) / (R^2*L))];
   (* If R0+vt>0.25, then some ions already escaped the gas jet layer. The factor
    ((0.25^2*0.5-R0^2*L0)/(R^2*L)) estimates the fraction of hot ions that are still inside the gas jet.
   nD = N/(Pi*R^2*L); (* Average atomic density of deuterium in cm^3 *)
   dY = 1/2*N*nD*timeinterval*sigmavBOSCH[T];
   (* Number of neutrons produced during t ~ t+timeinterval *)
   (*If[R0<v*t<0.25,dYieldBeamTarget=N*nD0*AVGsigma[T/2]*v*timeinterval,dYieldBeamTarget=0];*)
   If[v*t < 0.25 - R0, dYieldBeamTarget = (R^2*If[L > 0.5, 0.5, L] - R0^2*L0) / (R^2*L)*N*nD0*
      AVGsigma[T/2]*v*timeinterval,
    If[v*t < 0.25, dYieldBeamTarget = ((0.25^2*0.5 - R0^2*L0) / (R^2*L))*N*nD0*AVGsigma[T/2]*
       v*timeinterval, dYieldBeamTarget = 0]];
   (* (R^2*If[L>0.5,0.5,L]-R0^2*L0)/(R^2*L)*N was used instead of N since not all the hot
    ions are in the cold background region. For the same reason, for 0.25-R0< vt<0.25,
   ((0.25^2*0.5-R0^2*L0)/(R^2*L)) was multiplied to get the fraction of hot ions inside the gas jet. *)
   Y += dY + dYieldBeamTarget; (* Neutron Yield *)
   YieldBeamTarget += dYieldBeamTarget; (* Beam Target Contribution only *)
   N = N - 2*dY - YieldBeamTarget; (* The total number of hot D ions after the fusion reactions at time t *)
   AppendTo[list1, {t, Y}]; n++];
  Print["Total Yield = ", Y, " (n/shot)     Ion temperature after passing through the gas jet = ",
   T, " keV"]; Print["Beam Target Contribution =", YieldBeamTarget, " (n/shot) "];
  list1]
```

```
Last[NeutronProduction3[10^16, 10]][[2]]
```

Total Yield = 9.60803×10^6 (n/shot) Ion temperature after passing through the gas jet = 6.51061 keV

Beam Target Contribution =4.55347×10^6 (n/shot)

9.60803×10^6

```
Show[Yield3, Yield3BB, Yield3BT, intersectY3]
```

Total Yield = 9.60803×10^6 (n/shot) Ion temperature after passing through the gas jet = 6.51061 keV

Beam Target Contribution =4.55347×10^6 (n/shot)

Total Yield = 9.60803×10^6

Beam Target Contribution =4.55347×10^6

Total Yield = 9.60803×10^6

Beam Target Contribution =4.55347×10^6

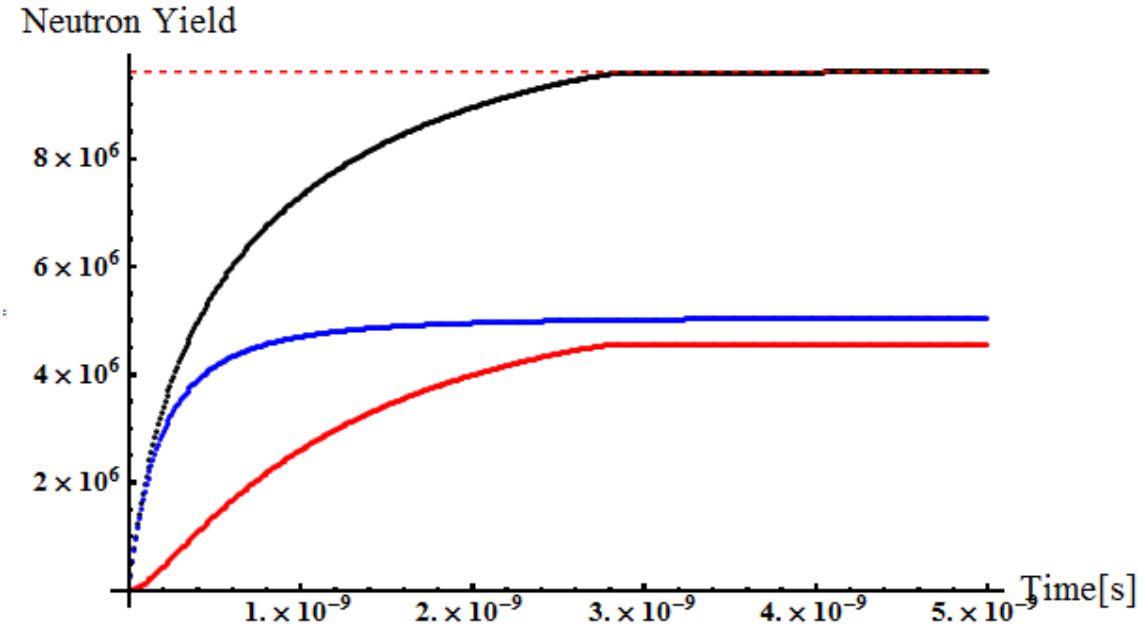

Figure 84. Total neutron yield as a function of time along with the beam-beam contribution and the beam-target contribution (w/ modified code).

APPENDIX C

Hamamatsu PMT	R1617	R2228	R928	R3788
Price (PMT + socket)	$805	$1,378	$878	$591
Photocathode	Multi-alkali (500K)	Multi-alkali (501K)	Multi-alkali (562U)	Bi-alkali (452U)
Cathode sensitivity at 633nm (mA/W)	20	37	41	13
Quantum efficiency at 633nm	4%	7%	8%	2.5%
Spectral response	300~850nm	300~900nm	185~900nm	185~750nm
Gain	1.0×10^{6}	7.5×10^{5}	1.0×10^{7}	1.0×10^{7}
Rise time	2.5ns	15ns	2.2ns	2.2ns
PMT Housing			Included (Thorlabs, $96)	Included (Thorlabs, $96)
Lead time	3~4 weeks	3~4 weeks	3~4 weeks	3~4 weeks
Note.		Peak sensitivity at 600nm	High gain and sensitivity	

Table 6. Comparison of a few PMTs for the Rayleigh scattering measurements with a He-Ne laser.

APPENDIX D

Summary of the calibration results of the other 5 neutron detectors

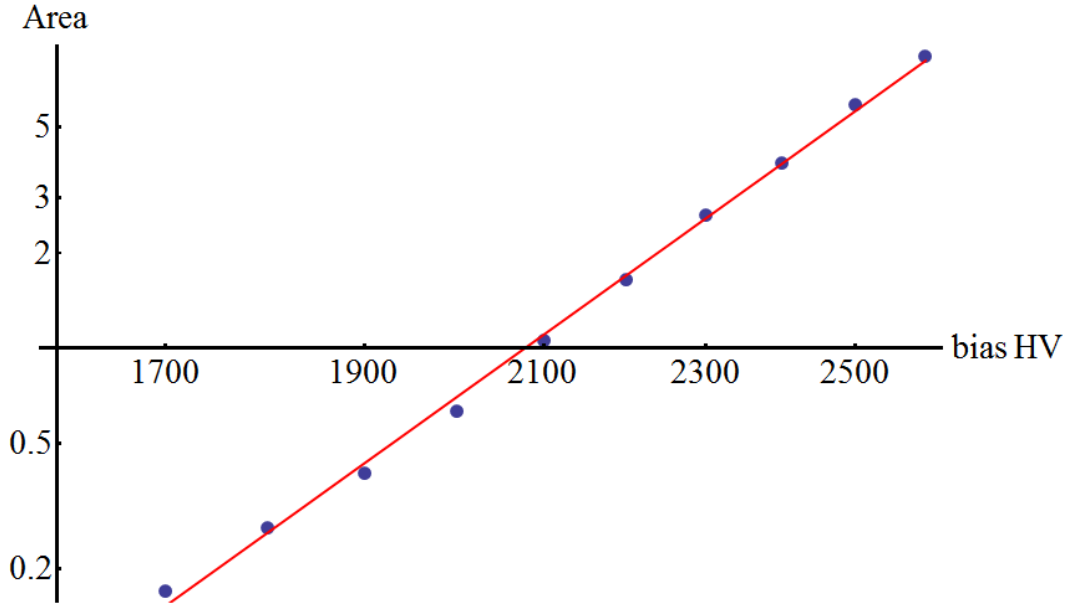

Figure 85. Single neutron event area was measured varying the high voltage bias of the EJ-200 2nd detector (slope=9.4).

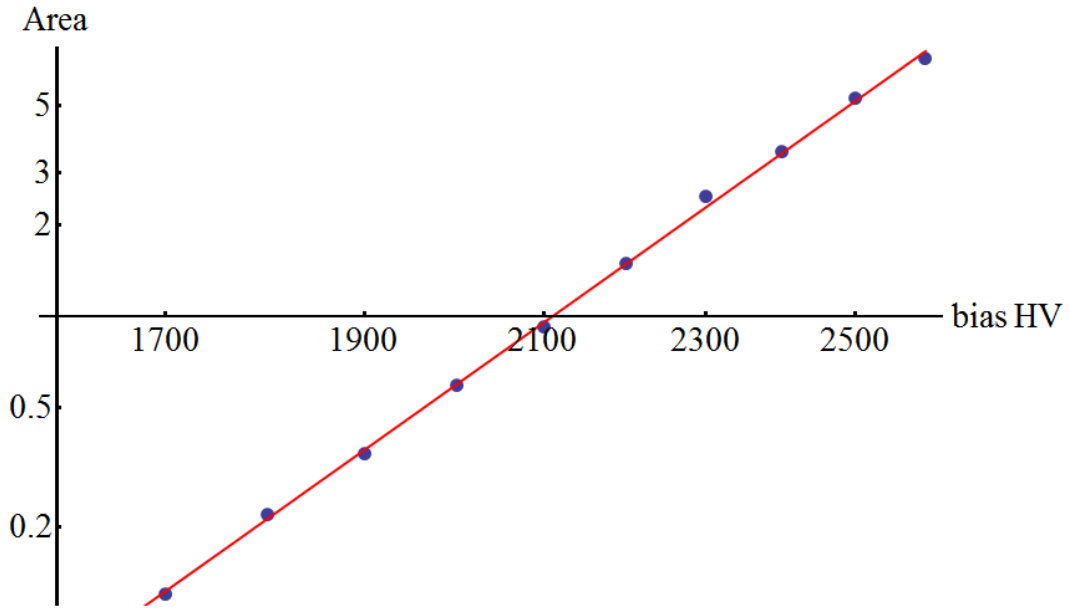

Figure 86. Single neutron event area was measured varying the high voltage bias of the EJ-232Q 1st detector (slope=9.7).

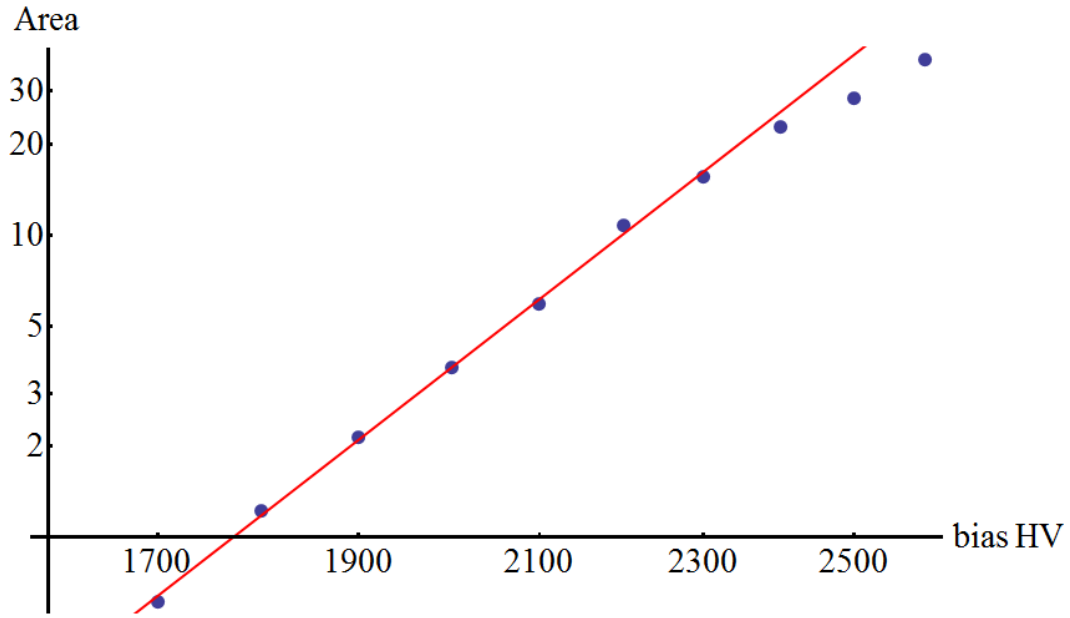

Figure 87. Single neutron event area was measured varying the high voltage bias of the EJ-232Q 2nd detector (slope=10.7).

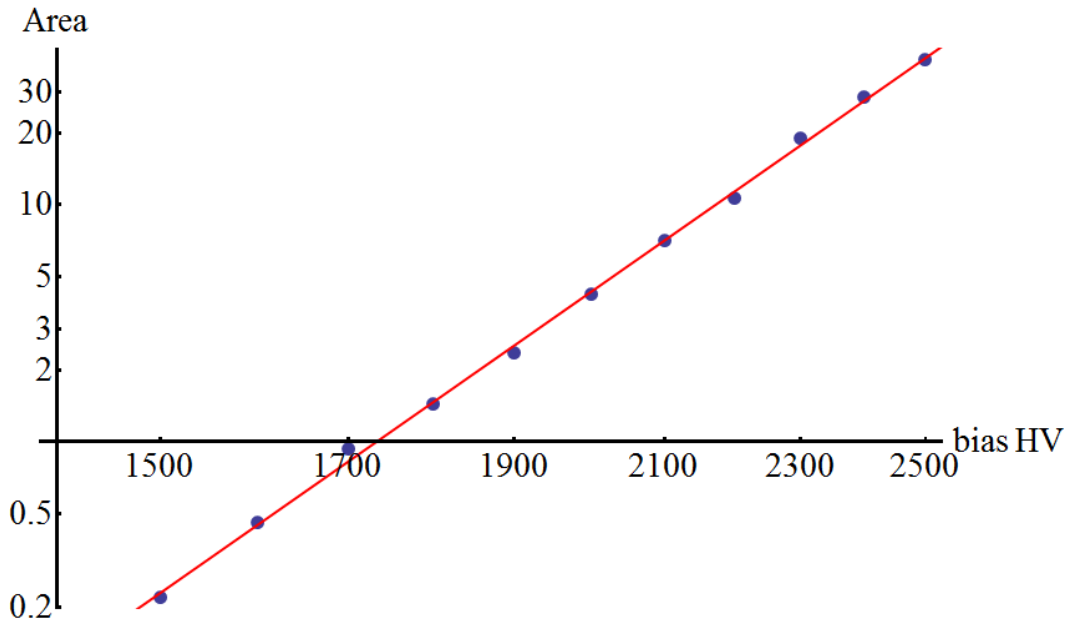

Figure 88. Single neutron event area was measured varying the high voltage bias of the EJ-232Q 3rd detector (slope=10.2).

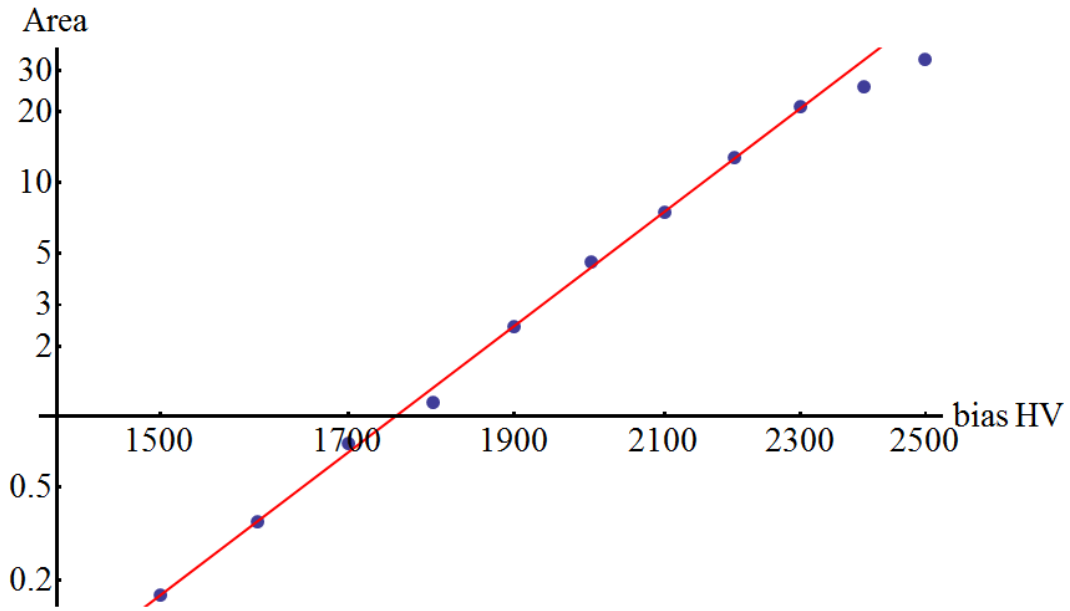

Figure 89. Single neutron event area was measured varying the high voltage bias of the EJ-232Q 4th detector (slope=11.2).

* ; too much noise, **; saturation

HV (volts) EJ-200 1st	Neutron events	Avg. area (Vns)	Avg. peak (V)	Total shots
-1500	361	-0.28	-0.04	7154
-1600	678	-0.50	-0.06	8590
-1700	619	-0.94	-0.11	8209
-1800	445	-1.53	-0.17	3978
-1900	444	-2.68	-0.30	6125
-2000	582	-4.45	-0.50	6569
-2100	324	-7.05	-0.81	6199
-2200	446	-11.37	-1.33	5733
-2300	515	-17.79	-2.13	6021
-2400**	273	-25.80	-3.05	2205
-2500**	262	-36.99	-4.41	2034

Table 7. Single neutron event area vs. HV bias for EJ-200 1st detector.

HV (volts) EJ-200 2nd	Neutron events	Avg. area (Vns)	Avg. peak (V)	Total shots
-1700*	121	-0.17	-0.035	9398

-1800*	147	-0.27	-0.056	6789
-1900	365	-0.40	-0.068	8904
-2000	482	-0.63	-0.104	9193
-2100	227	-1.06	-0.169	7359
-2200	349	-1.65	-0.256	6915
-2300	442	-2.63	-0.415	8643
-2400	329	-3.86	-0.58	6375
-2500	468	-5.89	-0.883	8740
-2600	294	-8.39	-1.390	4574

Table 8. Single neutron event area vs. HV bias for EJ-200 2nd detector.

HV (volts) EJ-232Q 1st	Neutron events	Avg. area (Vns)	Avg. peak (V)	Total shots
-1700*	159	-0.12	-0.027	9398
-1800*	113	-0.22	-0.051	6789
-1900	206	-0.35	-0.067	8904
-2000	234	-0.59	-0.119	9193
-2100	138	-0.92	-0.188	7359
-2200	149	-1.50	-0.313	6915
-2300	217	-2.50	-0.54	8643
-2400	165	-3.52	-0.752	6375
-2500	235	-5.27	-1.114	8740
-2600	221	-7.16	-1.655	4574

Table 9. Single neutron event area vs. HV bias for EJ-232Q 1st detector.

HV (volts) EJ-232Q 2nd	Neutron events	Avg. area (Vns)	Avg. peak (V)	Total shots
-1700	142	-0.61	-0.114	9398
-1800	261	-1.23	-0.217	6789
-1900	279	-2.14	-0.390	8904
-2000	329	-3.66	-0.709	9193
-2100	187	-5.94	-1.22	7359
-2200	194	-10.75	-2.31	6915
-2300	261	-15.64	-3.55	8643
-2400**	234	-22.78	-5.18	6375
-2500**	321	-28.41	-6.06	8740
-2600**	237	-38.13	-6.86	4574

Table 10. Single neutron event area vs. HV bias for EJ-232Q 2nd detector.

HV (volts) EJ-232Q 3rd	Neutron events	Avg. area (Vns)	Avg. peak (V)	Total shots
-1500	327	-0.221	-0.039	7154
-1600	324	-0.456	-0.081	8590
-1700	299	-0.93	-0.169	8209
-1800	210	-1.44	-0.257	3978
-1900	168	-2.37	-0.47	6125
-2000	216	-4.18	-0.87	6569
-2100	120	-7.03	-1.36	6199
-2200	181	-10.65	-2.20	5733
-2300**	192	-19.12	-4.66	6021
-2400**	121	-28.42	-6.56	2205
-2500**	123	-40.94	-7.97	2034

Table 11. Single neutron event area vs. HV bias for EJ-232Q 3rd detector.

HV (volts) EJ-232Q 4th	Neutron events	Avg. area (Vns)	Avg. peak (V)	Total shots
-1500	312	-0.173	-0.031	7154
-1600	354	-0.357	-0.065	8590
-1700	336	-0.77	-0.139	8209
-1800	196	-1.15	-0.217	3978
-1900	146	-2.42	-0.46	6125
-2000	199	-4.55	-0.92	6569
-2100	149	-7.41	-1.55	6199
-2200	183	-12.76	-2.78	5733
-2300**	189	-21.00	-4.75	6021
-2400**	101	-25.50	-5.83	2205
-2500**	106	-33.50	-6.87	2034

Table 12. Single neutron event area vs. HV bias for EJ-232Q 4th detector.

APPENDIX E

Double plasma mirror setup on the TPW

A pair of uncoated BK7 glass windows was inserted at 45 degrees between the target and the f/40 focusing mirror.

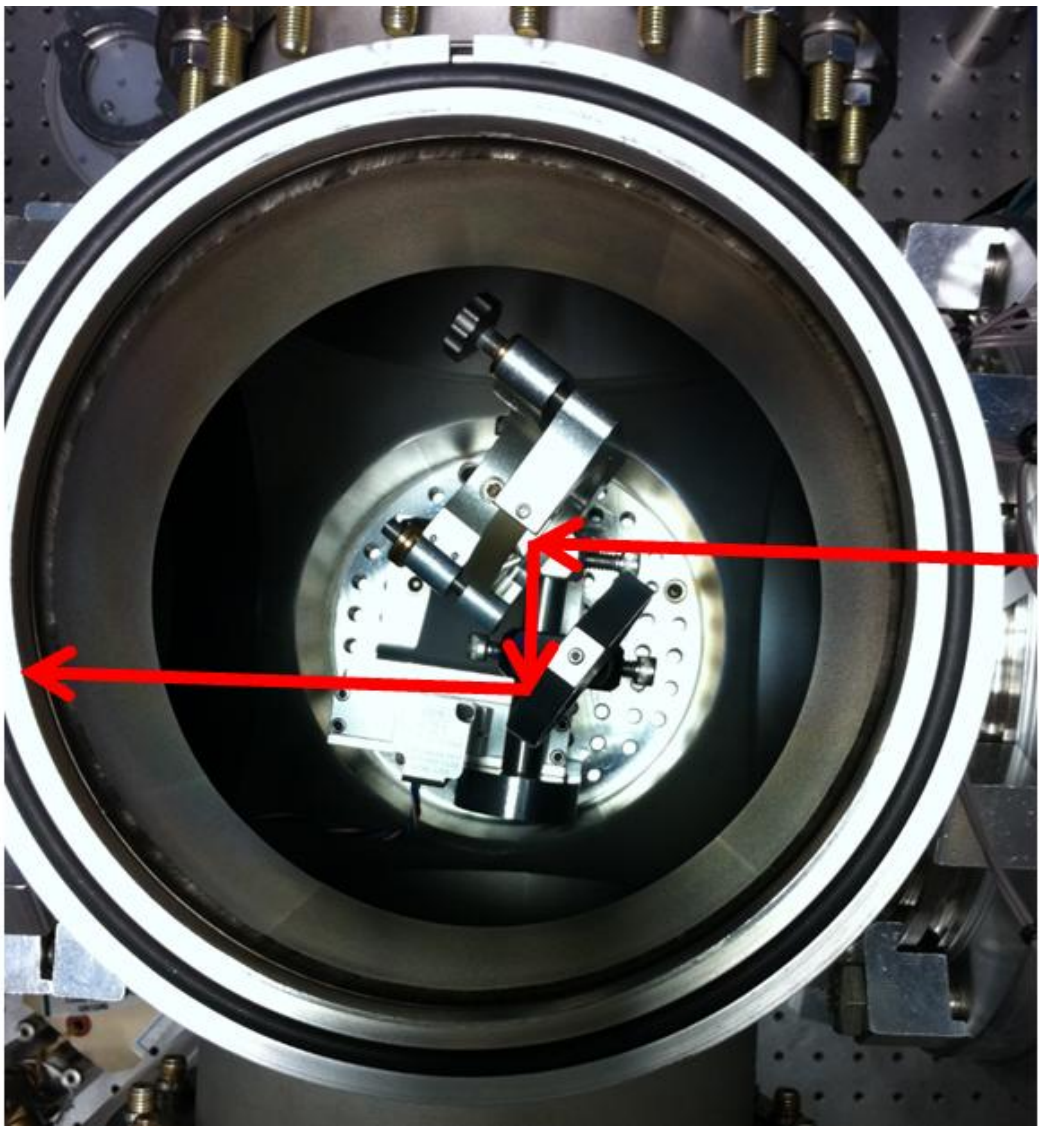

Figure 90. Two plasma mirrors are installed in the chamber. The incoming laser beam path is shown as red lines, and the propagation direction is indicated with arrows.

Figure 91. With plasma mirrors set up, the reflected laser beam from the front surface of each mirror is the rightmost spot on an IR card in our setup. The laser comes from the right. Three reflected beams are shown on an IR card. (Top) These three spots look dim when the ambient light is on. (Bottom)

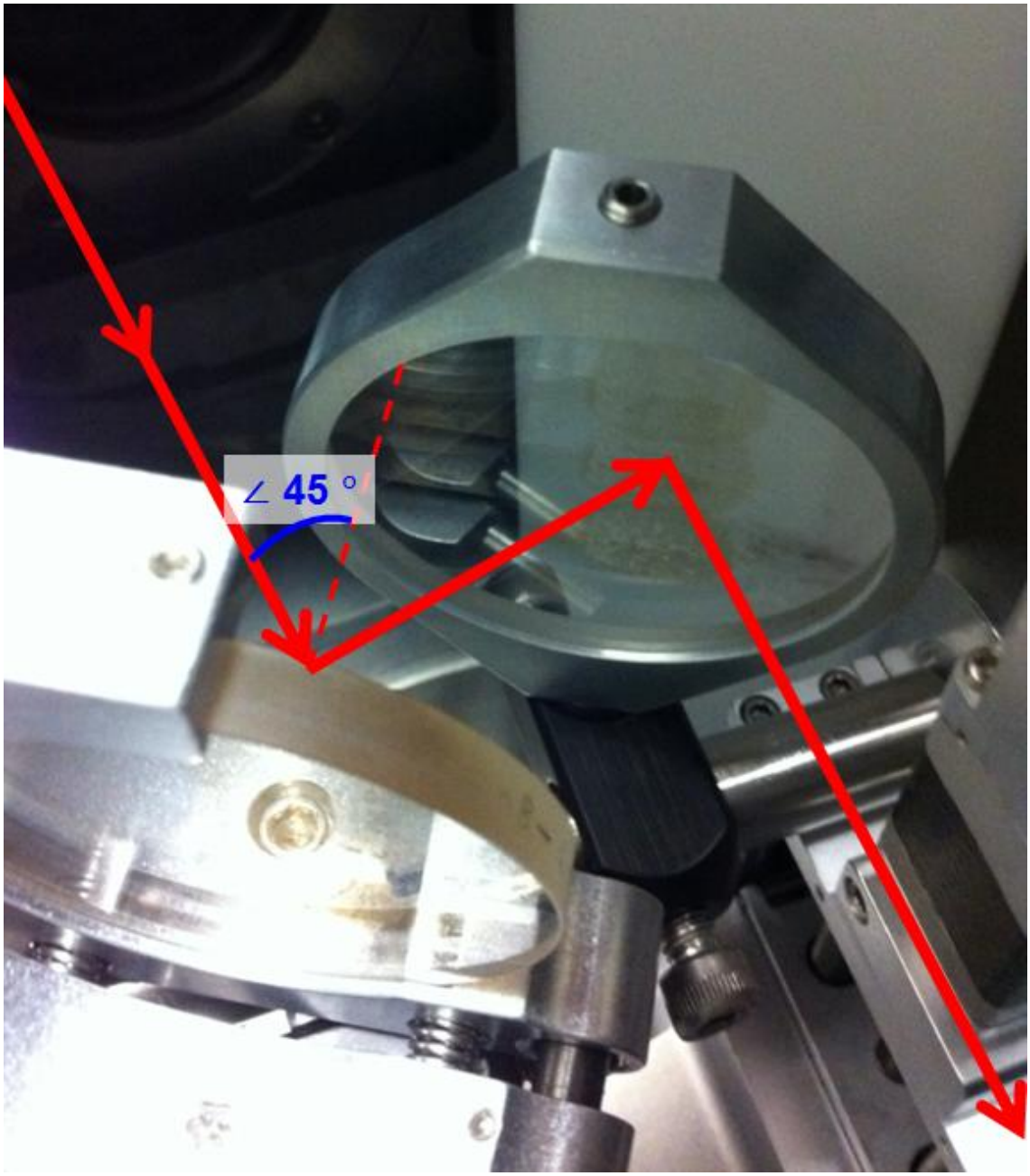

Figure 92. Two used plasma mirrors are shown. The incoming laser beam is at 45 degrees from the surface normal of the mirror as shown in the figure. The beam path is shown as red lines, and the laser propagation direction is indicated with arrows. Three burn marks are shown on each mirror because this image was taken after three full energy shots. After three system shots, we rotated the mirrors by 180 degrees, and used for three more shots.

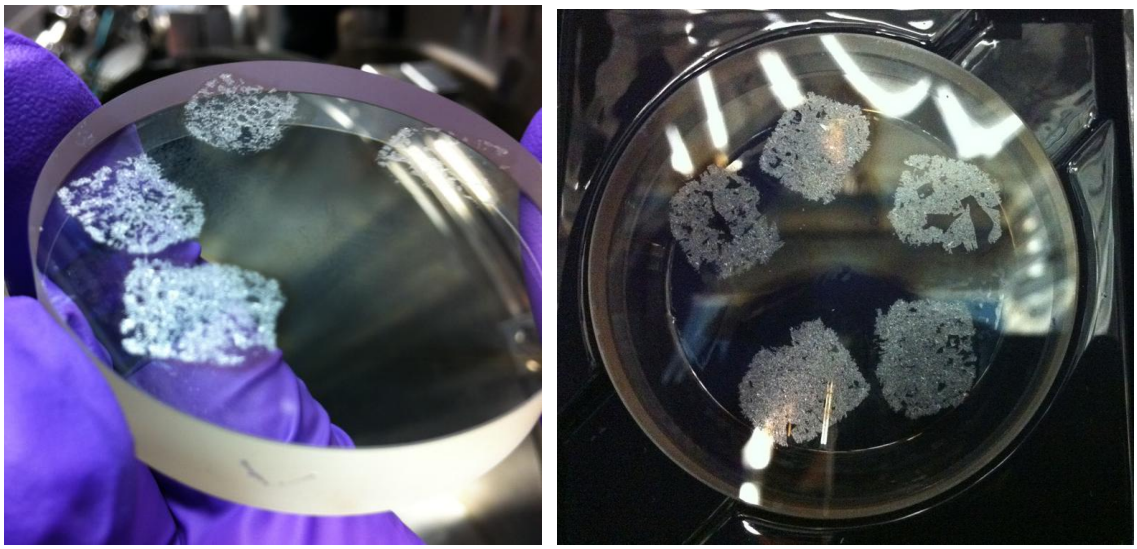

Figure 93. A used plasma mirror after 4 full energy shots is shown (left). Four distinct burn marks are shown on the surface of the glass plate. A different plasma mirror after 5 full energy shots are shown also (right).

APPENDIX F

Alternative detection method for 3 MeV & 14.7 MeV protons – CR-39 stacks

We want to measure 3 MeV protons or 14.7 MeV protons while blocking any other charged particles such as T(1.01 MeV), ^{3}He (0.82 MeV), and ^{4}He (3.6 MeV). For this purpose, we can start with the following design shown in Figure 94.

Again, the expected fusion reactions are:

1. D + D → T (1.01 MeV) + p (3.02 MeV) (50%)
2. D + D → ^{3}He (0.82 MeV) + n (2.45 MeV) (50%)
3. D + ^{3}He → ^{4}He (3.6 MeV) + p (14.69 MeV) (100%)

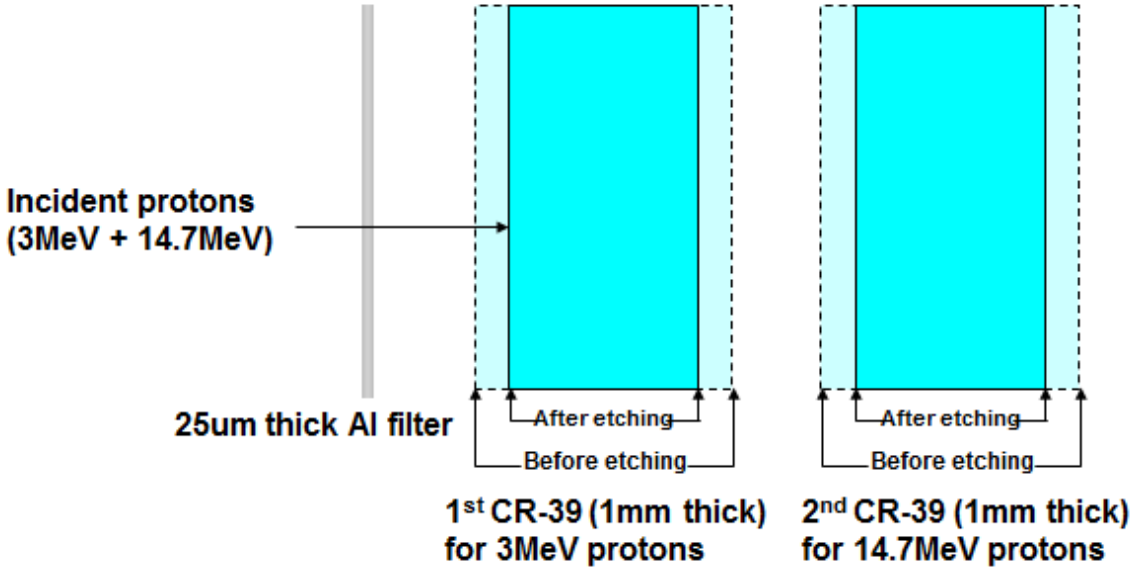

Figure 94. Schematic drawing of the CR-39 track detector for proton yield measurements.

The above design is based on the following calculations using the TRIM code.[50] Figure 95.(a), (b), and (c) show that 25 μm aluminum filter can block all the other charged particles.

(a) Input beam: 1.01 MeV Tritium, Range: 9.94 um

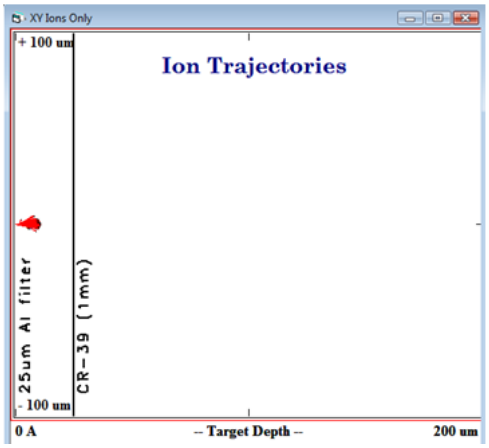

(b) Input beam: 0.82 MeV ^{3}He ion, Range: 2.57 um

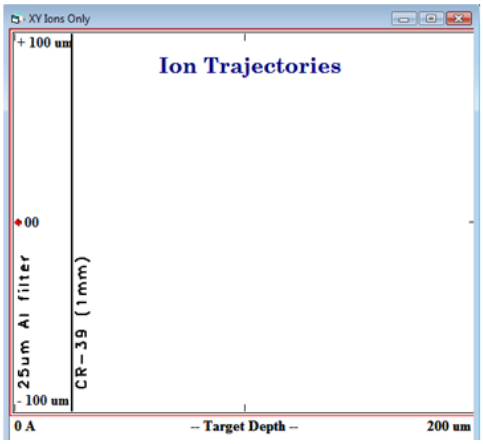

(c) Input beam: 3.6 MeV ^{4}He ion, Range: 13.6 um

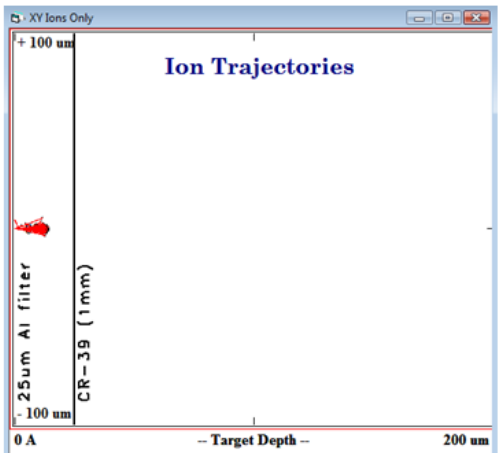

Figure 95. (a) Range of the 1 MeV tritium ion, (b) range of the 0.82 MeV ^{3}He, and (c) range of the 3.6 MeV ^{4}He ion in a 25 mm thick aluminum filter

When we design the detectors just as in Figure 94, the energy loss of the proton at the surface of the second CR-39 is expected to be about 0.6 eV/Å according to the SRIM calculation shown in Figure 96 (b).

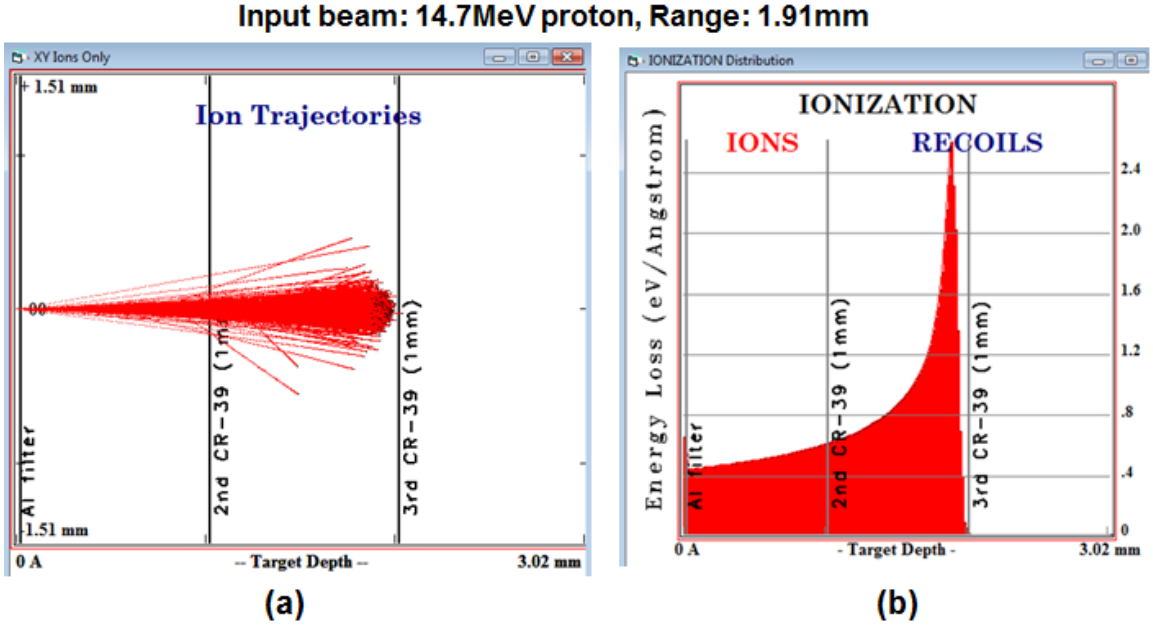

Figure 96. (a) Trajectories of the 14.7 MeV protons are shown in an XY plane. (b) Energy loss per angstrom is shown as a function of the penetration depth for 14.7 MeV protons.

We can modify the initial design by inserting a 400 mm thick aluminum filter between the two CR-39 detectors to increase the dE/dx of the 14.7 MeV protons at the surface of the second CR-39. Then, we will have bigger tracks on the second CR-39 after etching. The simulation results are shown in Figure 97 (a) and (b). At the surface of the second CR-39, the energy loss per angstrom is about 1 eV/Å, and we expect bigger tracks after NaOH etching.

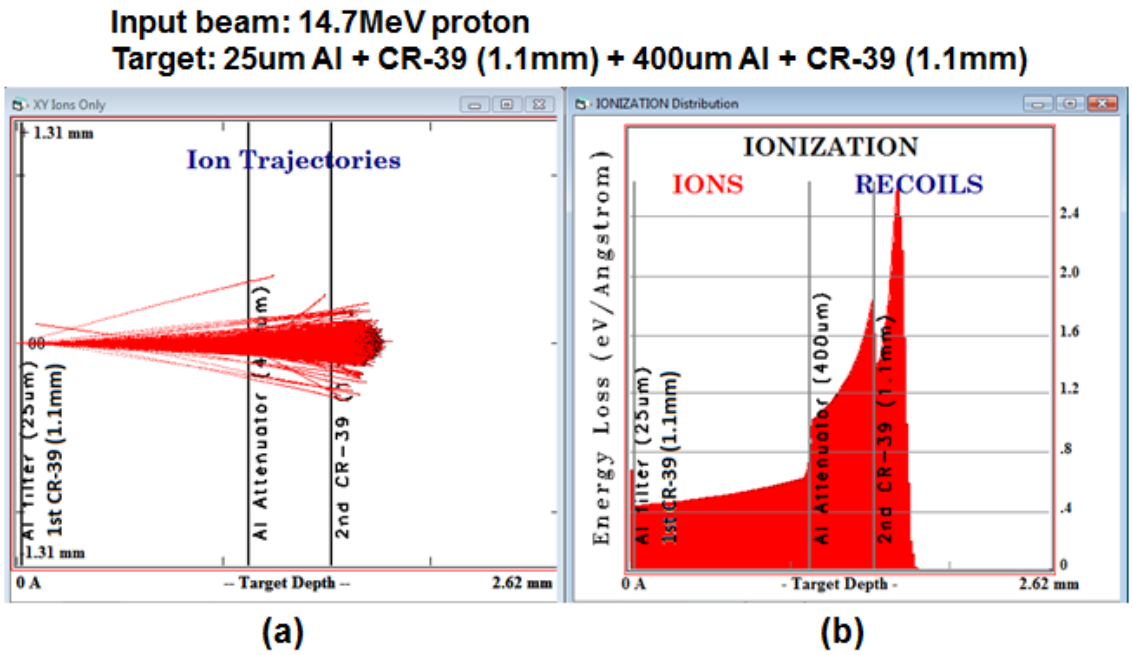

Figure 97. (a) Trajectories of the 14.7 MeV protons are shown in an XY plane. (b) Energy loss per angstrom is shown as a function of the penetration depth with a modified design for the detector.

References

[1]P. A. Franken, A. E. Hill, C. W. Peters, and G. Weinreich, Phys. Rev. Lett. **7,** 118 (1961).

[2]M. Lewenstein, P. Balcou, M. Y. Ivanov, A. Lâ€™Huillier, and P. B. Corkum, Phys. Rev. A **49,** 2117 (1994).

[3]M. D. Perry and G. Mourou, Science **264,** 917 (1994).

[4]T. Ditmire, R. A. Smith, J. W. G. Tisch, and M. H. R. Hutchinson, Phys. Rev. Lett. **78,** 3121 (1997).

[5]M. Protopapas, C. H. Keitel, and P. L. Knight, Rep. Prog. Phys. **60,** 389 (1997).

[6]Y. I. Salamin, S. X. Hu, K. Z. Hatsagortsyan, and C. H. Keitel, Physics Reports **427,** 41 (2006).

[7]A. Modena, Z. Najmudin, A. E. Dangor, C. E. Clayton, K. A. Marsh, C. Joshi, V. Malka, C. B. Darrow, C. Danson, D. Neely, and F. N. Walsh, Nature **377,** 606 (1995).

[8]N. Bloembergen, R. K. Chang, S. S. Jha, and C. H. Lee, Phys. Rev. **174,** 813 (1968).

[9]G. A. Mourou, T. Tajima, and S. V. Bulanov, Reviews of Modern Physics **78,** 309 (2006).

[10]E. Esarey, C. B. Schroeder, and W. P. Leemans, Reviews of Modern Physics **81,** 1229 (2009).

[11]T. E. Cowan, A. W. Hunt, T. W. Phillips, S. C. Wilks, M. D. Perry, C. Brown, W. Fountain, S. Hatchett, J. Johnson, M. H. Key, T. Parnell, D. M. Pennington, R. A. Snavely, and Y. Takahashi, Phys. Rev. Lett. **84,** 903 (2000).

[12]Y. Jiang, T. Lee, W. Li, G. Ketwaroo, and C. G. Rose-Petruck, Opt. Lett. **27,** 963 (2002).

[13]R. A. Snavely, M. H. Key, S. P. Hatchett, T. E. Cowan, M. Roth, T. W. Phillips, M. A. Stoyer, E. A. Henry, T. C. Sangster, M. S. Singh, S. C. Wilks, A. MacKinnon, A. Offenberger, D. M. Pennington, K. Yasuike, A. B. Langdon, B. F. Lasinski, J. Johnson, M. D. Perry, and E. M. Campbell, Phys. Rev. Lett. **85,** 2945 (2000).

[14]A. Macchi, F. Cattani, T. V. Liseykina, and F. Cornolti, Phys. Rev. Lett. **94,** 165003 (2005).

[15]E. L. Clark, K. Krushelnick, J. R. Davies, M. Zepf, M. Tatarakis, F. N. Beg, A. Machacek, P. A. Norreys, M. I. K. Santala, I. Watts, and A. E. Dangor, Phys. Rev. Lett. **84,** 670 (2000).

[16]T. Ditmire, J. Zweiback, V. P. Yanovsky, T. E. Cowan, G. Hays, and K. B. Wharton, Nature **398,** 489 (1999).

[17]J. Zweiback, R. A. Smith, T. E. Cowan, G. Hays, K. B. Wharton, V. P. Yanovsky, and T. Ditmire, Phys. Rev. Lett. **84,** 2634 (2000).

[18]K. W. Madison, P. K. Patel, D. Price, A. Edens, M. Allen, T. E. Cowan, J. Zweiback, and T. Ditmire, Phys. Plasmas **11,** 270 (2004).

[19]P. B. Parks, T. E. Cowan, R. B. Stephens, and E. M. Campbell, Phys. Rev. A **63,** 063203 (2001).

[20]G. Grillon, P. Balcou, J. P. Chambaret, D. Hulin, J. Martino, S. Moustaizis, L. Notebaert, M. Pittman, T. Pussieux, A. Rousse, J. P. Rousseau, S. Sebban, O. Sublemontier, and M. Schmidt, Phys. Rev. Lett. **89,** 065005 (2002).
[21]I. Last and J. Jortner, Phys. Rev. Lett. **87,** 033401 (2001).
[22]P. B. Corkum, Phys. Rev. Lett. **71,** 1994 (1993).
[23]F. Krausz and M. Ivanov, Reviews of Modern Physics **81,** 163 (2009).
[24]A. W. Castleman and R. G. Keesee, Science **241,** 36 (1988).
[25]J. Zweiback, T. E. Cowan, R. A. Smith, J. H. Hartley, R. Howell, C. A. Steinke, G. Hays, K. B. Wharton, J. K. Crane, and T. Ditmire, Phys. Rev. Lett. **85,** 3640 (2000).
[26]E. W. Gaul, M. Martinez, J. Blakeney, A. Jochmann, M. Ringuette, D. Hammond, T. Borger, R. Escamilla, S. Douglas, W. Henderson, G. Dyer, A. Erlandson, R. Cross, J. Caird, C. Ebbers, and T. Ditmire, Appl. Opt. **49,** 1676 (2010).
[27]T. Ditmire, S. Bless, G. Dyer, A. Edens, W. Grigsby, G. Hays, K. Madison, A. Maltsev, J. Colvin, M. J. Edwards, R. W. Lee, P. Patel, D. Price, B. A. Remington, R. Sheppherd, A. Wootton, J. Zweiback, E. Liang, and K. A. Kielty, Radiat. Phys. Chem. **70,** 535 (2004).
[28]W. Bang, H. J. Quevedo, G. Dyer, J. Rougk, I. Kim, M. McCormick, A. C. Bernstein, and T. Ditmire, Rev. Sci. Instrum. **83,** 063504 (2012).
[29]A. P. Higginbotham, O. Semonin, S. Bruce, C. Chan, M. Maindi, T. D. Donnelly, M. Maurer, W. Bang, I. Churina, J. Osterholz, I. Kim, A. C. Bernstein, and T. Ditmire, Rev. Sci. Instrum. **80,** 063503 (2009).
[30]W. Bang, M. Barbui, A. Bonasera, G. Dyer, H. J. Quevedo, K. Hagel, K. Schmidt, F. Consoli, R. D. Angelis, P. Andreoli, E. Gaul, T. Borger, A. C. Bernstein, M. Martinez, M. Donovan, M. Barbarino, S. Kimura, J. Sura, J. Natowitz, and T. Ditmire, Phys. Rev. Lett. (In preparation).
[31]W. Bang, G. Dyer, H. J. Quevedo, J. Rougk, E. Gaul, T. Borger, F. Aymond, M. Martinez, M. Donovan, A. C. Bernstein, and T. Ditmire, Phys. Plasmas (In preparation).
[32]G. Doumy, F. QuÃ©rÃ©, O. Gobert, M. Perdrix, P. Martin, P. Audebert, J. C. Gauthier, J. P. Geindre, and T. Wittmann, Phys. Rev. E **69,** 026402 (2004).
[33]A. Lévy, T. Ceccotti, P. D'Oliveira, F. Réau, M. Perdrix, F. Quéré, P. Monot, M. Bougeard, H. Lagadec, P. Martin, J.-P. Geindre, and P. Audebert, Opt. Lett. **32,** 310 (2007).
[34]V. P. Krainov and M. B. Smirnov, Physics Reports **370,** 237 (2002).
[35]D. Bauer, Laser and Particle Beams **21,** 489 (2003).
[36]P. Agostini, F. Fabre, G. Mainfray, G. Petite, and N. K. Rahman, Phys. Rev. Lett. **42,** 1127 (1979).
[37]Y. Gontier and M. Trahin, Journal of Physics B: Atomic and Molecular Physics **13,** 4383 (1980).
[38]F. Fabre, G. Petite, P. Agostini, and M. Clement, Journal of Physics B: Atomic and Molecular Physics **15,** 1353 (1982).
[39]L. V. Keldysh, Sov. Phys. JETP **20,** 1307 (1964).

[40]L. D. Landau and E. M. Lifshitz, *Quantum Mechanics* (Pergamon, New York, 1965).
[41]M. V. Ammosov, N. B. Delone, and V. P. Krainov, Sov. Phys. JETP **64** (1986).
[42]S. Augst, D. D. Meyerhofer, D. Strickland, and S. L. Chint, J. Opt. Soc. Am. B **8,** 858 (1991).
[43]F. Brunel, Phys. Rev. Lett. **59,** 52 (1987).
[44]B. N. Breizman, A. V. Arefiev, and M. V. Fomyts'kyi, Physics of Plasmas **12,** 056706 (2005).
[45]G. J. Pert, Journal of Physics A: General Physics **5,** 506 (1972).
[46]L. Schlessinger and J. Wright, Phys. Rev. A **20,** 1934 (1979).
[47]R. D. Jones and K. Lee, Physics of Fluids **25,** 2307 (1982).
[48]J. Zweiback, T. E. Cowan, J. H. Hartley, R. Howell, K. B. Wharton, J. K. Crane, V. P. Yanovsky, G. Hays, R. A. Smith, and T. Ditmire, Phys. Plasmas **9,** 3108 (2002).
[49]J. T. Larsen and S. M. Lane, J. Quant. Spectrosc. Radiat. Transfer **51,** 179 (1994).
[50]J. F. Ziegler, M. D. Ziegler, and J. P. Biersack, Nuclear Instruments and Methods in Physics Research Section B: Beam Interactions with Materials and Atoms **268,** 1818 (2010).
[51]H. S. Bosch and G. M. Hale, Nucl. Fusion **32,** 611 (1992).
[52]D. Strickland and G. Mourou, Optics Communications **56,** 219 (1985).
[53]P. Maine, D. Strickland, P. Bado, M. Pessot, and G. Mourou, Quantum Electronics, IEEE Journal of **24,** 398 (1988).
[54]M. D. Perry, D. Pennington, B. C. Stuart, G. Tietbohl, J. A. Britten, C. Brown, S. Herman, B. Golick, M. Kartz, J. Miller, H. T. Powell, M. Vergino, and V. Yanovsky, Opt. Lett. **24,** 160 (1999).
[55]M. Aoyama, K. Yamakawa, Y. Akahane, J. Ma, N. Inoue, H. Ueda, and H. Kiriyama, Opt. Lett. **28,** 1594 (2003).
[56]R. Baumgartner and R. Byer, Quantum Electronics, IEEE Journal of **15,** 432 (1979).
[57]M. Martinez, E. Gaul, T. Borger, F. Aymond, D. Hammond, M. Ringuette, R. Escamilla, T. Ditmire, J. Caird, A. Erlandson, I. Iovanovic, C. Ebbers, and B. Molander, in *Adaptive optics on petawatt lasers: current performance of the Texas Petawatt Laser*, San Francisco, California, USA, 2011 (SPIE), p. 79130H.
[58]D. E. Spence, P. N. Kean, and W. Sibbett, Opt. Lett. **16,** 42 (1991).
[59]B. C. Stuart, M. D. Feit, S. Herman, A. M. Rubenchik, B. W. Shore, and M. D. Perry, J. Opt. Soc. Am. B **13,** 459 (1996).
[60]F. Canova, R. Clady, J.-P. Chambaret, M. Flury, S. Tonchev, R. Fechner, and O. Parriaux, Opt. Express **15,** 15324 (2007).
[61]J. Itatani, J. Faure, M. Nantel, G. Mourou, and S. Watanabe, Optics Communications **148,** 70 (1998).
[62]L. M. Frantz and J. S. Nodvik, J. Appl. Phys. **34,** 2346 (1963).
[63]M. Tanaka, H. Kiriyama, Y. Ochi, Y. Nakai, H. Sasao, H. Okada, H. Daido, P. Bolton, and S. Kawanishi, Optics Communications **282,** 4401 (2009).
[64]K. Ertel, C. Hooker, S. J. Hawkes, B. T. Parry, and J. L. Collier, Opt. Express **16,** 8039 (2008).
[65]W. H. Carter and E. Wolf, J. Opt. Soc. Am. **65,** 1067 (1975).

[66]R. Winston and W. T. Welford, J. Opt. Soc. Am. **69,** 532 (1979).
[67]J. Vrabec, G. K. Kedia, and H. Hasse, Cryogenics **45,** 253 (2005).
[68]O. F. Hagena, Rev. Sci. Instrum. **63,** 2374 (1992).
[69]F. Dorchies, F. Blasco, T. Caillaud, J. Stevefelt, C. Stenz, A. S. Boldarev, and V. A. Gasilov, Phys. Rev. A **68,** 023201 (2003).
[70]R. A. Smith, T. Ditmire, and J. W. G. Tisch, Rev. Sci. Instrum. **69,** 3798 (1998).
[71]H. Lu, G. Ni, R. Li, and Z. Xu, J. Chem. Phys. **132,** 124303 (2010).
[72]T. Ditmire, E. Springate, J. W. G. Tisch, Y. L. Shao, M. B. Mason, N. Hay, J. P. Marangos, and M. H. R. Hutchinson, Phys. Rev. A **57,** 369 (1998).
[73]A. J. Bell, J. M. Mestdagh, J. Berlande, X. Biquard, J. Cuvellier, A. Lallement, P. Meynadier, O. Sublemontier, and J. P. Visticot, J. Phys. D: Appl. Phys. **26,** 994 (1993).
[74]A. Dewaele, J. H. Eggert, P. Loubeyre, and R. Le Toullec, Phys. Rev. B **67,** 094112 (2003).
[75]D. S. Ayres, A. M. Cormack, A. J. Greenberg, R. W. Kenney, D. O. Caldwell, V. B. Elings, W. P. Hesse, and R. J. Morrison, Physica **43,** 105 (1969).
[76]R. Kodama, P. A. Norreys, K. Mima, A. E. Dangor, R. G. Evans, H. Fujita, Y. Kitagawa, K. Krushelnick, T. Miyakoshi, N. Miyanaga, T. Norimatsu, S. J. Rose, T. Shozaki, K. Shigemori, A. Sunahara, M. Tampo, K. A. Tanaka, Y. Toyama, T. Yamanaka, and M. Zepf, Nature **412,** 798 (2001).
[77]M. D. Cable and S. P. Hatchett, J. Appl. Phys. **62,** 2233 (1987).
[78]J. D. Strachan, H. Adler, P. Alling, C. Ancher, H. Anderson, J. L. Anderson, D. Ashcroft, C. W. Barnes, G. Barnes, S. Batha, M. G. Bell, R. Bell, M. Bitter, W. Blanchard, N. L. Bretz, R. Budny, C. E. Bush, R. Camp, M. Caorlin, S. Cauffman, Z. Chang, C. Z. Cheng, J. Collins, G. Coward, D. S. Darrow, J. DeLooper, H. Duong, L. Dudek, R. Durst, P. C. Efthimion, D. Ernst, R. Fisher, R. J. Fonck, E. Fredrickson, N. Fromm, G. Y. Fu, H. P. Furth, C. Gentile, N. Gorelenkov, B. Grek, L. R. Grisham, G. Hammett, G. R. Hanson, R. J. Hawryluk, W. Heidbrink, H. W. Herrmann, K. W. Hill, J. Hosea, H. Hsuan, A. Janos, D. L. Jassby, F. C. Jobes, D. W. Johnson, L. C. Johnson, J. Kamperschroer, H. Kugel, N. T. Lam, P. H. LaMarche, M. J. Loughlin, B. LeBlanc, M. Leonard, F. M. Levinton, J. Machuzak, D. K. Mansfield, A. Martin, E. Mazzucato, R. Majeski, E. Marmar, J. McChesney, B. McCormack, D. C. McCune, K. M. McGuire, G. McKee, D. M. Meade, S. S. Medley, D. R. Mikkelsen, D. Mueller, M. Murakami, A. Nagy, R. Nazikian, R. Newman, T. Nishitani, M. Norris, T. Oâ€™Connor, M. Oldaker, M. Osakabe, D. K. Owens, H. Park, W. Park, S. F. Paul, G. Pearson, E. Perry, M. Petrov, C. K. Phillips, S. Pitcher, A. T. Ramsey, D. A. Rasmussen, M. H. Redi, D. Roberts, J. Rogers, R. Rossmassler, A. L. Roquemore, E. Ruskov, S. A. Sabbagh, M. Sasao, G. Schilling, J. Schivell, G. L. Schmidt, S. D. Scott, R. Sissingh, C. H. Skinner, J. A. Snipes, J. Stevens, T. Stevenson, B. C. Stratton, E. Synakowski, W. Tang, G. Taylor, J. L. Terry, M. E. Thompson, M. Tuszewski, C. Vannoy, A. von Halle, S. von Goeler, D. Voorhees, R. T. Walters, R. Wieland, J. B. Wilgen, M. Williams, J. R. Wilson, K. L. Wong, G. A. Wurden, M. Yamada,

K. M. Young, M. C. Zarnstorff and S. J. Zweben, Phys. Rev. Lett. **72,** 3526 (1994).
[79]C. L. Ruiz, R. J. Leeper, F. A. Schmidlapp, G. Cooper, and D. J. Malbrough, Rev. Sci. Instrum. **63,** 4889 (1992).
[80]B. Wolle, F. Gadelmeier, G. Beikert, K. Hubner, and R. Batzner, Rev. Sci. Instrum. **70,** 1190 (1999).
[81]G. W. Cooper and C. L. Ruiz, Rev. Sci. Instrum. **72,** 814 (2001).
[82]C. L. Ruiz, G. W. Cooper, S. A. Slutz, J. E. Bailey, G. A. Chandler, T. J. Nash, T. A. Mehlhorn, R. J. Leeper, D. Fehl, A. J. Nelson, J. Franklin, and L. Ziegler, Phys. Rev. Lett. **93,** 015001 (2004).
[83]J. A. Frenje, C. K. Li, F. H. Seguin, D. G. Hicks, S. Kurebayashi, R. D. Petrasso, S. Roberts, V. Y. Glebov, D. D. Meyerhofer, T. C. Sangster, J. M. Soures, C. Stoeckl, C. Chiritescu, G. J. Schmid, and R. A. Lerche, Rev. Sci. Instrum. **73,** 2597 (2002).
[84]M. Jose, B. Lipo, E. M. Roberto, S. Patricio, and S. Leopoldo, Meas. Sci. Technol. **19,** 087002 (2008).
[85]K. W. Madison, P. K. Patel, M. Allen, D. Price, and T. Ditmire, J. Opt. Soc. Am. B **20,** 113 (2003).
[86]K. W. Madison, P. K. Patel, M. Allen, D. Price, R. Fitzpatrick, and T. Ditmire, Phys. Rev. A **70,** 053201 (2004).
[87]H. Y. Lu, J. S. Liu, C. Wang, W. T. Wang, Z. L. Zhou, A. H. Deng, C. Q. Xia, Y. Xu, X. M. Lu, Y. H. Jiang, Y. X. Leng, X. Y. Liang, G. Q. Ni, R. X. Li, and Z. Z. Xu, Phys. Rev. A **80,** 051201 (2009).
[88]F. Buersgens, K. W. Madison, D. R. Symes, R. Hartke, J. Osterhoff, W. Grigsby, G. Dyer, and T. Ditmire, Phys. Rev. E **74,** 016403 (2006).
[89]W. Mannhart, Technical Report Series **273,** 415 (1987).
[90]J. W. Meadows, Phys. Rev. **157,** 1076 (1967).
[91]M. B. Chadwick, P. Oblozinsky, M. Herman, N. M. Greene, R. D. McKnight, D. L. Smith, P. G. Young, R. E. MacFarlane, G. M. Hale, S. C. Frankle, A. C. Kahler, T. Kawano, R. C. Little, D. G. Madland, P. Moller, R. D. Mosteller, P. R. Page, P. Talou, H. Trellue, M. C. White, W. B. Wilson, R. Arcilla, C. L. Dunford, S. F. Mughabghab, B. Pritychenko, D. Rochman, A. A. Sonzogni, C. R. Lubitz, T. H. Trumbull, J. P. Weinman, D. A. Brown, D. E. Cullen, D. P. Heinrichs, D. P. McNabb, H. Derrien, M. E. Dunn, N. M. Larson, L. C. Leal, A. D. Carlson, R. C. Block, J. B. Briggs, E. T. Cheng, H. C. Huria, M. L. Zerkle, K. S. Kozier, A. Courcelle, V. Pronyaev, and S. C. van der Marck, Nucl. Data Sheets **107,** 2931 (2006).
[92]R. Hartke, D. R. Symes, F. Buersgens, L. E. Ruggles, J. L. Porter, and T. Ditmire, Nucl. Instrum. Methods Phys. Res. A **540,** 464 (2005).
[93]V. Y. Glebov, D. D. Meyerhofer, C. Stoeckl, and J. D. Zuegel, Rev. Sci. Instrum. **72,** 824 (2001).

[94]N. Sinenian, M. J. Rosenberg, M. Manuel, S. C. McDuffee, D. T. Casey, A. B. Zylstra, H. G. Rinderknecht, M. G. Johnson, F. H. Seguin, J. A. Frenje, C. K. Li, and R. D. Petrasso, Rev. Sci. Instrum. **82,** 103303 (2011).
[95]F. H. Seguin, J. A. Frenje, C. K. Li, D. G. Hicks, S. Kurebayashi, J. R. Rygg, B. E. Schwartz, R. D. Petrasso, S. Roberts, J. M. Soures, D. D. Meyerhofer, T. C. Sangster, J. P. Knauer, C. Sorce, V. Y. Glebov, C. Stoeckl, T. W. Phillips, R. J. Leeper, K. Fletcher, and S. Padalino, Rev. Sci. Instrum. **74,** 975 (2003).
[96]D. T. Casey, J. A. Frenje, F. H. Seguin, C. K. Li, M. J. Rosenberg, H. Rinderknecht, M. J. E. Manuel, M. G. Johnson, J. C. Schaeffer, R. Frankel, N. Sinenian, R. A. Childs, R. D. Petrasso, V. Y. Glebov, T. C. Sangster, M. Burke, and S. Roberts, Rev. Sci. Instrum. **82,** 073502 (2011).
[97]T. Fennel, K. H. Meiwes-Broer, J. Tiggesbaumker, P. G. Reinhard, P. M. Dinh, and E. Suraud, Reviews of Modern Physics **82,** 1793 (2010).
[98]T. Ditmire, T. Donnelly, A. M. Rubenchik, R. W. Falcone, and M. D. Perry, Phys. Rev. A **53,** 3379 (1996).
[99]J. Zweiback and T. Ditmire, Phys. Plasmas **8,** 4545 (2001).
[100]K. J. Mendham, N. Hay, M. B. Mason, J. W. G. Tisch, and J. P. Marangos, Phys. Rev. A **64,** 055201 (2001).
[101]K. B. Wharton, C. D. Boley, A. M. Komashko, A. M. Rubenchik, J. Zweiback, J. Crane, G. Hays, T. E. Cowan, and T. Ditmire, Phys. Rev. E **64,** 025401 (2001).
[102]B. K. F. Young, B. G. Wilson, D. F. Price, and R. E. Stewart, Phys. Rev. E **58,** 4929 (1998).
[103]E. Springate, N. Hay, J. W. G. Tisch, M. B. Mason, T. Ditmire, M. H. R. Hutchinson, and J. P. Marangos, Phys. Rev. A **61,** 063201 (2000).
[104]I. Last and J. Jortner, Phys. Rev. A **60,** 2215 (1999).

Vita

Woosuk Bang was born in Seoul, Korea, in 1980, the son of Hyomu Bang and Bohwa Lee. After an early graduation from the Gyeonggi Science High School, he entered KAIST in 1998. He served military service from 2001 to 2004. He received his B.S. in Physics (Summa Cum Laude) from KAIST in 2005. In fall of 2005, he entered the Physics graduate program of the University of Texas at Austin. He started working for Dr. Ditmire since April, 2006.

Email address: dws223@physics.utexas.edu

This dissertation was typed by the author.